



City Research Online

City, University of London Institutional Repository

Citation: Gowree, E. R. (2014). Influence of Attachment Line Flow on Form Drag.
(Unpublished Doctoral thesis, City University London)

This is the accepted version of the paper.

This version of the publication may differ from the final published version.

Permanent repository link: <https://openaccess.city.ac.uk/id/eprint/12239/>

Link to published version:

Copyright: City Research Online aims to make research outputs of City, University of London available to a wider audience. Copyright and Moral Rights remain with the author(s) and/or copyright holders. URLs from City Research Online may be freely distributed and linked to.

Reuse: Copies of full items can be used for personal research or study, educational, or not-for-profit purposes without prior permission or charge. Provided that the authors, title and full bibliographic details are credited, a hyperlink and/or URL is given for the original metadata page and the content is not changed in any way.

Influence of Attachment Line Flow on Form Drag

By

Erwin R. Gowree

School of Engineering and Mathematical Sciences
City University London

Thesis submitted as part of the requirement for the fulfilment of
a degree of Doctor of Philosophy

May 20, 2014

Contents

List of Figures	viii
List of Tables	xxvi
Acknowledgement	1
Declaration	2
Summary	3
Nomenclature	6
1 Introduction	12
1.1 Economical and Enviromental Considerations	13
1.2 Optimisation of Mission Performance	17
1.3 Drag	18
1.4 Transition and Flow Control	21
1.5 Aim of Current Study	26

1.6	Overview of Thesis	27
2	The Prediction of Turbulent Boundary Layers and Viscous Drag on Swept Wings	29
2.1	Infinite Swept Wing Condition	29
2.2	Two-Dimensional Momentum Integral Method	34
2.2.1	Entrainment in Turbulent Boundary Layers	37
2.2.2	Equilibrium in Turbulent Boundary Layers	38
2.2.3	The Effect of Lag in Entrainment	40
2.3	Three-Dimensional Momentum Integral Method	45
2.4	Numerical Modelling in Callisto	48
2.4.1	Governing Equations	49
2.4.2	Solution of Governing Equations	52
2.4.3	Attachment Line Modelling	54
2.5	Validation of Callisto against Experiment	55
2.5.1	Callisto Coupled with Garabedian and Korn's Method	55
2.5.2	Summary of Experimental Test Cases Used for Validation	56
2.5.3	Prediction of Pressure Distribution	58
2.5.4	Prediction of Sectional or Profile Drag	62

2.5.5	Break-down of Drag Components	65
2.6	Drag Reduction through Attachment Line Control	68
2.7	Approximations in the Numerical Method	74
3	Experiment and Instrumentation	79
3.1	Designing the Experimental Model	79
3.1.1	Estimation of Model Dimensions	80
3.1.2	Experimental Domain Length	82
3.1.3	Attachment Line Boundary Layer Thickness	84
3.1.4	The Experimental Model	85
3.2	Surface Pressure Measurement	87
3.3	Boundary Layer Traverse	88
3.4	Hot Wire Measurements	91
3.5	Optical Micro-Measurement Technique	93
3.5.1	Principle and Set-Up	94
3.5.2	Calibration of the Optical System	96
3.5.3	Commissioning the Traverse Gear	98
3.5.4	Near Wall Alignment of Hot Wire Probes	100
3.6	Wall Shear Stress Measurement using Preston's Technique	109

4	Hot Wire Anemometry	112
4.1	Principle of Operation	112
4.2	Measurement of a Single Velocity Component	113
4.2.1	Response of a Single-Normal Probe	113
4.2.2	Calibration of Single-Normal Probe	116
4.2.3	Correction for Temperature Drift	117
4.3	Measurement of Two Velocity Components	122
4.3.1	Response of Single-Yawed Probe	122
4.3.2	Calibration of a Single-Yawed Probe	125
4.4	Data Analysis	133
4.4.1	Velocity Measurement Using Single-Normal Probes	133
4.4.2	Velocity Measurement Using Single-Yawed Probes	133
5	The Flow at the Attachment Line	139
5.1	Inviscid Flow along the Leading Edge of an Infinite Yawed Cylinder . . .	139
5.2	The Attachment Line Boundary Layer	144
5.2.1	Laminar Attachment Line	146
5.2.2	Turbulent Attachment Line	149
5.3	Attachment Line Contamination and Instability	156

5.3.1	Attachment Line Contamination	156
5.3.2	Attachment Line Instability	159
5.3.3	Attachment Line Control	164
5.4	Present Experimental Measurements	169
5.4.1	Attachment Line Static Pressure	169
5.4.2	Attachment Line Hot-wire Signal	171
5.4.3	Laminar Attachment Line	173
5.4.4	Turbulent Attachment Line	175
5.4.5	Relation Between Turbulent R_θ and \bar{R}	181
5.4.6	Empirical Relation for Turbulent Attachment Line	184
5.4.7	Attachment Line Control	188
6	The Flow Near the Attachment Line	194
6.1	Topology of Viscous Three Dimensional Flows	194
6.2	Viscous Flow on Swept Wings	198
6.2.1	Laminar and Transitional	198
6.2.2	Turbulent	200
6.2.3	Relaminarisation Downstream of Turbulent Attachment Line . . .	206
6.3	Present Experimental Measurements	208

6.3.1	Surface Pressure Measurement	208
6.3.2	Velocity Profiles at the Attachment Line	209
6.3.3	Streamwise Velocity Profiles Downstream of Attachment Line	213
6.3.4	Crossflow Velocity Profiles Downstream of Attachment Line	220
6.3.5	Cross-over Velocity Profiles	226
6.3.6	Estimation of Surface Shear Stress	230
6.3.7	Evolution of the Boundary Layer	232
6.3.8	Possibility of Relaminarisation	236
7	Leading Edge Modelling in Callisto	240
7.1	Comparison of Callisto against Current Experiment	240
7.2	Modification of Momentum Integral Equation at the Leading Edge	243
7.3	Comparison of Modified Callisto against Experiment	247
7.4	Attachment Line Control Revisited	253
8	Conclusions	256
8.1	Main Objective	256
8.2	Experiment	256
8.3	Numerical Analysis	258
8.4	Recommendation for Further Work	258

References	260
A The Numerical Method	271
A.1 The functions f_1 to f_4	271
A.2 Closure Relationships	272
B Experimental Model	275
B.1 Location of pressure tappings	275
C Uncertainty Analysis	277
C.1 Pressure and Velocity Measurements	277
C.2 Traverse Mechanism and Optical System	279
C.3 Hot-wire Measurements	280

List of Figures

1.1	The yearly average nominal and inflation adjusted crude oil price per barrel. Data accessed on the 21st October 2013 from www.inflation.com . . .	14
1.2	Break down of the GHG emission in 2001 from all the industry in the USA presented by the FAA.	14
1.3	Schematic representation of the composition of the exhaust gases exiting a jet engine during both ideal and actual combustion cases from, Green [50].	15
1.4	The breakdown of the drag arising from the external flow around and aircraft, from Torenbeek [118]	19
1.5	The percentage break-down of the total drag from a large commercial aircraft, from Marec [78]. Where the ‘friction’ drag represents all viscous drag	20
1.6	Common wing tip devices used for reduction of induced drag. Figures obtained from www.airliners.net	20
1.7	Schematic representation of the mechanism of transition	22
1.8	Schematic representation of the three main types of instabilities that might occur on a swept wing, from Joslin [66]	23

1.9	Demonstrators of NLF in flight.	24
1.10	Demonstrators of HLFC in flight.	25
2.1	Schematic representation of the streamline on a swept and slightly tapered wing	29
2.2	The axis and velocity vector convention based on the infinite-sweep assumption	30
2.3	Schematic representation of the non-orthogonal coordinates system in Callisto, from Atkin [12]	49
2.4	A graphical representation of the RAE 5237 and 5240 symmetrical aerofoil. 57	
2.5	The pressure distribution around an unswept RAE 5225 aerofoil measured experimentally by and computed using BVGK and 2D CVGK.	59
2.6	Zero-lift pressure distribution on the RAE 5237 and RAE 5240 sections swept at $\Lambda = 25^\circ$ and $Re = 14.4 \times 10^6/m$. Comparison between experimental, 2D BVGK with sweep transformation and 3D (infinite-swept) CVGK analysis	60
2.7	Zero-lift pressure distribution on the RAE 5237 and RAE 5240 sections swept at $\Lambda = 25^\circ$ and $Re = 31.2 \times 10^6/m$. Comparison between experimental, 2D BVGK with sweep transformation and 3D (infinite-swept) CVGK analysis	61
2.8	Zero-lift pressure distribution for high Mach number case on the RAE 5237 and RAE 5240 sections swept at $\Lambda = 25^\circ$ and $Re = 14.4 \times 10^6/m$ and $31.2 \times 10^6/m$. Comparison between experimental, 2D BVGK with sweep transformation and 3D (infinite-swept) CVGK analysis	62

2.9	Comparison between experimental and numerical results obtained from BVGK and CVGK on the unswept RAE 5225 aerofoil.	63
2.10	Zero-lift profile drag for the RAE 5237 (top) and 5240 (bottom) section swept at $\Lambda = 25^\circ$ and $Re = 14.4 \times 10^6/m$. Comparison between experimental, 2D BVGK with sweep transformation and 3D (infinite-swept) CVGK analysis.	64
2.11	Zero-lift profile drag for the RAE 5237 (top) and 5240 (bottom) section swept at $\Lambda = 25^\circ$ and $Re = 31.2 \times 10^6/m$. Comparison between experimental, 2D BVGK with sweep transformation and 3D (infinite-swept) CVGK analysis.	65
2.12	Comparison of the two dimensional friction (top) and form (bottom) drag estimated from BVGK, unswept CVGK and by transforming the results from the swept CVGK calculation to two dimension using the transformation in section 2.1 at $Re = 31.2 \times 10^6/m$	67
2.13	Comparison of the three dimensional friction (top) and form (bottom) drag estimated from swept CVGK calculation and the unswept BVGK and CVGK calculations where the results were transformed into the equivalent three dimension using the transformation in section 2.1 at $Re = 31.2 \times 10^6/m$	68
2.14	Difference in drag between the turbulent attachment line and the laminar cases with varying transition location on the upper surface but fixed at 1% chord on the lower surface	70
2.15	Development of the streamwise momentum thickness along the aerofoil and in the far wake for the fully turbulent case and those with transition downstream.	71

2.16	A 'zoom-in' the region of $0.9 < x/c < 1.1$ from figure 2.15 to better demonstrate the reduction in the streamwise momentum thickness.	72
2.17	The pressure distribution and the development of the displacement thickness on the upper surface of the supercritical aerofoil.	73
2.18	A 'zoom-in' the region of $0.9 < x/c < 1.1$ from figure 2.17 to show the reduction in the streamwise displacement thickness.	74
2.19	The local skin friction coefficient on the upper surface of the supercritical aerofoil for a fully turbulent case and those with transition downstream. . .	75
2.20	The inviscid flow at the vicinity of the attachment line	75
3.1	Comparison between a NACA 0050 and a circular cylinder profile faired to a teardrop	81
3.2	The pressure distribution predicted by CVGK around a NACA0050 aerofoil swept by 60°	81
3.3	Schematic representation of the external streamline starting from the attachment and evolving downstream.	83
3.4	GA drawing of the experimental model	86
3.5	The swept panel wing mounted between the floor and the ceiling of the T2 wind tunnel.	87
3.6	Schematic representation of the traverse mechanism to illustrate the main components.	90
3.7	Side and top view of the traverse mechanism.	90

3.8	The single-normal boundary layer probe for single velocity component measurement and single-yawed probe slanted by 45° for two velocity component measurement (pictures extracted from Dantec Dynamics catalogue).	91
3.9	Set-up for the HWA data acquisition	92
3.10	Schematic representation of optical set-up illustrating the principle of operation	94
3.11	Photographic representation of the of the optical set-up	96
3.12	Snap shot of the spacing of 300μ between the jaws of a digital calliper	97
3.13	Digitised image showing the greyscale intensity of the spacing between the jaws of the calliper	97
3.14	Binarised plot of the colour intensity with threshold placed at 1.5×10^4	97
3.15	Photographic image of the hot wire before (LHS) and after (RHS) 1 step displacement generated by the traverse gear	99
3.16	The baseline and the final intensity trace after 1 step displacement of the hot wire	99
3.17	Photographic image of the hot wire before (LHS) and after (RHS) 40 step displacement generated by the traverse gear	100
3.18	The baseline and the final intensity trace after 40 steps displacement of the hot wire	100
3.19	Schematic representation of the optical set-up illustrating the principle of the dual magnification phase	101

3.20	Set-up for the alignment of the hot wire probe on a flat plate	102
3.21	The real and reflected image of the probe captured using the CCD camera during the alignment on the flat plate	103
3.22	Colour intensity trace of the real and reflected image along the axis touch- ing the tips of the hot wire support	103
3.23	The blurred image of the side view of the probe support and wind tunnel model obtained from the dual magnification phase set-up shown in figure 3.19	104
3.24	The modified optical set-up using a single lens for near-wall positioning .	105
3.25	The side view of the probe support and wind tunnel model obtained from the modified set-up shown in figure 3.24	105
3.26	The optical set-up on an inclined optical bed and the extension bracket to support the probe for measurements downstream of the attachment line. .	107
3.27	The side view of the probe support and wind tunnel model at the down- stream measurement stations	108
3.28	Alignment of the hot wire support	108
3.29	Schematic representation of surface shear stress measurement using Pre- ston's method where the static pressure is obtained from the surface pres- sure tapping.	111
3.30	Schematic and photographic representation of surface shear stress mea- surement device using Preston's method where static pressure is obtained from the static tube mounted on top of the Pitot tube.	111

4.1	Response of the hot wire probe with a velocity vector normal to the sensor wire, figure adapted from Bruun [21], p.84	115
4.2	Schematic representation of the hot wire probe mounted along the tunnel centre-line for calibration.	116
4.3	The Power law relation expressed by equation 4.6	117
4.4	Change in the temperature of the freestream air inside the tunnel working section with respect to speed during the calibration test.	119
4.5	The Power law relation expressed by equation 4.10	120
4.6	The hot-wire voltage output with change in temperature during the wind-off test	121
4.7	The Power law relation expressed by equation 4.10, where A has been adjusted based on equation 4.14	121
4.8	Break-down of the velocity components based on the hot-wire sensor coordinates system, figure adapted from Bruun [21], p.72	122
4.9	Variation of the yaw coefficients with changes in the yaw angle at $\beta = 0$ and $\beta = 90^\circ$, from Bruun [21]	124
4.10	Schematic representation of the hot wire probe mounted along the tunnel centre-line for calibration and connected to the six component balance for yaw calibration	126
4.11	Velocity calibration of SY probe yawed by 45° in the starboard side	127
4.12	Yaw calibration of the SY probe at constant velocity with the probe initially orientated in the clockwise direction, for the estimation of α_e	130

4.13	Yaw calibration of the SY probe at constant velocity with the probe initially orientated in the anti-clockwise direction, for the estimation of α_e .	130
4.14	Yaw calibration of the SY probe at constant velocity with the probe initially orientated in the clockwise direction, for the estimation of k .	131
4.15	Yaw calibration of the SY probe at constant velocity the probe initially orientated in the anti-clockwise direction, for the estimation of k .	131
4.16	The variation of α_e with speed	132
4.17	The variation of k^2 with speed	132
4.18	Illustration of the response of an SY probe to the velocity vector both in the clockwise and anti-clockwise orientation	134
5.1	The coordinate along the circumference of a circular cylinder.	139
5.2	The variation of the attachment line pressure coefficient along the span of the faired cylinder tested by Arnal et al. [5]	141
5.3	The variation of the effective sweep angle along the normalised span of the model tested by Arnal et al. [5] with geometric sweep of 50°	141
5.4	The flow at the frontal part of a yawed cylinder which is a similar representation of the flow at the leading edge of a swept wing, figure adapted from Poll [92] and Joslin [66].	142
5.5	McLean's [79] numerical solutions of spanwise variation of the AL along the leading edge of a Boeing 727-200, using a fully 3D and an infinite-swept method.	145

5.6	Comparison of the laminar velocity profiles measured experimentally by Gaster and Poll with the ‘swept-Hiemenz’ flow theory.	149
5.7	Comparison of the turbulent velocity profiles captured experimentally by Cumpsty and Head [36] (symbols) and those predicted by McLean [79] (lines) using the 3D boundary layer method.	150
5.8	Relation between R_{θ} and \bar{R} established from the results of Cumpsty and Head [36], Gaster [45], Spalart [110], McLean [79], van Ouheusden [119] and Smith [109].	151
5.9	The variation of C_f with respect to \bar{R} Cumpsty and Head [36].	152
5.10	The velocity profile of the turbulent AL based on the law of the wall, by Cumpsty and Head [36].	153
5.11	Relation between shape-factor, H and \bar{R} established by Cumpsty and Head [36], Gaster [45], Spalart [110], van Ouheusden [119] and Smith [109].	154
5.12	Schematic representation of the supersonic flow at the leading edge of a swept cylinder mounted on a wedge, from Poll [91].	155
5.13	\bar{R} at the onset of transition for various Mach numbers measured at the edge of the attachment line, from Bellone [14].	155
5.14	Attachment line contamination due to the presence of disturbances occurring at the wing and fuselage junction.	157
5.15	Natural transition along the span of the swept cylinder and forced transition due to the presence of a large roughness strip. Due to wing taper, in the outboard region $\bar{R} < 500$ so the figure on the left hand side should be interpreted only qualitatively.	157

5.16	Spanwise position of where the first burst and complete turbulence were observed during the Poll's [92] experiment using trip wires to force transition.	158
5.17	The diameter of trip wire required for attachment line transition at a given wind tunnel speed, figure from Gaster [45]	160
5.18	The location of free transition along the span of the swept cylinder, from Poll [92]	161
5.19	The appearance of the first burst and complete turbulence at a particular spanwise position at varying \bar{R} and trip wire diameter, from Poll [91] . . .	162
5.20	Comparison of the numerical results from the linear stability with the experimental results by Poll[92]	163
5.21	The 'Gaster Bump', leading edge decontamination device [45]	164
5.22	The leading edge fences for attachment line control tested by Seyfang [107].	165
5.23	The distribution of the pressure coefficient and streamline on the model with the positive (LHS) and negative (RHS) bumps	166
5.24	The amount of suction required to relaminarise a turbulent attachment line at a particular \bar{R} , Arnal et al. [5]. A comparison with previous experimental and numerical studies as well.	168
5.25	The amount of suction required to relaminarise the attachment line on the A320 fin, figure from Schrauf [103]	169
5.26	Static pressure distribution at the in-board pressure station for $\bar{R} = 540$.	170
5.27	The variation of the effective sweep in the spanwise direction.	170

5.28	The hot wire voltage signal at the upstream station, $y = 0.5m$ and $z = 200\mu m$	172
5.29	The hot wire voltage signal at the downstream station, $y = 0.9m$ and $z = 200\mu m$	172
5.30	Laminar velocity profiles compared with swept Hiemenz flow and Gaster's experimental measurements using η estimated from equation 5.19.	174
5.31	Laminar velocity profiles compared with Hiemenz flow and Gaster's experimental measurements. Where η is calculated from velocity gradient at the leading edge determined from the pressure distribution.	174
5.32	Mean turbulent velocity profiles captured from the current experiment and compared with Cumpsty and Head's experimental measurements, where $\zeta = z/\delta^*$	176
5.33	Comparison between the momentum thickness obtained by Cumpsty and Head's with those calculated from the current experimental measurements.	177
5.34	Comparison between the shape factor calculated from the current experimental measurements with those obtained by Cumpsty and Head [36], Gaster [45], van Ouheusden [119], Spalart [110] and Smith [108].	178
5.35	Comparison of the attachment line skin coefficient obtained from the current experiment with those from Cumpsty and Head [36], van Ouheusden [119], Spalart [110] and Poll [91] given by equation 5.29.	179
5.36	The turbulent velocity profile plotted in wall units using wall shear stress estimated from Preston tubes. The inner region is represented by the 'universal log-law' chosen by Patel [87] and Cumpsty and Head [36].	179

5.37	The turbulent velocity profile plotted in wall units, where the inner region is represented by the ‘universal log-law’ given in Cebeci and Cousteix [24].	180
5.38	The turbulent velocity profile plotted in wall units for various \bar{R} based on effective sweep.	181
5.39	The relation between R_θ and \bar{R} together with the corrected current experimental results based on effective sweep.	182
5.40	Comparison between of the attachment line skin friction coefficient measurement during the current experiment with previous empirical relations.	184
5.41	Comparison between Coles ‘law of the wake’ model coupled with Granville’s model for the wake function, at $\eta = 1.0$ and the experimental turbulent profiles.	187
5.42	Comparison between Coles ‘law of the wake’ model coupled with Granville’s model for the wake function, at $\eta = 1.2$ and the experimental turbulent profiles.	187
5.43	The four hot wire measurement stations downstream of the attachment line decontamination device.	189
5.44	Hot wire signal at the leading edge region of the device.	190
5.45	Hot wire signal in the aft region of the device.	191
5.46	Hot wire signal at 200mm downstream of the device, with larger resolution in \bar{R}	191
5.47	Hot wire signal at 500mm downstream of the device, with larger resolution in \bar{R}	192

5.48	The laminar velocity profile downstream of the leading edge device at $\bar{R} = 375$	193
6.1	Schematic representation of the viscous flow at the leading edge of a swept wing.	195
6.2	Schematic representation of the streamwise and crossflow velocity profile in a three dimensional boundary layer, figure adapted from McLean [79].	196
6.3	The three dimensional velocity profile upstream and downstream of a point of inflection in the external streamline, where s is tangential and n orthogonal to a point along the streamline. Figure adapted from Cebeci and Cousteix [24]	197
6.4	The variation in the location of transition at different wind speed for a series of sweep angle.	199
6.5	Streamwise velocity profiles captured by Cumpsty and Head [37] at various chordwise station along the swept circular cylinder. The solid lines represents Thompson's profile [113] and \circ , the experimental measurements.	201
6.6	Streamwise velocity profiles captured by Cumpsty and Head [37] presented on a law-of-wall plot.	202
6.7	Crossflow velocity profiles captured by Cumpsty and Head [37] and compared with Mager profiles given by equation 6.6. The solid lines represents Mager's profile [77] and \circ , the experimental measurements.	203
6.8	Johnston triangular form of the crossflow velocity profile presented by [33]	204

6.9	Crossflow velocity profiles captured experimentally by Cumpsty and Head [37] and represented in Johnston’s hodograph plot. Where ‘ Δ ’ represents measurements using the ‘original’ traverse and ‘ \circ ’, represents the measurement made by a modified, ‘slender’ traverse	205
6.10	Hot-film signal of the boundary layer formed at the leading of the swept wing tested by Mukund et al. [81], at angle of incidence of 18° (LHS) and 16° (RHS). Where ‘L’-numeric and ‘T’-numeric stands for laminar and turbulent regions respectively and ‘LSB’ denotes laminar separation bubble.	208
6.11	The pressure distribution around the leading edge of the experimental model along the line-of-flight chord.	209
6.12	Schematic representation of the streamwise and crossflow velocity profiles along a diverging streamline at the leading edge of a swept wing . . .	210
6.13	Comparison of the velocity profile at the attachment line captured using the SN and SY probe, where the k yaw calibration coefficient was employed.	211
6.14	Comparison of the velocity profile at the attachment line captured using the SN and SY probe, where the α_e yaw calibration coefficient was employed.	212
6.15	Streamwise velocity profiles downstream of the attachment line at $\bar{R} = 425$	214
6.16	Streamwise velocity profiles downstream of the attachment line at $\bar{R} = 500$	214
6.17	The streamwise profiles captured on the port side of the model represented in the law of the wall plots using the measured wall shear stress. The universal log-law is given by $u_s^+ = 2.5 \ln z^+ + 5.24$	217

6.18	The streamwise profiles captured on the port side of the model represented in the law of the wall plots using the adjusted shear stress. The universal log-law is given by $u_s^+ = 2.5 \ln z^+ + 5.24$	218
6.19	The streamwise profiles captured on the starboard side of the model represented in the law of the wall plots using the adjusted shear stress. The universal log-law is given by $u_s^+ = 2.5 \ln z^+ + 5.24$	219
6.20	Cross-flow velocity profiles downstream of the attachment line, $\bar{R} = 425$.	221
6.21	Crossflow velocity profiles downstream of the attachment line, $\bar{R} = 500$.	221
6.22	Schematic representation of the clockwise and anticlockwise orientation of the hot-wire probe at the attachment line and downstream along the diverging streamlines on the port and starboard side of the model.	222
6.23	Triangular representation of the crossflow velocity profiles measured from both sides of the model at $\bar{R} = 425$	223
6.24	Triangular representation of the crossflow velocity profiles measured from both sides of the model at $\bar{R} = 500$	224
6.25	The streamline divergence angle, ψ at different chordwise locations.	226
6.26	The streamline divergence angle, ψ at different positions along the circumference of the leading edge.	227
6.27	The chordwise and spanwise velocity components at the edge of the boundary layer, along the leading edge of the experimental model	228
6.28	The local skin friction coefficient in the vicinity of the attachment line. . .	231
6.29	Development of the streamwise momentum thickness in the vicinity of the attachment line.	233

6.30	Development of the streamwise shape factor in the vicinity of the attachment line.	234
6.31	Development of the normal boundary layer integral quantities defined by equation 2.53 at , $\bar{R} = 425$, where the subscript ‘i’ and ‘j’ represents ‘1’ or ‘2’.	235
6.32	Development of the normal boundary layer integral quantities defined by equation 2.53 at , $\bar{R} = 500$, where the subscript ‘i’ and ‘j’ represents ‘1’ or ‘2’.	236
6.33	Launder’s acceleration parameter calculated using the conditions along the external streamline using equation 6.11	237
6.34	The streamwise velocity profiles downstream of the attachment line represented in wall units using the c_f estimated from the Clauser-plots. . . .	238
7.1	Comparison between θ measured during the current experiment and those obtained numerically from Callisto, using both a low and a high resolution mesh. The error bars are within $\pm 15\%$	241
7.2	Comparison between H measured during the current experiment and those obtained numerically from Callisto, using both a low and a high resolution mesh. The error bars are within $\pm 3\%$	242
7.3	Comparison between c_f measured during the current experiment and those obtained numerically from Callisto, using both a low and a high resolution mesh. The error bars are within $\pm 15\%$	242

7.4	Comparison between θ measured during the current experiment and those obtained numerically from the previous and modified version of Callisto, using both a low and a high resolution mesh. The error bars are within $\pm 7\%$	248
7.5	Comparison between H measured during the current experiment and those obtained numerically from the previous and modified version of Callisto, using both a low and a high resolution mesh. The error bars are within $\pm 3\%$	249
7.6	Comparison between c_f measured during the current experiment and those obtained numerically from the previous and modified version of Callisto, using both a low and a high resolution mesh. The error bars are within $\pm 15\%$	250
7.7	Comparison between θ measured during the current experiment and those obtained numerically using the effective sweep angle. The error bars are within $\pm 5\%$	250
7.8	Comparison between c_f measured during the current experiment and those obtained numerically using the effective sweep angle. The error bars are within $\pm 15\%$	251
7.9	Development of the individual parameters in equation 7.19i in the vicinity of the attachment line.	252
7.10	Comparison of the drag difference between a fully turbulent flow and the flow with varying transition location on the upper surface, but fixed at 1% chord on the lower surface, from the earlier method of Callisto and the new method including the modification to the leading edge modelling. . .	254

7.11	Comparison of the development of momentum thickness predicted by the earlier version and the latest version of Callisto on a supercritical aerofoil.	254
7.12	Comparison of the development of local skin friction predicted by the earlier version and the latest version of Callisto on a supercritical aerofoil.	255
C.1	Deviation of the experimental results during the calibration of the SN-probe with respect to King's Law, where the error bounds represents 2% of the experimental results	282
C.2	Schematic view from the front of the hot wire while mounted on the traverse.	283
C.3	Comparison of current experimental laminar attachment line velocity profile against swept Hiemenz theory and Gaster's measurements, with 5% error bars in the current results.	285

List of Tables

1.1	The concentration , lifetime and radiative forcing of GHGs from [51].	16
3.1	Theoretical estimation of the experimental parameters with variation of sweep angle for $Q_\infty = 45m/s$ and $\bar{R} = 500$	86
B.1	Chordwise position of pressure tappings on the port and starboard sides of the model.	276
C.1	The sources of uncertainty while converting the hot wire voltage signal into the equivalent velocity.	281
C.2	The sources of uncertainty while converting the hot wire voltage signal into the equivalent velocity	284

Acknowledgement

I would like to thank EADS IW for the financial support, Mr P. Beckwith for manufacturing the wind tunnel model and Mr M. Smith for manufacturing the traverse mechanism. Also, Prof M. Gaster who provided very helpful advice on hot wire anemometry and during the discussion of other technical aspects of the project and Dr S. Gruppetta for his assistance with the optical system. I am also greatly indebted to Prof C. Atkin for his guidance, patience and encouragement and also for ensuring that the project was heading in the right direction and covering my financial needs.

I would also like to express gratitude to Mother and Father, and the rest of my family and friends for their indirect support and last but not the least, my late Grandmother, Marie-Leonne Gowree, who shall be always remembered.

Declaration

I grant powers of discretion to the University Librarian to allow the thesis to be copied in whole or in part without further reference to the author. This permission covers only single copies made for study purposes, subject to normal conditions of acknowledgements.

Summary

Numerical analysis conducted using Callisto, which is Airbus's three-dimensional momentum integral boundary layer code coupled with Green's lag-entrainment method has shown that there might be a small but worthwhile form drag reduction through attachment line control, up to about 0.4 – 0.6 counts for an aircraft. However, in order to overcome numerical issues in the modelling a few approximations have been made in the method while calculating the flow very near the leading ledge. The detail of the leading edge flow needs to be verified if the drag results are to be trusted.

Therefore, an experiment carried out, aiming to capture the velocity profiles starting from the attachment line and up to about 3% chord downstream. In order to design the experimental model, a systematic approach was used based on previous semi-empirical work on the attachment line flow. The model was designed so that the attachment line boundary layer is turbulent due to contamination from the turbulent boundary layer from the wall (floor) of the wind tunnel and thick enough to give a sensible experimental domain size including sufficient chord wise extent for hot-wire measurement. The velocity profiles were captured by means of hot wire anemometry using a micro displacement traverse designed and manufactured in-house. Due to the precision required for capturing the very thin turbulent velocity profile, a digital optical system was developed to assess the performance of the traverse. The optical system also proved to be beneficial for near wall alignment of the hot wire probe and the experimental rig was able to capture the flow in the laminar sub-layer in few cases.

From the hot wire signal, the critical condition for attachment line contamination was demonstrated to be $\bar{R} \approx 245$ or $R_\theta \approx 100$, which is in agreement with previous studies. The laminar velocity profiles were first captured and good agreement was found with theory. The turbulent velocity profiles were then captured, up to $\bar{R} \leq 540$, and were found to be in agreement with previous experimental results. While representing the velocity profile in wall units a better agreement with the universal log-law was found compared to previous experimental results and revised attachment line Reynolds number, \bar{R} , criteria for the intermittent and fully turbulent states are proposed as $250 < \bar{R}_{eff} < 360$ and $\bar{R}_{eff} > 360$ respectively. The momentum thickness and shape factor agreed well with other numerical results. $R_\theta > 315$ was found to be the minimum condition for turbulent attachment line flow, which is in good agreement with the value of 320 proposed by Preston for flows on a flat plate. From the skin friction results, the turbulent attachment line boundary layer was found to be similar to fully developed pipe flow and fully turbulent boundary layer on flat plate, further semi-empirical analysis, using mixing length theory, suggesting that it obeyed the law of the wake as well.

Downstream of the attachment line both the streamwise and the crossflow velocity profiles were captured, although the lack of any comparable results in the literature did not allow for any comparison. In wall units, the streamwise velocity profiles plotted using the skin friction measured directly using Preston's technique demonstrated strong Reynolds number dependence, but the magnitude of Launder's acceleration parameter was too low to support the idea that the boundary layer might be undergoing relaminarisation at the lower \bar{R} case. This was confirmed when the profiles were plotted using the skin friction estimated from Clauser's technique, where closer agreement was observed with the universal log-law. Cross-over crossflow velocity profiles were present from $x/c > 0.003$; from previous studies on laminar flows, it was suggested that such behaviour was due to the presence of a point of inflection in the trajectory of the external streamline. However this argument was ruled out due to the absence of an inflection point in the current inviscid flow measurements. From a simple analysis it has been suggested that this behaviour

may be due to turbulent shear stress downstream of the attachment line. In addition, unexpected non-monotonic behaviour in the development of momentum thickness, θ , and local skin friction, c_f , is observed in the vicinity of the attachment line.

From a first comparison of the flow at the leading edge, the experimental and computational θ and c_f were different by about 15% and the trends were also inconsistent. Therefore, based on the measured behaviour of the viscous flow in the vicinity of the attachment line, a modification to the governing lag-entrainment equation in Callisto was proposed, in order to compute the flow immediately downstream of the attachment line. This was not possible in the previous version of Callisto owing to a singularity in the governing equation which is resolved by the new model. Comparison of the results from the modified version of Callisto with experiment showed a significant improvement as the momentum thickness was predicted to be within 5% to those obtained experimentally. More importantly, non-monotonic behaviour in the experimental θ and c_f was also replicated in the numerical results, supporting the experimental observations. Despite the significant improvement in the leading edge modelling using the proposed modification, the profile drag prediction was not significantly affected as the predicted momentum thickness in the far wake was the same from both the old and the new version of Callisto. Therefore, the drag benefit predicted during the initial analysis can be considered robust.

Nomenclature

Roman Symbols

A, B The hot wire calibration constants

AR Wing aspect ratio

C_D Coefficient of drag

C_{D_0} Coefficient of profile drag

C_f Coefficient of form drag

C_{D_p} Coefficient of pressure drag

C_{D_v} Coefficient of viscous drag

C_{D_w} Coefficient of wave drag

c_E Coefficient of entrainment

C_f Coefficient of skin friction drag

c_f local skin friction coefficient

c_{f_0} Coefficient of skin friction in an equivalent zero pressure gradient or flat plate flow

c chord length of the wing

C_L Coefficient of lift

C_p	Coefficient of pressure
c_τ	Coefficient of turbulent shear stress
c_{τ_m}	Coefficient of maximum turbulent shear stress
d	External diameter of miniature Pitot tube
D	Drag force
E	Hot wire voltage output
f_{1-4}	Correlation functions for the three dimensional integral properties
\bar{f}	normal stress correlation factor
G	Shape Parameter of velocity defect profile
H	Incompressible shape factor
$H_{\delta-\delta^*}, H_1$	Entrainment shape factor
\bar{H}	Compressible shape factor
k	Thermal conductivity of the air in the vicinity of the hot wire
k_1	Velocity gradient in direction of potential flow at attachment line
k_a	Thermal conductivity of the ambient air
V_e	Effective cooling velocity
K, C_q	Suction coefficient
K_s	Launder's acceleration parameter along the streamline
L	Lift force
M	Mach number
Nu	Nusselt number

P_0	Total pressure
P_s	Static pressure
\bar{q}^2	Mean fluctuating velocity
Q_∞	Freestream velocity
R	Radius of curvature of external streamline
R	Range
R_{20}	The resistance of the hot-wire sensor at $20^\circ C$
\bar{R}	Attachment line Reynolds number based on velocity gradient
R_δ	Reynolds number based on boundary layer thickness
Re	Freestream Reynolds number
R_θ	Reynolds number based on momentum thickness
R_{TOT}	Total resistance of hot-wire sensor and the leads
R_w	Operational resistance of the hot-wire sensor
s'	Distance along the circumference of the circular leading
sfc	Specific fuel consumption
s, n	Coordinates along and normal to an external streamline respectively
T_a	Ambient air temperature around the hot wire
T_m	Mean of the hot wire sensor and ambient temperature
T_s	Operating temperature of the hot wire sensor
U_1, V_1	Local chordwise and spanwise velocity components at boundary layer edge
U_s	External streamwise velocity

u', v', w' The fluctuating velocity components

\bar{u}, \bar{v} and \bar{w} Time averaged mean of the viscous velocity component

U, V, W The external chordwise, spanwise and normal velocity component, along the x, y and z direction respectively

u, v, w x, y and z velocity component inside the viscous layer

W_i Initial weight

W_f Final weight

x, y, z Cartesian coordinate system in the chordwise, spanwise and normal direction respectively

Greek Symbols

β Angle between external and limiting streamline or hot wire pitch angle

β_0 Angle between external and wall streamline in Chapter 6

ξ, η Orthogonal curvilinear coordinates system in the streamwise, crosswise and normal direction respectively

δ Boundary layer thickness

δ_{AL} Attachment line displacement thickness

δ^* Boundary layer displacement thickness

ϵ Oswald efficiency or dissipation of turbulent energy

η Attachment line characteristic length

γ Isentropic ratio

κ_T x-axis curvature due to taper

Λ Wing sweep back angle

λ	Scaling factor of dissipation length
Λ_{eff}	Effective sweep angle
λ_i	Coefficient define in Appendix section
μ	Dynamic viscosity
ν	Kinematic viscosity
ϕ_i	Coefficient define in Appendix section
Π	Pressure gradient parameter
ψ	Angle between projection of external streamline and x-direction or stream function
ρ	Density
θ	Boundary layer momentum thickness
τ_w	Wall shear stress
τ_{01} and τ_{02}	Wall shear stress in the streamwise and crossflow direction respectively
τ	Turbulent shear stress
θ_{AL}	Attachment line momentum thickness
θ	Angular displacement along a 2D circular cylinder
α	The hot wire yaw angle
$\bar{\alpha}$	The nominal hot wire yaw angle
α_e	Effective hot wire yaw angle
ζ	Diffusion function

Subscripts

0 Zero pressure gradient, flat plate flows and conditions at the wall

$2D$	Two dimensional
$3D$	Three dimensional
AL	Conditions at the attachment line
$crit$	Conditions at equilibrium
∞	Freestream conditions
iw	The equivalent inviscid flow
$crit$	Critical conditions
max	Conditions occurring at maximum
s	along the streamwise direction

Chapter 1

Introduction

Since the pioneering flight by the Wright brothers to demonstrate sustainable flight, aviation has grown tremendously. The introduction of the supercritical aerofoil and the turbojet, now superseded by high by-pass ratio turbofan, has enabled commercial aircraft to cruise at transonic speed, reducing journey times significantly. Still, there is an ever-increasing demand for faster and longer range aircraft. Based on the current civil jet configuration, higher cruise speed would lead to further increase in structural load and aerodynamic drag which will increase fuel consumption, thus increasing the emission of ‘green house gases’ (GHG) and operating costs. One way of reducing fuel consumption is by the optimisation of aerodynamic performance through the reduction of drag and this is the aim of the current study.

Nowadays, aircraft wing design relies enormously on numerical prediction tools which reduce the time and cost involved during wind tunnel and flight testing. Most of the numerical methods solve simplified forms of the Navier-Stokes equations. The advances in computer power over the last two decades has enabled the industrialisation of high-order numerical methods based on ‘Reynolds Averaged Navier-Stokes’ (RANS) coupled with various types of turbulence model for the prediction of fully turbulent flows on complex geometries. The increased computer resources have made possible direct calculation of

the full Navier-Stokes equation (DNS), but restricted to simple geometries or configurations. Numerical simulations over aircraft wings or a whole aircraft configurations is still restricted to RANS solvers using the various types of turbulence model calibrated experimentally.

Low-order methods such as integral methods coupled with semi-empirical auxiliary relations were employed extensively in the era where computational power was scarce due to their low memory requirement and rapid turn around time. The main advantage of these methods today is that they can be easily coupled with other specialised prediction tools such as transition prediction methods and they are very useful in the study of flow control strategies for the reduction of viscous drag. For example, numerical analysis conducted using Callisto, which is Airbus's three dimensional turbulent boundary layer code based on von Karman's momentum integral method coupled with Green's 'lag-entrainment' method [52] has shown that there might be a small but worthwhile form drag reduction through attachment line control. However, the modelling of the turbulent attachment line in Callisto is not robust and, in order to overcome numerical issues in the algorithm, a few approximations have been made near the leading ledge and these needs to be experimentally verified, if the results are to be trusted. An experiment has therefore been proposed aiming to capture the velocity profile starting from the attachment line and extending up to about 3% chord downstream.

1.1 Economical and Environmental Considerations

An elaborate study of the economic and environmental issues associated with current and future civil aviation operations has been presented by Green [51] and [50], emphasising mainly on the emission of GHG and is briefly revisited in this section. From an economical perspective, Figure 1.1, the crude oil price has risen sharply over the last fifteen years and even with a drop due to the recent global economic crisis at the end of 2008, it still remained around twice the price seen in the 1990s. Following the end of the economic

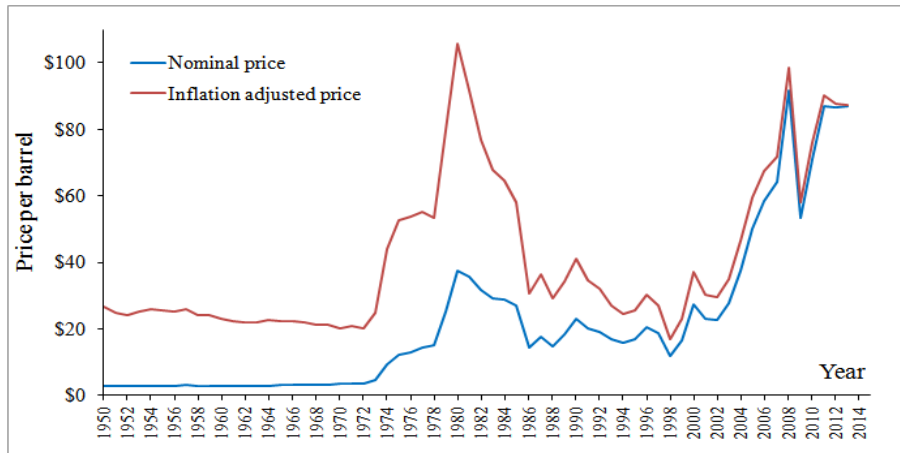


Figure 1.1: The yearly average nominal and inflation adjusted crude oil price per barrel. Data accessed on the 21st October 2013 from www.inflation.com

crisis, the crude oil price rose again and is very unlikely to drop down to previous low values judging by the trend from the last two decades. This will strike hard at the profit margin of the airlines as the direct operating costs will increase in addition to the hefty environmental taxes that they risk being subjected to due to GHG emissions and other sustainability considerations.

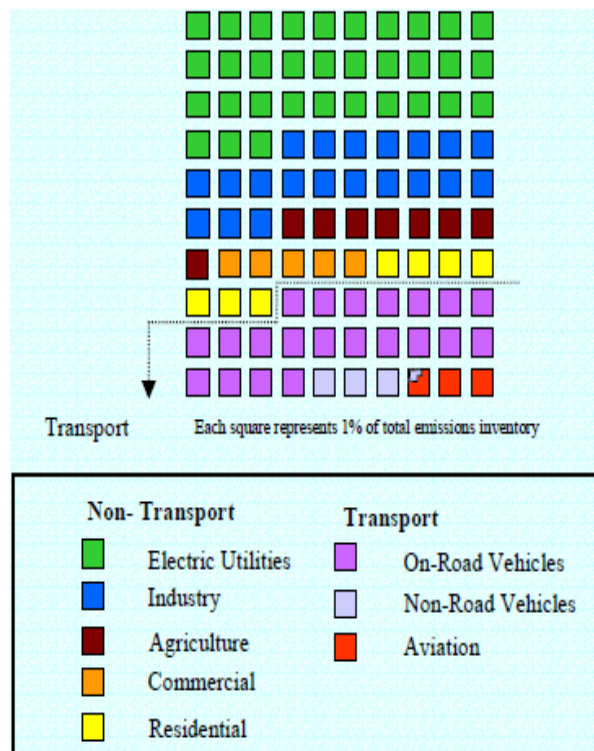


Figure 1.2: Break down of the GHG emission in 2001 from all the industry in the USA presented by the FAA.

Figure 1.2, shows the breakdown of the GHG emission from various sectors in the US (similar figures should be expected for Europe) following a study conducted in 2001. The aviation sector accounts for less than 3% of the overall emissions. Similar to most internal combustion engines operating on derivatives of hydrocarbons, the exhaust gas ejected from an aircraft engine consists of carbon dioxide (CO_2), carbon monoxide (CO), water vapour (H_2O), nitrogen oxides (NO_x), oxides of sulphur (SO_x), unburned or partially combusted hydrocarbons (also referred as volatile organic compounds ($VOCs$)), particles and particles precursors. A detailed break-down of the composition of an aircraft engine exhaust was provided by Green [50] which has been reproduced here as figure 1.3. Despite the small overall GHG contribution from aviation, most of these emissions take place in a critical part of the earth's atmosphere, namely the tropopause and the stratosphere, where they might affect the ozone layer directly and where there are no environmental cycles to absorb them.

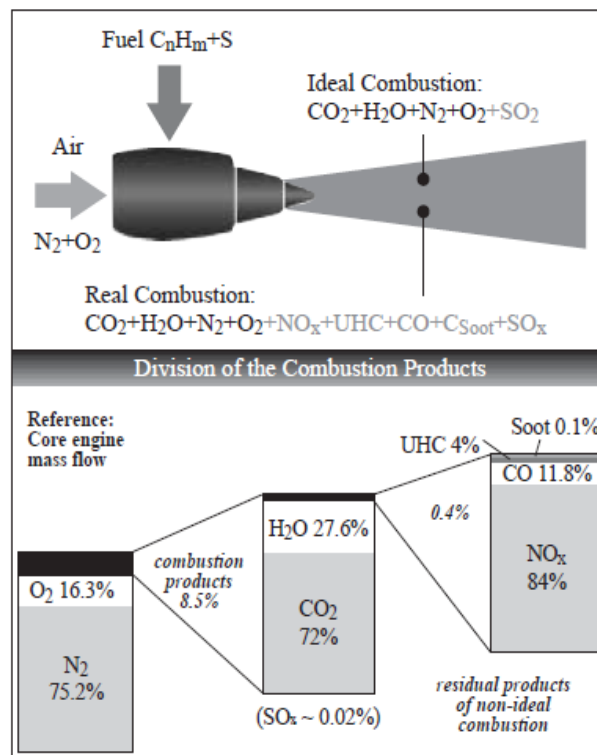


Figure 1.3: Schematic representation of the composition of the exhaust gases exiting a jet engine during both ideal and actual combustion cases from, Green [50].

The main GHG component, CO_2 , is considered to be of greatest concern due to its ability to absorb and trap the high wavelength infra-red waves from solar radiation reflected by

Table 1.1: The concentration , lifetime and radiative forcing of GHGs from [51].

Gas	Pre-1970 Conc. ppm	Actual Conc. ppm	lifetime years	Increased RF W/m^2
CO_2	280	385	approx. 100	1.66
CH_4	0.7	1.8	12	0.48
O_3	0.025	0.034	hours-days	0.35
N_2O	0.27	0.322	114	0.16
Halocarbons	0	0.001	5-10000	0.34
NO_x			days	
Contrails and cirrus clouds			hours	

the earth's surface and the lower atmosphere. This absorption contributes to a rise in the overall temperature closer to the earth atmosphere or the troposphere and it is reversed in the region of the stratosphere. Based on some of the models used in the analysis of global climate change, the green-house effect can be quantified in terms of Radiative Forcing (RF), which is defined by Intergovernmental Panel of Climate Change (IPCC) as a measure of 'the change in the balance between radiation coming into the atmosphere and radiation going out', a positive value representing warming of earth's atmosphere and vice versa. In the study conducted by Green [51] a list of the properties of some GHG directly related to human action, such as their concentration, lifetime and radiative forcing, were provided and all reproduced in Table 1.1 (note that the RF value has been modified to 4.8 based on the updated source). Studying the data from Table 1.1, once again CO_2 can be considered as the most harmful as it produces the largest increase in RF and has a long lifetime of approximately 100 years. But, these models are changing rapidly and while new ones being proposed, yet, CO_2 still remains as a major concern.

Alarmed by the current environmental situation, many governmental bodies have already started implementing new measures in order to enforce measures trying to reduce emissions, such as 20% reduction in emission targeted by 2020. This will be in the form of hefty taxation policies which will definitely affect the profit margin of commercial aviation, resulting in soaring air fares. In an era where fossil fuel reserves are being depleted at a rapid rate and the sustainable fuel or power sources such as biofuel and solar power

are still in their infancy, the required reduction of fuel consumption can be achieved by optimisation of mission performance, through increase in aerodynamic and propulsive efficiency and reduction of operating weight empty.

1.2 Optimisation of Mission Performance

The mission performance of a commercial aircraft is governed by three parameters, namely the specific fuel consumption (*sfc*) associated with the engines, the weight of the aircraft and the payload at takeoff, the fuel load and the airframe aerodynamic efficiency which is given by the lift to drag ratio (*L/D*). These parameters feature in what is called the ‘Breguet range equation’ which in its simplified, can be expressed as

$$R = \frac{Q_{\infty} L}{sfc D} \ln \left(\frac{MTOW}{OWE} \right) \quad (1.1)$$

From equation 1.1 the range, *R*, could be improved either by reducing *OWE/MTOW* for a constant cruise speed, or through reduction of the *sfc* or the drag, *D*, which will result in an increase in *L/D* for a fixed cruise condition. The introduction of carbon fibre composites has led to the reduced empty weight and the airframes of two most recent long haul aircraft, the Airbus A350 and Boeing 787, have been manufactured with at least 50% carbon fibre material. Still, there are some limitations for the migration towards an ‘all-carbon-fibre’ airframe due to the requirement for lightning strike protection which helps in managing the high voltage discharge and also restrictions on satisfying the structural requirements, as the propagation rate of cracks are faster in carbon fibre composites. On the propulsion side, the introduction of high by-pass ratio turbo-fan engines has contributed enormously to the reduction of *sfc*. According to Green [51], further improvement at cruise condition is mainly possible through the increase in the thermal efficiency, however this requires higher turbine entry temperature which will favour the production of *NO_x*. Alternative propulsion systems, such as the open rotor which provides significantly larger

by-pass ratio are being considered but there are still issues related to acoustics and other unwanted effects at high Mach number that need to be addressed.

The aerodynamic efficiency which is governed by the L/D and can be improved by either increasing the lift, L , or reducing drag, D . However most of the commercial aircraft spend a large proportion of their mission at cruise condition where the lift is fixed by the weight of the aircraft, thus the only way of optimising performance will be through reduction of drag. The total drag for an aircraft at cruise which will be elaborated in the section that follows, consists of the profile drag, C_{D_0} and the induced drag, C_{D_i} . The induced drag is inversely proportional to the aspect ratio, AR and can be further reduced with increase in AR . However, this contributes to additional weight due to structural requirements which affects the lift and hence the L/D . Therefore, the profile drag presents more opportunities for improving aerodynamic efficiency.

1.3 Drag

The breakdown of the total drag on an aircraft is presented in Figure 1.4. On a commercial transonic aircraft the total drag can be either separated into the sum of the friction or pressure drag or it can be addressed as the sum of the vortex drag which occurs due to the formation of the horse-shoe vortex system, the wave drag, from the formation of the pockets of locally supersonic flow and the wake drag, from the action of viscous shear stress. The total drag can be also expressed as

$$C_D = C_{D_0} + \frac{C_L^2}{\pi AR \epsilon} \quad (1.2)$$

where C_{D_0} is usually referred as the profile drag and the second term on the right-hand side of equation 1.2 is referred as the lift-dependent or induced drag, where C_L , denotes lift coefficient, AR , the aspect ratio and ϵ , the Oswald efficiency factor.

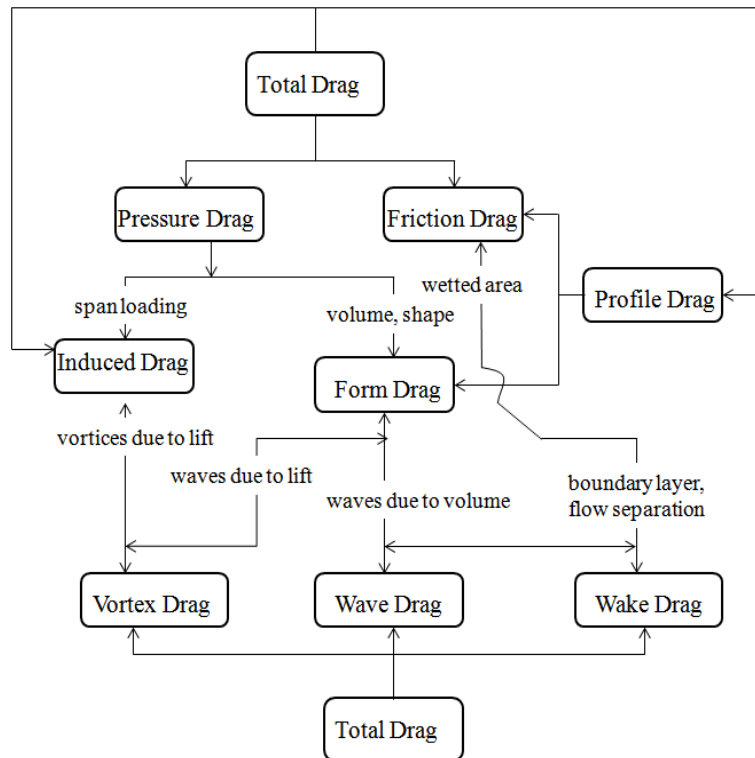


Figure 1.4: The breakdown of the drag arising from the external flow around and aircraft, from Torenbeek [118]

Based on Marec's [78] investigation the largest contributor to the drag from a swept-wing commercial aircraft emanates from the friction drag which accounts for almost 48% of the total drag, followed by induced drag at 37%, where the after-body, interference, wave and parasitic drag all together contributes to approximately 15% (see Figure 1.4). It is not clear whether Marec's 'friction drag' represents the overall viscous drag in which case it will constitute the form drag as well. According to Green [51], who referred to Marec's result, the friction drag included the pressure drag at subcritical conditions, however the results presented in 'figure 10' in reference [51] do not seem to be coherent with the numbers quoted by Marec, the original source. Regardless of this anomaly, the viscous drag is still the largest contributor to the total drag and therefore presents the best opportunity for drag reduction as a small percentage reduction will result in large overall benefits.

The induced drag is a direct effect of the formation of the horse-shoe vortex system on finite wings and is inversely proportional to AR , and the magnitude of the wing tip vortex. Wing-tip devices such as blended winglets or sharklets and wing tip fences shown in figure

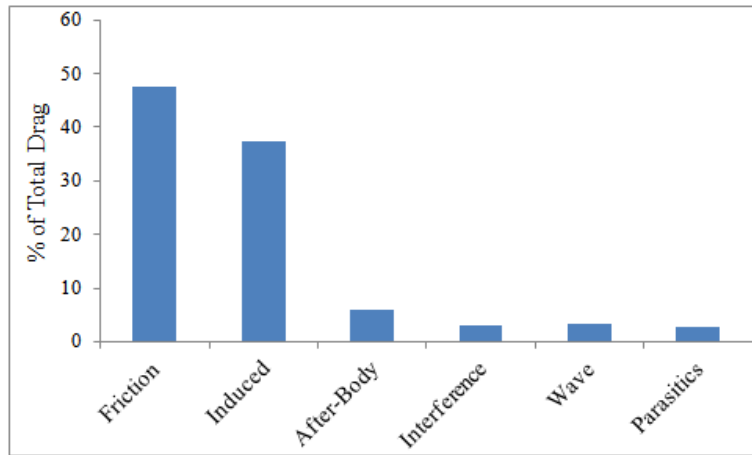


Figure 1.5: The percentage break-down of the total drag from a large commercial aircraft, from Marec [78]. Where the ‘friction’ drag represents all viscous drag

1.6 have demonstrated their effectiveness in reducing induced drag. Winglets, which are nowadays blended with the wing can help in increasing the effective span of wings and also the wing loading due to the non-planar lift contribution. The effect of wing tip devices is still not very clear and according to Ogilvie [84], recent A380 wake vortex problems suggest that local trailing vortex mitigation has no effect on global wake vortex development. Nevertheless, these devices have been designed in such a way that they have minimal effect to the profile drag and which will justify the total drag benefit.



Figure 1.6: Common wing tip devices used for reduction of induced drag. Figures obtained from www.airliners.net

From Figure 1.4 the profile drag which is usually referred as the viscous drag can be further decomposed into the friction drag and the form drag, which forms part of the pressure drag. It can be expressed as

$$C_{D_0} = C_f + C_{D_f} \quad (1.3)$$

where C_f represents the friction drag and C_{D_f} the form drag.

In simple terms the skin friction drag is related to the velocity gradient at the surface, its magnitude is usually governed by the shape of the velocity profile and the skin friction drag is higher for a turbulent boundary layer than for a laminar layer. As viscous drag accounts for almost 50% of the total drag, larger benefits in overall drag reduction can be achieved by increasing the amount of laminar flow on aircraft wings. There is a limit on the extent of laminar flow allowable on a transonic wing because of the formation of the normal shock and at that point a turbulent boundary layer is unavoidable as it is able to sustain the adverse pressure gradient and remain attached. The form drag is a direct result of the change in the effective shape of the aerofoil due to the displacement effect generated by the presence of the boundary layer and shares the same mechanism as the after-body drag category in Figure 1.5 whose contribution is relatively small. Viscous drag reduction is achievable through flow control strategies which will be reviewed in the following section.

1.4 Transition and Flow Control

Research in flow control for viscous drag reduction can be traced back to the 1930s, where the main focus was directed towards the design of laminar flow aerofoils. Interest in flow control technologies such as suction arose later, in the following 20 years, and in the 1960s there were many activities in Europe (Handley Page Limited) and US (Northrop Corporation) looking at implementing practical laminar flow control technologies. But the drop in fuel price in the early 1980s, seen in Figure 1.1, hampered further research as the economic benefit from laminar flow fell below the cost of implementation. The aim of laminar flow control is to delay the process of transition which leads to the formation

of a turbulent boundary layer through the process shown schematically in Figure 1.7. On a transonic wing transition can be triggered by the amplification of either ‘Tollmien-Schlichting’ (TS) or ‘crossflow’ (CF) types of instabilities represented schematically in figure 1.8. ‘Taylor-Görtler’ instabilities share some features of CF instabilities but are rare on aircraft wings.

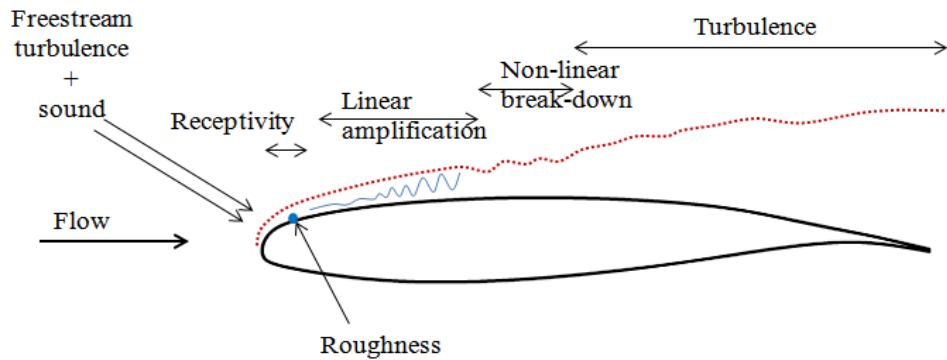


Figure 1.7: Schematic representation of the mechanism of transition

According to Saric and Reed [100], Görtler instability arises mainly in the presence of surface non-uniformity such as concavity and this type of disturbance was initially studied by Rayleigh. These stationary instabilities result in the formation of counter-rotating vortices which are aligned in the direction of the streamwise component and undergo non-linear breakdown. The ‘Tollmien-Schlichting’ instabilities were initially introduced during theoretical studies of Tollmien [117] and Schlichting [102] and were later observed experimentally by Schubauer and Skramstad [104]. These instabilities are wave-like and are amplified linearly in the streamwise direction as shown in Figure 1.7 and 1.8. The sources of this type of instability are mainly freestream turbulence, sound waves or two-dimensional roughness. Under the effect of wing sweep an additional velocity component, known as the crossflow, is introduced orthogonal to the streamwise direction resulting in a three-dimensional boundary layer. Due to the inflectional nature of the crossflow velocity profile, it destabilises rapidly and leads to the formation of vortices which are aligned with the direction of the inviscid flow. This instability can be considered as inviscid unlike the TS instability where amplification occurs mainly in the viscous layer. CF also exhibits non-linear break-down which can occur very close to the leading edge of swept wings at

flight conditions, where favourable pressure gradient near the leading edge (LE) becomes an influential parameter. A detailed review of the investigations on cross-flow instability during the previous two decades is presented by Saric et al. [101].

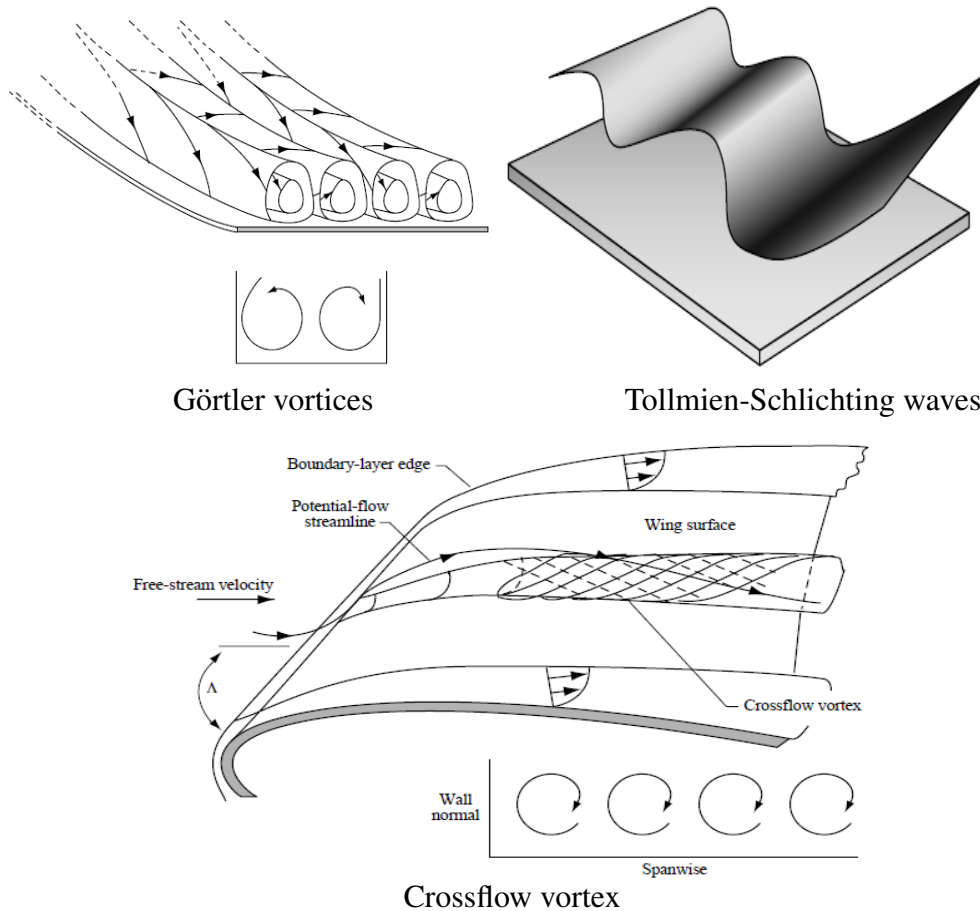


Figure 1.8: Schematic representation of the three main types of instabilities that might occur on a swept wing, from Joslin [66]

Nowadays, the study of laminar flow control is divided into two branches. The first, ‘natural laminar flow control’ (NLF), uses aerofoil shaping to achieve a desired pressure gradient which can slow down the growth of instabilities or cause them to decay. The second, ‘hybrid laminar flow control’ (HLFC) is usually a combination of suction to control the dominant cross-flow modes at the leading edge followed by pressure gradient modification to generate a pressure distribution which stabilises the TS modes. The effectiveness of suction in controlling cross-flow instabilities was demonstrated in the 1950s and a detailed historical review of the methods applied in flight conditions is presented by Braslow [20] and by Joslin [66] who also described the evolution of transition prediction

tools for laminar flow control. The study published by Arnal and Archambaud [3] details a series of flight experiments where NLF and HLFC have been demonstrated successfully and a few examples are presented in Figure 1.9 and 1.10 respectively.



ATTAS I - Wing [105]

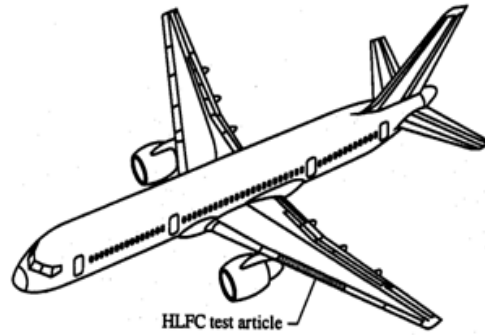
DASSAULT Falcon 50 - Fin [3]

Figure 1.9: Demonstrators of NLF in flight.

However the main form of transition mechanism that requires prior consideration on swept wings with large leading edge radii is attachment line contamination which renders most of the flow control techniques ineffective, as this phenomenon ensures that the boundary layer is fully turbulent right from its origin. Indeed, early attempts to establish laminar flow control technologies were hindered by an inability to obtain laminar flow right from the leading edge of swept wings, for instance during the flight tests conducted in the early 1950s by Gray [48][49]. This was initially suspected to be a consequence of crossflow instability leading to transition very close to the attachment line. Independent investigations by Pfenninger [89], Gaster [45] and later by Poll [92][91][93] confirmed that apparent subcritical instability was actually due to attachment line contamination. In simple terms the attachment line is the spanwise flow connecting all the points where the flow streamlines bifurcate into one part proceeding towards the upper surface and the other towards the lower surface, Figure 5.4. The dominant spanwise velocity component at the leading edge of a swept wing, is responsible for the convection of flow perturbations at the wing-fuselage junction or any other sources such as fuselage boundary layer turbulence into the attachment line. In Pfenninger's and Gaster's investigations, the amplification of these instabilities was studied and it was demonstrated that, if the attachment line Reynolds number is below a certain critical value the disturbances will decay along



AIRBUS A320 - Fin [3]



BOEING 757 - Wing [3]



DASSAULT FALCON 50 - Wing [66]



NASA F-16XL - Wing [66]

Figure 1.10: Demonstrators of HLFC in flight.

the attachment line, otherwise they will amplify rapidly leading to transition straight on the attachment line. Currently, on most commercial transonic aircraft attachment line contamination is present and all of the flow on the wing is turbulent.

Gaster [45] proposed a method of decontaminating the attachment line by placing a ‘bump’ along the leading edge which causes the turbulent flow at the attachment line to stagnate at the bump and a fresh laminar attachment line boundary layer to develop downstream. This type of device was extensively used by Arnal et al [5], [4], [3] during the implementation of NLF and HLFC techniques. In addition to Gaster’s device, Seyfang [107] also proposed various types of leading edge fence, as passive methods for the prevention of attachment line contamination. Poll and Danks [94] successfully demonstrated that active methods such as distributed wall suction could be also used to relaminarise the attachment line. This was supported by the study conducted by Arnal et al. [5]. The excrescence drag which is part of the parasitic drag from Figure 1.5 or weight penalties from the passive or active control methods respectively, can be offset if the laminar flow

is preserved further downstream for additional skin friction drag benefit. The reduction of drag will improve the sfc and considering equation 1.1 this could improve the aerodynamic efficiency, but the additional weight due to the suction system will affect the OWE and hence the benefit will be compromised. Still, on conventional swept wings the boundary layer is bound to undergo transition very rapidly downstream due to cross-flow instabilities and therefore the gain purely from attachment line control is questionable.

1.5 Aim of Current Study

More recently, numerical work by Gaster and Atkin [46], conducted using CVGK, which is a coupling between the turbulent, momentum integral boundary layer code, Callisto, owned by Airbus UK and the viscous Garabedian and Korn (VGK) full potential method, demonstrated that there might be a small but worthwhile drag reduction if the attachment line could be relaminarised regardless of whether or not transition occurs straight after. The benefit seems to arise from the form drag component as the initial reduction in displacement thickness, due to the presence of a laminar attachment line, results in a slightly lower value of the momentum thickness at the trailing edge and hence lower profile drag. The net profile drag reduction between the case with a laminar attachment line which transitions at $0.005 < x/c < 0.01$ and a fully turbulent case was found to be about 0.4 to 0.6 counts (1 drag count signifies to $C_D = 10^{-4}$) on each wing.

However, confidence in the CVGK analysis is undermined by a necessary numerical fix in the Callisto method. The streamline analogy used by Green's Lag-Entrainment method in three dimensions leads to singular governing equations at the attachment line and in a very confined region downstream due to high streamline curvature. To overcome these numerical issues a modified form of the governing equations is solved for the attachment line flow and these results are then extrapolated to a point about 0.5% of chord downstream of the attachment line where the three dimensional governing equations are no longer singular. An experimental campaign was therefore proposed to review the turbu-

lent attachment line flow and to validate the leading edge approximation, which will be discussed in section 2.7, by mapping the turbulent flow in this relatively unexplored region, starting from the attachment line and progressing downstream to $x/c = 0.03$. The experimental results would also be useful also for leading edge modelling and validation of higher order numerical methods.

The experimental model was designed to achieve an attachment line Reynolds number, similar to that of conventional aircraft at cruise condition, in a relatively low speed wind tunnel (5-55 m/s). Boundary layer traverse measurement were made using constant temperature hot wire anemometry and, considering the thickness of the boundary layer expected in the experimental domain (1-3mm), a traverse mechanism with very fine resolution was designed to capture the velocity profile accurately. A digital-optical set-up was implemented to calibrate and commission the traverse mechanism with micro-precision and it was also employed for the near wall alignment of the hot wire probe which was an advantage during the measurement of the turbulent boundary. A single-normal (SN) type hot wire probe was utilised for the measurement at the attachment line and for the measurement downstream a single-yawed (SY) type probe was needed to capture the streamwise and crossflow velocity components in the three dimensional boundary layer where a rather involved calibration and data reduction process was required.

1.6 Overview of Thesis

Following this brief explanation of the rationale for the current investigation, the background of the three dimensional momentum integral method is presented in Chapter 2, where its performance is validated with respect to previous experimental results. It is also demonstrated that there is an opportunity for drag reduction through attachment line control and conditional on further experimental analysis to validate or improve the leading edge modelling. The experimental campaign is presented Chapter 3, which describes the design of the experimental model and the instrumentation used for the data acquisition.

The use of the SY hot wire probe is not very common, therefore the principle behind the calibration and data reduction is presented in the Chapter 4, dedicated to hot wire anemometry.

In Chapter 5, the flow at the attachment line is reviewed and the results obtained from the present experimental measurement are compared with those obtained from previous investigations. The experimental results show good agreement with the limited experimental data on turbulent attachment line from the literature and it is demonstrated that the turbulent attachment line exhibits similar behaviours to those in fully developed pipe flows and fully turbulent flows on flat plates. The flow downstream of the attachment line is reviewed in Chapter 6 and the streamwise and crossflow velocity profiles captured in the three dimensional boundary layer are presented. However there is a lack of supporting experimental or numerical studies of the turbulent flow in the vicinity of an attachment line. Based on the behaviour of the three dimensional turbulent flow near the attachment line, a modification to the leading edge modelling in Callisto is proposed in Chapter 7. Further numerical analysis has been conducted to validate the revised model and the form drag benefit predicted initially. The major findings are summarised in Chapter 8, where recommendations for further studies are proposed.

Chapter 2

The Prediction of Turbulent Boundary Layers and Viscous Drag on Swept Wings

2.1 Infinite Swept Wing Condition

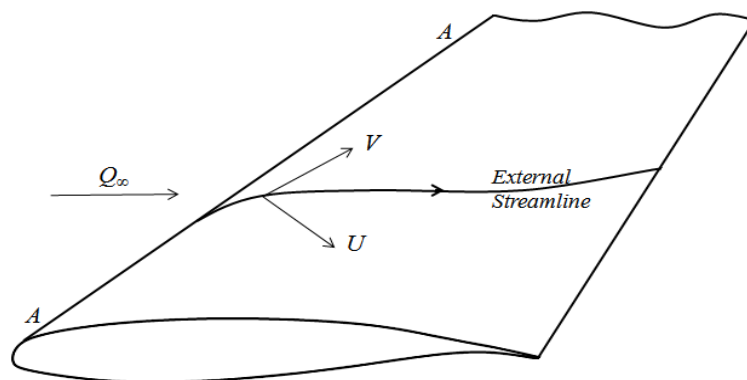


Figure 2.1: Schematic representation of the streamline on a swept and slightly tapered wing

Compared to aerofoils or two-dimensional wings, the flow on swept wings is more complex due to the introduction of an additional, spanwise, velocity component. At the leading edge, more precisely at the point of attachment, the chordwise velocity component,

$U = 0m/s$ and therefore the spanwise component, V dominates and the attachment line flow develops in the spanwise direction together with an attachment line boundary layer. Immediately downstream of the attachment line the spanwise velocity component is still dominant but there is rapid acceleration in the chordwise direction and this results in the formation of highly curved external streamline, as shown in Figure 2.1. The attachment line boundary layer will be further explored in Chapters 5 and 6.

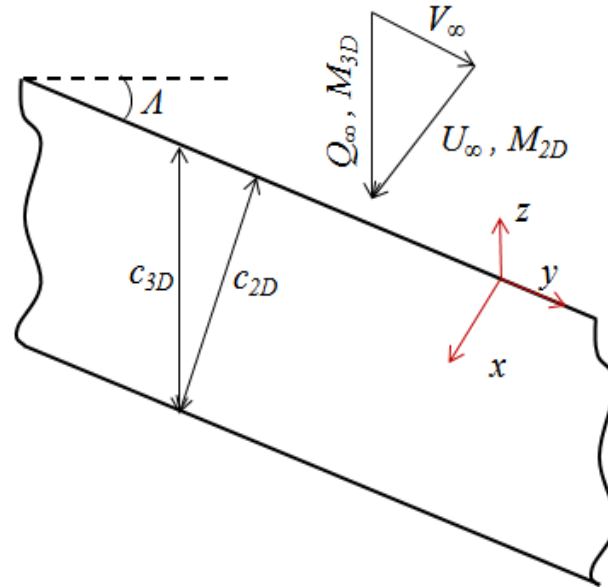


Figure 2.2: The axis and velocity vector convention based on the infinite-sweep assumption

The prediction of the viscous flow over a swept wing is a computationally intensive task as it requires solving the governing Navier-Stokes or boundary layer equations in three dimensions. However, the effort involved can be significantly reduced by employing the independence principle, which is valid while applying infinite-swept or infinite-yawed assumption. Here the flow field quantities are assumed to be constant along the y -direction, such that the isobars lie along the spanwise directions. Further simplification leads to the reduction of the problem to calculating the development only of the inviscid flow normal to the leading edge using two dimensional theory and then superimposing a uniform spanwise velocity on the two dimensional solution to yield the three-dimensional inviscid flow development (see figure 2.2 for the direction convention).

Following Lock's transformation [74] which was also employed by Thompson et al.

[116], an equivalence is defined relating the infinite swept and two dimensional flows. The chord lengths are related by

$$c_{3D} = \frac{c_{2D}}{\cos \Lambda} \quad (2.1)$$

and the thickness to chord ratio by

$$\frac{t}{c_{3D}} = \frac{t}{c_{2D}} \cos \Lambda \quad (2.2)$$

The freestream Mach numbers are related by

$$M_{3D} = \frac{M_{2D}}{\cos \Lambda} \quad (2.3)$$

and the pressure coefficients by

$$C_{P_{3D}} = C_{P_{2D}} \cos^2 \Lambda \quad (2.4)$$

Thompson et al. [115] demonstrated that equation 2.4 can be also derived while transforming the Euler equation from two-dimensional to three-dimensional coordinates. As the lift coefficient is a function of the pressure distribution the sectional lift along the line-of-flight can be determined using

$$C_{L_{3D}} = C_{L_{2D}} \cos^2 \Lambda \quad (2.5)$$

According to Thompson et al. these transformations can be extended to the various drag components shown in figure 1.4, where the drag from the infinite swept wings can be

calculated from that obtained while assuming the unswept conditions. Firstly, assuming that the normal pressure drag is directly proportional to the pressure distribution, the three-dimensional normal pressure drag can be expressed by the simple relation below.

$$C_{D_{P,3D}} = C_{D_{P,2D}} \cos^3 \Lambda \quad (2.6)$$

From basic principles the total drag can be expressed as

$$C_D = C_{D_P} + C_f \quad (2.7)$$

By replacing the pressure drag from equation 2.6 into equation 2.8 the total drag becomes

$$C_D = C_{D_{P,2D}} \cos^3 \Lambda + C_f \quad (2.8)$$

At this stage a method for transforming the skin friction drag, which is a strong function of the Reynolds number, is required. From Cook et al. [29] it is assumed that the equivalent Reynolds number can be expressed in terms of the velocity component based on the chord normal to the leading edge, but the characteristic length remains equivalent to the line-of-flight chord. Hence,

$$Re_{2D} = \frac{U c_{LOF}}{\nu} \quad , \quad Re_{2D} = \frac{Q_{\infty} c_{2D}}{\nu} \quad \text{or} \quad Re_{2D} = \frac{Q_{\infty} c_{LOF}}{\nu} \cos \Lambda \quad (2.9)$$

rather than the freestream Reynolds number,

$$Re = \frac{Q_{\infty} c_{LOF}}{\nu} \quad (2.10)$$

This argument is supported by ‘sheared’ flat plate analogy proposed by Cooke [31] where the skin friction drag coefficient is assumed to be independent of the sweep, although this approximation is debatable for viscous flow on swept wings.

Therefore, based on the two-dimensional turbulent skin friction law on flat plates, for an infinite-swept wing the skin friction drag takes the form

$$C_{f_{3D}} = C_{f_{2D}} \cos^{1/5} \Lambda \quad (2.11)$$

As the form drag is a component of the normal pressure drag, in three dimensions it can be expressed as

$$C_{D_{F,3D}} = C_{D_{F,2D}} \cos^3 \Lambda \quad (2.12)$$

and similarly the wave drag

$$C_{D_{W,3D}} = C_{D_{W,2D}} \cos^3 \Lambda \quad (2.13)$$

Following Ashill et al. [7], by substituting for the corresponding drag components the total viscous drag on an infinite-swept wing can be calculated from

$$C_{D_{V,3D}} = (C_{D_{V,2D}} - C_{D_{f,2D}}) \cos^3 \Lambda + C_{D_{f,2D}} \cos^{1/5} \Lambda \quad (2.14)$$

and including the wave drag, the profile drag can be estimated using

$$C_{D_0} = (C_{D_{V,2D}} - C_{D_{f,2D}}) \cos^3 \Lambda + C_{D_{f,2D}} (\cos)^{1/5} + C_{D_{W,2D}} \cos^3 \Lambda \quad (2.15)$$

This approach was validated by the study conducted by Thompson et al. and most importantly by the experimental results gathered by Ashill et al. which will be used for validation of the current numerical method, Callisto, in section 2.5. Nevertheless, in Callisto the development of the turbulent boundary layer is predicted in three dimensions and therefore the above transformations are not required for the estimation of the profile drag, except while accounting for C_{Dw} .

2.2 Two-Dimensional Momentum Integral Method

In 1921, von Karman [120] proposed a method for predicting the development of a boundary layer based on the principle of conservation of momentum in a control volume. By integrating the two-dimensional momentum equation, from the governing incompressible boundary layer equations, over the height of the boundary layer

$$\int_{z=0}^{z=\delta} \left(u \frac{\partial u}{\partial x} + w \frac{\partial u}{\partial z} - U_e \frac{\partial U_e}{\partial x} \right) dz = -\frac{\tau_w}{\rho} \quad (2.16)$$

While satisfying continuity, the momentum integral equation can be expressed as

$$\frac{d\theta}{dx} = \frac{c_f}{2} - \frac{1}{U_{iw}} \frac{dU_{iw}}{dx} \theta (H + 2) \quad (2.17)$$

where the velocity at the edge of the boundary layer, U_e . From Prandtl's first-order boundary layer theory the static pressure is assumed to be constant in the direction normal to the boundary layer, therefore the inviscid flow is equivalent to ρU_e . During the calculation of the outer flow an inner boundary condition is usually required, however in the presence of the boundary layer the curvature of the wall is modified due to the displacement effect and this is usually more pronounced in highly curved streamlines. Following higher order analysis, Lock and Williams [76] demonstrated that during numerical analysis it is impor-

tant to account for the effect of the variation of the equivalent inviscid flow (EIF) through the boundary layer, thus they proposed that, U_{iw} , which is the EIF at the wall to be a more robust boundary condition rather than U_e . The wall shear stress, τ_w , can be expressed in terms of the skin friction coefficient,

$$\frac{c_f}{2} = \frac{\tau_w}{\rho_e U_{iw}^2} \quad (2.18)$$

For a compressible flow the two-dimensional momentum integral equation can be expressed as

$$\frac{d\theta}{dx} = \frac{\tau_w}{\rho_{iw} U_{iw}^2} - \frac{1}{U_{iw}} \frac{dU_{iw}}{dx} \theta (H + 2 - M_{iw}^2) \quad (2.19)$$

Where the momentum thickness is defined by

$$\theta = \int_{z=0}^{z=\infty} \frac{\rho u}{\rho_{iw} U_{iw}} \left(1 - \frac{u}{U_{iw}}\right) dz \quad (2.20)$$

The shape factor can be expressed as

$$H = \frac{\delta^*}{\theta} \quad (2.21)$$

where the displacement thickness takes the form

$$\delta^* = \int_{z=0}^{z=\infty} \left(1 - \frac{\rho u}{\rho_{iw} U_{iw}}\right) dz \quad (2.22)$$

For a given local skin friction relation and pressure or velocity gradient over a profile, the development of the momentum thickness can be predicted and hence the profile drag.

For the case of a flat plate the overall skin friction drag reduces to the integration of the momentum thickness along the length of the plate (x-direction) due to the absence of the pressure gradient. Therefore,

$$\frac{d\theta}{dx} = \frac{c_f}{2} \quad (2.23)$$

Equation 2.17 can be also expressed as

$$\frac{d}{dx} (\rho_{iw} U_{iw}^2 \theta) = \tau_w - (\rho_{iw} U_{iw}^2 \delta^*) \frac{dU_{iw}}{dx} \quad (2.24)$$

and while integrating till the Trefftz plane, where $x = \infty$ would lead to

$$\rho_{iw} U_{iw}^2 \theta_{\infty} = \int_0^{\infty} \left[\tau_w + \delta^* \frac{dp}{dx} \right] dx \quad (2.25)$$

From equation 2.25 the first term on the right hand side represents the skin friction and the term on the left hand side represents the pressure or form drag. The form drag is directly proportional to the product of the displacement thickness and the pressure gradient it encounters and hence a reduction of the displacement in the region of adverse pressure gradient would result in a form drag benefit. The profile or sectional drag given by equation 2.26 is related to momentum deficit in the Trefftz plane.

$$C_{D_0} = \frac{2\theta_{\infty}}{c} \quad (2.26)$$

2.2.1 Entrainment in Turbulent Boundary Layers

The von Karman momentum integral method introduced above is applicable to both laminar and turbulent boundary layers, however it has been predominantly used for the prediction of turbulent boundary layers coupled with auxiliary equations for the development of the skin friction and the shape factor. To better represent the physical mechanisms within a turbulent boundary flow, Head [56] proposed a method for capturing the effect of entrainment from the irrotational inviscid flow into the turbulent viscous layer. Initially, Head assumed that the quantity of fluid entrained per unit area was a function of mainly the boundary layer shape parameter and the velocity at the edge of the boundary layer. The dependency on Reynolds number was neglected assuming that the mixing was similar to a turbulent jet or wake. The parameter, E is the quantity of fluid entrained inside the boundary layer and the rate of entrainment per unit length can be written as

$$\frac{dE}{dx} = \frac{d}{dx} [U_{iw} (\delta - \delta^*)] \quad (2.27)$$

or

$$\frac{d}{dx} [U_{iw} (\delta - \delta^*)] = f (H_1, U_{iw}, \delta - \delta^*) \quad (2.28)$$

where, H_1 , represents the entrainment shape factor given by

$$H_1 = \frac{\delta - \delta^*}{\theta} \quad (2.29)$$

The quantity, $U_{iw} (\delta - \delta^*)$, represents the volume of fluid flowing in the boundary layer in two dimensions. Equation 2.28 can be written in non-dimensional form as

$$\frac{1}{U_{iw}} \frac{d}{dx} [U_{iw} (\delta - \delta^*)] = F(H_1) \quad (2.30)$$

Head suggested that a further auxiliary equation could be obtained by expressing $H_1 = f(H)$ and expanding equation 2.30. By substituting for $d\theta/dx$ from the momentum integral equation and following the mathematical steps shown in ref. [56]

$$\theta \frac{dH}{dx} = \left[\frac{dH_1}{dH} \right]^{-1} \left\{ c_E - H_1 \left[\frac{c_f}{2} - (H + 1) \frac{\theta}{U_{iw}} \frac{dU_{iw}}{dx} \right] \right\} \quad (2.31)$$

where the function, F , from equation 2.30 has been substituted by the entrainment coefficient, c_E .

Head concluded that the results computed from this rapid method were in fair agreement with the limited experimental results. Further experiments were required to validate the crude assumptions and formulate more robust auxiliary equations.

2.2.2 Equilibrium in Turbulent Boundary Layers

The entrainment method was improved by Head and Patel [57] through the introduction of the concept of equilibrium in turbulent boundary layers which is applicable in the velocity-defect region of the boundary layer where the entrainment process occurs predominantly. According to Green et al. [52], in equilibrium flows the velocity and the shear stress profiles are constant in the streamwise direction, so there is no change in the shape factor, $dH/dx = 0$, nor in the maximum shear-stress coefficient, $dc_{\tau m}/dx = 0$. This analogy for turbulent boundary layers is equivalent to the self-similar approximation for laminar boundary layers. This assumption was made in line with Rotta's [99] observation, who suggested that the equilibrium flows can be represented by the shape parameter which defines the velocity-defect profile, G , and the pressure-gradient parameter, Π given

by equations 2.32 and 2.33 respectively.

$$G = \frac{H-1}{H} \sqrt{\frac{2}{c_f}} \quad (2.32)$$

$$\Pi = \frac{\delta^*}{\tau_w} \frac{dp}{dx} \quad (2.33)$$

Green et al. suggested that the shape parameter and pressure-gradient parameter can be coupled into a single relation given by equation 2.34, which was derived from experimental results obtained for flows where the equilibrium assumption is valid together with the analysis of Mellor and Gibson [80] which was in good agreement with the empirical relation proposed by Nash and McDonald [83] which was in a different form.

$$G = 6.432 (1 + 0.8\Pi)^{1/2} \quad (2.34)$$

By substituting for G and Π from equation 2.32 and 2.33 respectively equation 2.34 can be expanded to

$$\frac{H-1}{H} = 6.432 \left(\frac{c_f}{2} - 0.8H \frac{\theta}{U_{iw}} \frac{dU_{iw}}{dx} \right)^{1/2} \quad (2.35)$$

or

$$\left(\frac{\theta}{U_{iw}} \frac{dU_{iw}}{dx} \right)_{EQ} = \frac{1.25}{H} \left[\frac{c_f}{2} - \left(\frac{H+1}{6.432H} \right)^2 \right] \quad (2.36)$$

Applying the equilibrium flow assumption, $dH/dx = 0$ to the entrainment relation given by equation 2.31 leads to an identity for the entrainment coefficient in equilibrium flows:

$$(c_E)_{EQ} = H_1 \left[\frac{c_f}{2} - (H + 1) \left(\frac{\theta}{U_{iw}} \frac{dU_{iw}}{dx} \right)_{EQ} \right] \quad (2.37)$$

The terms on the left hand side of equations 2.36 and 2.37 appear in the 'lag-entrainment' method that will be covered in section 2.2.3. These two parameters can be expressed as functions of H , H_1 and C_f using the empirical relations for shape factor, H and skin friction outlined by Green et al. and will be introduced in the next section.

2.2.3 The Effect of Lag in Entrainment

An improvement to the above entrainment method was proposed by Green et al. through the introduction of an extra equation for a better representation of the turbulence structure. The basis of this method was established by Bradshaw, Ferriss and Atwell [19] who formulated a model for the turbulent shear stress by applying the turbulent energy equation, in the form given by Townsend, outside the viscous sublayer region of an incompressible, two-dimensional mean flow. From Bradshaw et al. and Green et al., the mean turbulent energy equation can be expressed as

$$\underbrace{\frac{1}{2}\rho \left(U \frac{\partial \bar{q}^2}{\partial x} + W \frac{\partial \bar{q}^2}{\partial z} \right)}_{\text{advection}} - \underbrace{\tau \frac{\partial U}{\partial z}}_{\text{production}} + \underbrace{\frac{\partial}{\partial z} \left(\overline{pw} + \frac{1}{2} \rho \overline{q^2 w} \right)}_{\text{diffusion}} + \underbrace{\rho \epsilon}_{\text{dissipation}} = 0 \quad (2.38)$$

where,

$$q^2 = u^2 + v^2 + w^2, \quad \tau = -\rho \overline{uw} \quad \text{and} \quad \epsilon \approx \nu \left(\overline{\partial u / \partial x} \right)^2 \quad (2.39)$$

Equation 2.38 was further modified to a semi-empirical, partial differential equation for shear stress using the parameters below which were proposed by Bradshaw et al.

$$a_1 \equiv \frac{\tau}{\rho q^2}, \quad L \equiv \frac{(\tau/\rho)^{3/2}}{\epsilon} \quad \text{and} \quad G = \frac{\frac{\overline{pw}}{\rho} + \frac{1}{2} \overline{q^2 w}}{\left(\frac{\tau_{max}}{\rho}\right)^{1/2} \frac{\tau}{\rho}} \quad (2.40)$$

Substituting these definitions into equation 2.38 results in

$$\underbrace{\overline{U} \frac{\partial}{\partial x} \left(\frac{\tau}{2a_1 \rho} \right)}_{\text{advection}} + \underbrace{\overline{W} \frac{\partial}{\partial z} \left(\frac{\tau}{2a_1 \rho} \right)}_{\text{advection}} - \underbrace{\frac{\tau}{\rho} \frac{\partial \overline{U}}{\partial z}}_{\text{production}} + \underbrace{\left(\frac{\tau_m}{\rho} \right)^{1/2} \frac{\partial}{\partial x} \left(G \frac{\tau}{\rho} \right)}_{\text{diffusion}} + \underbrace{\frac{\left(\frac{\tau}{\rho} \right)^{3/2}}{L}}_{\text{dissipation}} = 0 \quad (2.41)$$

where, G can also be expressed as a function of the boundary layer velocity profile.

$$\frac{G}{\left(\tau_{max}/\rho U_{iw}^2\right)^{1/2}} = \zeta = f\left(\frac{z}{\delta}\right) \quad (2.42)$$

From Bradshaw et al. the shear stress profile can be related to the parameters G , L and a_1 representing the diffusion, dissipation and advection respectively and can be also represented empirically. Based on this assumption and following the necessary substitutions, Green et al. derived an ordinary differential equation for maximum shear stress in the form below.

$$\underbrace{\frac{\delta}{c_{\tau m}} \frac{dc_{\tau m}}{dx}}_{\text{advection}} = 2a_1 \frac{U_{iw}}{\overline{U}} \left[\underbrace{\frac{\delta}{U_{iw}} \frac{\partial \overline{U}}{\partial z}}_{\text{production}} - \underbrace{\frac{\delta}{L} c_{\tau m}^{1/2}}_{\text{dissipation}} - \underbrace{c_{\tau m} \zeta'}_{\text{diffusion}} \right] - \underbrace{\frac{2\delta}{U_{iw}} \frac{dU_{iw}}{dx}}_{\text{advection}} \quad (2.43)$$

Referring back to section 2.2.2, in equilibrium flows the velocity and shear stress profile, including the max shear stress, $c_{\tau m}$, are assumed to be constant in the streamwise direction. Therefore, according to Green et al. equation 2.43 can be altered to equation 2.44 where the left hand side of the equation equates to zero.

$$\frac{\delta}{c_{\tau m}} \frac{dc_{\tau m}}{dx} = 2a_1 \frac{U_{iw}}{\overline{U}} \frac{\delta}{L} \left(c_{\tau m EQ}^{1/2} - c_{\tau m}^{1/2} \right) + \left(\frac{2\delta}{U_{iw}} \frac{dU_{iw}}{dx} \right)_{EQ} - \frac{2\delta}{U_{iw}} \frac{dU_{iw}}{dx} \quad (2.44)$$

However, as pointed out by Green et al. equation 2.44 has to be converted into a differential equation in terms of entrainment coefficient instead of the current maximum shear stress form so that it can be coupled with the momentum integral equations. In its current form equation 2.44 is valid for flows where the maximum shear stress, τ_m , occurs between the wall and $z/\delta < 0.2$. The term, $2a_1 U_{iw} \delta / \bar{U} L$, is heavily dependent on the position of τ_m . For book-keeping Green et al. suggested that for $z/\delta \geq 0.2$, $c_{\tau m}$ could be replaced by c_τ or it was equivalent to the resulting value of $\tau / \rho_{iw} U_{iw}^2$ at $z/\delta = 0.2$. By doing so equation 2.44 can be modified to

$$\frac{\delta}{c_\tau} \frac{dc_\tau}{dx} = 2a_1 \frac{U_{iw}}{\bar{U}} \frac{\delta}{L} \left(c_{\tau EQ}^{1/2} - c_\tau^{1/2} \right) + \left(\frac{2\delta}{U_{iw}} \frac{dU_{iw}}{dx} \right)_{EQ} - \frac{2\delta}{U_{iw}} \frac{dU_{iw}}{dx} \quad (2.45)$$

From equation 2.41 one can observe that the derivatives in the normal or z -direction have been neglected, namely the advection term, $\bar{W} \partial \tau / \partial z$, and the diffusion term, $\partial(G\tau) / \partial z$, during the derivation of equation 2.45.

According to Green et al., in most flows with adverse pressure gradients the maximum shear stress, τ_m , is encountered at $z/\delta > 0.2$, thus $\partial \tau / \partial z$ becomes significant mainly in the presence of a strong favourable pressure gradient. However, a comparison with two-dimensional sink flow, suggested equation 2.45 might be employed for most flows of practical interest with an acceptable degree of accuracy. Equation 2.45 could be further reduced by substituting the term, $2a_1 U_{iw} \delta / \bar{U} L$ by a numerical coefficient. From Bradshaw et al. [19], $a_1 = 0.15$ and, for a flow where the maximum shear stress occurred within $0.2 < z/\delta < 0.5$, L/δ was approximately 0.09, however a value of 0.08 was preferred by Green et al.. Based on Mellor and Gibson's [80] investigation, $U_{iw} / \bar{U} \approx 1.5$ at the location of τ_m , in an adverse pressure gradient, but no justification was proposed by Green et al. as far as favourable pressure gradients were concerned.

By substituting for the corresponding parameters, equation 2.45 can be simplified to

$$\frac{\delta}{c_\tau} \frac{dc_\tau}{dx} = 5.6 \left(c_{\tau_{EQ}}^{1/2} - c_\tau^{1/2} \right) + 2 \left(\frac{\delta}{U_{iw}} \frac{dU_{iw}}{dx} \right)_{EQ} - \frac{2\delta}{U_{iw}} \frac{dU_{iw}}{dx} \quad (2.46)$$

The final step involves formulating a relation between c_τ and c_E in order to replace the c_τ from equation 2.46. The linear relation between c_τ and c_E proposed by Bradshaw et al. was deemed unsatisfactory by Green et al. for some cases. The variation of c_E against c_τ was shown in figure Fig. 3a of reference [52] for Reynolds number based on displacement thickness, R_{δ^*} , of 10^3 and 10^5 , following an analytical approximation a relation between c_E and c_τ could be expressed as

$$c_\tau = 0.024c_E + 1.2c_E^2 + 0.32c_{f_0} \quad (2.47)$$

where, c_{f_0} is the flat plate skin friction coefficient that can be represented by the correlation given by Winter and Gaudet [122]

$$c_{f_0} = \frac{0.01013}{\log_{10} R_\theta - 1.02} - 0.00075 \quad (2.48)$$

To reduce the number of unknowns from the entrainment equation a relation was formulated based on the results of the analytical study of Mellor and Gibson [80], while applying the shape parameter relation given by equation 2.49 which was approximated from the experimental results of East and Hoxey [39] and Thompson's [113] two-parameter profile family.

$$H_1 = 3.15 + \frac{1.72}{H - 1} - 0.01 (H - 1)^2 \quad (2.49)$$

By replacing equation 2.49 and its derivative with respect to x in equation 2.47 and at the same time applying the assumption proposed by Green et al. the 'lag-entrainment'

equation takes its basic form as

$$\theta (H_1 + H) \frac{dc_E}{dx} = \frac{c_e (c_E + 0.002) + 0.2667c_{f_0}}{c_e + 0.01} \left[2.8 \left\{ \left(0.32c_{f_0} + 0.024c_{E_{EQ}} + 1.2c_{E_{EQ}}^2 \right)^{1/2} - \left(0.32c_{f_0} + 0.024c_E + 1.2c_E^2 \right)^{1/2} \right\} + \left(\frac{\delta}{U_{iw}} \frac{dU_{iw}}{dx} \right)_{EQ} - \left(\frac{\delta}{U_{iw}} \frac{dU_{iw}}{dx} \right) \right] \quad (2.50)$$

Further improvement to the prediction method was possible by modelling the extraneous influences on the turbulence structure which, according to Green et al. were predominantly due to longitudinal surface curvature, freestream turbulence and flow convergence or divergence especially close to the leading edge of a wing or if present near separation. To account for the influence of longitudinal curvature on the turbulence structure the method suggested by Bradshaw [15] was implemented. The influence of the streamline convergence or divergence on the turbulence structure was addressed using another approximation proposed by Bradshaw [17], which states that extra rate of strain is equivalent to the eddy viscosity augmented by a certain factor. From reference [52] the introduction of these terms did not affect the modelling considerably as they could be accounted for simply by multiplying the dissipation by term in equation 2.43 by a certain factor. The ‘lag-entrainment’ method was also extended to handle the flow in the near-field wake.

For a compressible flow Green et al. utilised the form of the ordinary differential equation for shear stress (equation 2.43 with additional terms for compressibility) proposed by Bradshaw and Ferriss [18]. By employing similar steps to those outlined above, and approximating the effect of compressibility on the turbulence structure, shape parameters and skin friction, the compressible ‘lag-entrainment’ was obtained:

$$\frac{(0.01 + c_e)}{(0.02c_E + c_e^2 + 0.2667c_{f_0})} \delta \frac{dc_E}{dx} = 2.8 \{c_{\tau_{EQ}}^{1/2} - c_{\tau}^{1/2}\} + \left(\frac{\delta}{U_{iw}} \right)_{EQ} \quad (2.51)$$

$$- \frac{\delta}{U_{iw}} \frac{dU_{iw}}{dx} \left\{ 1 + 0.075M^2 \frac{(1 + 0.2M^2)}{(1 + 0.1M^2)} \right\}$$

This method was heavily used at the Royal Aircraft Establishment in the 1970's coupled to both two and three dimensional full potential and transonic small perturbation methods notably with the Garabedian and Korn [42] full potential method. The earliest implementation was abbreviated as VGK, followed by AVGK and then BVGK where higher order terms were implemented. So far, BVGK has been considered the most efficient and has been used predominantly for the design of supercritical wing sections, which were then converted to three dimensional sections using Lock's transformation [74]. In CVGK, this method has been extended to three dimensional flows and the formulation will be visited in the section that follows.

2.3 Three-Dimensional Momentum Integral Method

According to Smith [109], in the streamline coordinates system, where the streamwise component, s is along the projection of the streamline and n is the orthogonal component usually referred to as the crossflow component, the three dimensional momentum integral equations can be written as

$$\frac{\partial \theta_{11}}{\partial s} + \frac{\partial \theta_{12}}{\partial n} = \frac{\tau_{01}}{\rho U_{iw}^2} - \frac{1}{U_{iw}} \frac{\partial U_{iw}}{\partial s} \theta_{11} (H + 2 - M_{iw}^2) - \theta_{11} \frac{1}{r} \frac{\partial r}{\partial s} \quad (2.52)$$

$$\theta_{22} \frac{1}{r} \frac{\partial r}{\partial s} + M_{iw}^2 \theta_{12} \frac{1}{U_{iw}} \frac{\partial U_{iw}}{\partial n}$$

$$\begin{aligned} \frac{\partial \theta_{21}}{\partial s} + \frac{\partial \theta_{22}}{\partial n} = & \frac{\tau_{02}}{\rho U_{iw}^2} - 2\theta_{21} \left(\frac{1}{U_{iw}} \frac{\partial U_{iw}}{\partial s} + \frac{1}{r} \frac{\partial r}{\partial s} \right) - \theta_{11} (H+1) \frac{1}{U_{iw}} \frac{\partial U_{iw}}{\partial n} \\ & - \frac{1}{U_{iw}} \frac{\partial U_{iw}}{\partial n} \theta_{22} + \theta_{21} M_{iw}^2 \frac{\partial U_{iw}}{\partial s} + \theta_{22} M_{iw}^2 \frac{1}{U_{iw}} \frac{\partial U_{iw}}{\partial n} \end{aligned} \quad (2.53)$$

and the three dimensional entrainment equation takes the form

$$\begin{aligned} \frac{\partial (\delta - \delta_1)}{\partial s} - \frac{\partial \delta_2}{\partial n} = & c_E - (\delta - \delta_1) \left[\frac{1}{r} \frac{\partial r}{\partial s} + (1 - M_{iw}^2) \frac{1}{U_{iw}} \frac{\partial U_{iw}}{\partial s} \right] \\ & - \delta_2 M_{iw}^2 \frac{1}{U_{iw}} \frac{\partial U_{iw}}{\partial n} \end{aligned} \quad (2.54)$$

The velocities, U and V and the shear stresses τ_{01} and τ_{02} are the velocity and skin friction components in the streamwise (s) and crossflow (n) directions respectively and the boundary layer integral quantities are defined as

$$\begin{aligned} \delta_1 &= \int_0^\delta \left(1 - \frac{\rho U}{\rho_{iw} U_{iw}} \right) dz, & \delta_2 &= - \int_0^\delta \frac{\rho U}{\rho_{iw} U_{iw}} dz \\ \theta_{11} &= \int_0^\delta \frac{\rho U}{\rho_{iw} U_{iw}} \left(1 - \frac{U}{U_{iw}} \right) dz, & \theta_{12} &= \int_0^\delta \frac{\rho V}{\rho_{iw} U_{iw}} \left(1 - \frac{U}{U_{iw}} \right) dz \\ \theta_{21} &= - \int_0^\delta \frac{\rho UV}{\rho_{iw} U_{iw}^2} dz, & \theta_{22} &= - \int_0^\delta \frac{\rho V^2}{\rho_{iw} U_{iw}^2} dz \end{aligned} \quad (2.55)$$

where ζ represents the direction normal to the surface and the two dimensional, chordwise displacement thickness, δ^* , has been replaced by streamwise displacement thickness, δ_1 .

Smith suggested that the boundary layer integral quantities could be approximated by an explicit velocity profile family, where the streamwise profile was assumed to be similar to that proposed by Spence [111] for the two dimensional boundary layer and could be expressed as

$$\frac{U}{U_{iw}} = \left(\frac{z}{z_\delta} \right)^n \quad (2.56)$$

Following the study conducted by Mager, a generalised form of the crossflow profiles was derived as

$$\frac{V}{U_{iw}} = \left(1 - \frac{z}{z_\delta} \right)^2 \tan \beta \frac{U}{U_{iw}} \quad (2.57)$$

where β represents the angle between the limiting streamline (surface streamline) and external streamline of the inviscid flow. From the study conducted by Smith [108] the streamwise boundary layer integral parameters could be expressed as function of the shape parameter,

$$\bar{H} = \frac{\int_0^\delta \left(1 - \frac{U}{U_{iw}} \right) \frac{\rho}{\rho_{iw}} dz}{\theta_{11}} \quad (2.58)$$

the streamwise momentum thickness, θ_{11} and the limiting streamline angle, β . Hence, the crossflow integral quantities

$$\begin{aligned} \theta_{21} &= \tan \beta f_1(\bar{H}) \theta_{11} \\ \theta_{12} &= \tan \beta f_2(\bar{H}) \theta_{11} \\ \delta_2 &= \tan \beta f_3(\bar{H}) \theta_{11} \\ \theta_{22} &= \tan^2 \beta f_4(\bar{H}) \theta_{11} \end{aligned} \quad (2.59)$$

where the functions, f_1 , f_2 , f_3 and f_4 are defined in the appendix A.1. The crossflow wall shear stress was assumed to depend on the streamwise skin friction coefficient,

$$\frac{\tau_{02}}{\rho U_{iw}^2} = \tan \beta \frac{C_f}{2} \quad (2.60)$$

The skin friction and shape parameters can be determined using semi-empirical auxiliary equations similar to those employed by Green et al. [52] for compressible flow. Initially Smith [108] demonstrated that, by transforming from streamline coordinates to Cartesian coordinates and at the same time applying the yawed-wing assumption, the governing three dimensional momentum integral and entrainment equations could be expressed in a form suitable to deal with the flow over infinite-swept wing. Later Ashill and Smith [8] extended the method to include the effect of ‘lag-entrainment’ and wing taper. Where the governing ordinary differential equations for yawed wings which can be expressed in matrix form, equation 2.61, and solved using a Runge-Kutta algorithm.

$$\begin{bmatrix} A_{11} & A_{12} & A_{13} \\ A_{21} & A_{22} & A_{23} \\ A_{31} & A_{32} & A_{33} \end{bmatrix} \begin{bmatrix} \frac{d\theta_{11}}{dx} \\ \frac{da}{dx} \\ \frac{d(\delta-\delta_1)}{dx} \end{bmatrix} = \begin{bmatrix} \lambda_1 \\ \lambda_2 \\ \lambda_3 \end{bmatrix} \quad (2.61)$$

The coefficients A_{ij} and λ_n have been defined in ‘Appendix C’ of reference [8], where a represents $\tan \beta$. This formulation is a better representation of the flow on infinite-swept wings and a similar approach has been adopted for the latest implementation of ‘lag-entrainment’, Callisto, which will be elaborated in the next section.

2.4 Numerical Modelling in Callisto

Callisto is an extension of the infinite-swept-tapered method developed by Ashill and Smith [8] which includes the ‘lag-entrainment’ model formulated by Green et al. [52]. Further changes were made to couple the viscous calculation with an inviscid solver to account for boundary layer displacement effects, using Lock and Williams’ [73] ‘viscous-

inviscid-interaction'(VII) method. The governing equations in Callisto originate mainly from the work of Ashill and Smith [8] and Ashill [6] except for the implementation of the non-orthogonal coordinate system shown in figure 2.3, which allows for the solution to be obtained along the line-of-flight rather than chord normal to the leading edge. It also contains improvements in terms of the solution scheme to increase the accuracy of the predictions. A detailed description of the numerical modelling has been presented by Atkin [12] and a brief account of the core governing equations will be presented in this section.

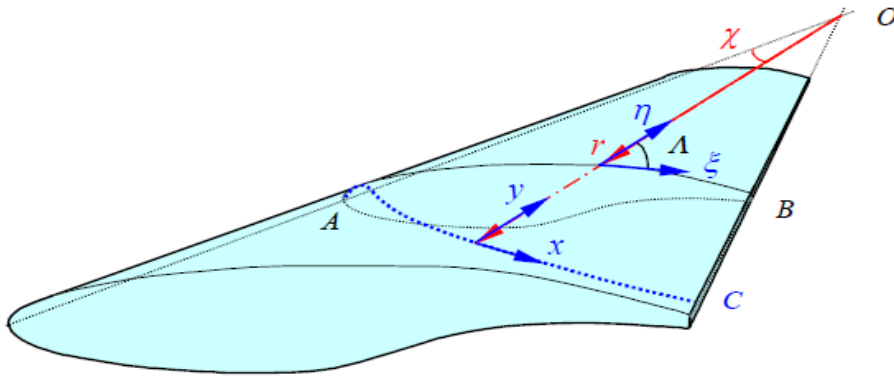


Figure 2.3: Schematic representation of the non-orthogonal coordinates system in Callisto, from Atkin [12]

2.4.1 Governing Equations

The latest implementation of the governing equations in Callisto emanates from the work analysis conducted by Ashill [6] where they were expressed in orthogonal Cartesian coordinates. Following Atkin's [12] transformation, to the non-orthogonal (ξ, η) coordinates shown in figure 2.3, the streamwise momentum equation was expressed as

$$(A_\theta \quad A_{\bar{H}} \quad A_\beta \quad A_U) \cdot \frac{d}{d\xi} (\theta \quad \bar{H} \quad \beta \quad U_{iw}) = A_0 \quad (2.62)$$

where

$$\begin{aligned}
A_A &= \theta [\cos \psi (1 + \bar{f}) - \sin \psi \tan \beta f_2] \\
A_\theta &= \frac{\partial A_A}{\partial \theta} = \cos \psi (1 + \bar{f}) - \sin \psi \tan \beta f_2 + \cos \psi \bar{f}_\theta \theta \\
A_{\bar{H}} &= \frac{\partial A_A}{\partial \bar{H}} = -\sin \psi \tan \beta \frac{df_2}{d\bar{H}} \theta + \cos \psi f_{\bar{H}} \theta \\
A_\beta &= \frac{\partial A_A}{\partial \beta} = -\sin \psi \sec^2 \beta f_2 \theta + \cos \psi \bar{f}_\beta \theta \\
A_U &= [\cos \psi (H + 2 + 2\bar{f}) + \sin \psi \tan \psi (1 - \tan^2 \beta f_4) - M_{iw}^2 A_\theta] \frac{\theta}{U_{iw}} + \cos \psi \bar{f}_U \theta \\
A_0 &= \sin \Lambda \left[\frac{c_f}{2} + \kappa_T \theta (\sin \psi + \cos \psi \tan \beta f_2) \right] - \kappa_T \theta \cos \Lambda A_\theta - \cos \psi \bar{f}_\xi \theta
\end{aligned} \tag{2.63}$$

and ψ represents the streamline divergence angle shown in figure 2.20 and is a function of the external chordwise and spanwise velocity components

$$\tan \psi = \frac{V_1}{U_1}, \quad \sin \psi = \frac{V_1}{U_{iw}}, \quad \cos \psi = \frac{U_1}{U_{iw}} \tag{2.64}$$

The entrainment equation is expressed as

$$(E_\theta \ E_{\bar{H}} \ E_\beta \ E_U) \cdot \frac{d}{d\xi} (\theta \ \bar{H} \ \beta \ U_{iw}) = E_0 \tag{2.65}$$

where the coefficients from equation 2.65 are defined as

$$\begin{aligned}
E_\theta &= \cos \psi H_1 + \sin \psi \tan \beta f_3 \\
E_{\bar{H}} &= \frac{\partial E_\theta}{\partial \bar{H}} \theta = \left(\cos \psi \frac{dH_1}{d\bar{H}} + \sin \psi \tan \beta \frac{df_3}{d\bar{H}} \right) \theta \\
E_\beta &= \frac{\partial E_\theta}{\partial \beta} \theta = \sin \psi \sec^2 \beta f_3 \theta \\
E_U &= (\sec \psi H_1 - M_{iw}^2 E_\theta) \frac{\theta}{U_{iw}} \\
E_0 &= \sin \Lambda [c_E + \kappa_T \theta (\sin \psi H_1 - \cos \psi \tan \beta f_3)] - \kappa_T \theta \cos \Lambda E_\theta
\end{aligned} \tag{2.66}$$

The normal or crossflow momentum equation has the form

$$(N_\theta \ N_{\bar{H}} \ N_\beta \ N_U) \cdot \frac{d}{d\xi} (\theta \ \bar{H} \ \beta \ U_{iw}) = N_0 \quad (2.67)$$

where,

$$\begin{aligned} N_\theta &= \tan \beta (\cos \psi f_1 - \sin \psi \tan \beta f_4) \\ N_{\bar{H}} &= \frac{\partial N_\theta}{\partial \bar{H}} \theta = \tan \beta \left(\cos \psi \frac{df_1}{d\bar{H}} - \sin \psi \tan \beta \frac{df_4}{d\bar{H}} \right) \theta \\ N_\beta &= \frac{\partial N_\theta}{\partial \beta} \theta = \sec^2 \beta (\cos \psi f_1 - 2 \sin \psi \tan \beta f_4) \theta \\ N_U &= \left[2 \sec \psi \tan \beta f_1 - \sin \psi (1 + H + \tan^2 \beta f_4) - M_{iw}^2 N_\theta \right] \frac{\theta}{U_{iw}} \\ N_0 &= \sin \Lambda \tan \beta \left[\frac{c_f}{2} + \kappa_T \theta (\sin \psi f_1 + \cos \psi \tan \beta f_4) \right] - \kappa_T \theta \cos \Lambda N_\theta \end{aligned} \quad (2.68)$$

and the transpiration equation is written

$$(W_\theta \ W_{\bar{H}} \ W_\beta \ W_U) \cdot \frac{d}{d\xi} (\theta \ \bar{H} \ \beta \ U_{iw}) - \sin \Lambda \frac{V_n}{U_{iw}} = W_0 \quad (2.69)$$

where

$$\begin{aligned} W_\theta &= \cos \psi H - \sin \psi \tan \beta f_3 \\ W_{\bar{H}} &= \frac{\partial W_\theta}{\partial \bar{H}} \theta = \left(\cos \psi \frac{\partial H}{\partial \bar{H}} - \sin \psi \tan \beta \frac{df_3}{d\bar{H}} \right) \theta \\ W_\beta &= \frac{\partial W_\theta}{\partial \beta} \theta = -\sin \psi \sec^2 \beta f_3 \theta \\ W_U &= \left(\cos \psi U_{iw} \frac{\partial H}{\partial U_{iw}} + \sec \psi H - M_{iw}^2 W_\theta \right) \frac{\theta}{U_{iw}} \\ W_0 &= \kappa_T \theta \sin \Lambda (\sin \psi H + \cos \psi \tan \beta f_3) - \kappa_T \theta \cos \Lambda W_\theta \end{aligned} \quad (2.70)$$

The coefficients of the three dimensional shape parameters, f_1 to f_4 are the same as those employed by Smith [109] and Ashill and Smith [8] and are defined in appendix A.1.

From Atkin [12], in non-orthogonal coordinates the ‘lag’ equation can be derived by

transforming equation 54 from Ashill [6] which in a form similar to equation 2.51 and rearranged into

$$L_E \frac{dc_E}{d\xi} = L_0 - L_U \frac{dU_{iw}}{d\xi} \quad (2.71)$$

where,

$$\begin{aligned} L_E &= \cos \psi \theta \\ L_U &= \cos \psi F \left[1 + 0.075 M_{iw}^2 \frac{(1 + 0.2M^2)}{(1 + 0.1M^2)} \right] \frac{\theta}{U_{iw}} \\ L_0 &= F \sin \Lambda \left[\frac{2.8}{H + H_1} \left(\sqrt{c_{\tau EQ_0}} - \lambda \sqrt{c_\tau} \right) + \left(\frac{\theta}{U_{iw}} \frac{\partial U_{iw}}{\partial s} \right)_{EQ} \right] \end{aligned} \quad (2.72)$$

and, from Green et al. [52] and later by Ashill [6], the coefficient F can be defined as

$$F = \frac{c_\tau}{1.2 (0.01 + c_E) (1 + 0.1M_{iw}^2)} \quad (2.73)$$

The four governing differential equations can be expressed in matrix form as

$$\begin{bmatrix} A_\theta & A_{\bar{H}} & A_\beta & A_U \\ E_\theta & E_{\bar{H}} & E_\beta & E_U \\ N_\theta & N_{\bar{H}} & N_\beta & N_U \\ W_\theta & W_{\bar{H}} & W_\beta & W_U \end{bmatrix} \frac{d}{d\xi} \begin{bmatrix} \theta \\ \bar{H} \\ \beta \\ U_{iw} \end{bmatrix} = \begin{bmatrix} A_0 \\ E_0 \\ N_0 \\ W_0 + \frac{\sin \Lambda}{U_{iw}} V_n \end{bmatrix} \quad (2.74)$$

2.4.2 Solution of Governing Equations

The number of unknowns in equation 2.74 can be reduced through the formulation of semi-empirical relations for the shape parameter, skin friction, equilibrium entrainment parameters and corrections to the normal stress due to low-Reynolds-number effects in the terms, \bar{f} , \bar{f}_{EQ} , ν_1 and ν_2 . By doing so, the number of unknowns in the equation reduces

to five, namely the four derivatives with respect to ξ and the transpiration velocity, V_n . In fact one or the other of $dU_{iw}/d\xi$ or V_n is prescribed by the external, inviscid flow. This is usually $dU_{iw}/d\xi$ (direct mode solution) but, near separation, there is a bifurcation in the boundary layer solution, with both attached and separated solutions obtainable for certain $dU_{iw}/d\xi$. In this case the solution must be switched to inverse mode, whereby V_n is specified and $dU_{iw}/d\xi$ emerges from the solution. V_n must be corrected iteratively to match the conditions in the external, inviscid flow.

The scheme adopted by Atkin [12] for solving matrix equation 2.74, in direct mode involves rearranging equation 2.69 to express the transpiration velocity individually as

$$V_n = U_{iw}\Lambda \left(W_0 - W_U \frac{dU_{iw}}{d\xi} - W_\theta \frac{d\theta}{d\xi} - W_{\bar{H}} \frac{d\bar{H}}{d\xi} - W_\beta \frac{d\beta}{d\xi} \right) \quad (2.75)$$

Therefore, for a given $dU_{iw}/d\xi$, the matrix equation can be reduced to a 3×3 system given by

$$\begin{bmatrix} A_\theta & A_{\bar{H}} & A_\beta \\ E_\theta & E_{\bar{H}} & E_\beta \\ N_\theta & N_{\bar{H}} & N_\beta \end{bmatrix} \frac{d}{d\xi} \begin{bmatrix} \theta \\ \bar{H} \\ \beta \end{bmatrix} = \begin{bmatrix} A_0 - A_U \frac{dU_{iw}}{d\xi} \\ E_0 - E_U \frac{dU_{iw}}{d\xi} \\ N_0 - N_U \frac{dU_{iw}}{d\xi} \end{bmatrix} \quad (2.76)$$

Mathematically closure has now been obtained and the governing matrix equation can be solved for the derivatives with respect to ξ up to the point of flow separation and this is referred as the direct mode. When solving in inverse mode, V_n is prescribed and equation 2.74 is solved as a 4×4 system. To avoid the complexity of solving an adjoint inviscid system, the inviscid flow continues to be obtained in direct mode, and the coupled system is known as ‘semi-inverse’. More sophisticated schemes known as ‘quasi-simultaneous’ involve including a simplified sensitivity relation between V_n and $dU_{iw}/d\xi$ in equation 2.74. More details about the solution schemes and the coupling of the viscous-inviscid interaction are presented in reference [12] and the auxiliary semi-empirical relation for

the shape parameter, skin friction, equilibrium entrainment parameters are described in the appendix A.2.

2.4.3 Attachment Line Modelling

The computation of the boundary layer in Callisto begins at the attachment line where the chordwise velocity component, $U_1 = 0$. However at this condition the governing equations for the turbulent boundary layer, in the non-orthogonal co-ordinate system become singular when $\psi = 90^\circ$ and $\beta = 0^\circ$, hence simplifying assumptions are required for the calculation of the initial conditions. For the computation of the laminar boundary layer, Callisto is coupled to BL2D which is a differential method developed by Atkin [11] at QinetiQ. It solves the compressible laminar boundary layer equations on an infinite-swept-tapered wing and at the attachment line it returns the solution of the 'swept Hiemenz flow' described in section 5.2.1.

For the turbulent attachment line the method proposed by Smith [108] is adopted in Callisto. By assuming that the three dimensional integral quantities, θ_{12} , θ_{21} , θ_{22} and δ_2 and the crossflow skin friction, T_{02} are equal to zero at the attachment line, they can be neglected. The three dimensional momentum integral and entrainment equation then reduce to

$$-f_2\theta\frac{d\beta}{dx} + \frac{k_1}{V_1}\theta = \frac{c_f}{2} \quad (2.77)$$

$$f_3\theta\frac{d\beta}{dx} + H_1\frac{k_1}{V_1}\theta = c_E \quad (2.78)$$

$$2f_4\left(\theta\frac{d\beta}{dx}\right)^2 + \left(\frac{c_f}{2} - 3f_1\frac{k_1}{V_1}\theta\right)\left(\theta\frac{d\beta}{dx}\right) + (H+1)\left(\frac{k_1}{V_1}\theta\right)^2 = 0 \quad (2.79)$$

To estimate the conditions at a turbulent attachment line the three simultaneous equations above can be solved using Newton's method described by Atkin [10]. A comparison between the turbulent attachment solution by Smith [108] against other experimental and numerical results can be obtained from Figures 5.8 and 5.11.

2.5 Validation of Callisto against Experiment

2.5.1 Callisto Coupled with Garabedian and Korn's Method

Callisto can operate either in stand-alone mode for a given pressure distribution or coupled with Euler or full-potential solvers which can provide the equivalent inviscid flow (EIF) input. The most recent development with Callisto involved coupling with the VII method VGK, the viscous Garabedian and Korn [42] algorithm (Callisto-VGK, abbreviated as CVGK), which was implemented earlier as the method presented in reference [9]. The coupling between the viscous and the inviscid solver follows the Lock and Williams [76] method where the transpiration velocity predicted by the viscous solver generates the boundary conditions to recalculate the EIF, which is defined as the inviscid flow solution or identical to the real viscous flow outside the viscous layer. Purely two dimensional methods such as BVGK can determine the transpiration velocity from the displacement surface (δ^*), but Callisto calculates V_n directly from equation 2.75. This step is repeated until a converged solution for the boundary layer is obtained. More information about the modelling in BVGK can be obtained from reference [9]

From the solution of the turbulent boundary layer, in CVGK the profile drag is determined from the momentum thickness predicted in the far wake, $\theta_{far} \approx \theta_\infty$. Therefore, the profile drag given by equation 2.26 can be re-written as

$$C_{D_{local}} = 2 \frac{(\theta_{far,up} + \theta_{far,low})}{c_{local}} \quad (2.80)$$

where, $C_{D_{local}}$ represents the profile drag at a particular spanwise station and $\theta_{far,up}$ and $\theta_{far,low}$ denote the momentum thicknesses in the far wake associated with the upper and lower surfaces respectively. A second method of calculating the profile drag in Calisto/CV GK is based on the Squire and Young [112] method, which maps the momentum thickness at the trailing edge of an aerofoil directly to a value in the far wake.

$$\theta_{far,SqY} = \theta_{SqY} = \theta_{TE} \left(\frac{M_{TE}}{M_{\infty}} \right)^{\left[\frac{\bar{H}_{TE} + \bar{H}_{\infty} + 4}{2} \right]} \left(\frac{1 + \frac{\gamma-1}{2} M_{TE}}{1 + \frac{\gamma-1}{2} M_{\infty}} \right)^{\left[\frac{\bar{H}_{TE} + \bar{H}_{\infty} + 14}{4} \right]} \quad (2.81)$$

where, θ_{TE} is the momentum thickness at the trailing edge and incompressible shape factor at infinity, \bar{H}_{∞} can be calculated using

$$\bar{H}_{\infty} = 1 + 0.4M_{iw}^2 \quad (2.82)$$

2.5.2 Summary of Experimental Test Cases Used for Validation

Two dimensional prediction capability was validated against experimental measurements on an RAE 5225 profile, summarised by Lock [75]. The same experimental results were later used by Ashill et al. [9] to validate some further modifications to the VGK method (BVGK). More details of the experimental campaign are presented in this reference. The test was conducted at the RAE 8ft tunnel at Bedford, for a Mach number range of 0.504 to 0.749 and freestream Reynolds number of 6 and 20 million based on chord length. Transition was fixed at 5% chord on both surfaces using air-injection, as this method proved to add less excrescence drag compared with conventional tripping methods such as two or three-dimensional roughness. The local static pressures were measured using surface mounted pressure tappings; the sectional drag was determined using the Pitot and static pressure tubes on a wake rake placed suitably downstream of the trailing edge. The

accuracy claimed in measuring the pressure coefficient was ± 0.001 and the derived drag coefficient was accurate to ± 0.0001 (± 1 drag count).

The swept wing analysis was validated using the results presented by Ashill et al. [7], also acquired from an experiment conducted in the 8ft tunnel at RAE Bedford. The models tested during this campaign were the un-cambered derivatives of the RAE 52XX family designed to replicate a variety of trailing edge pressure recovery strategies. The tests were conducted at zero incidence to avoid complex lift corrections. The swept wing panel consisted of a common forward section which could be fitted with modular aft sections to achieve a desired rear loading. The model was also equipped with centre and tip bodies to reduce the spanwise variation in static pressures, thus approaching the infinite-swept condition.

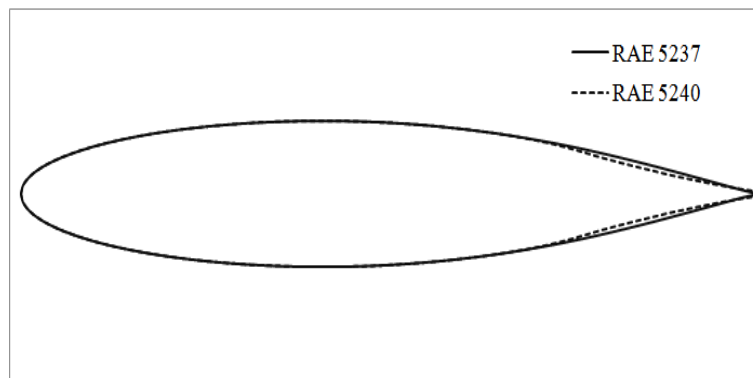


Figure 2.4: A graphical representation of the RAE 5237 and 5240 symmetrical aerofoil.

The Mach number covered during the infinite-swept wing test ranged from 0.6 to 0.85, for unit Reynolds numbers of 14.4 and 31.2 per metre, the chord length in the unswept configuration was equal to 0.475m. The local static pressure was measured using the surface mounted pressure tappings. The sectional drag was measured by integrating wake Pitot pressures captured downstream of the trailing edge; however correction for errors due to the displacement effect was not introduced. The accuracy in measuring the pressure coefficient was estimated to be approximately ± 0.002 and the drag coefficient was obtained within an accuracy of ± 0.0003 (± 3 drag counts). For the CVGK validation exercise only the test results for the RAE 5237 and 5240 profiles shown in Figure 2.4 were used. The main difference between the two aerofoils can be observed at the rear portion, where the

RAE 5240 has a concave surface as opposed to RAE 5237; hence the 5240 experiences a less steep adverse pressure gradient, described as a relaxing type pressure distribution by Ashill et al.

2.5.3 Prediction of Pressure Distribution

Despite the extensive internal validation of Callisto by Airbus(used for A400M and A350 design), there are no published results for the validation of CVGK. Thus the validation of CVGK was a requirement for the current study. The initial validation was conducted for the unswept wing; the experimental conditions were used as main inputs to both BVGK and CVGK, with transition specified at 5% chord on the upper and the lower surfaces. The laminar boundary layer analysis in BVGK was conducted using the default Thwaites method, whereas CVGK was coupled with BL2D for the prediction of the laminar part. The predicted pressure distributions were compared against the experimental pressure distributions which were obtained by digitising the plots presented in reference [74]. From figure 2.5 the difference in lift coefficient between all the cases is about ± 0.014 and can be considered negligible. Therefore the main variation in the shape of the pressure distribution arises from the change in Mach number, where at $M = 0.504$ and $M = 0.702$ the effect is less pronounced, but more significant at $M = 0.735$ and $M = 0.749$ due to the formation of a weak normal shock at 50% chord.

In general, a good agreement can be observed between the experimental and both BVGK and CVGK predictions, except at $M = 0.735$, where the pressures right after the suction peak are underestimated by both numerical methods. At $M = 0.749$, the location of the shock seems to be slightly different from the prediction of the two numerical methods. Still, the prediction of the overall two-dimensional pressure distribution could be regarded to be within an acceptable accuracy.

Considering the flow around infinite-swept wings the computations was conducted around

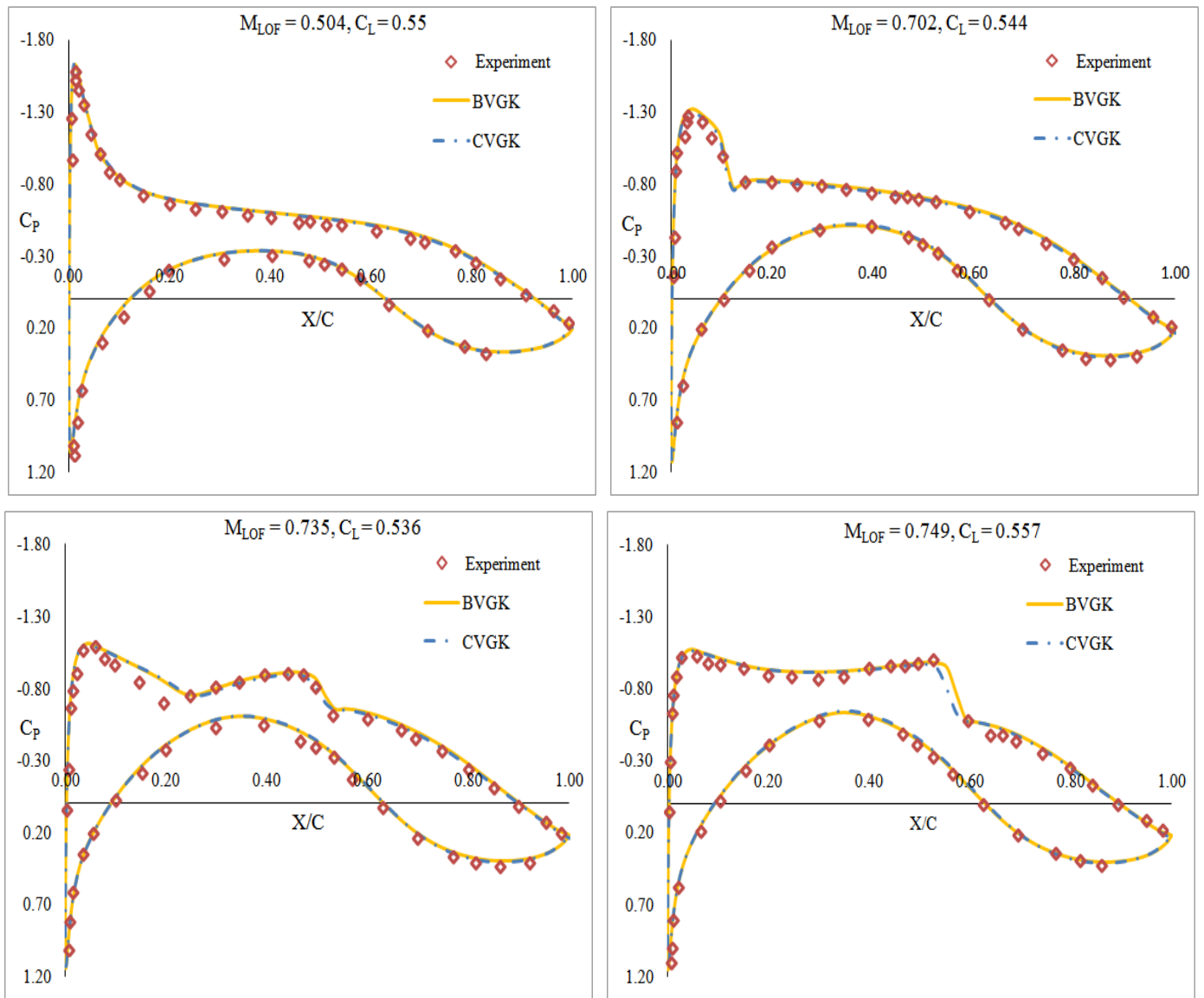


Figure 2.5: The pressure distribution around an unswept RAE 5225 aerofoil measured experimentally by and computed using BVGK and 2D CVGK.

the RAE 5237 and 5240 at zero incidence and swept by 25° to match the freestream conditions obtained to Ashill et al. [7]. Once again the transition was fixed at 5% chord on both surfaces and the laminar calculation in CVGK was undertaken by BL2D. The pressure distribution computed from CVGK could be compared directly with the experimental pressure captured at 54.9% of the semi-spanwise location of the swept panel model where the flow could be assumed to be consistent with the infinite-swept assumption. However, the solution from BVGK had to be transformed manually along the line-of-flight chord using equation 2.4. The results from both methods are compared with the experimental

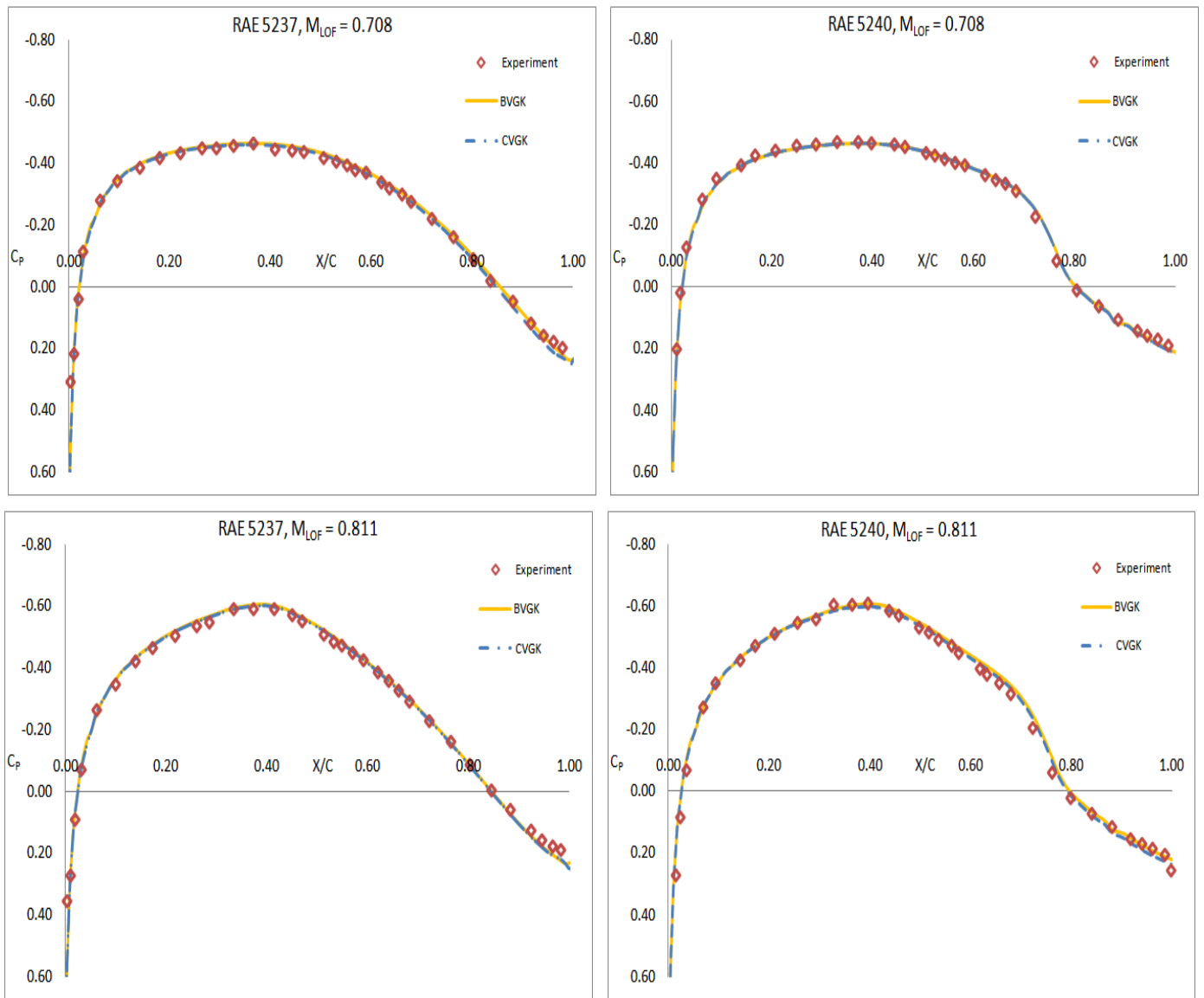


Figure 2.6: Zero-lift pressure distribution on the RAE 5237 and RAE 5240 sections swept at $\Lambda = 25^\circ$ and $Re = 14.4 \times 10^6/m$. Comparison between experimental, 2D BVGK with sweep transformation and 3D (infinite-swept) CVGK analysis

results in Figures 2.6 and 2.7 at unit Reynolds numbers of 14.4 million and 31.2 million per metre respectively at subcritical Mach number and both Reynolds numbers at higher Mach number in figure 2.8.

Comparing Figures 2.6 and 2.7, RAE 5240 shows a steeper aft pressure recovery than RAE 5237, but once again an outstanding agreement can be found between the experimental and the numerical results, except in the region very close to trailing edge of RAE 5237, where the flow might be mildly separated, although this is very difficult to identify

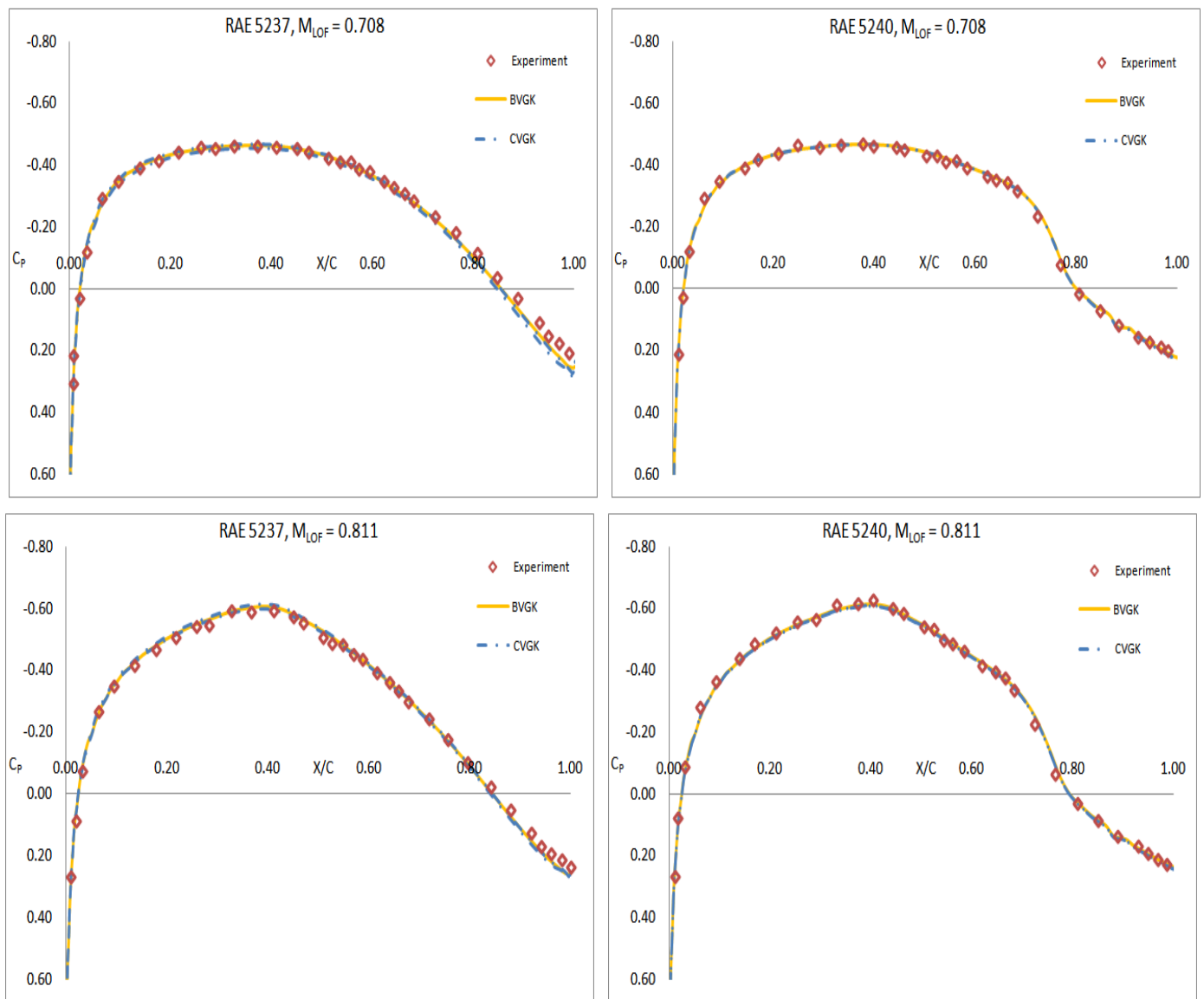


Figure 2.7: Zero-lift pressure distribution on the RAE 5237 and RAE 5240 sections swept at $\Lambda = 25^\circ$ and $Re = 31.2 \times 10^6/m$. Comparison between experimental, 2D BVGK with sweep transformation and 3D (infinite-swept) CVGK analysis

from the experimental pressures. For both Reynolds number cases, in Figure 2.8 the location of the normal shock at $M_{LOF} = 0.842$ is slightly forward, where the worst case scenario was on the RAE 5237. Although the shock position was better captured on the RAE 5240, the region right after the shock was not captured very well. This is shock-induced separation which even RANS methods struggle to predict. But, it is improved at around 80% chord. This effect was less pronounced on 5237. Overall, the prediction from the numerical method seems to be performing with reasonable accuracy with respect to the experimental results.

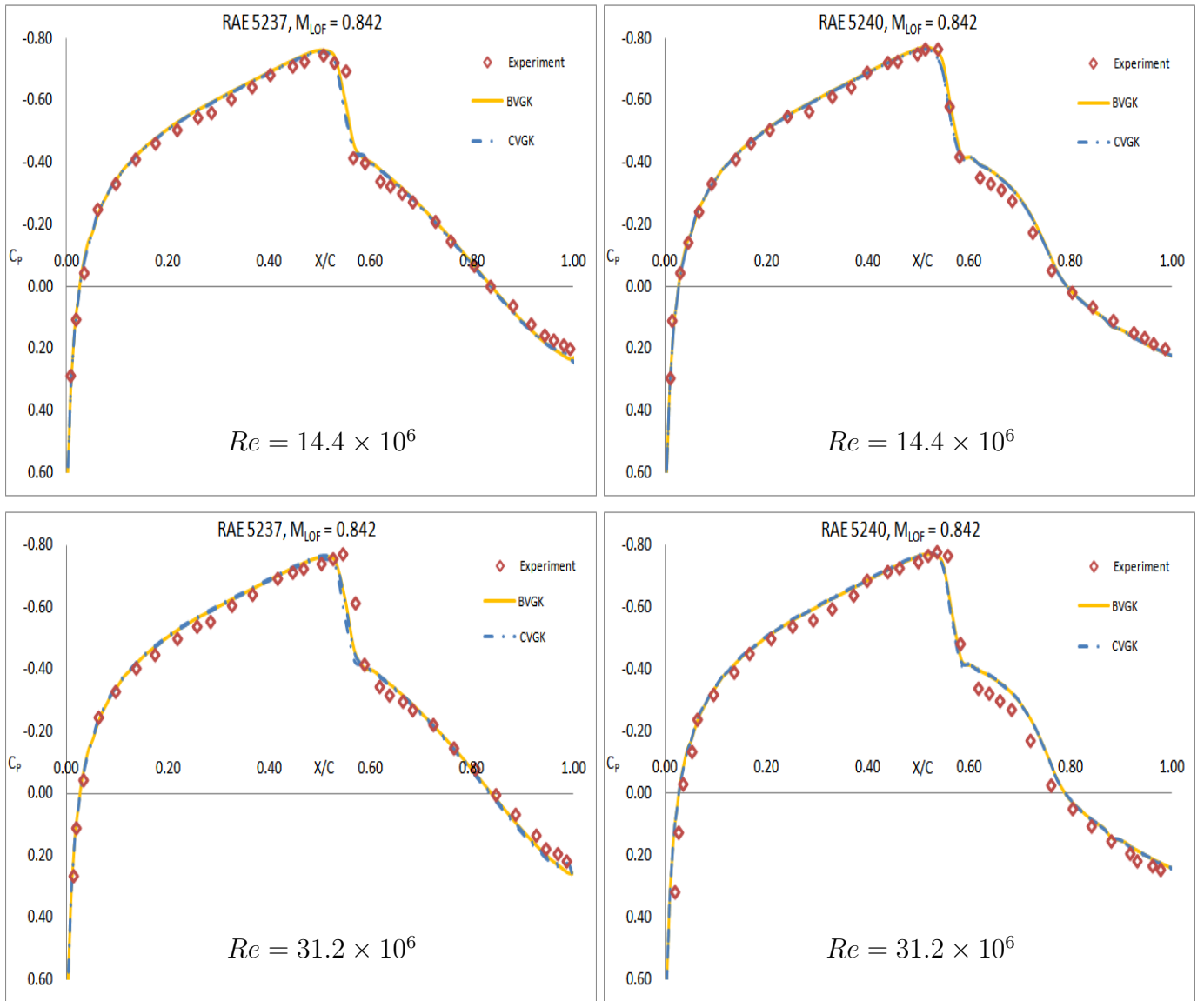


Figure 2.8: Zero-lift pressure distribution for high Mach number case on the RAE 5237 and RAE 5240 sections swept at $\Lambda = 25^\circ$ and $Re = 14.4 \times 10^6/m$ and $31.2 \times 10^6/m$. Comparison between experimental, 2D BVGK with sweep transformation and 3D (infinite-swept) CVGK analysis

2.5.4 Prediction of Sectional or Profile Drag

For the two dimensional analysis the variation of profile drag with C_L was analysed at $M = 0.735$. The calculation of wave drag in both CVGK and BVGK is undertaken by the MACHCONT algorithm, developed by the Aircraft Research Association (ARA), but the current analysis was mainly focussed at subcritical Mach numbers before the drag rise. The viscous drag calculation method given by equation 2.80 was employed for CVGK

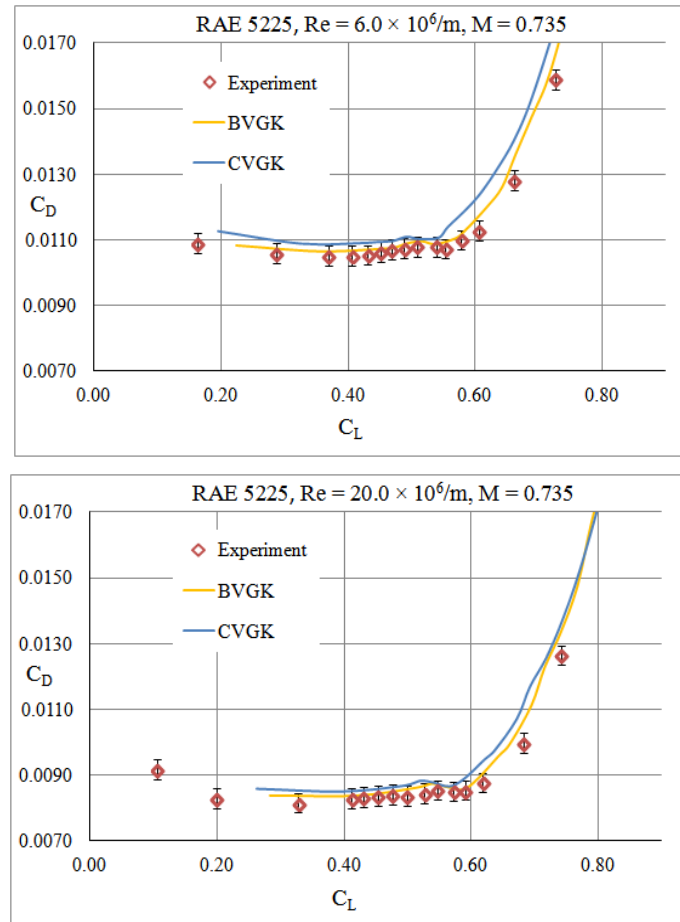


Figure 2.9: Comparison between experimental and numerical results obtained from BVGK and CVGK on the unswept RAE 5225 aerofoil.

and BVGK and the overall sectional drag was obtained by adding the viscous drag to the wave drag from VGK. These results are compared against the drag determined from the wake rake measurement in figure 2.9. At a Reynolds number of 6 million, for $C_L < 0.6$, both numerical methods predict the profile drag within ± 3 drag counts, where BVGK shows closer agreement even at higher C_L . However, at a Reynolds number of 20 million the prediction from CVGK was slightly improved for $C_L < 0.6$ and for higher C_L it deteriorated again and better agreement with BVGK is shown.

During the analysis of the infinite-swept wings, the two-dimensional viscous drag predicted by BVGK had to be converted into the equivalent three-dimensional drag using the transformation introduced in section 2.1. By substituting for the corresponding two-dimensional drag components into equation 2.15, the profile drag for the swept wing case

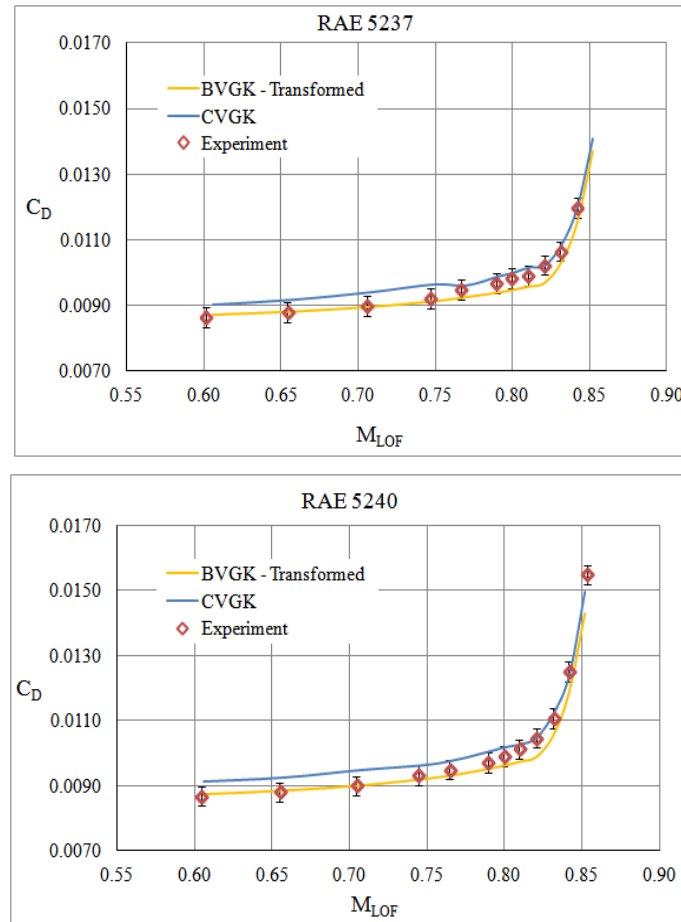


Figure 2.10: Zero-lift profile drag for the RAE 5237 (top) and 5240 (bottom) section swept at $\Lambda = 25^\circ$ and $Re = 14.4 \times 10^6/m$. Comparison between experimental, 2D BVGK with sweep transformation and 3D (infinite-swept) CVGK analysis.

was determined. For CVGK the profile drag can be determined directly by substituting the calculated three dimensional momentum thickness at the far wake into equation 2.80. The drag predicted on the swept RAE 5237 and 5240 using both CVGK and BVGK is compared against experimental measurements by Ashill et al. [7] in Figures 2.10 and 2.11. The drastic rise in profile drag from these figures at $M > 0.8$ is associated with the rapid increase in wave drag and once again the current study focuses mainly on the results at $M < 0.8$, thus the deterioration in the accuracy beyond this point is noted but not pursued.

A comparison between the experimental and numerical results is shown in Figures 2.10 and 2.11 with an error bound of ± 3 drag counts, shown for the experimental results. At $M < 0.8$, for both Reynolds number cases, the predictions from CVGK and BVGK lie

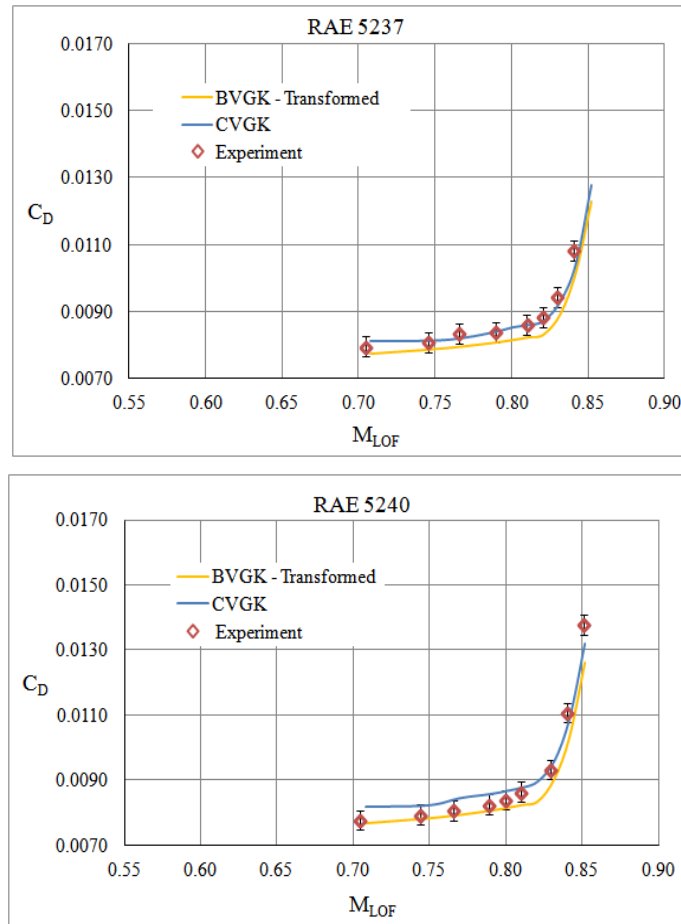


Figure 2.11: Zero-lift profile drag for the RAE 5237 (top) and 5240 (bottom) section swept at $\Lambda = 25^\circ$ and $Re = 31.2 \times 10^6/m$. Comparison between experimental, 2D BVGK with sweep transformation and 3D (infinite-swept) CVGK analysis.

within the ± 3 drag counts error bound, where at $Re = 14.4 \times 10^6$, the BVGK results are closer to the experimental data and at $M > 0.8$, the prediction from CVGK seemed to have improved in comparison with BVGK. But, at $Re = 31.2 \times 10^6$, CVGK shows better performance, especially on the RAE 5237 aerofoil. However, for both aerofoil the prediction was within the ± 3 drag counts error bound.

2.5.5 Break-down of Drag Components

In section 2.5.4 it was shown that both BVGK and CVGK are capable of predicting the profile drag on infinite-swept wings within the accuracy achievable during experimental measurements. However from Figure 2.10 and 2.11 the net difference between the predic-

tion from the two numerical methods is approximately 4 drag counts, thus further analysis was required to identify the sources of the discrepancy observed between the numerical methods. The ‘lag-entrainment’ models used in BVGK and CVGK are almost identical, however CVGK solves the three dimensional momentum integral equation marching along the line-of-flight direction and BVGK solves the two-dimensional form where the solution is transformed into the infinite-swept equivalent using the method illustrated in section 2.1. The predicted and measured pressure distributions are in excellent agreement as shown in Figures 2.6, 2.7 and 2.8 which supports the use of equation 2.6 for the transformation of pressure coefficient from two-dimensional to infinite-swept wings.

Therefore, there is more doubt about the transformation of the drag components, as the three dimensional skin friction drag from BVGK was based on a sheared flat plate assumption and the three dimensional form drag was assumed to be proportional to the inviscid pressure field, as it is a component of the normal pressure drag. This might be true for the inviscid pressure drag, but in the presence of highly curved streamlines on swept wings, the viscous component of the pressure drag or the form drag will be strongly related to the quantities of the three-dimensional boundary layer which are not well represented in BVGK.

Coupled with the above, a supplementary unswept CVGK analysis was conducted on the RAE 5240 aerofoil using the same boundary conditions applied in BVGK so as to replicate the two dimensional numerical analysis. The analysis was undertaken only for $Re = 31.2 \times 10^6/m$ and at $M < 0.78$ as the formation of the strong shock on the unswept aerofoil at higher Mach number gave rise to a large region of separated flow that both numerical methods were unable to handle. The skin friction, C_f , and form drag, C_{DF} , components obtained from the two-dimensional calculation using CVGK are presented in Figure 2.12, together with the three dimensional results transformed to the equivalent two-dimensional values by rearranging equation 2.15. For the friction drag there is no difference between the two dimensional results from CVGK and BVGK, but a difference of ± 3 drag counts (limit of error bounds) can be observed between the two dimensional

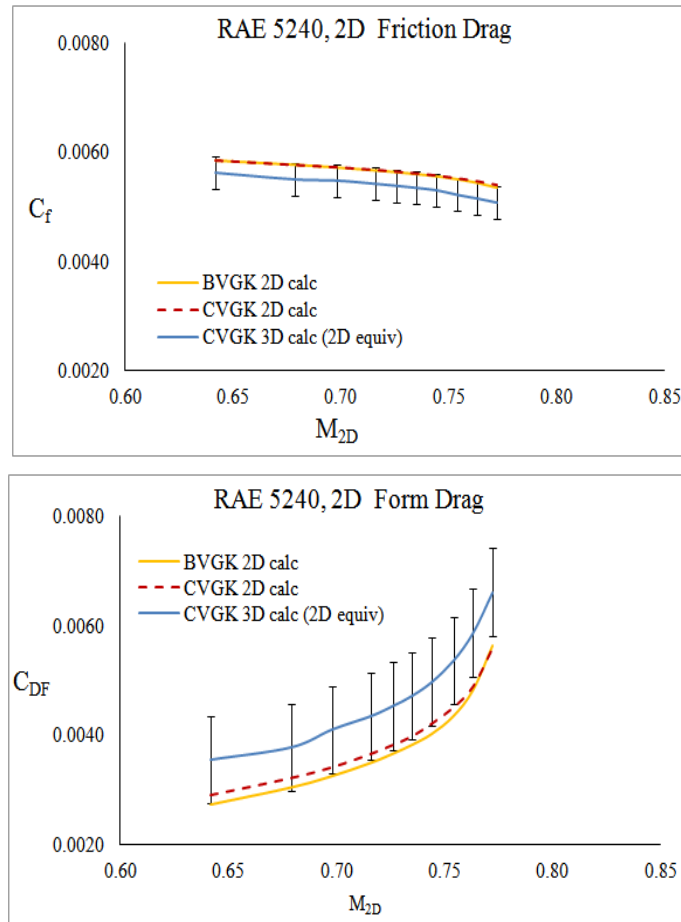


Figure 2.12: Comparison of the two dimensional friction (top) and form (bottom) drag estimated from BVGK, unswept CVGK and by transforming the results from the swept CVGK calculation to two dimension using the transformation in section 2.1 at $Re = 31.2 \times 10^6/m$

results and the transformed three-dimensional CVGK solution. Therefore, this raises the question whether the sheared flat plate assumption is applicable for a swept wing.

As far as the form drag is concerned, from the plot at the bottom of Figure 2.12 the two-dimensional calculation from CVGK seems to have over-predicted the drag by approximately $2counts$, and the three-dimensional calculation by $8counts$ when compared to BVGK. The main difference in the two dimensional modelling between CVGK and BVGK is the viscous-inviscid interaction scheme, where CVGK employs a transpiration velocity model and BVGK uses the displacement thickness. Taking into account the fact that the form drag is directly related to the displacement thickness, the two-dimensional modelling in BVGK might be better than that in CVGK. However, the large difference

observed while transforming the form drag from two to three dimensions or vice-versa suggests that the equation 2.6 is not adequate, as the effects of the three dimensional viscous flows are not well represented. A similar effect can be observed while repeating the analysis for a three dimensional calculation, where the results are shown in figure 2.13.

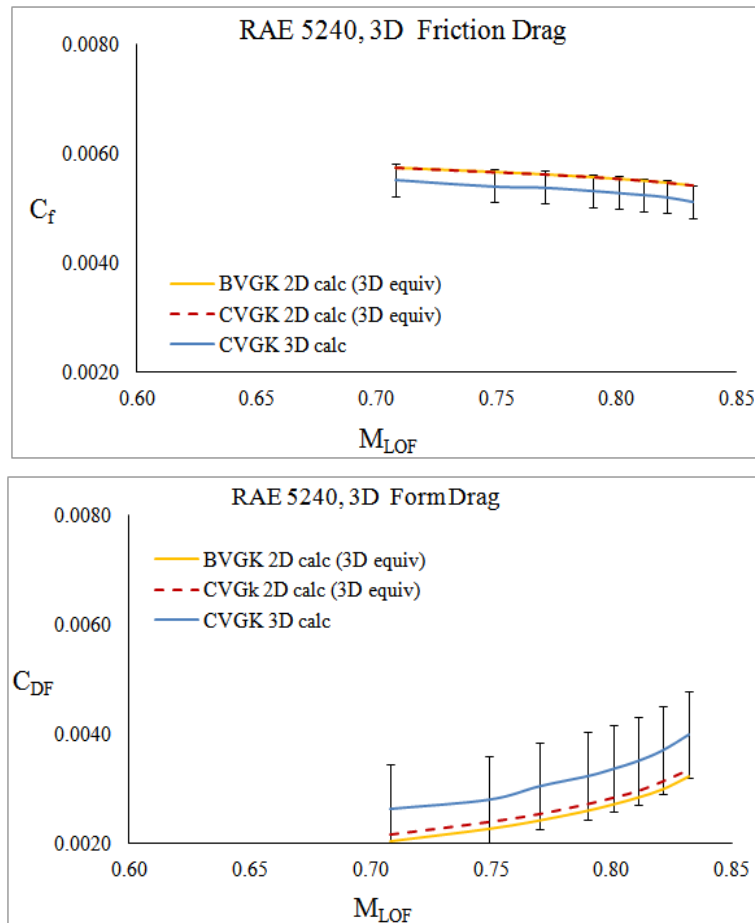


Figure 2.13: Comparison of the three dimensional friction (top) and form (bottom) drag estimated from swept CVGK calculation and the unswept BVGK and CVGK calculations where the results were transformed into the equivalent three dimension using the transformation in section 2.1 at $Re = 31.2 \times 10^6/m$

2.6 Drag Reduction through Attachment Line Control

Previous studies by Pfenninger [89], Gaster [45] and Poll [92], demonstrated that, if the attachment line Reynolds number $\bar{R} > 250$ or $R_{\theta} > 100$, the attachment line boundary layer will be susceptible to contamination and transition to turbulence. If the attachment

line is turbulent the rest of the flow on the wing is bound to be turbulent and this is common on most swept wing aircraft. More details about attachment line contamination or instability is presented in section 5.3 and in section 5.3.3 a few methods of decontaminating or relaminarising the contaminated attachment line are presented. The active control system based on distributed wall suction seems the most effective, capable of maintaining laminarity up to $\bar{R} \approx 700$. Due to rapid amplification of cross-flow instability modes, transition is still likely to occur very close to the leading edge at this \bar{R} in the absence of any cross-flow control system. In this section a numerical analysis has been conducted using CVGK to investigate the drag benefit solely through attachment line control, regardless of whether the boundary layer will transition right after. A comparison is made between the case of a turbulent attachment line and cases where the attachment line is laminar, but where transition remains close to the leading edge, so that any benefit arises purely from a laminar attachment line rather than the additional laminar flow downstream.

CVGK has demonstrated the ability to predict profile drag fairly accurately with respect to experimental measurements. Armed with this confidence, the possibility of drag reduction through attachment line control is investigated on an infinite swept wing with a supercritical aerofoil. From the initial inviscid flow calculation using the Garabedian and Korn algorithm, \bar{R} can be estimated using the velocity gradient at the leading edge, the freestream condition and sweep angle (see equation 5.9). An attachment line contamination criterion for \bar{R} is used by Callisto, to determine whether attachment line flow will be calculated either by BL2D (laminar) or by Smith's approach, equations 2.77 to 2.79 (turbulent). In the laminar case the BL2D method is applied until a user-defined transition point. Apart from at the attachment line, turbulent flow is calculated using the approach described in section 2.4.

The supercritical profile chosen was swept-tapered with leading and trailing edge sweep angles of 30.3° and 20.5° respectively. The simulations were conducted at attachment line Reynolds numbers, $\bar{R} = 374$ and $\bar{R} = 528$ and constant Mach number of 0.815, which is the usual cruise condition for a short range airliner. The initial calculation was for a

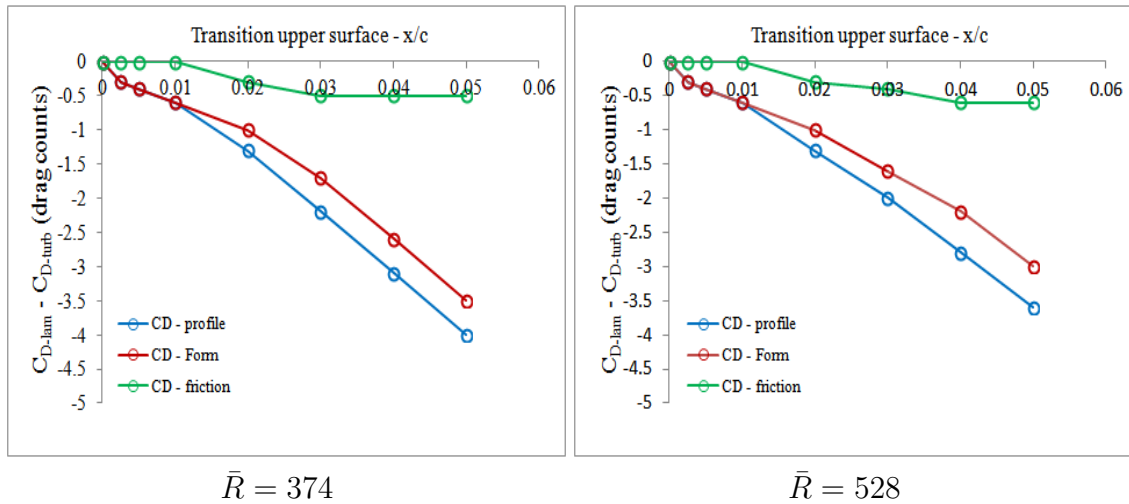


Figure 2.14: Difference in drag between the turbulent attachment line and the laminar cases with varying transition location on the upper surface but fixed at 1% chord on the lower surface

turbulent attachment line followed by calculations with transition ranging from 0.25% to 5% of chord on the upper surface, but fixed at 1% of chord on the lower surface. The differences in the profile, C_{D_0} , friction, C_f , and form, C_{D_f} , drag between the turbulent and laminar cases have been presented in figure 2.14 for the two Reynolds number cases.

From Figure 2.14, the profile drag reduces unevenly as transition moves further from the attachment line. For $x/c \leq 0.01$ the difference in skin friction is almost negligible, however the modelling in this region is questionable due to the leading edge approximation that will be addressed in the section that follows. At $x/c \geq 0.01$, a slight increase in C_f can be noted but it starts to plateau again at $x/c > 0.03$. Therefore the main contribution to the drag reduction even with transition as far aft as $x/c = 0.05$ appears to be from the form drag component. This benefit is slightly reduced at higher Reynolds number as shown in the figure on the right hand side.

Figure 2.15 shows corresponding small reductions in the momentum thickness, θ , at the trailing edge or more clearly in the far wake, especially with transition at 5% chord, where the reduction is better represented in Figure 2.16. From linear stability analysis conducted by Schrauf [103] on the A320 fin at flight conditions, transition due to crossflow modes was predicted at $x/c \leq 0.02$. However, the Reynolds number of a wing is larger and

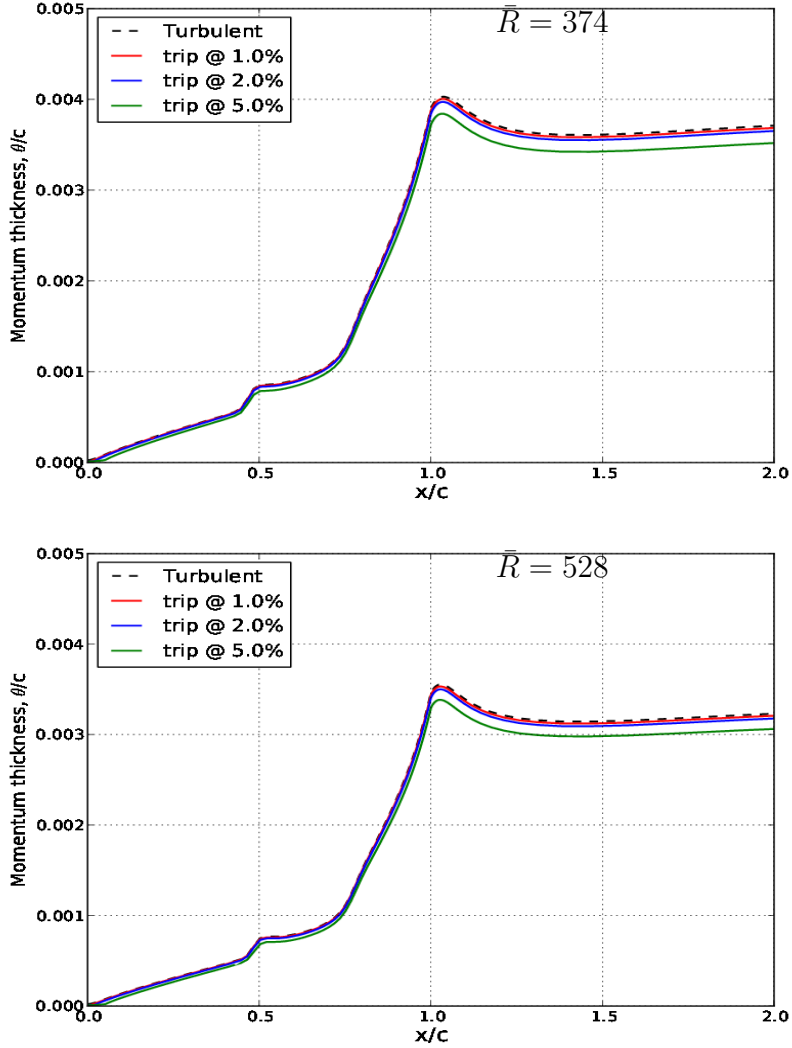


Figure 2.15: Development of the streamwise momentum thickness along the aerofoil and in the far wake for the fully turbulent case and those with transition downstream.

transition will be more likely to occur further upstream. Using the linear stability code, CoDS, transition was estimated to occur in the region $0.005 < x/c < 0.01$. With transition in this region the drag reduction benefit is approximately 0.4 to 0.6 *counts* in each case.

The pressure distribution and the development of the displacement thickness, δ^* , on the upper surface of the aerofoil are presented in figure 2.17, for the fully turbulent and for the laminar cases with transition at $x/c = 0.01, 0.02$ and 0.05 , at lift coefficient, $C_L = 0.58$. The similarity between the pressure distributions suggests that the state of the viscous flow does not alter the loading on the aerofoil with transition so close to the leading edge.

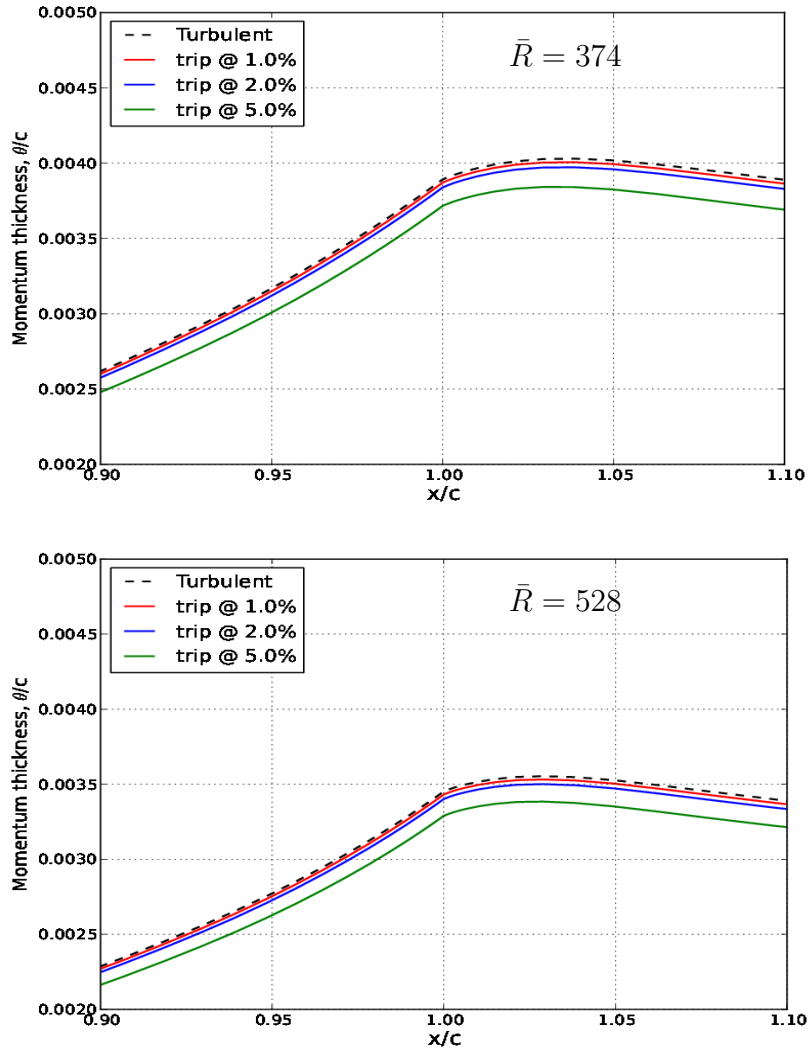


Figure 2.16: A 'zoom-in' the region of $0.9 < x/c < 1.1$ from figure 2.15 to better demonstrate the reduction in the streamwise momentum thickness.

Due to the short region of laminar flow at the attachment line the displacement thickness is slightly reduced and this effect is amplified, as expected, over the adverse pressure gradient region. This effect is clearer in 2.18 which shows a blow-up of the region of $0.9 < x/c < 1.1$ in Figure 2.17, where the sharp rise in δ^* right at the trailing is the contribution of the δ^* from the lower surface which has not been plotted in Figure 2.18. Considering the terms on the right hand side of the modified two dimensional momentum integral equation given by equation 2.25, the reduction in displacement thickness in an adverse pressure gradient should result in a reduction in form drag.

The reduction in displacement thickness, δ^* , is due to the lower 'starting value' for the

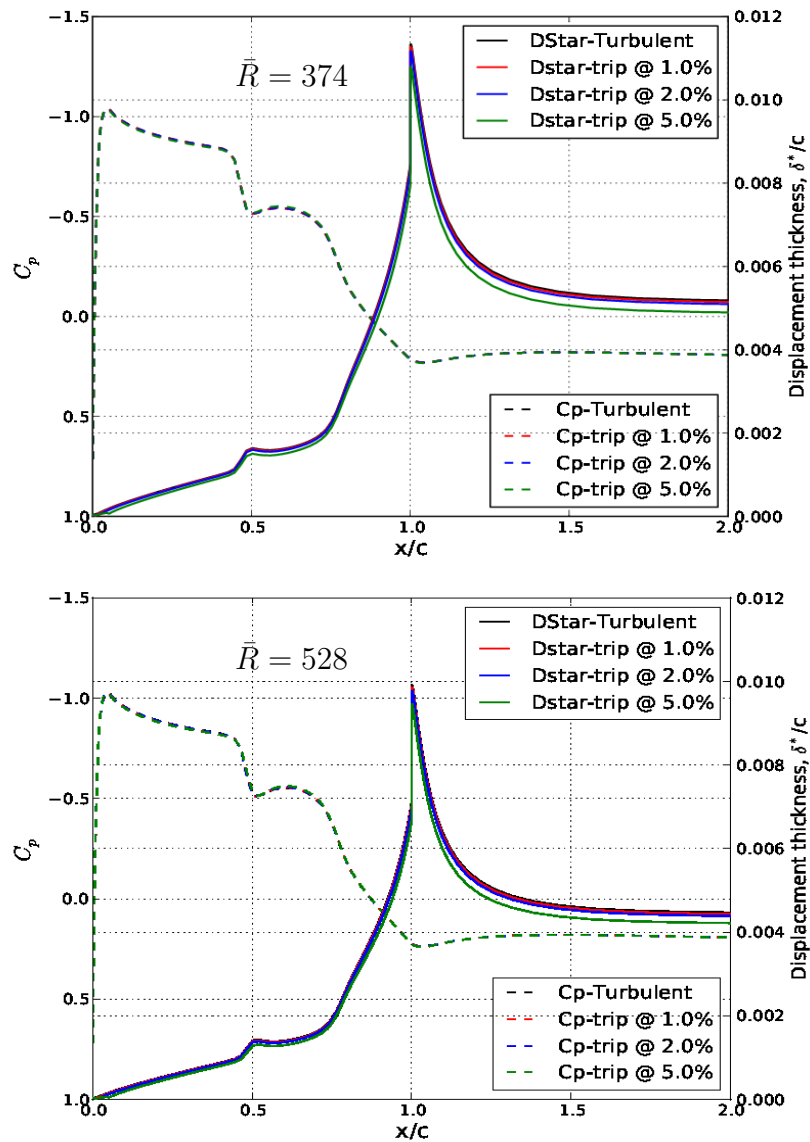


Figure 2.17: The pressure distribution and the development of the displacement thickness on the upper surface of the supercritical aerofoil.

laminar attachment line. From figure 2.19, the skin friction increases sharply at transition even exceeding the value of the turbulent attachment line when transition is very close to the leading edge ($x/c = 0.01$) and catches up with that of the baseline turbulent case downstream. Referring back to equation 2.25, the unchanged local skin friction supports the fact that the drag reduction is mainly through the form drag component, due to the reduced displacement thickness subjected to the adverse pressure gradient downstream of the mid-chord shock wave.

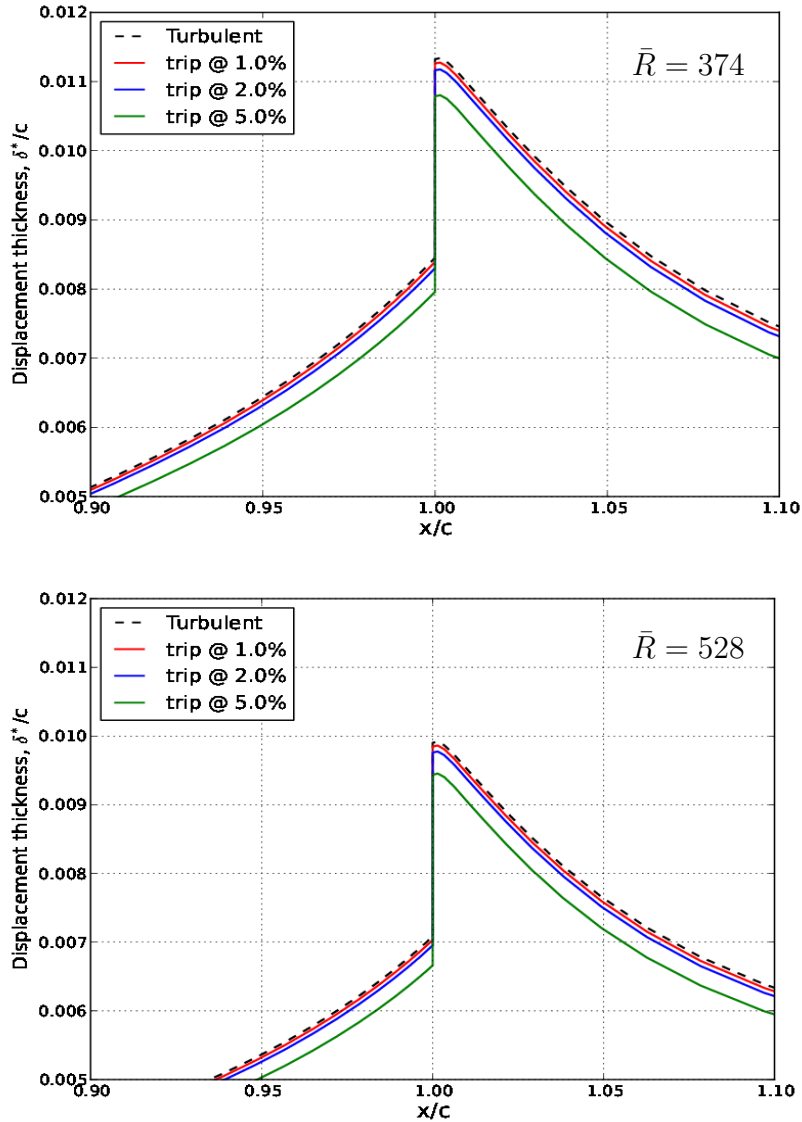


Figure 2.18: A 'zoom-in' the region of $0.9 < x/c < 1.1$ from figure 2.17 to show the reduction in the streamwise displacement thickness.

2.7 Approximations in the Numerical Method

Figure 2.20 shows the path of an external streamline in the vicinity of the attachment line ($A - A$). Right at the attachment line the angle between the external streamline and chordwise direction $\psi_0 = \pi/2$ as the chordwise velocity component $U_1 = 0$ and the flow is purely spanwise.

In this case the skin friction will be acting along the direction of the attachment line,

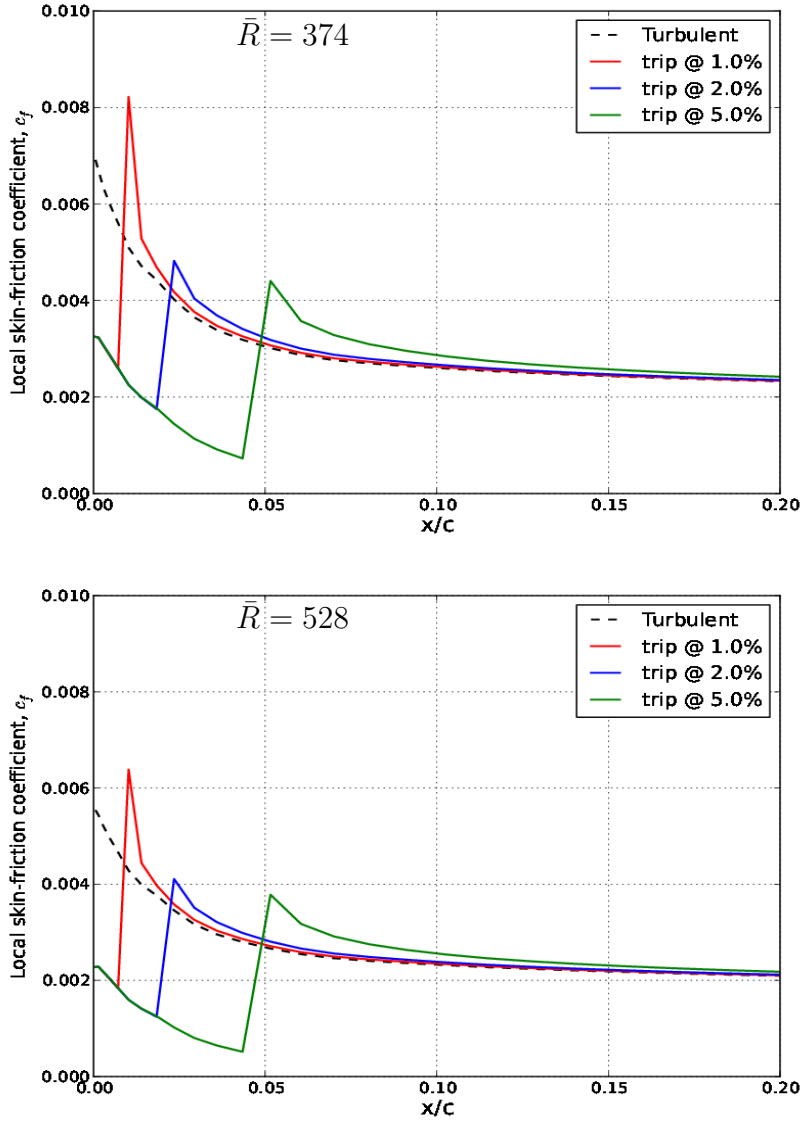


Figure 2.19: The local skin friction coefficient on the upper surface of the supercritical aerofoil for a fully turbulent case and those with transition downstream.

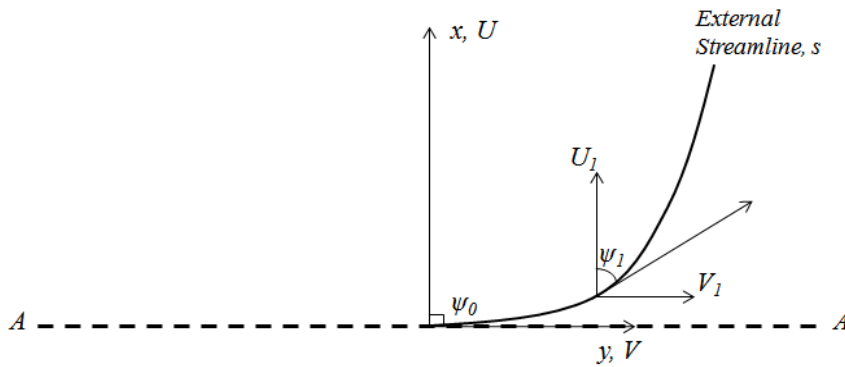


Figure 2.20: The inviscid flow at the vicinity of the attachment line

hence the angle between the limiting and the external streamline, β , will be zero as well. Substituting $\psi = \pi/2$ and $\beta = 0$ in to the governing momentum integral equations (equation 2.62 to 2.70) results in an undefined solution of the governing three dimensional ‘lag-entrainment’ equations at the attachment line as

$$\begin{aligned}
 A_A = A_\theta = A_{\bar{H}} = A_\beta = A_U = A_0 = 0 \\
 E_A = E_\theta = E_{\bar{H}} = E_\beta = E_U = E_0 = 0 \\
 N_A = N_\theta = N_{\bar{H}} = N_\beta = N_U = N_0 = 0 \\
 W_A = W_\theta = W_{\bar{H}} = W_\beta = W_U = W_0 = 0
 \end{aligned}
 \tag{2.83}$$

This issue was also encountered by Smith [109] and the latter’s approach has been adopted in Callisto, where the turbulent attachment line calculation was undertaken by solving a reduced form of the governing equations while assuming that the crossflow boundary layer integral quantities and skin friction at the attachment line are negligible. This yielded a simpler set of governing equations 2.77 to 2.79 which could be solved using a different numerical scheme.

The numerical issue still persists downstream of the attachment line as ψ is very large and β is very small, therefore the switch to the full system of equations is delayed until a chordwise position downstream where $\psi_1 \leq 80^\circ$. The turbulent attachment line solution has to be extrapolated to that position, sacrificing accuracy for numerical stability. For most of the practical cases this approximated region accounts for less than 1% of the chord length and so far this approximation is considered to have negligible effect in the prediction from Callisto. Similar difficulties were encountered by Thompson and Macdonald [116] and a numerical approach similar to that in Callisto was adopted. Various initial conditions were studied by extrapolating the attachment line solution to different streamwise positions downstream of the attachment line, and the effect on the rest of the solution was studied. It was concluded that if the approximation is applied within a few percent chord of the attachment line, the prediction of the boundary layer integral quan-

tities downstream is not affected. However, the form drag benefit predicted by CVGK through attachment line control is highly dependent on the behaviour of the flow in the region where the numerical fix is applied. Therefore further scrutiny is required to improve or validate the leading edge approximation.

A second area of concern is the assumption of a minimum R_θ for a turbulent boundary layer to exist. In the current analysis the criterion proposed by Preston [96] is employed: according to the latter, $R_\theta = 320$ can be considered as the minimum Reynolds number required to sustain a fully developed turbulent boundary on a flat plate. If R_θ at transition is below 320 then it is increased to this value prior to the remainder of the turbulent calculation. This approximation becomes questionable when transition is very close to the leading edge due to the resulting drastic change in R_θ , moving from the laminar attachment line where R_θ is rather small. There are two ways to interpret $R_\theta \geq 320$. The first is as implemented, and described earlier and the second is by ensuring that the flow is laminar until R_θ naturally reaches 320. Under normal circumstances the wall shear stress in a turbulent boundary layer is larger than that of a laminar one so at transition, the local skin friction is supposed to increase considerably. This behaviour can be observed in figure 2.19. For transition at $x/c = 0.01$ the local skin friction exceeds even the maximum value attained by the turbulent case.

In theory, due to the numerical fix at the leading edge, the boundary layer integral quantities will be slightly under-predicted during the baseline turbulent calculation. Actually, this discrepancy should act in favour of the drag difference between the turbulent and the laminar cases and therefore the net drag reduction from relaminarisation of the attachment line has been underestimated. Still, an experimental campaign is required to understand the behaviour of the fully turbulent flow in the vicinity of the attachment line, in order to verify the drag reduction benefit observed. Boundary layer traverse measurements in that region, using hot wire anemometry, should reveal more detail of the development of the viscous flow in the confined region where the numerical approximation is applied. As the boundary layer is expected to be very thin, a traversing mechanism with very fine reso-

lution will be required together with a system allowing, very close ‘near-wall’ alignment in order to capture the flow in the viscous sublayer as well. The experimental results will be further analysed to derive a modification to the leading edge modelling, so that the full system of equations may be solved immediately downstream of the attachment line.

Chapter 3

Experiment and Instrumentation

3.1 Designing the Experimental Model

The experimental model needed for the current study had to satisfy two main requirements: firstly to generate a turbulent attachment line thick enough to capture the velocity profile using hot-wire anemometry, and secondly to generate an experimental domain length with adequate measurement stations. At the same time the model should achieve an \bar{R} similar to that present on the wing of commercial transonic aircraft during cruise condition, which ranges between $174 < \bar{R} < 400$ on regional aircraft and $285 < \bar{R} < 570$ on long haul aircraft. In this case $\bar{R} = 500$ was targeted so as to ensure that the attachment line was in a fully turbulent state due to contamination from the disturbances emanating from the floor of the wind tunnel on which the model was mounted. By applying swept Hiemenz flow and potential flow theory around a circular cylinder a relation between \bar{R} , free-stream velocity, sweep angle and LE radius of curvature was formulated in section 5.1. Therefore, for a given free-stream velocity, the required leading edge radius of curvature of the model could be calculated as a function of sweep angle. A method for estimating the minimum length of the experimental domain was also derived, based on the magnitude of the spanwise and chordwise velocity components at the attachment line

and a few chordwise locations downstream. These trades helped in the selection of the final configuration.

3.1.1 Estimation of Model Dimensions

In order to express the attachment line Reynolds number, \bar{R} , as a function of the leading edge radius of curvature, sweep angle and freestream flow conditions, the inviscid flow was assumed to be the potential flow around a swept circular cylinder. Circular leading edges were used by Gaster [45] and Cumpsty and Head [36] during their experiments. Using equation 5.11, for a range of sweep angles the leading edge radius of curvature to achieve an $\bar{R} = 500$ can be calculated for a given free-stream velocity. In this case a velocity of 45m/s was selected, which is about 80% of the maximum achievable air speed inside the empty test section ($1.80\text{m} \times 1.12\text{m} \times 0.81\text{m}$) of the T2 wind tunnel in the Handley Page Laboratory at City University London. The second column of table 3.1 shows the leading edge radii of curvature calculated for the sweep angles ranging from 40° to 70° . An inversely proportional relation can be observed between these two parameters. A high sweep will therefore be beneficial as this will result in a smaller leading edge radius and hence lower wind tunnel blockage. However, before deciding on the final configuration of sweep angle and leading edge radius, it was important to verify whether the chosen configuration would generate a boundary layer of sufficient thickness to traverse and an experimental domain of sufficient downstream extent. Further details about these two important sizing parameters is presented in the sections that follow.

However, due to the fact that faired circular cylinders are prone to earlier flow separation (at the shoulder) a NACA0050 was preferred, so as to keep the effects of blockage due to the wake to a minimum level. A comparison between the two profiles shown in figure 3.1 confirms the fact that the NACA0050 also meets the requirements as the leading edges of both profiles are similar up to about 20% chord, which is well beyond the main area of focus for the current study. The flow around an infinite-swept NACA0050 with 60°

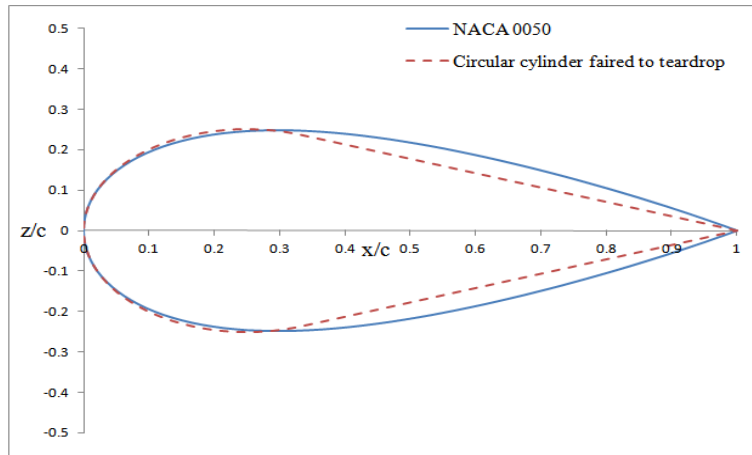


Figure 3.1: Comparison between a NACA 0050 and a circular cylinder profile faired to a teardrop

sweep angle was calculated using CVGK, with transition fixed at 20% chord on both sides, and from the pressure distribution presented in figure 3.2 the separation point was estimated to be at around 75%, considerably further aft than for a faired cylinder. The modelling of separation in CVGK is not very reliable, hence the unusual trend in the pressure distribution downstream of the separation point.

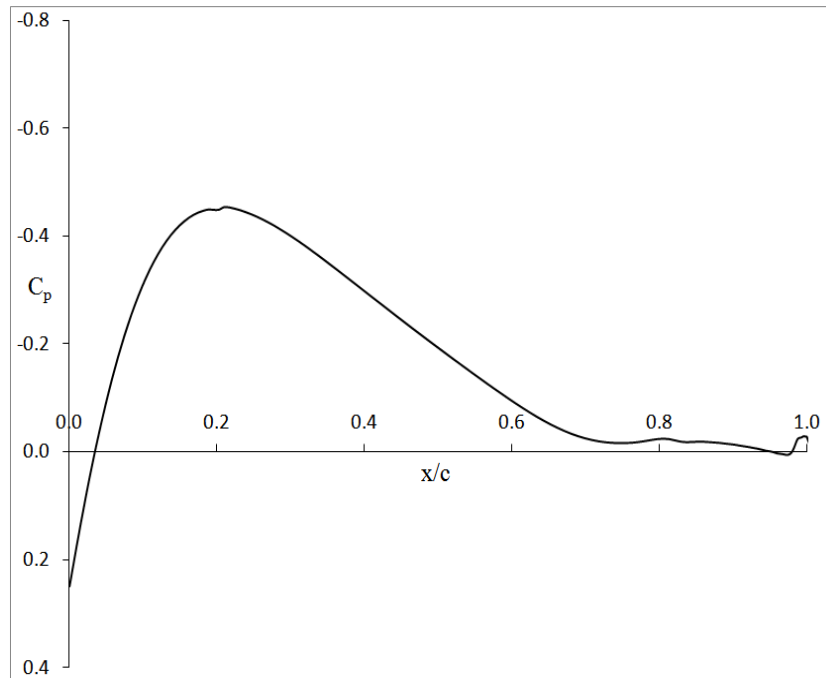


Figure 3.2: The pressure distribution predicted by CVGK around a NACA0050 aerofoil swept by 60°

3.1.2 Experimental Domain Length

The experimental domain length is measured along the circumference of the leading edge of the model. It originates at the attachment line and extends to the point where the streamline divergence angle $\psi_{crit} \approx 80^\circ$ which captures the region where the numerical fix operates in Callisto (which also signifies the critical region given by the subscript 'crit'). The length of this domain should be sufficient to include a good number of measurement stations, assuming a spacing of at least $5mm$ between each station.

By assuming the infinite-swept wing conditions, the local chordwise and spanwise velocity components of the attachment line can be expressed by the equations below:

$$U = Q_\infty \cos \Lambda k s' \quad (3.1)$$

$$V = Q_\infty \sin \Lambda \quad (3.2)$$

From potential flow theory around a cylinder, very close to the leading edge, the chordwise velocity component can be expressed as equation 3.3 where s' is the length of the arc along the leading edge curvature assuming that it can be approximated as a circular cylinder

$$U = \frac{2U_\infty s'}{r} \quad (3.3)$$

Figure 3.3 is a schematic representation of development of the diverging streamline at the leading edge of an infinite-swept wing. The angle between the direction of the external streamline, s , and the chordwise direction, x , is given by ψ (introduced earlier in sections 2.4.1 and 2.7), where:

$$\psi = \tan^{-1} \left(\frac{U}{V} \right) \quad (3.4)$$

At the attachment line, $\psi_{AL} = \frac{\pi}{2}$, therefore ψ_{crit} can be expressed as

$$\tan \left[\frac{\pi}{2} - \psi_{crit} \right] = \frac{U_{crit}}{V_{crit}} \quad (3.5)$$

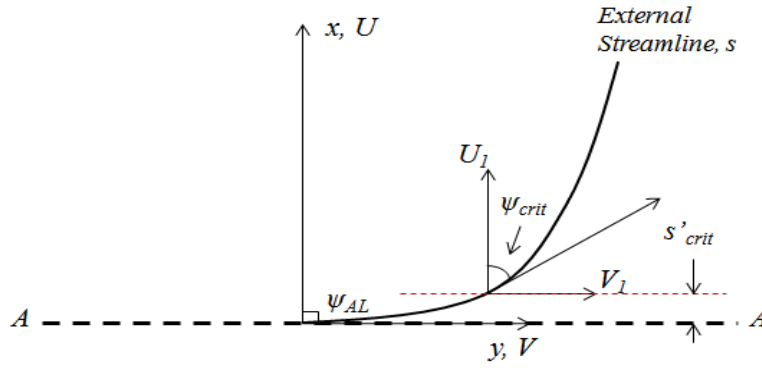


Figure 3.3: Schematic representation of the external streamline starting from the attachment and evolving downstream.

From the infinite-swept assumption the spanwise velocity component, V , is assumed to be constant in the chordwise direction. Due to the small difference in streamline curvature moving from ψ_{AL} to ψ_{crit} ($\Delta\psi \leq 10$), the distance along the streamline, s , can be assumed to be equivalent to s' . By substituting for the chordwise velocity component given by equation 3.3, and assuming that the freestream, chordwise component, $U_\infty = Q_\infty \cos \Lambda$, and the spanwise component given by equation 3.2, equation 3.5 becomes

$$\tan \left[\frac{\pi}{2} - \psi_{crit} \right] = \frac{2s'}{r \tan \Lambda} \quad (3.6)$$

Through further rearrangement of equation 3.6, a method for estimating the length of the experimental domain can be derived as

$$s'_{crit} = \frac{r \tan \left[\frac{\pi}{2} - \psi_{crit} \right] \times \tan \Lambda}{2} \quad (3.7)$$

3.1.3 Attachment Line Boundary Layer Thickness

The second requirement was to ensure that the attachment line boundary layer generated was thick enough for the velocity profile to be captured accurately. The analysis of Hiemenz for laminar attachment line is well established and can be used for the initial prediction of the boundary layer integral quantities. Using equation 5.28, for a desired \bar{R} the momentum thickness could be estimated for known freestream conditions and sweep angle.

The laminar attachment line boundary layers will be thinner than the turbulent attachment line boundary layer but the swept Hiemenz flow analysis can still provide a lower limit for the thickness of the boundary layer, which can be used to establish the requirements of the boundary layer traverse gear. From swept Hiemenz analysis, the shape factor of the attachment line boundary layer, $H = 2.54$ and from Blasius solution of flow on a flat plate, $H = 2.59$. Based on the relatively small difference in the shape factor, the Blasius solution can be used to obtain an estimate the integral quantities of the laminar attachment line boundary layer. From Blasius solution, the boundary layer thickness can be expressed as

$$\frac{\delta}{x} = \frac{4.9}{\sqrt{Re_x}} \quad (3.8)$$

and the momentum thickness,

$$\frac{\theta}{x} = \frac{0.664}{\sqrt{Re_x}} \quad (3.9)$$

Hence, following the necessary substitution the boundary layer thickness can be estimated as

$$\delta = 7.4\theta \quad (3.10)$$

3.1.4 The Experimental Model

From equation 5.28 the corresponding momentum thickness, θ , for a laminar attachment line was determined for a range of sweep angles and radii of curvature and similarly the boundary layer thickness and the experimental domain were estimated using equation 3.10 and 3.7 respectively. From the results presented in table 3.1 it can be observed that the leading edge radius of curvature is inversely proportional to sweep angle, so increasing the sweep angle will result in a smaller radius which helps in reducing the wind tunnel blockage and wall interference. However, with a smaller radius a thinner boundary layer will be generated hence increasing the complexity in capturing the turbulent boundary layer profile. For the present work a sweep angle of 60° was chosen for the model and the resulting leading edge radius of curvature of $0.114m$ offering moderate blockage in T2 wind tunnel. For this configuration a boundary layer thickness of approximately $6 \times 10^{-4}m$ was estimated using the swept Hiemenz flow method which is thin but still capturable using a finely resolved traverse mechanism. Nevertheless, for the equivalent turbulent attachment line the boundary layer thickness is expected to be at least 3 times thicker. Therefore the sweep angle and leading edge radius of curvature suggested initially seemed to be the most appropriate compromise.

Based on the thickness to chord ratio of 50% the chord length of the swept panel model was estimated to be $0.456m$ normal to leading edge. The span was constrained by the height of the working section as the model was mounted between the floor and the ceiling so that the infinite-swept condition was approached despite the use of flat walls. The span

Table 3.1: Theoretical estimation of the experimental parameters with variation of sweep angle for $Q_\infty = 45m/s$ and $\bar{R} = 500$.

Λ/deg	r/mm	θ/mm	δ/mm	s'/mm
40	318.1	0.108	0.809	23.5
45	242.6	0.0981	0.735	21.4
50	187.9	0.0905	0.679	19.7
55	146.6	0.0847	0.635	18.5
60	114.4	0.0801	0.601	17.5
65	88.3	0.0765	0.574	16.7
70	66.4	0.0738	0.553	16.1

was reduced by $2cm$ in order to allow for ease of fitting the model inside the working section. The dimensions of the model are shown in Figure 3.4 and Figure 3.5 shows the model mounted inside the working section of the T2 wind tunnel. The main difficulty encountered during the measurement of a turbulent boundary layer is capturing velocities very close to the wall. Due to heat transfer between the sensor and the surface of the model, hot wires are limited in terms of proximity to the surface. Following the heat transfer study between hot wire probes and walls made of different materials, Wills [121] concluded that wooden surfaces allowed for closer hot wire alignment than metal surfaces due to the lower thermal conduction property of wood, and thus wood was preferred for the current experimental model.

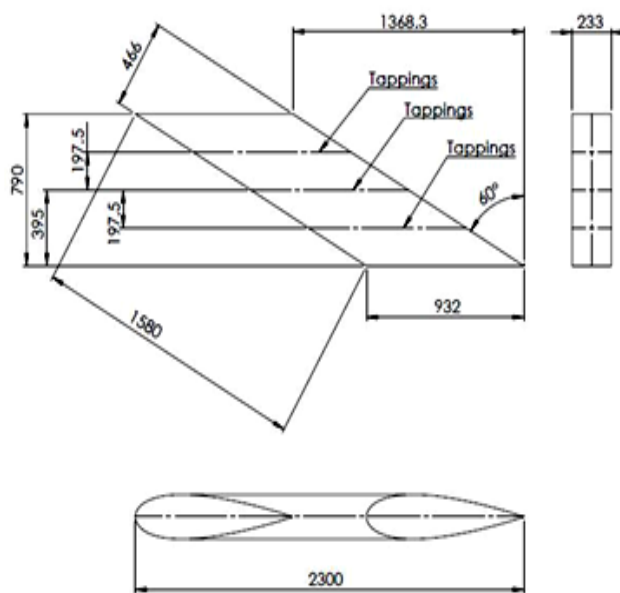


Figure 3.4: GA drawing of the experimental model

The model was fabricated in sections which were individually shaped to a NACA0050 aerofoil section. The tip of the final assembly was cut at the correct sweep angle to allow the model to be mounted flat between the floor and ceiling of the working section. The main issue associated with wood is the surface finish. As the experiment was concerned with turbulent boundary layers the surface finish was not considered with high importance as long as it could be considered to be aerodynamically smooth whereby the roughness was contained within the laminar sublayer. A very fine grain sandpaper was used for the final surface finish until it was considered smooth enough upon physical contact.

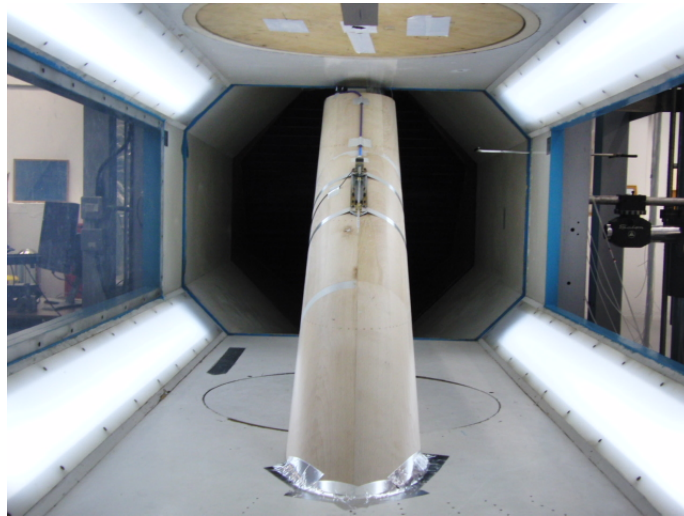


Figure 3.5: The swept panel wing mounted between the floor and the ceiling of the T2 wind tunnel.

3.2 Surface Pressure Measurement

The three dimensional model was equipped with 3 equally-spaced spanwise stations of surface mounted pressure tappings with an internal diameter of $0.5mm$ (as shown in figure 3.4) to measure the local static pressure. Each chordwise station contained 50 tappings and their positions are listed in table B.1. The tappings were more closely spaced at the leading edge so as to capture the behaviour of the flow more accurately in the region of main interest. Simultaneous pressure measurements were achieved using a computerised pressure measurement system where the pressure tappings were connected to a

64-channel array of ESP-64HD miniature electronic pressure transducer equipped with integrated DTC (Digital Temperature Compensation) which allowed for in-situ calibrations using the factory calibration data stored in a built-in EEPROM and A/D converter. The pressure scanners rated at 2.5psig were interfaced to a CANdaq acquisition system with a choice of CAN, Ethernet or RS232 output that can be connected to a PC for data acquisition and processing using software provided by Aerotech. The same pressure system was used by Badalamenti [13] who claimed an accuracy $\pm 0.06\%$ of the full scale deflection.

The model was symmetrical and the experiment was supposed to be conducted at zero lift condition. This characteristic of the model allowed it to be aligned by balancing the pressure distributions on both sides of the model, ensuring that the attachment line was right at the leading of the model ($x/c = 0.0$). Using the pressure system only 62 surface pressures could be measured at a time and the remaining two tappings were used for freestream total and static pressure. Initially each spanwise station measurement was made individually and the alignment was conducted by ensuring that the static pressures on each side were reasonably close to each other. Then, 19 tappings (9 on each side and 1 at the leading edge) at the leading edge of each spanwise station were connected to the pressure system and measured simultaneously to verify the alignment. The three spanwise pressure stations were also useful in identifying the spanwise extent over which the infinite-swept assumption was valid so that the boundary layer measurements were undertaken in that region.

3.3 Boundary Layer Traverse

Due to the dimension and the shape of the profile (gradient) of a turbulent boundary layer especially very close to the wall, a traverse mechanism with very fine resolution was required to scan the velocity profile and to capture the flow in the region of $z^+ < 5$ if possible with acceptable accuracy. However, the presence of very large surface curvature

at the leading edge presented major issues regarding the near-wall probe alignment which is simpler on flat and reflective surfaces. Most of the conventional commercial traverses which are usually mounted externally to the test section consist of slender traversing arms and other components which can add to the blockage which will be significant already due to the size of the model. For similar types of measurement Cumpsty and Head [36], [37] used a traverse with a slender arm. However these types of traverses can be prone to vibration, especially those with circular cross-section due to the generation of von Karman vortices even at moderate speeds of $25m/s$ for a diameters as small as $10mm$. This can be avoided by using faired cross-sections in the shape of a aerofoil profiles. Still, at high speed, the whole working section vibrates and the slender arm would probably not vibrate at the same natural frequency, even if it were mounted on the frame supporting the working section, and this could introduce noise into the hot-wire measurements. Considering these issues, the use of a compact surface mounted traverse was favoured for the boundary layer traverse measurement of the current experiment.

This type of traverse is not readily available on the market and the device had to be designed and built in house. The traverse is illustrated schematically in figure 3.6 and photographically in Figure 3.7 (side and top of final traverse). It is driven by the Nanotec GmbH & Co LS2018S0604 linear actuator which consists of a ST2018 stepper motor and TR62 translation screw with a range of 50mm. The stepper motor has an angular resolution of 1.8° per step, or a linear resolution of $10\mu m$ per step in the linear actuator mode, with a non-accumulative accuracy of 5% due to backlash and errors from the electronic components. Micro-stepping can be achieved to a ratio of 1/64 using the SMCI12 controller which is supplied by Nanotec. The linear actuator is operated from a PC via NanoPro software, also supplied by Nanotec.

As shown in Figure 3.6, the linear actuator is fixed to a flat steel base of dimensions $220mm \times 37mm$. Two brass strips, with bevelled edges to give an inverted-trapezoidal cross section, are also fixed on each side of the steel base. These act as rails to hold a grooved sliding wedge firmly to the steel base as shown in Figure 3.6. This ensures a

single degree of freedom for the wedge so that the translational motion is purely in the longitudinal direction. When the linear actuator pulls the sliding wedge towards the right-hand side the hot-wire probe pitches up, away from the surface; and vice versa. The slope of the wedge has a tangent of 0.5 and produces a vertical displacement $5\mu\text{m}$ for a single linear actuator step of $10\mu\text{m}$.

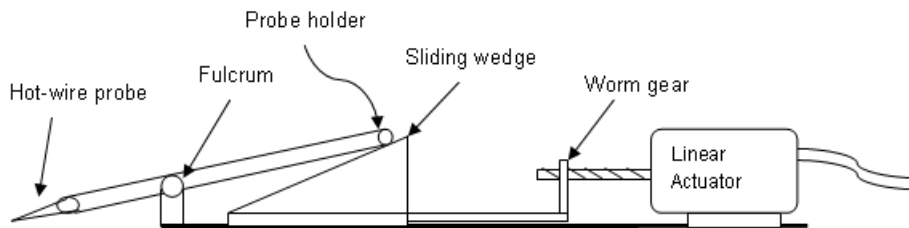


Figure 3.6: Schematic representation of the traverse mechanism to illustrate the main components.

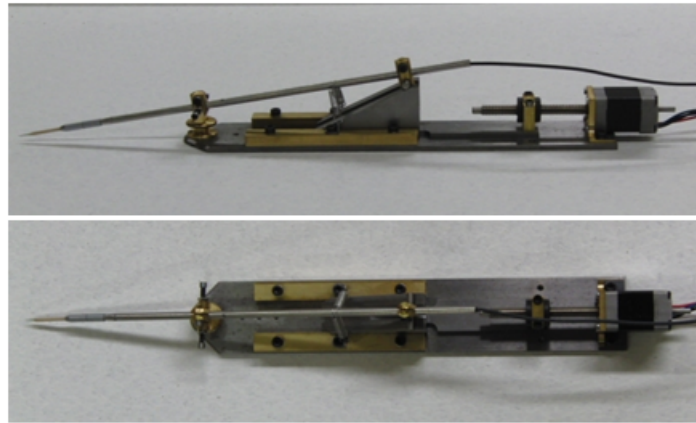


Figure 3.7: Side and top view of the traverse mechanism.

Further gearing can be obtained by adjusting the probe holder so that the arm length on the left-hand side of the pivot is half the length on the right-hand side. In this way the ratio between the linear displacements by the actuator and the resulting vertical pitch of the probe can be reduced by a factor of 4, hence increasing the resolution while traversing. By doing so, a resolution of $2.5\mu\text{m}$ per step is expected to be achieved by the traverse gear, which is half the diameter of the hot-wire probe. The SMCI12 controller possesses built-in micro-stepping capabilities up to a ratio of 1/64 (finest resolution of 0.028 degrees per step) and therefore a further reduction can be achieved if needed. However, with micro-stepping the accuracy of the stepper motor starts to deteriorate and becomes worse as the ratio decreases. For the current application a resolution of $5\mu\text{m}$ per step was deemed

adequate and micro-stepping was not required. But, if needed, it was advisable to stay within the ratio of 1/4 (quarter of a step) as the error at this condition was within an acceptable tolerance.

3.4 Hot Wire Measurements

Generally, during the measurement of turbulent boundary layers, a system with high frequency response is required in order to cope with the very rapidly varying nature of the physical quantities in the flow. In this case hot wire anemometry (HWA) has proven to be a very reliable technique for the measurement of both the mean and fluctuating velocity components with high frequency response and high signal-to-noise ratio in subsonic flows of moderate turbulence intensity levels. The current experiment is concerned with the measurement mainly of time-mean velocity components, but as the boundary layer addressed during the experiment would be relatively thin, the microscopic nature of the sensor wire (diameter of approximately $5\mu m$) permits measurements with reduced intrusive effects. In addition, the HWA was readily available in-house and it is a simpler and cheaper system to operate in comparison with Laser-Doppler Anemometry (LDA) or Particle-Image Velocimetry (PIV), which is not very reliable for measurements in a confined control volume.

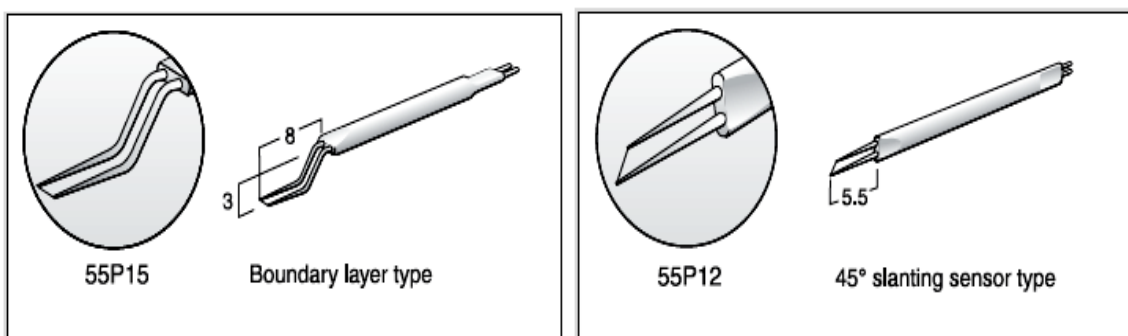


Figure 3.8: The single-normal boundary layer probe for single velocity component measurement and single-yawed probe slanted by 45° for two velocity component measurement (pictures extracted from Dantec Dynamics catalogue).

During the boundary layer measurement the Dantec Dynamics hot wire probes, namely

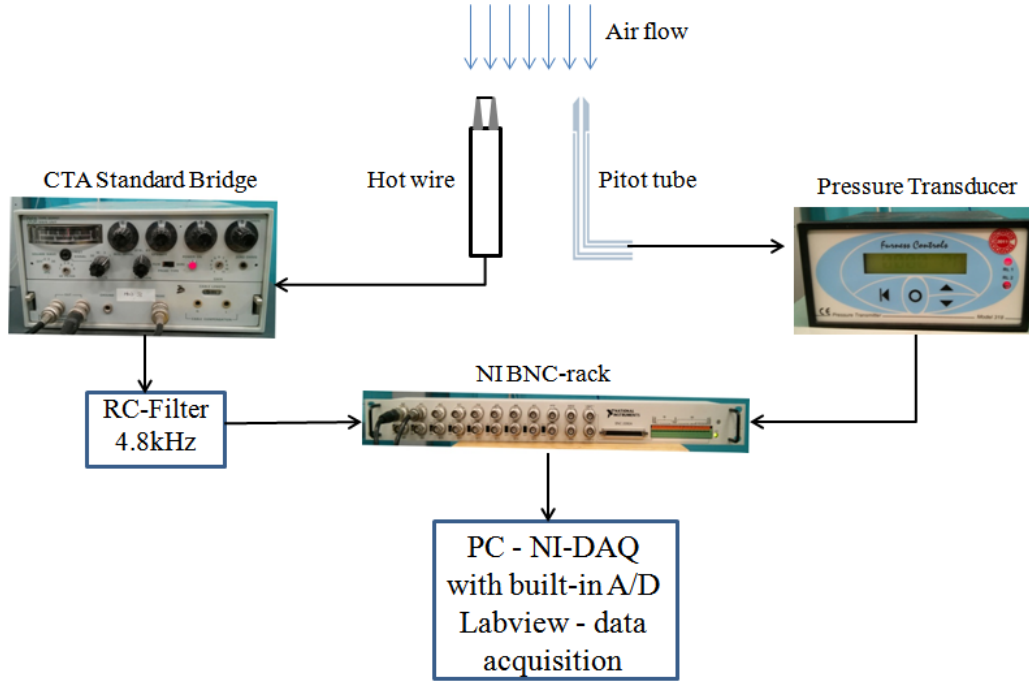


Figure 3.9: Set-up for the HWA data acquisition

the 55P15 (SN) boundary layer probe for single velocity component, and the 55P12 (SY) for two velocity components, (see Figure 3.8) were connected to the DISA 55M10 CTA Standard Bridge (M-Unit) module which consists of a Wheatstone bridge equipped with a servo mechanism. The M-Unit was in turn interfaced with the National Instruments (NI) DAQ card which possesses a built-in A/D converter and installed in a PC for data acquisition in NI-Labview. More details of the set-up can be found in Figure 3.9. The point to be noted was that the CTA input and output was controlled mainly by the M-Unit and the hot wire output signal was pre-filtered through a low-pass (RC) filter with a cut-off frequency of 4.8kHz prior to any storage in Labview. An overheat ratio of approximately 2.0 was employed and therefore the total operating resistance was estimated to be approximately 7.4Ω , where this value varied slightly depending on the types of probe used, and the M-Unit was adjusted accordingly. Using equation 3.11 the operating mean temperature of the wire, T_s , was calculated to be approximately 270°C .

$$R_w = R_{TOT} + \alpha_{20} R_{20} (T_s - T_a) \quad (3.11)$$

where R_w represents the M-unit operational resistance and R_{TOT} the total resistance of the hot wire probe including the leads at ambient temperature could be measured from the M-Unit. R_{20} represents the resistance of the wire at $20^\circ C$, and α_{20} the temperature coefficient of the wire at $20^\circ C$ which were also provided by the manufacturer. Finally, T_a represents the ambient temperature.

Labview was favoured for data acquisition due to the fast sampling rate achievable which is advantageous for the measurement of turbulent boundary layers. According to Bradshaw [16] the maximum frequency observable in a subsonic turbulent boundary layer is about $30kHz$, thus a sampling rate of $100kHz$ was applied during the boundary layer measurement in order to ensure that the Nyquist criterion (sampling frequency at least twice the value of the frequency of the physical quantities being measured) was met.

Following further recommendation from Prof. M. Gaster the signal was pre-filtered using a low-pass filter with a cut-off frequency of $4.8kHz$ prior to any storage or post-processing. This was to eliminate the high frequency electronic noise that starts to appear within the M-Unit when the frequency response of the servo-loop increases to account for increase in the frequency of the turbulence mechanism in the flow. As the cut-off frequency was significantly lower than the initially suggested sampling frequency, the final sampling frequency could have been reduced while still being compliant with the Nyquist criterion: however the sampling rate was kept at the initially stated value, as the data acquisition system was able to cope with the large amount of data. More details about the principle of operation, calibration and estimation of the velocity components is presented in Chapter 4.

3.5 Optical Micro-Measurement Technique

Given the size of the hot wire sensor and the resolution of the vertical displacement required during the boundary layer traverse, it was important to ensure that the traverse

gear was operating with high precision so that the boundary layer profile could be captured accurately. Therefore a simple digital-optical system was designed to assess the performance of the traverse by magnification of the probe prior to calculation of the micro-displacement generated by the stepper motor, following a calibration process. Furthermore, the optical system proved to be beneficial for probe alignment purposes and for positioning the hot wire very close to the surface of the experimental model.

3.5.1 Principle and Set-Up

The principle behind the current optical system is fairly simple: it is based on the magnification of an object or target, which in this case was the hot wire sensor and the model surface, and the image was captured live from a digital camera. The optical system design included back illumination (white light LED illuminator LIU004, Thorlabs Ltd) of the object and a pair of identical achromatic doublet lenses (Linco Photonics AC254-100-A-ML, focal length $f'=100\text{mm}$). The system is illustrated schematically in Figure 3.10 and photographically in Figure 3.11, where the image of the wire was captured using a CCD camera (QImaging Rolera). The set-up could be configured for different magnification settings by varying the ratio of the image distance (distance of CCD camera from the lens pair) to object distance (distance of hot-wire probe from lens pair) and the principle is summarised below.

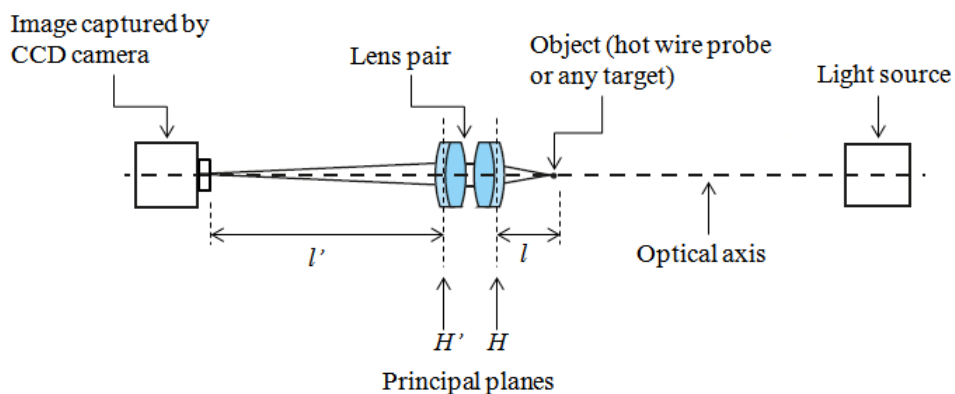


Figure 3.10: Schematic representation of optical set-up illustrating the principle of operation

From Jenkins and White [63] the path of a ray of light emerging from a medium and passing through a spherical surface can be represented by the relation given in equation 3.12

$$\frac{n}{s} + \frac{n'}{s'} = \frac{n' - n}{r} \quad (3.12)$$

where s represents the distance from the object and the principle plane, s' the distance between principle plane and the image, and r the focal length. If the light path passes through two different media then n would be the refractive index of the medium in which the object lies and n' the refractive index of the medium where the image is located. See ‘FIGURE 3K’ and ‘pp. 56’ from reference [63] for more details about the derivation.

If the ray of light is travelling through a thin lens and the same medium, which would be air for the current application, the power of that lens can be expressed as

$$\frac{1}{l} + \frac{1}{l'} = \frac{1}{f} \quad (3.13)$$

Based on the optical system in Figure 3.10, f denotes the focal length of the lens and l , represents the distance between the object and the primary principle plane H , and l' the distance between the secondary principle plane and the image in focus. By simplifying the lens formula the magnification can be expressed as

$$M = \frac{l}{l'} \quad (3.14)$$

The use of achromatic doublet lenses was favoured in order to minimise the chromatic and spherical aberration, thus reduces the blurring or fringing effect captured on the CCD sensor. Chromatic aberration is due to change in the refractive index for different wavelength of various colours of light and the spherical aberration is due to the curvature of the

lens surface which allows some of the light to be scattered away from the point of focus.

3.5.2 Calibration of the Optical System

The optical system was first calibrated by placing a reference target at the object plane instead of the hot-wire probe shown in figure 3.11. The reference targets used were either a USAF resolution target (black on clear glass used in transmission, Edmund Optics) or the inner spacing between the jaws of a digital calliper. These targets of known dimensions enabled the calibration of the image obtained with the CCD camera using the procedure described below. The jaws of the digital calliper were set at $300 \pm 1\mu m$, placed in front of the lens and translated back and forth to bring into focus, so that this calibration gauge was located exactly at the object plane. Figure 3.12 shows the image captured with a magnification of 9 times (9x), where the lighter region shows the gap in between the jaws of the calliper.

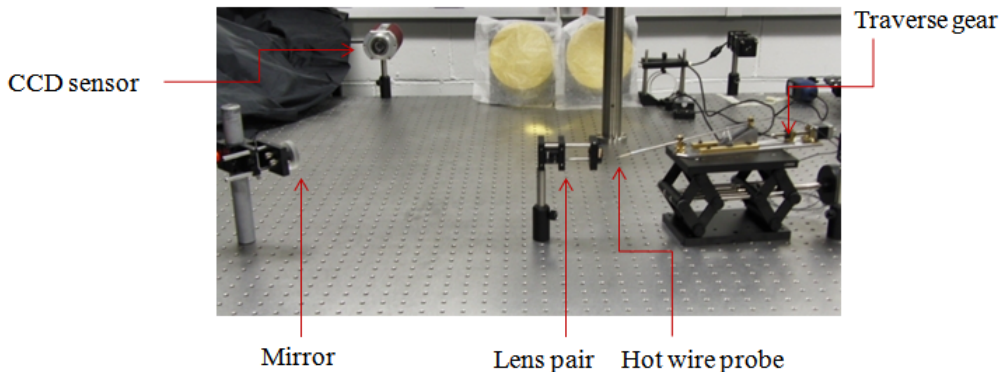


Figure 3.11: Photographic representation of the of the optical set-up

A short program was written in Matlab to digitise the graphical plot shown in figure 3.12 and this helped in plotting the colour intensity along a reference horizontal cross-section, at a vertical position of 200 pixels. The digital image is shown in Figure 3.13. The edges of the calliper jaws (the darkest parts) were assigned the minimum value (intensity = 0). The data was reprocessed by applying a threshold value of 1.5×10^4 on the colour intensity shown in Figure 3.13 and, through binarisation, the number of pixels representing the grey region in Figure 3.12 was determined and shown in figure 3.14. From the binarised image

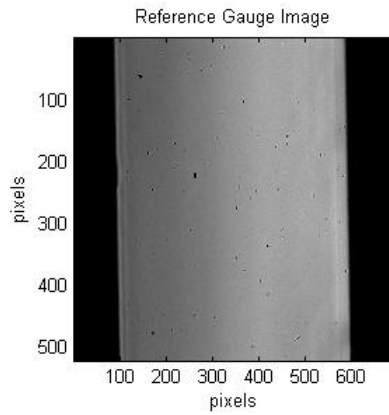


Figure 3.12: Snap shot of the spacing of 300μ between the jaws of a digital calliper

the pixel count (with an accuracy of 2 pixels) representing a length of $300\mu m$ could be determined, therefore providing a conversion factor between pixels on the CCD and object plane coordinates. The CCD camera used had square pixels and therefore the calibration is identical in both horizontal and vertical directions.

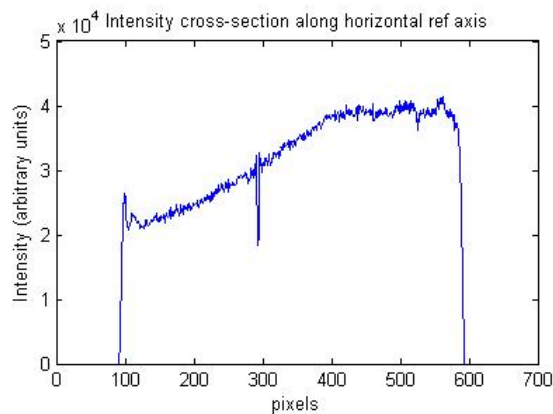


Figure 3.13: Digitised image showing the greyscale intensity of the spacing between the jaws of the calliper

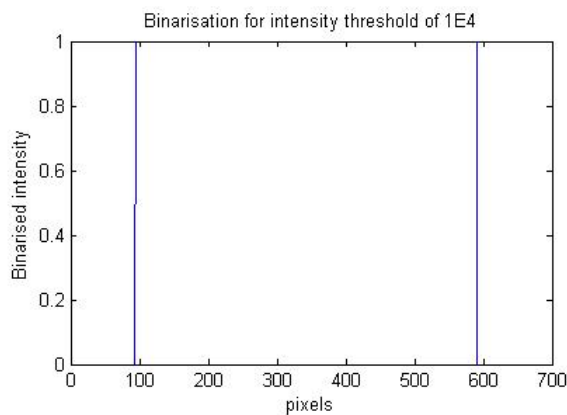


Figure 3.14: Binarised plot of the colour intensity with threshold placed at 1.5×10^4

3.5.3 Commissioning the Traverse Gear

After having calibrated the system, the vertical displacement of the hot-wire probe (generated by the traverse mechanism) could be measured by comparing the images of a reference position and final displaced position. Figure 3.15 shows the initial position (reference position) of the hot wire and the position after one step of the stepper motor for an arm ratio (AR) 1:2. A cross-section of the image along the vertical direction (averaged over the range of $100 \geq x \leq 200$ pixels) is plotted in Figure 3.16, showing the pixel intensity values at both positions. The minimum point on the troughs of the intensity plots, which represents the centre of the hot wire, has shifted by a very small amount along the x-axis and this represents the displacement of the probe in pixels. Using the relationship between pixel and physical space established above, a displacement of $2.41\mu m$ was measured for this particular case.

In order to measure finer displacements the magnification of the optical set-up has to be increased, however in doing so the resultant image would become blurred owing to an increase in optical aberrations, and the accuracy would be compromised. Instead of measuring the displacement for every single step, the displacement of a range of steps can be measured and the mean of that sample can be derived. Therefore, using this particular technique, the minimum displacement achievable by the traverse gear was estimated and (in this case) the magnification from the optical set-up was increased approximately to 20x. Again, using the snap shot of the initial reference position and the position after 40 quarter steps (which is shown in figure 3.17), and applying similar procedures to those outlined above, the minimum measurable displacement generated by the traverse gear was estimated to be $0.60 \pm 0.04\mu m$ for a quarter of a step motion generated by the stepper motor. The quarter of a step motion was achieved by using the micro-stepping function available from the controller.

In theory the wire is supposed to move by $2.50\mu m$ for the given pitching arm ratio and, using the optical measurement system, a displacement of $2.41\mu m$ was obtained. This

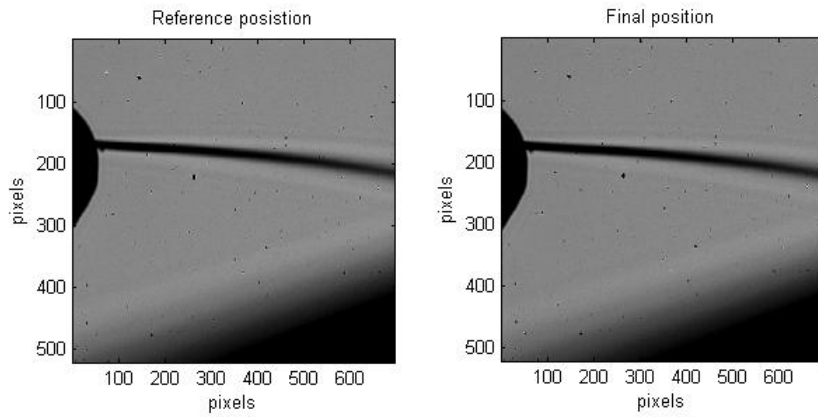


Figure 3.15: Photographic image of the hot wire before (LHS) and after (RHS) 1 step displacement generated by the traverse gear

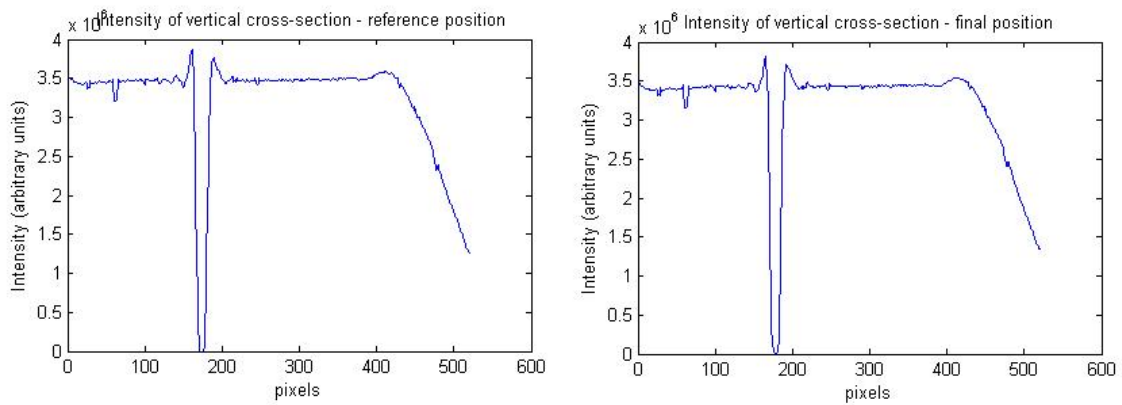


Figure 3.16: The baseline and the final intensity trace after 1 step displacement of the hot wire

shows an error of 3.7%. As the stepper motor operates with non-accumulative accuracy of $\pm 5\%$ per step the discrepancy between the theoretical and measured value is justifiable. Similarly, for the finer measurements of quarter steps an accuracy of 4.2% was obtained. The minimum achievable displacement of the traverse gear can be further reduced by increasing the micro-stepping ratio, but for the current investigation it was unnecessary as a resolution of $5\mu m$ per step was deemed adequate to capture the profile of the turbulent boundary layer.

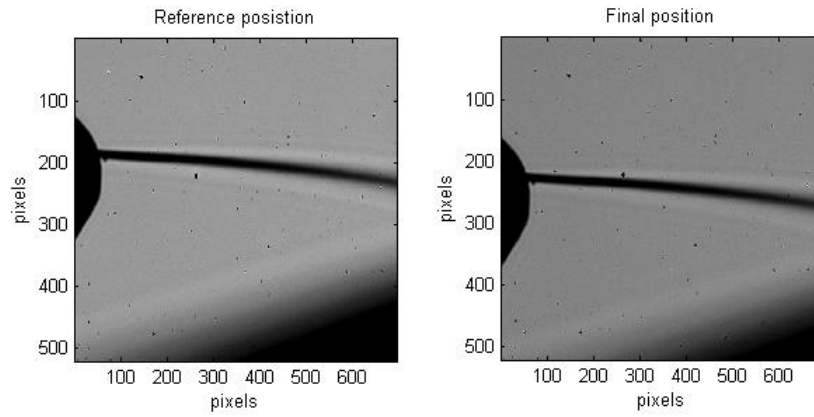


Figure 3.17: Photographic image of the hot wire before (LHS) and after (RHS) 40 step displacement generated by the traverse gear

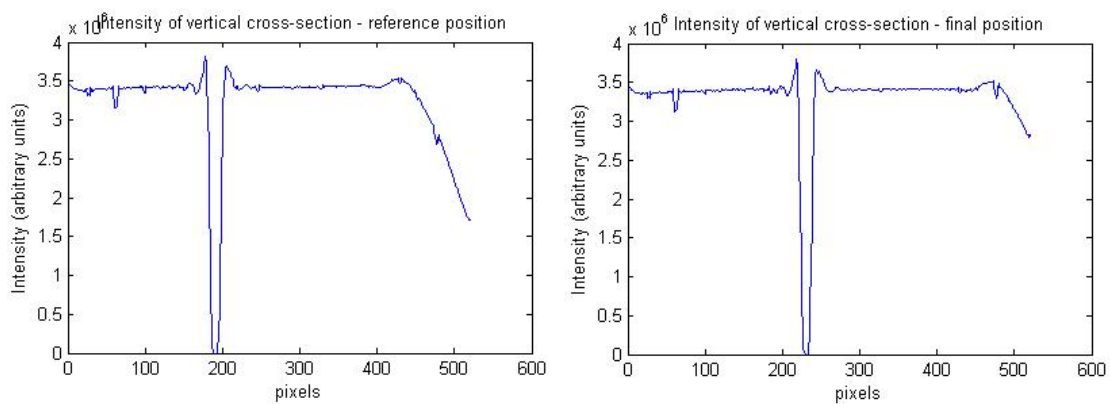


Figure 3.18: The baseline and the final intensity trace after 40 steps displacement of the hot wire

3.5.4 Near Wall Alignment of Hot Wire Probes

The optical technique was easily transferrable from the optical bench shown in Figure 3.11 to a more confined wind-tunnel environment due to the simplicity of the set-up, and was used to align the hot-wire probe as close as possible to the model surface. During the alignment a class 2A laser was shone through the centre of the optics to define the optical axis, and this allowed accurate positioning of the lenses with respect to the model, hot-wire probe and the LED back illuminating light source. A first attempt was made to keep the optical system outside the test section of the wind tunnel using a two-step magnification phase shown schematically in Figure 3.19. The optical principle here is similar to that applied above, except the introduction of the single lens as an intermediate stage.

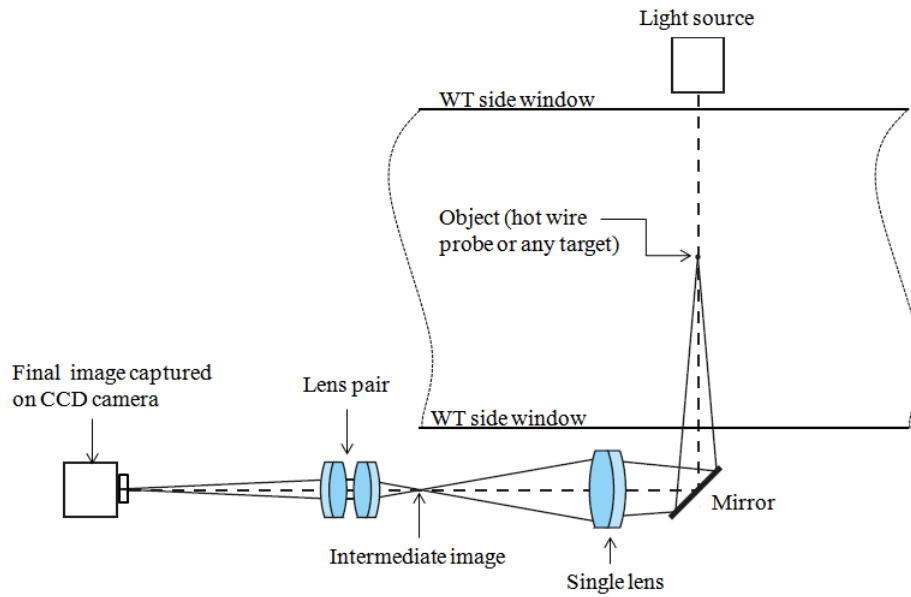


Figure 3.19: Schematic representation of the optical set-up illustrating the principle of the dual magnification phase

From equation 3.14, for a lens with a given focal length the magnification is inversely proportional to the distance between the object and the primary principle plane, l . In order to keep the optics outside the test section this minimum distance should be $l \approx 60\text{cm}$ which is half the width of the working section plus the thickness of the side window and a certain amount of clearance for an object located at the middle. Therefore, for a magnification of at least $10x$ a bigger lens would be required with a longer focal length resulting in quite a large distance between the secondary plane and image in focus. This could be avoided by inserting the intermediate lens and its image could be used as the object for the second doublet lens served as the magnifier (see Figure 3.19 for more details).

Initially the alignment of a probe above a flat plate with a reflective metallic surface was attempted, as illustrated in Figure 3.20, to test the feasibility of the new set-up. The optics were kept outside the working section and a magnification process similar to that in figure 3.19 was employed. Due to the reflective nature of the surface, both the real image of the side of the hot-wire probe support and its mirror image could be captured by the CCD camera, as shown in Figure 3.21. Again, through the digitisation process, the variation of the greyscale intensity along a vertical axis touching the tip of the hot wire support on both images could be plotted, in Figure 3.22. From figure 3.22 the troughs represent the

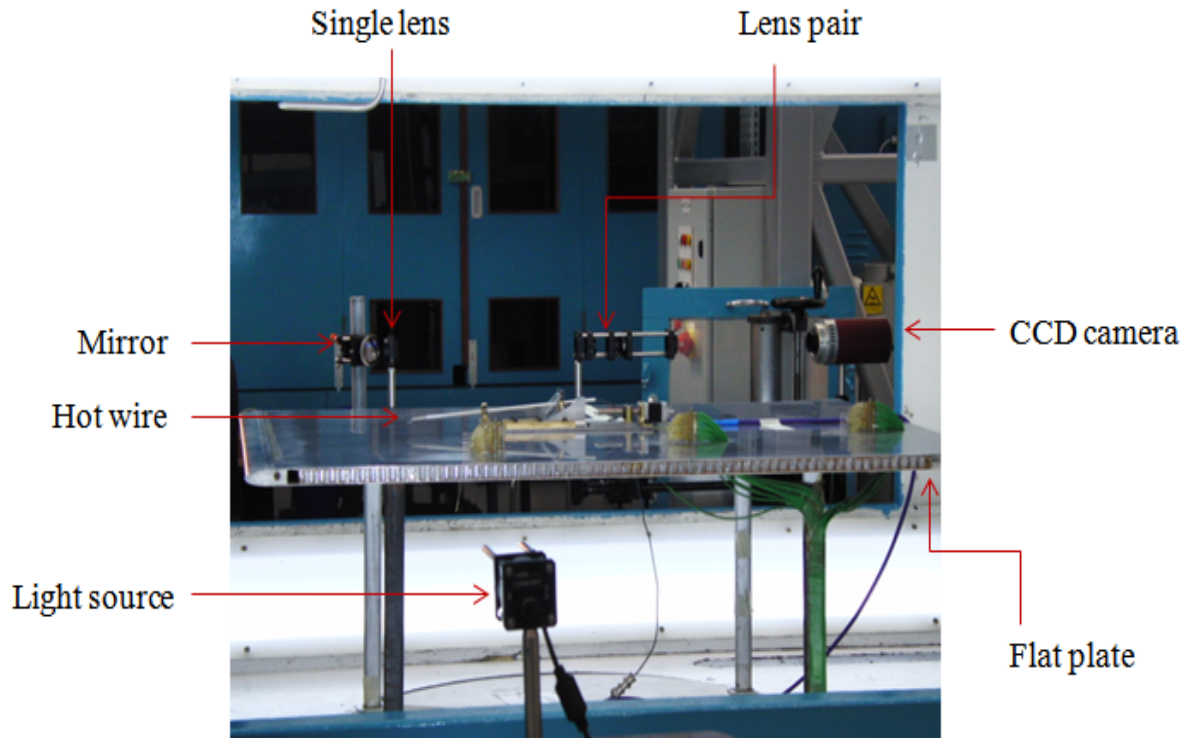


Figure 3.20: Set-up for the alignment of the hot wire probe on a flat plate

centre of the tips of the hot wire supports and the number of pixels between the end of the first trough and beginning of the second one shows the separation between the two images. Dividing the number of pixels representing this spacing by two and multiplying by the physical dimension representing one pixel, obtained from the calibration, would provide the spacing between the tip of the hot wire support and the surface of the flat plate. This was equal to $163\mu m$.

The system also assisted in monitoring qualitatively the low frequency, large amplitude vibration of the probe at the higher speed testing. From the observations made there was no significant vibration and deflection of the probe in the plane of the boundary layer traverse, however the working section started shaking at speed greater than 45 m/s and the whole image would move on the screen used to display the data captured from the CCD sensor. Any high frequency vibration associated with von Karman vortex shedding from the wire support and probe holder could have been captured if a high speed camera (with a specification of at least 20-30k frames per second) had been used, but this exercise was not within the scope of the current study.

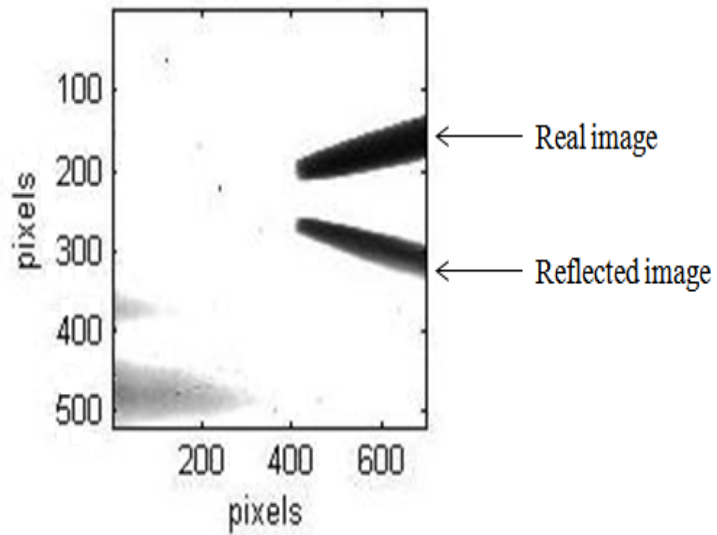


Figure 3.21: The real and reflected image of the probe captured using the CCD camera during the alignment on the flat plate

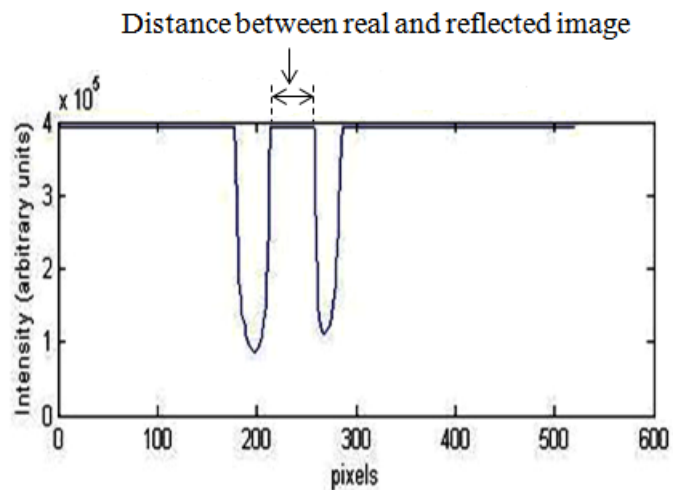


Figure 3.22: Colour intensity trace of the real and reflected image along the axis touching the tips of the hot wire support

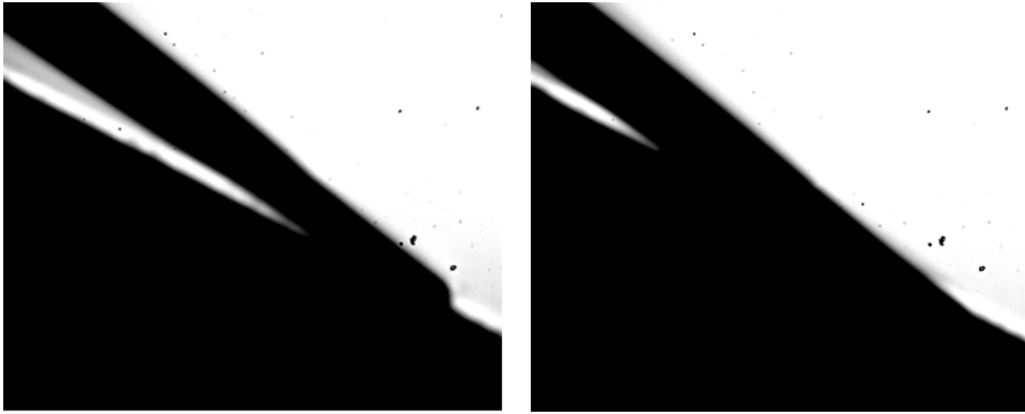


Figure 3.23: The blurred image of the side view of the probe support and wind tunnel model obtained from the dual magnification phase set-up shown in figure 3.19

However, near-wall alignment on the actual experimental model was somehow more complicated due to the non-reflective nature of the wooden surface. Also, due to the relatively large distance between the object plane and optics which led to a two stage magnification, the optical aberrations became more severe and the resultant optical system did not yield reasonable image quality due to blurring from the surface of the model as well. An example of the resulting images of the side view of the hot-wire supports, at two different locations with respect to the model's surface, are shown in Figure 3.23. From the figure, on the left-hand side, the hot wire appears to be in contact with the surface but in fact that was not the case. Whereas, from the figure on the right-hand side the support was in contact with the surface but the image suggests that it was past the point of contact and had started to bend against the surface of the model. Hence, the optical system was modified and the target was magnified only through a single magnification phase, similar to the set-up used for the calibration of the traverse mechanism (Figure 3.10). This meant that the optical bed had to be shifted inside the test section as shown in Figure 3.24, closer to the probe and the model surface, using a coarser traverse mechanism for wind-off near-wall alignment. In doing so the magnification of the system was affected as there were restrictions on the minimum distance the lens could be placed with respect to the target due to the large leading edge radius of the model.

Figure 3.25, obtained with the revised arrangement, shows an improved side view of the hot wire support and the wind tunnel model before (figure left-hand side) and when (figure

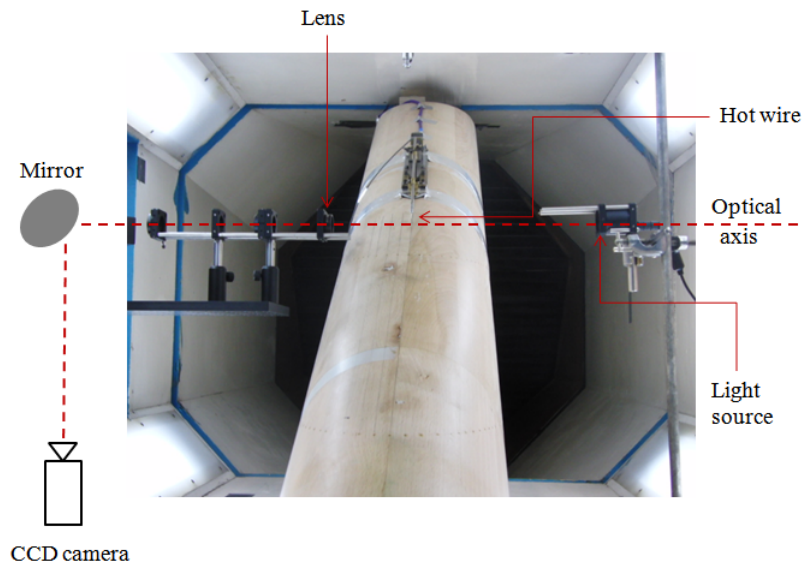


Figure 3.24: The modified optical set-up using a single lens for near-wall positioning

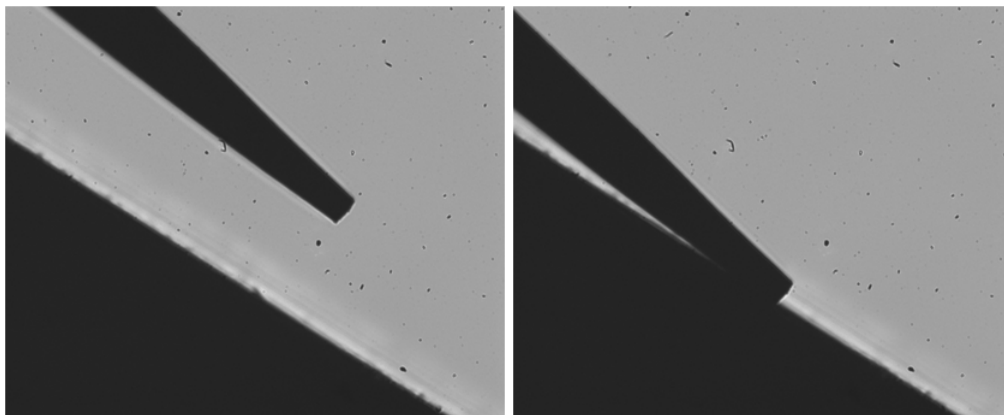


Figure 3.25: The side view of the probe support and wind tunnel model obtained from the modified set-up shown in figure 3.24

right-hand side) contact was established between the wire supports and the wall. Depending on the type of hot-wire probe, and the angle through which it was driven towards the surface, there was a minimum achievable distance between the sensor wire and the wall. This was due to the wire support, which was substantially thicker than the sensor wire, coming into contact with the wall and prohibiting any further displacement. Therefore the minimum probe-to-wall distance achievable during the experiment was equivalent of the perpendicular distance between the centre of the hot wire and the tip of the support in contact with the wall. Again using, the magnification method devised in section 2.4, this distance was determined to be approximately $60\mu m$.

The probe-wall positioning was conducted by driving the probe towards the wall using the fine traverse until contact was established. Further movements had to be minimised or else the wire supports would start to bend and damage the fragile sensor wire. This could also introduce errors in the initial measurements of velocity profile close to wall, due to the deflection introduced to the wire support under the effect of bending, and this discrepancy would accumulate through the rest of the measurements taken further away from the wall. In addition to the digital image display on the computer screen, another way of confirming whether contact was established with the surface was by operating the hot wire as a proximity sensor, due to the heat transfer between the hot wire and the wall. Using the real time signal display capability in NI-Labview, the step change in the amplitude of the hot wire signal was monitored and, as the wire approached the wall, an increase in the output voltage could be observed. Upon contact the largest step change in the signal was shown, together with the maximum voltage output, and those stayed more or less constant for any further step motion of the traverse.

The alignment above was purely concerned with the measurement at the attachment line. For downstream flow measurements the traverse gear had to be modified in order to support and position the hot wire at the measuring stations downstream. Two extension brackets were manufactured, each containing 5 holes for clamping the primary shaft (traverse) and the secondary shaft (probe holder) as shown in Figure 3.26. The brackets were mounted, one upstream and the other downstream of the fulcrum and held the secondary shaft parallel to the primary shaft. As the ratio between the moment arm was kept at a value of 1, the vertical displacement generated by the traverse mechanism per step was same as that quoted above. The hot wire could be transferred to a different chordwise position on the model by clamping the secondary shaft into the different holes along the length of the brackets, the fourth and final station was located at $x/c = 0.03$ (where 'station 0' is at $x/c = 0.0$, 'station 1' at $x/c = 0.005$, 'station 2' at $x/c = 0.01$, 'station 3' at $x/c = 0.02$, 'station 4' at $x/c = 0.03$)

For the extended probe support arrangement the optical method did not vary from the one

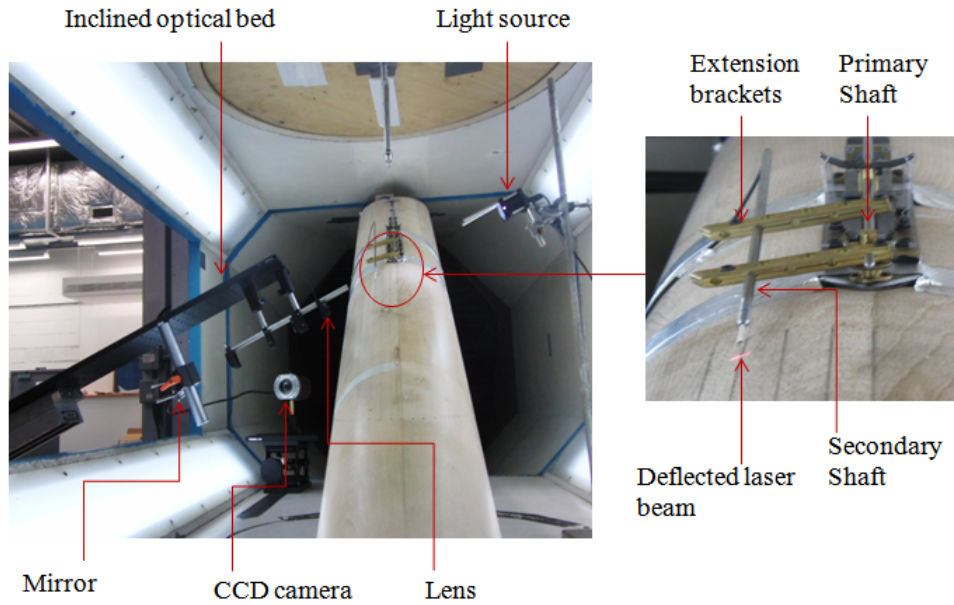


Figure 3.26: The optical set-up on an inclined optical bed and the extension bracket to support the probe for measurements downstream of the attachment line.

used above except from the inclination of the optical bed (platform) about the horizontal axis using the adjustable angle plate on which it was mounted. This was to ensure that the optical axis would pass through the centre of the lenses and the light source without being interfered by the curved surface. Again a laser beam was sent through the centre of the optics to define the optical axis, but this time it had to be as tangential as possible to the point where the boundary layer measurement would be made (or the point of contact of the hot wire probe with the surface) for accurate positioning. The tangent point could be identified by driving the laser beam towards the surface and once the bottom part of the beam was in contact to the surface it would deflect, creating a red spot as shown in figure 3.26. The optimum tangential point could be obtained by repeating this process until the smallest spot size was observed. After defining the optical axis, the laser emitter was replaced by the CCD camera and the image was brought into focus. The resulting images have been shown in figure 3.27 for the alignment at 3 chordwise stations.

Using this method, the accuracy of the wall probe position is highly dependent on the step resolution used while approaching the wall. For the current experiment each step change was equal to a displacement of $5\mu m$ with an accuracy of $\pm 5\%$ as the moment arm

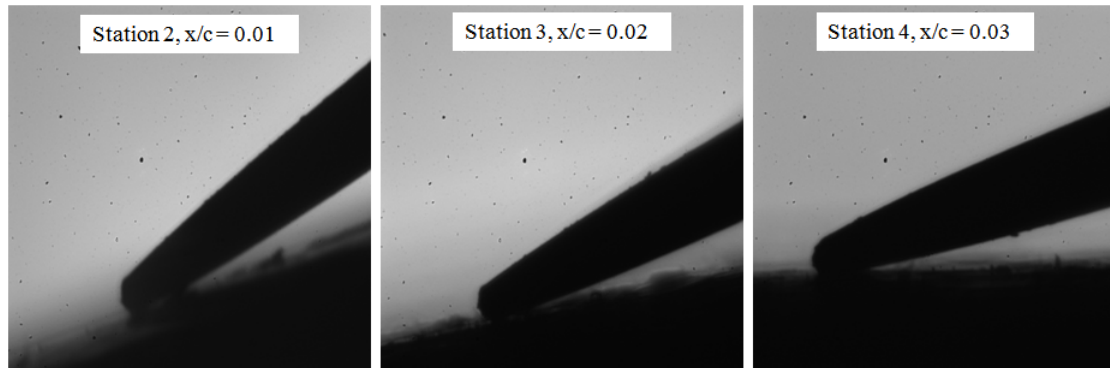


Figure 3.27: The side view of the probe support and wind tunnel model at the downstream measurement stations

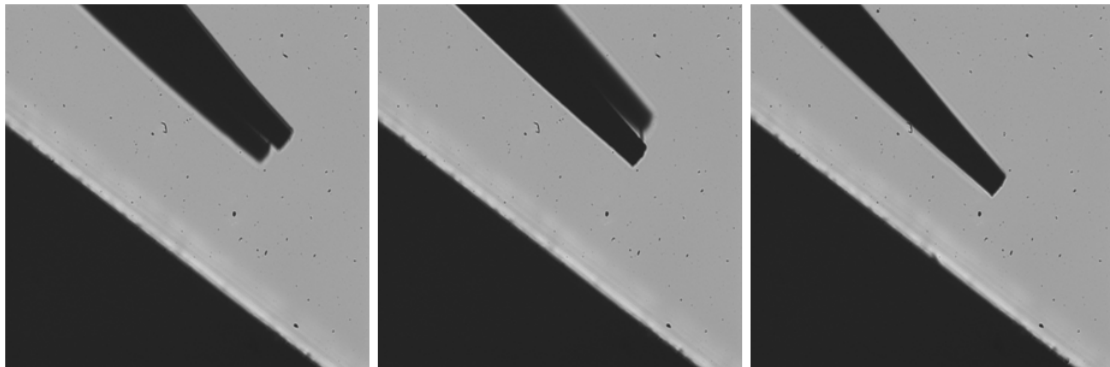


Figure 3.28: Alignment of the hot wire support

ratio was set to a value of 1. Therefore the error was dependent on the measured position immediately before contact was established. If, in the worst case scenario, this minimum probe height was half the displacement generated by the traverse, then the accuracy of the probe wall position was within $\pm 2.5\mu m$. This could be further reduced by employing finer step changes using micro-stepping. The optical system was also employed to ensure that the wire supports were parallel to each other and lying in the same plane. By comparing the three images presented in Figure 3.28, it is clear that from the first two pictures the wire supports were not aligned and, by rotating the probe in its holder they could be adjusted quite precisely, as confirmed by the third picture.

3.6 Wall Shear Stress Measurement using Preston's Technique

As the experiment was predominantly concerned with the measurement of turbulent boundary layers, the wall shear stress, τ_w , could be obtained using the technique developed by Preston [95], based on the characteristic of the 'inner' region of a fully developed flow in a pipe or turbulent boundary layer on a flat plate. Based on Preston's study, by mounting a tube of circular cross section and external diameter, d , in the plane parallel to the flow and well within the inner region of a fully turbulent boundary layer, the difference between the total pressure, P_0 and the static pressure P_s can be expressed as

$$\frac{(P_0 - P_s) d^2}{\rho_{iw} V_{iw}^2} = F \left(\frac{\tau_w d^2}{\rho_{iw} V_{iw}^2} \right) \quad (3.15)$$

using dimensional analysis arguments.

This hypothesis was confirmed by Preston through the measurement of fully developed flows in pipes and, based on the latter's observations a relation for estimating the surface shear stress was established. Later the method was extended to deal with fully developed turbulent boundary layers on flat plate by mounting a Pitot tube with an external diameter approximately 10 times less than the thickness of the boundary layer on the surface. While assuring contact was established between the wall and the tube, the static pressure was obtained using pressure tappings mounted normal to the flow and flush to the surface. The relation for the flow in pipes differs slightly from that for the flow on flat plates and, during the current investigation, the relation given by Ferriss [40], which accounts for the correction introduced by Head and Rechenberg [58] to the initial relation proposed by Preston, was adopted. The expression is given by equation 3.16.

$$\log_{10} \left(\frac{\tau_w d^2}{\rho_{iw} V_{iw}^2} \right) = 0.889 \log_{10} \left(\frac{[P_0 - P_s] d^2}{\rho_{iw} V_{iw}^2} \right) - 1.400 \quad (3.16)$$

According to Preston, the method is still applicable in flows with pressure gradients provided that the law of wall still holds and the Pitot tube is small enough to be fully immersed in the inner layer. But the investigation conducted by Patel [87] later demonstrated that the presence of strong favourable and adverse pressure gradients led to an over-estimation of the skin-friction due to a shift from the law of the wall behaviour, where the favourable pressure gradient case was shown to be the worst.

For the current study two different techniques were chosen. Firstly a hypodermic tube (Pitot tube) with $d = 0.4mm$ was used to measure the total pressure while the local static pressure was obtained simultaneously from the corresponding surface mounted pressure tapping as shown in Figure 3.29. The hypodermic tube was mounted at a distance of about 5 times the boundary layer thickness, or 50 times the internal diameter of the Pitot tube downstream of the static tube, in order to limit any interference due to surface imperfection caused by the surface tapping. Both tubes were connected to the FC0318 differential pressure transducer. As it is fair to assume that the static pressure does not vary in the direction normal to the boundary layer, the second method was devised by placing a small static pressure tube on top of the Pitot tube, as shown in Figure 3.30, where the combined height of the Pitot and static tubes was almost 3 times less than the thickness of the boundary layer. This was to prevent the effect imposed due to the boundary layer displacement thickness on the surface mounted static pressure tapings, and also the discrepancies due to the larger hole diameter of the surface static tapping in comparison to the diameter of the static tube in the Preston probe shown in Figure 3.30, which was at least 4 times smaller. For the measurement of shear stress at the attachment line the tube was mounted in the direction of the AL flow and the pressure difference between the Pitot and the static tubes was captured using the FC0318 pressure transducer and was passed into Labview for data acquisition and storage at different \bar{R} .

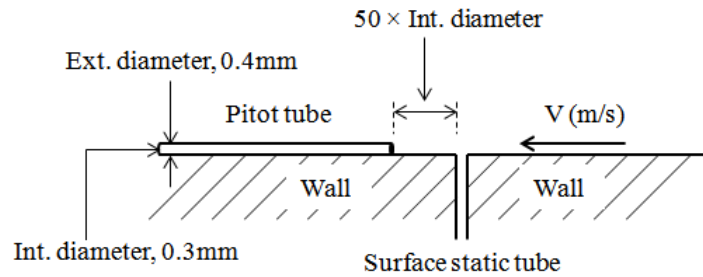


Figure 3.29: Schematic representation of surface shear stress measurement using Preston's method where the static pressure is obtained from the surface pressure tapping.

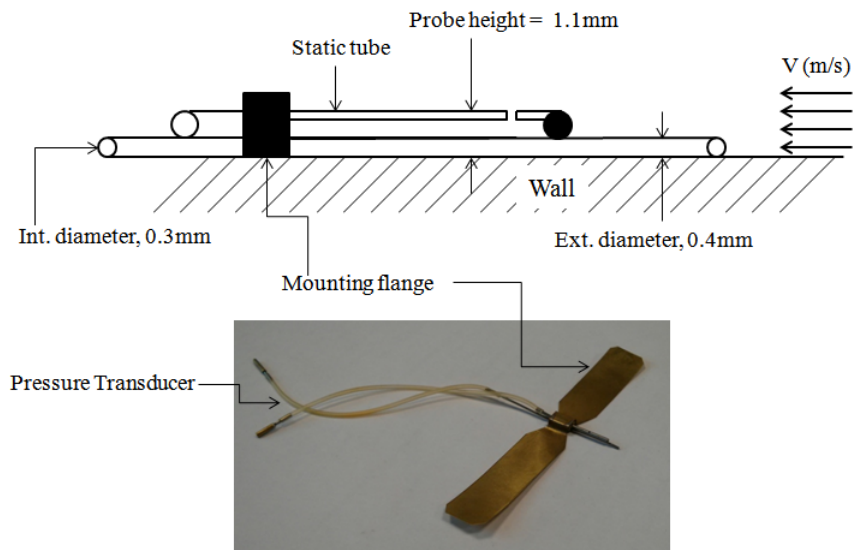


Figure 3.30: Schematic and photographic representation of surface shear stress measurement device using Preston's method where static pressure is obtained from the static tube mounted on top of the Pitot tube.

Chapter 4

Hot Wire Anemometry

4.1 Principle of Operation

In simple terms hot wire anemometry (HWA) is based on the principle of convective heat transfer between a microscopic sensor wire and the fluid flowing in its vicinity; or according to Perry [88] the hot wire is simply a ‘thermal transducer’. There are two predominant modes of hot-wire anemometry; the ‘constant current anemometry’ (CCA), during which the current passing through the sensor wire is kept constant, and ‘constant temperature anemometry’ (CTA) mode where the temperature is kept constant through a built-in feedback loop. Nowadays, CTA has gained more recognition and it is more commonly used due to its simplicity, better frequency response characteristics and ability to compensate for the thermal inertia of the sensor wire automatically through feedback control. Following King [69], in 1914 a semi-empirical relation for heat transfer through forced convection between a cylindrical sensor wire in a crossflow and the fluid in its proximity was established in terms of the Reynolds number, Re , and the Nusselt number, Nu . This relation is expressed by equation 4.1.

$$Nu = A + BRe^n \quad (4.1)$$

where Re is based on the local flow parameters viscosity, ν , and velocity, u , and the characteristic dimension of the wire (the diameter), d_w .

$$Re = \frac{Ud_w}{\nu} \quad (4.2)$$

For Nu , a relation for the heat transfer due to the change in the voltage or current passing through the wire has can be expressed as

$$Nu = \frac{Hd_w}{k} = \frac{E^2}{R_w \pi l k (T_w - T_a)} \quad (4.3)$$

where, H represents the heat transfer coefficient; k , the thermal conductivity of the fluid; E , the voltage output; R_w , the resistance of the wire; l , the length of the wire; and T_w and T_a the temperature of the hot wire and the ambient fluid respectively.

4.2 Measurement of a Single Velocity Component

4.2.1 Response of a Single-Normal Probe

The hot wire response can be also expressed by the power law given by equation 4.4 where A and B are functions of the physical characteristics of the wire

$$E^2 = A + BV_e^n \quad (4.4)$$

and the effective cooling velocity, V_e can be expressed as

$$V_e^2 = U_N^2 + k^2 U_T^2 + h^2 U_B^2 \quad (4.5)$$

where, U_N is the velocity normal to the sensor wire and U_T and U_B is the tangential and bi-normal components respectively. k and h are functions of α and β respectively and normally according to Bruun $k \approx 0.2$ and $h \approx 1.02$.

From the initial analysis conducted by King [69], the power, n , from equation 4.1 was expressed by a value of 0.5, however experimental studies conducted later, as summarised by Bruun [21] showed that this value can vary between approximately 0.42 to 0.50. The two constants ‘ A ’ and ‘ B ’ can be determined experimentally, following a calibration exercise, and by plotting the hot-wire voltage output, E^2 , with respect to the effective velocity, V_e , to the power of n . During the current study a value of 0.45 was assigned to n following private communication with Gaster [43].

Substituting the effective velocity, V_e , in equation 4.4 by equation 4.5, the hot wire response takes the form

$$E^2 = A + B (U_N^2 + k^2 U_T^2 + h^2 U_B^2)^{n/2} \quad (4.6)$$

Through Reynolds decomposition the velocity components can be expressed by the mean and fluctuating components represented by the ‘over-bar’ and the ‘prime’ symbols respectively. If the incoming velocity vector is normal to the sensor wire then the response reduces to a simpler system, as shown in figure 4.1, where Q represents the velocity vector and it could be substituted by the freestream velocity during calibration. By ensuring that the hot wire was aligned normal to the freestream flow inside the wind tunnel and assuming that the flow was uniform in that region, the tangential, U_T , and the binormal velocity component, U_B , could be neglected and hence the normal component, the hot

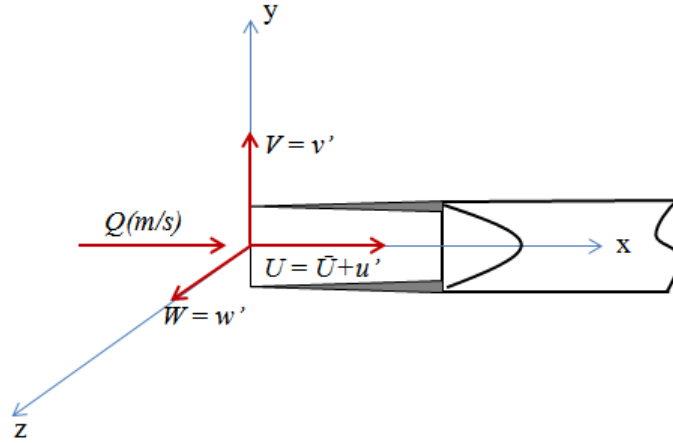


Figure 4.1: Response of the hot wire probe with a velocity vector normal to the sensor wire, figure adapted from Bruun [21], p.84

wire response reduces to

$$E^2 = A + B \left((\bar{U} + u')^2 + k^2 v'^2 + h^2 w'^2 \right)^{n/2} \quad (4.7)$$

In a wind tunnel with moderate freestream turbulence intensity, the transverse and normal fluctuating components are negligible in the freestream flow and the response can be further simplified to

$$E^2 = A + B \bar{U}^n \quad (4.8)$$

This response equation was employed during the calibration of the SN probe, which was aligned along the wind tunnel centreline axis and normal to the freestream velocity. It was also used during the measurement of the spanwise velocity component at the attachment line of the wind tunnel model where the chordwise velocity component is zero. More detail of the calibration of both the SN together with the method used to extract the velocity from the hot wire voltage output will be presented in the sections that follow.

4.2.2 Calibration of Single-Normal Probe

The hot wire probe was calibrated by mounting it as shown schematically in Figure 4.2. A Pitot-Static probe was mounted close and parallel to the hot-wire support, but separated by a distance of at least 5 diameters of the Pitot tube so as ensure that no flow interference was introduced by either device. Freestream air speed measurement was obtained by connecting the Pitot-Static tube to the Furness Control FC0318 differential pressure transducer, which was sent for factory recalibration and checked using a water column differential pressure manometer (distilled water) with an accuracy of $0.01 \text{ mmH}_2\text{O}$. The voltage output from the pressure transducer was fed into NI-Labview as shown in figure 3.9 and was converted into the equivalent dynamic pressure by applying the factory calibration. From the recorded dynamic pressure the freestream velocity was calculated based on the measured atmospheric pressure and temperature and the hot-wire voltage output was recorded simultaneously with the change in air speed during the calibration.

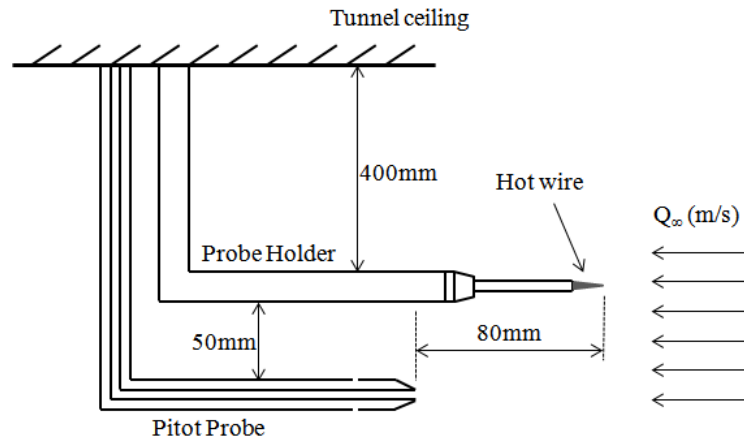


Figure 4.2: Schematic representation of the hot wire probe mounted along the tunnel centre-line for calibration.

$$E^2 = A + BQ_\infty^n \quad (4.9)$$

In this case, the hot wire response could be expressed by equation 4.9, where Q_∞ represents the freestream velocity. Following the calibration run which was conducted both

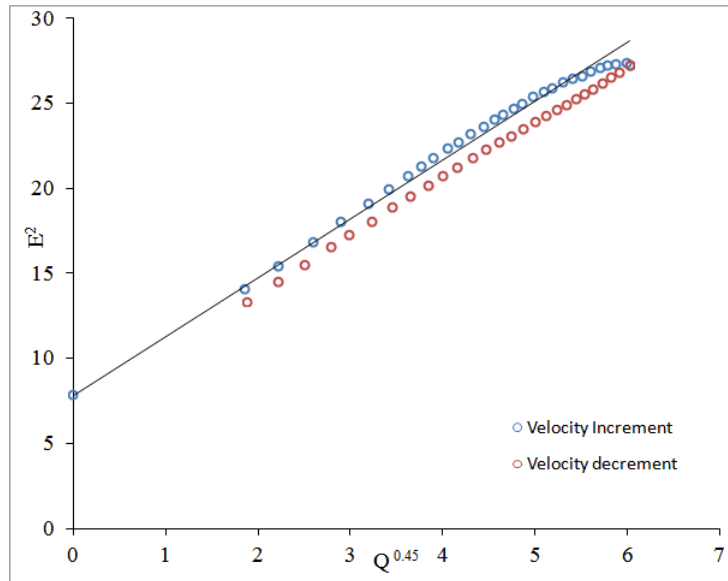


Figure 4.3: The Power law relation expressed by equation 4.6

with increasing and decreasing velocity (identified as velocity increment and velocity decrement cases) the two empirical coefficients A and B were determined by plotting the square of the hot wire voltage output, E^2 , against the corresponding freestream velocity, Q to the power of n , where $n = 0.45$. This result is presented in figure 4.3 for a velocity range of 4 to 55 m/s, where the data for both the velocity increment and velocity decrement have been plotted.

4.2.3 Correction for Temperature Drift

Considering the results from the velocity increment test, for freestream velocities less than 35 m/s one can observe that the voltage output increases linearly with an increase in the freestream velocity, but starts to deviate slightly at higher velocities. On the other hand, the result for the velocity decrement case demonstrates a better linear relation for the whole velocity range but is not in agreement with the velocity increment case. From Figure 4.4, which shows the change in the temperature of the ambient air inside the wind tunnel working section with the variation in tunnel speed during the calibration test, at $Q > 35$ m/s the temperature increases rapidly with further increase in velocity. Nevertheless, once the maximum velocity was reached and the calibration was undertaken for

the velocity decrement, a hysteresis was present between the two results and the drop in temperature was considerably less in comparison with the temperature rise during the velocity increment case.

This is a clear indication that the drift in the temperature of the ambient air in the wind tunnel had an effect on the hot wire voltage output. The operational resistance, R_w , set initially is dependent on the R_{20} and α_{20} and their values are specified by the manufacturer at a temperature of $20^\circ C$. Any significant fluctuations in ambient temperature, as observed during the calibration, would also result in a change in R_w . In addition, the heat transfer between the wire and the incoming stream of air would decrease slightly due to a reduction in the temperature difference between the two, thus resulting in a small reduction in the output voltage. In order to compensate for the errors introduced by temperature drift the method for temperature correction given by equation 4.10, initially formulated by Collis and Williams [28] and later modified by Abdel-Rahman et al. [1] was employed. By plotting the term on the left-hand side of equation 4.10 with respect to Re^n , computed from the calibration data, the values of A and B were determined.

$$Nu \left(\frac{T_m}{T_a} \right)^a = A + BRe^n \quad (4.10)$$

From equation 4.10, T_a , represents the freestream ambient temperature and T_m , the average of the wire temperature, T_w , and the ambient temperature; from Collis and Williams a is equal to -0.17 and from the hot wire response relation $n = 0.45$. The Nusselt number, Nu , and the Reynolds number, Re , are same as those defined above.

The thermal conductivity, k , and kinematic viscosity, ν , of the fluid in the vicinity of the wire, which are based on the ambient fluid temperature and the mean hotwire sensor temperature, can be estimated using the relations below.

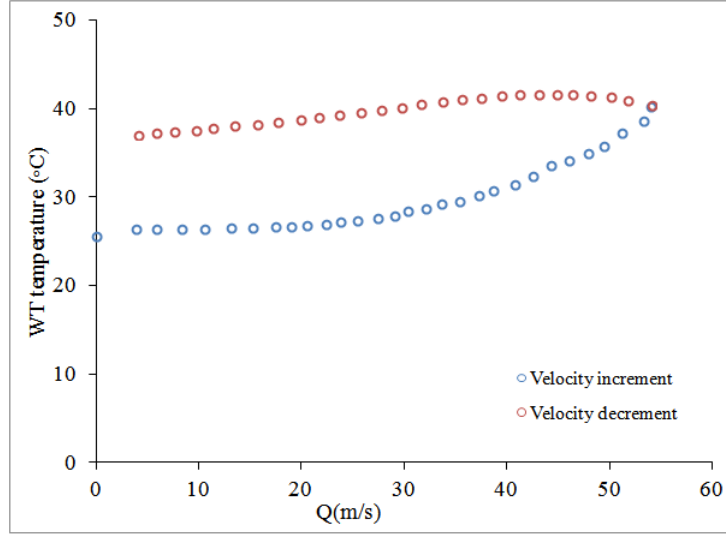


Figure 4.4: Change in the temperature of the freestream air inside the tunnel working section with respect to speed during the calibration test.

$$\frac{k}{k_a} = \left(\frac{T}{T_a} \right)^{0.86} \quad (4.11)$$

$$\frac{\nu}{\nu_a} = \left(\frac{T}{T_a} \right)^{1.9} \quad (4.12)$$

The thermal conductivity of the ambient fluid, k_a , can be estimated using the Kannu-luik and Carman relation quoted by Collis and William [28], and given by equation 4.13, where the units of k_a are $Wcm^{-1}C^{-1}$ and the viscosity can be estimated using Sutherlands law.

$$k_a = 2.41 \times 10^{-4} (1 + 0.00317T - 0.0000021T^2) \quad (4.13)$$

By applying the corrections presented above, the effect of the temperature drift seems to be reduced as a closer linear relation can be observed from figure 4.5. In addition, the trend in the velocity increment and decrement show a better correlation compared to figure 4.3, both in terms of the slope and the y-intercept. However, a small discrepancy can still

be seen in the y-intercept especially in the velocity decrement case and again this shows that the correction is not 100% effective. This discrepancy was assumed to be related to the R_{20} and α_{20} , which were also affected by the significant temperature drift and further correction was introduced to determine a more accurate value of the coefficient, A .

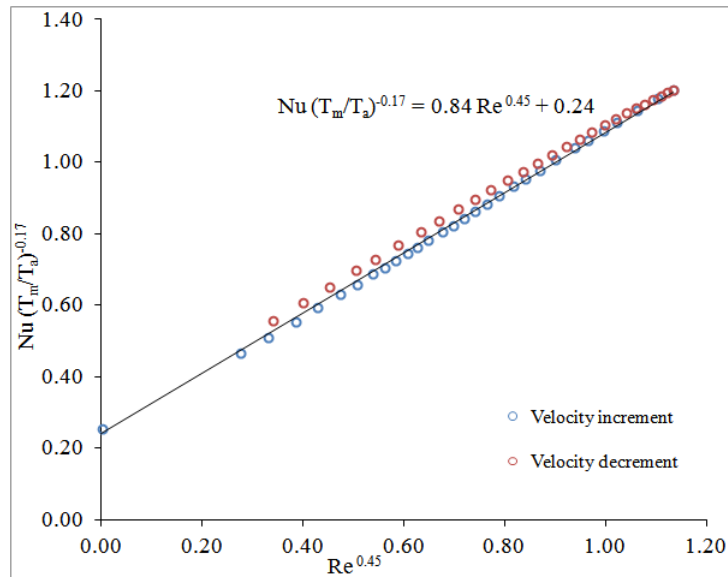


Figure 4.5: The Power law relation expressed by equation 4.10

From equation 4.10, when $Re = 0$, A is equivalent to the term on the left-hand side. By plotting the variation of A with respect to the change in the ambient air temperature inside the working section of the wind tunnel as shown in figure 4.6, a relation for the change in A with respect to temperature can be established. The results were obtained by running the tunnel at its maximum speed for a certain period of time until the ambient air inside the tunnel attained a temperature of approximately $50^{\circ}C$. Before taking any measurements the air inside the tunnel was allowed to settle for few minutes until the differential pressure transducer connected to the Pitot-static tube displayed a very small value (less 0.1 Pa) in order to ensure that there was minimum air flow due to the temperature gradient between the tunnel and the surroundings. The test was conducted twice to ensure repeatability. By plotting $Nu(T_m/T_a)^{0.17}$ with respect to variation in ambient air temperature a relation between A and change in ambient temperature was established as equation 4.14.

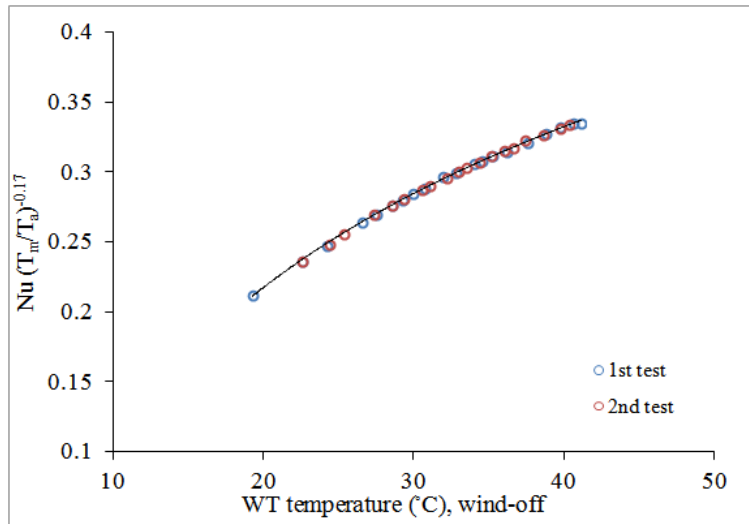


Figure 4.6: The hot-wire voltage output with change in temperature during the wind-off test

$$A = Nu \left(\frac{T_m}{T_a} \right)^{-0.17} = 0.166 \ln(T_a) - 0.28 \quad (4.14)$$

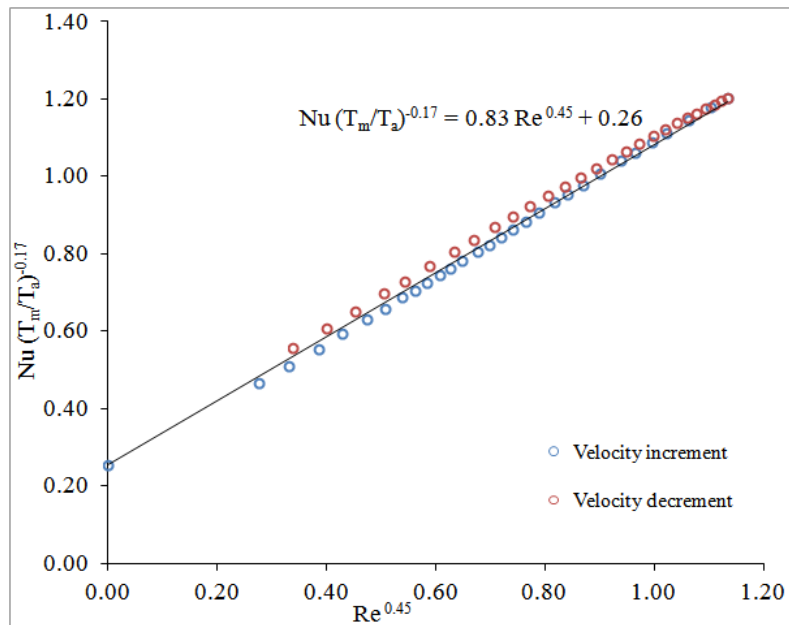


Figure 4.7: The Power law relation expressed by equation 4.10, where A has been adjusted based on equation 4.14

Using equation 4.6, A was estimated for a given ambient temperature and the y-intercept in Figure 4.5 was adjusted accordingly to give a slightly modified relation presented in Figure 4.7. Having estimated the calibration coefficients, A and B , the velocity of the air stream can be determined for a given hot wire voltage output by rearranging equation

4.10 and expressing the Re in terms of the velocity, kinematic viscosity and characteristic length based on diameter of the sensor wire.

4.3 Measurement of Two Velocity Components

4.3.1 Response of Single-Yawed Probe

Due to the presence of streamline curvature downstream of the attachment line, a system of three dimensional boundary layer will be present and thus the full response relation given by equation 4.6 applies. Hence, a more elaborate calibration and velocity analysis procedure is required. Figure 4.8 is a schematic representation of the response of the hot wire in three dimensions.

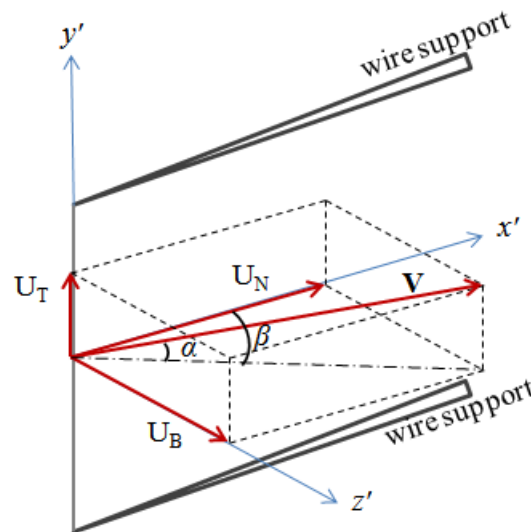


Figure 4.8: Break-down of the velocity components based on the hot-wire sensor coordinates system, figure adapted from Bruun [21], p.72

From the summary of previous studies on measurement using SY or yawed SN probes presented by Bruun [21], if yawing the wire with respect to the oncoming flow, the response of the hot wire becomes dependent on both the normal, U_N , and tangential, U_T , velocity components. Assuming that the wire remains in the $x' - y'$ (see figure 4.8) plane in which case the bi-normal component, U_B , can be assumed to be zero as $\beta = 0^\circ$. In this

case, the effective velocity in equation 4.5 can be expressed as

$$V_e^2 = U_N^2 + k^2 U_T^2 \quad (4.15)$$

Following Bruun, the hot wire response can be written as

$$E^2 = A + B \left(f(\alpha) \tilde{V} \right)^n \quad (4.16)$$

where the effective velocity,

$$V_e = \tilde{V} f(\alpha) \quad (4.17)$$

Where $f(\alpha)$ is usually referred as the yaw function and can be expressed in terms of the yaw angle, α , and various functions involving the yaw coefficients, k , m , b , α_e and ϵ

$$f(\alpha) = \begin{cases} (\cos^2 \alpha + k^2 \sin^2 \alpha)^{1/2} \\ \cos^m \alpha \\ [1 - b(1 - \cos^{1/2} \alpha)]^2 \\ \cos \alpha_e \\ \cos \alpha + \epsilon(\cos \alpha - \cos 2\alpha) \end{cases} \quad (4.18)$$

The sources from which these yaw functions were obtained have been quoted by Bruun [21] and, from the study conducted by Bruun and Tropea [23], using the first three yaw functions listed in equation 4.18 the behaviour of the yaw coefficients, k , m and b with varying yaw angle, for four different types of probe, have been duplicated in figure 4.9. For all four probes, the yaw coefficients, m and b , stayed constant for $20^\circ < \alpha < 70^\circ$ but, for a similar range of yaw angle, k varied inversely between 0.40 to 0.15, except the

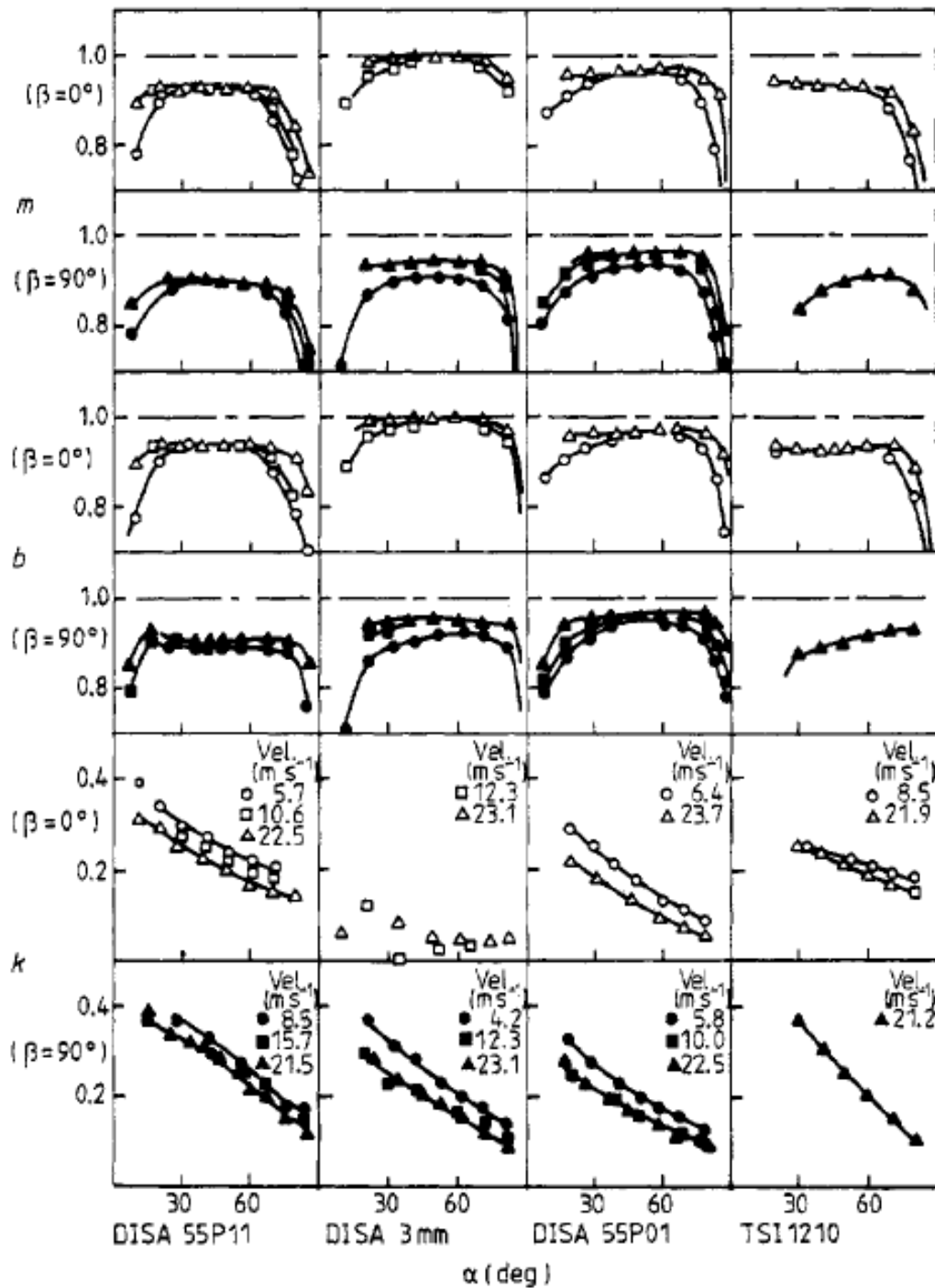


Figure 4.9: Variation of the yaw coefficients with changes in the yaw angle at $\beta = 0$ and $\beta = 90^\circ$, from Bruun [21]

‘DISA 3mm’ probe when pitched at $\beta = 0^\circ$ where there was no concise trend with α . In general the coefficients did not show large deviation at moderate velocities, however a slight variation could be observed at velocities less than $8m/s$ which might be due to the response of hot wire starting to deviate from the power law. This is commonly observed

during hot wire calibrations at low speeds.

For the current study the first yaw function, $f(\alpha) = (\cos^2 \alpha + k^2 \sin^2 \alpha)^{1/2}$, which was also the method preferred by Hinze [60], and the fourth function, $f(\alpha) = \cos \alpha_e$, proposed by Bradshaw [16] based on the ‘cosine law for the effective cooling velocity’, were chosen for further investigation. Prior to any velocity measurement the SY probe had to be calibrated both for velocity and yaw to determine the coefficients of the two yaw functions chosen. More details about the calibration process and calculation of the velocity components follow below.

4.3.2 Calibration of a Single-Yawed Probe

The set-up and process for calibrating the SY probe was more involved in comparison to that of the SN probe introduced earlier in section 4.2.2. Due to the additional yaw calibration, the SY probe was mounted to a six component balance fitted to the roof of the T2 wind tunnel test section as shown in Figure 4.10. The balance was equipped with a stepper motor and gearing mechanism that could generate a rotation about the vertical axis with an accuracy of $\theta = \pm 0.1^\circ$ and was used to yaw the SY probe with respect to the incoming freestream velocity. The probe was mounted in such a way that the wire lay in the horizontal plane and when the balance yawing mechanism was set to zero ($\theta = 0^\circ$), the wire was yawed to the freestream flow with the nominal yaw angle, $\bar{\alpha} \approx 45^\circ$ specified by the manufacturer. The actual yaw angle was expressed as

$$\alpha = \bar{\alpha} + \theta \tag{4.19}$$

Based on the sign convention chosen, positive yaw was assigned to the clockwise direction which, was towards starboard and negative yaw (anticlockwise) towards the port side of the test section. Thus, when $\alpha = 45^\circ$ or $\theta = 0^\circ$ the wire was considered to be yawed

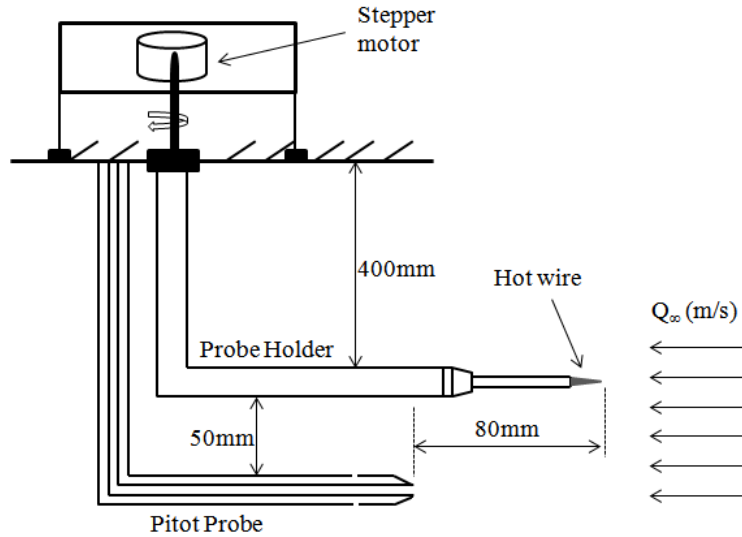


Figure 4.10: Schematic representation of the hot wire probe mounted along the tunnel centre-line for calibration and connected to the six component balance for yaw calibration

in the clockwise direction and, by rotating the probe about its axis by 180° , it could be brought into the anticlockwise direction, where the yaw angle, $\alpha = -45^\circ$.

From Bruun [21], equation 4.16 can be re-expressed as equation 4.20 below to account for the yaw effect on the probe.

$$E^2 = A + \hat{B}(\alpha) \tilde{V}^n \quad (4.20)$$

where,

$$\hat{B}(\alpha) = Bf(\alpha)^n \quad (4.21)$$

When accounting for the correction due to temperature drift

$$Nu \left(\frac{T_m}{T_a} \right)^a = A(T_a) + \hat{B}(\alpha) \tilde{Re}^n \quad (4.22)$$

Initially the velocity calibration was conducted using the process outlined in section 4.2.2, for both the clockwise and anticlockwise orientation, by setting $\theta = 0^\circ$. The relation given by the response equation 4.22, which accounts for the temperature drift as well, has been plotted in figure 4.11 for the calibration in both the clockwise and anticlockwise directions, where $n = 0.45$. From this result the calibration constant, $\hat{B}(\alpha)$, was estimated for $\bar{\alpha} = \pm 45^\circ$. While comparing these two values a percentage difference of less than 0.5% can be observed; this demonstrated that $\bar{\alpha}$ could be assumed 45° . Repeating the procedures outlined in section 4.2.3, a relation for the constant, A , was derived similar to equation 4.14. This would provide a method of accounting for the temperature drift as well.

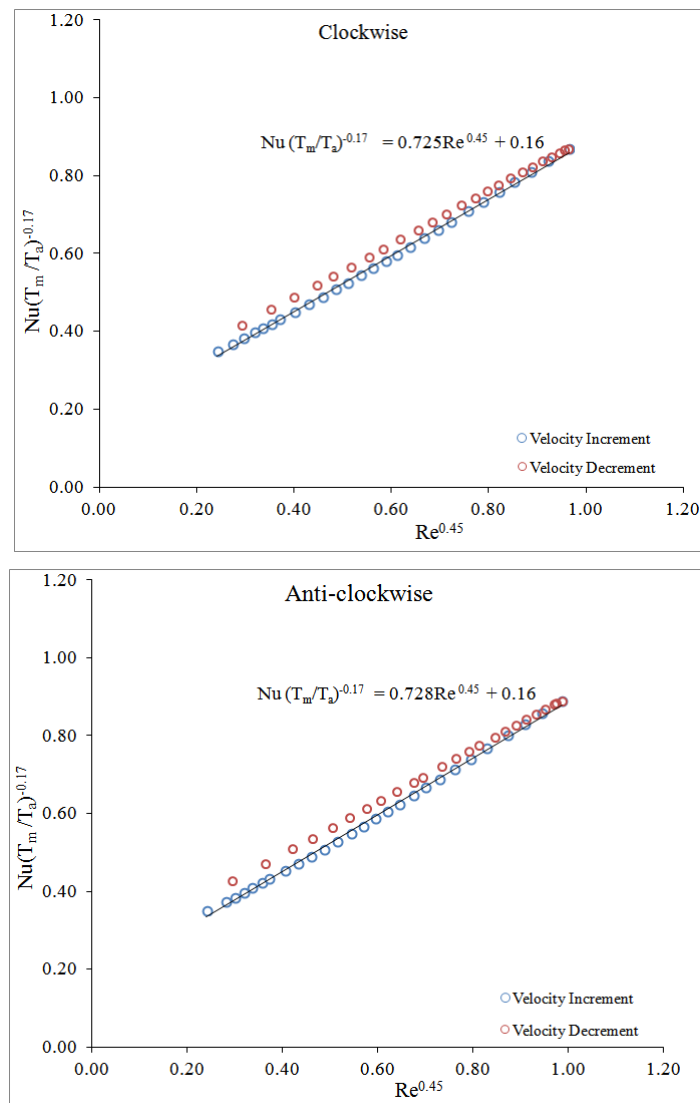


Figure 4.11: Velocity calibration of SY probe yawed by 45° in the starboard side

However, the calibration coefficient $\hat{B}(\alpha)$ is still a function of the yaw coefficients, k and α_e , due to the strong dependence on the yaw angle, so a yaw calibration is required in order to determine these yaw coefficients. According to Bradshaw [16], based on the study conducted by Friehe and Schwartz [41], the ‘cosine law’ is accurate for $0^\circ < \alpha < 60^\circ$ for infinitely long wires, in this case for small changes in θ it can be assumed that B and the yaw coefficient are stronger functions of θ than α . By making $\hat{B}(\alpha)$ the subject of the formula in equation 4.20 and, by using the nominal yaw angle of the wire, $\bar{\alpha}$ as the reference case, the hot wire response can be reduced to a function of the nominal and actual yaw angle only, as expressed by equation 4.23,

$$E_\theta = \left(\frac{E_\alpha^2 - A}{E_{\bar{\alpha}}^2 - A} \right)^{\frac{1}{n}} = \frac{f(\alpha)}{f(\bar{\alpha})} \quad (4.23)$$

Assuming the nominal yaw angle, $\bar{\alpha}$ is equivalent to α_e , therefore from the cosine-law the yaw function can be expressed as

$$f(\bar{\alpha}) = \cos(\alpha_e) \quad (4.24)$$

$$f(\alpha) = \cos(\bar{\alpha}_e + \theta) \quad (4.25)$$

By expanding equation 4.25 and substituting for $f(\alpha)$, together with $f(\bar{\alpha})$ from equation 4.24 into equation 4.23, the yaw function based on the effective yaw angle could be expressed in a linear form, $Y = aX$, by the relation

$$\cos \theta - E_\theta = \tan \alpha_e \sin \theta \quad (4.26)$$

By plotting, $\cos \theta - E_\theta$, against $\sin \theta$ the gradient of the straight line can be used to

estimate α_e (note that $\bar{\alpha}_e$ from equation 4.26 has been replaced by α_e to be consistent with equation 4.18 and the this applies to the rest of the analysis).

In Bruun [21], a similar relation for the other yaw functions, k , m and b has been presented and these were obtained from the investigation of Khan [68], where the yaw coefficient, k , which will be used for the current study, can be estimated by plotting $E_\theta^2 - 1$ against $E_\theta^2 \sin^2 \bar{\alpha} - \sin^2 \alpha$ as

$$E_\theta^2 - 1 = (1 - k^2) (E_\theta^2 \sin^2 \bar{\alpha} - \sin^2 \alpha) \quad (4.27)$$

In order to determine the yaw coefficients, calibrations at various yaw angles were conducted, while keeping the freestream speed constant using the set-up shown in Figure 4.10. During the calibration the voltage output of the hot-wire at each yaw angle ranging from $\alpha = 0^\circ$ to $\alpha = \pm 70^\circ$ was recorded and this was repeated for a set of constant speeds ranging between $5 - 40m/s$. The results obtained were used to plot the linear relations given by equation 4.26 and 4.27. Figures 4.12 and 4.13 present the relation given by equation 4.26 for the probe oriented in the clockwise and anti-clockwise direction respectively. Similarly, the relation given by equation 4.27 has been expressed in Figures 4.14 and 4.15.

The gradients of the lines of best fit from these plots were used to calculate the yaw coefficients, α_e and k , for a range of air speed and are presented in Figures 4.16 and 4.17 respectively. From Figure 4.16, the difference in the yaw coefficient, α_e , between the clockwise and the anticlockwise run was approximately 2%, except at $20m/s$ where the difference had doubled. But, the prime observation is the independence of α_e from velocity for $Q > 10m/s$. The small deviation at $Q < 10m/s$ might be associated with the discrepancies due to the hot wire response drifting from the power law which is usually observed during low speed calibrations, and which can be improved using spline or polynomial fit techniques.

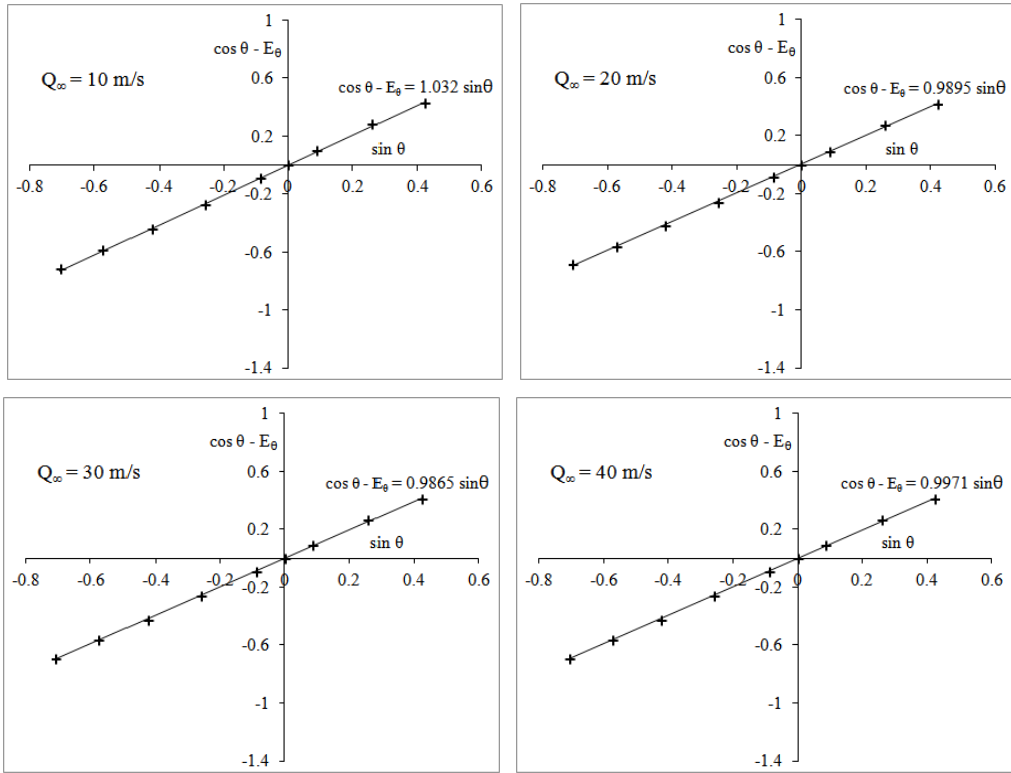


Figure 4.12: Yaw calibration of the SY probe at constant velocity with the probe initially orientated in the clockwise direction, for the estimation of α_e .

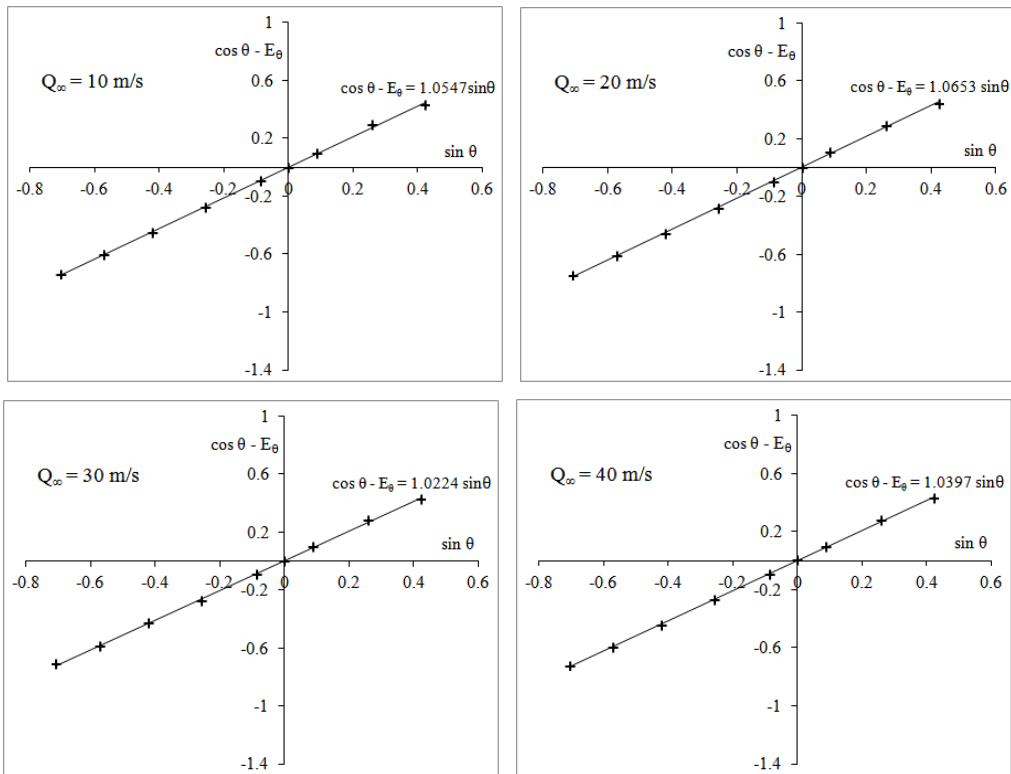


Figure 4.13: Yaw calibration of the SY probe at constant velocity with the probe initially orientated in the anti-clockwise direction, for the estimation of α_e .

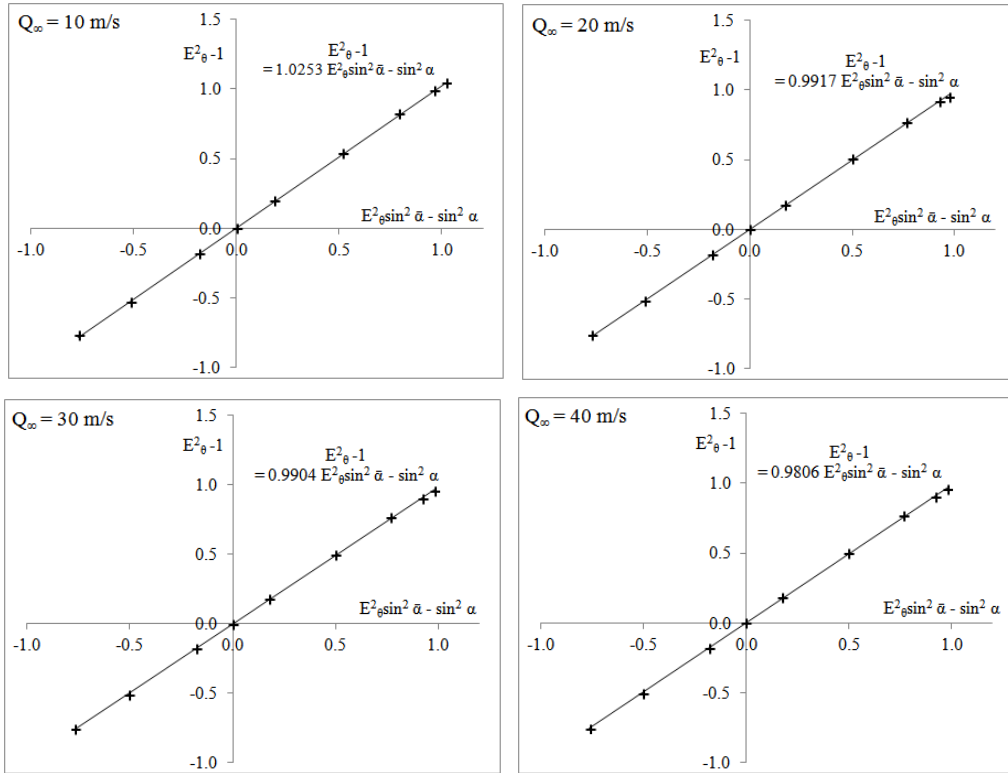


Figure 4.14: Yaw calibration of the SY probe at constant velocity with the probe initially orientated in the clockwise direction, for the estimation of k .

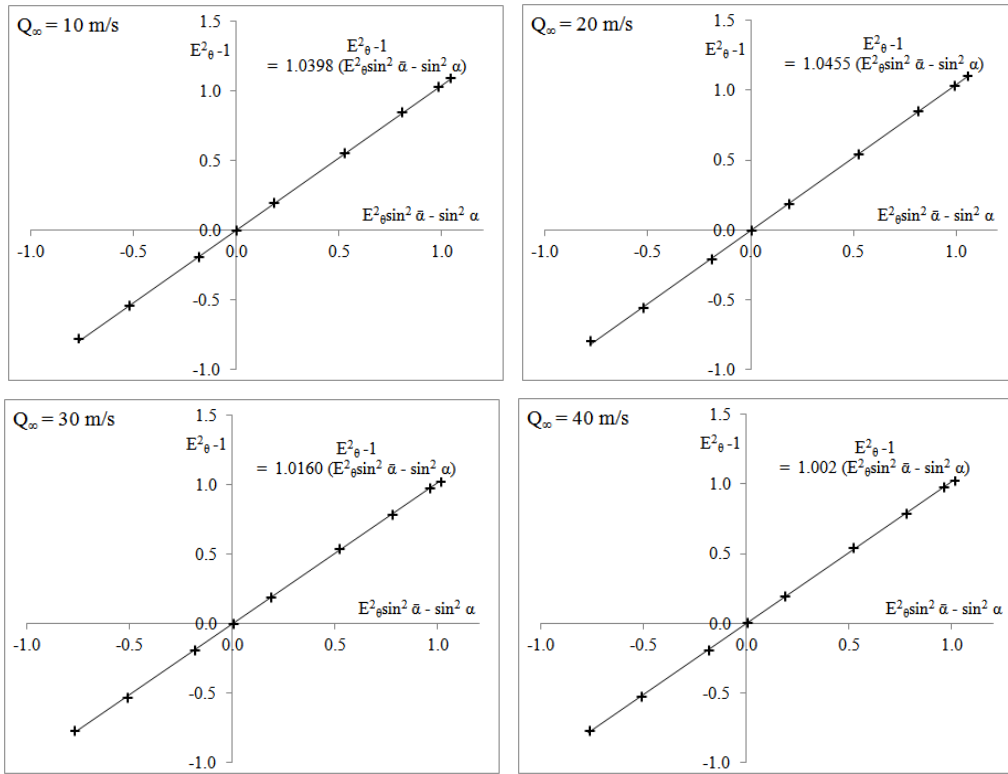


Figure 4.15: Yaw calibration of the SY probe at constant velocity the probe initially orientated in the anti-clockwise direction, for the estimation of k .

However, in Figure 4.17 there is a large scatter in the results for k^2 compared to those for α_e in Figure 4.16. This results in a significantly larger difference between the clockwise and anticlockwise calibrations. The anticlockwise case could be considered the more inferior as k^2 was negative for the whole velocity range. According to Bruun [21] the main source of discrepancy while estimating k is due to the strong dependence of the calibration coefficient A and n on the yaw angle. Negative values of k^2 have been observed during other experimental investigations as well. But further elaborate calibrations conducted by Bruun et al. [22] demonstrated that, if the discrepancies arising from the actual yaw angle, α , were reduced, the calibration should result in only positive k^2 . Still, small errors arising from the nominal yaw angle, $\bar{\alpha}$ would yield larger discrepancies in k and it was difficult to measure $\bar{\alpha}$ of the SY probe.

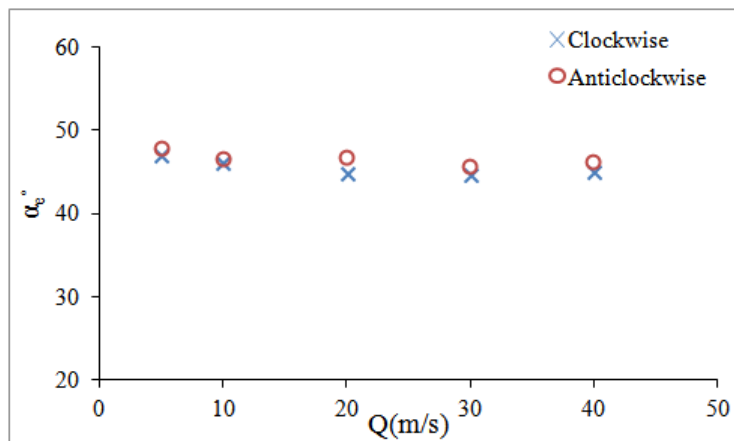


Figure 4.16: The variation of α_e with speed

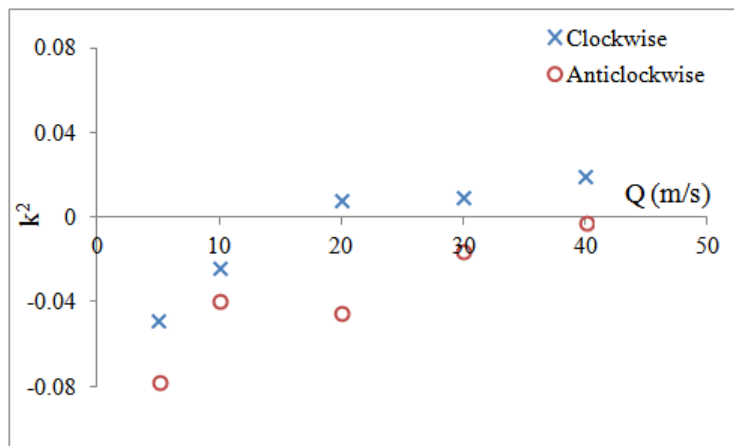


Figure 4.17: The variation of k^2 with speed

4.4 Data Analysis

4.4.1 Velocity Measurement Using Single-Normal Probes

For the case of the single velocity component measurement, the process of converting the output voltage signal into the equivalent velocity is fairly simple. This can be achieved by making the effective velocity in equation 4.4 the subject of the formula and substituting for the coefficients of the power law, A and B , estimated during the calibration process into equation 4.28.

$$V_e = \left[\frac{E^2 - A}{B} \right]^{\frac{1}{n}} \quad (4.28)$$

If the effect of temperature drift is accounted for, then by expressing the Re in terms of velocity in 4.10 and rearranging the equation, the velocity can be determined from equation 4.29.

$$V_e = \left[\frac{Nu \left(\frac{T_m}{T_a} \right)^a - A}{B} \right]^{\frac{1}{n}} \times \frac{\nu}{d_w} \quad (4.29)$$

4.4.2 Velocity Measurement Using Single-Yawed Probes

However, the process of extracting the velocity component from the measurement made using the SY probe was more involved due to coupling between various velocity components governing the response of the hot wire as shown in figure 4.8 (where $\alpha' = \bar{\alpha}$). The response of the SY probe can be reduced to the system shown in Figure 4.18 for both clockwise and anticlockwise directions.

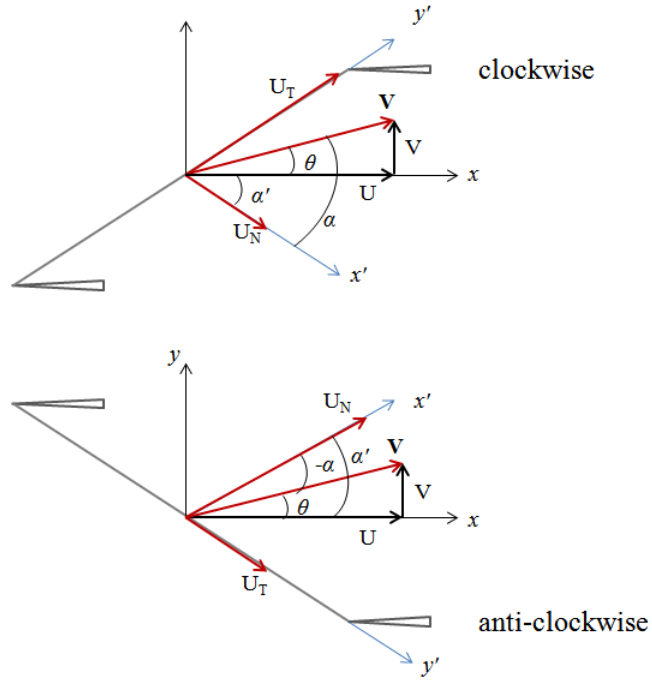


Figure 4.18: Illustration of the response of an SY probe to the velocity vector both in the clockwise and anti-clockwise orientation

Through vector transformation the response of the hot wire for the clockwise orientation could be expressed as

$$U_N = U \cos \alpha_1 + V \sin \alpha_1 \quad (4.30a)$$

$$U_T = -U \sin \alpha_1 + V \cos \alpha_1 \quad (4.30b)$$

and in the anticlockwise orientation

$$U_N = U \cos \alpha_2 + V \sin \alpha_2 \quad (4.31a)$$

$$U_T = -U \sin \alpha_2 - V \cos \alpha_2 \quad (4.31b)$$

Assuming that the binormal component, U_B , is negligible, by substituting for the corre-

sponding velocity component from equation 4.30 into equation 4.5 and considering the yaw function k , in the clockwise orientation the effective velocity can be represented in the form

$$V_{e_1}^2 = U^2 (\cos^2 \alpha_1 + k_1^2 \sin^2 \alpha_1) + V^2 (\sin^2 \alpha_1 + k_1^2 \cos^2 \alpha_1) + UV (1 - k_1^2) \sin 2\alpha_1 \quad (4.32)$$

and in the anticlockwise orientation as

$$V_{e_2}^2 = U^2 (\cos^2 \alpha_2 + k_2^2 \sin^2 \alpha_2) + V^2 (\sin^2 \alpha_2 + k_2^2 \cos^2 \alpha_2) - UV (1 - k_2^2) \sin 2\alpha_2 \quad (4.33)$$

where $V_{e_1}^2$ and $V_{e_2}^2$ represent the effective velocity and α_1 and α_2 the nominal yaw angle in the clockwise and anticlockwise directions respectively.

Having calculated the effective velocities using either equation 4.28 or 4.29 for both the clockwise and anti-clockwise orientation, the velocity components U and V of the flow can be calculated by solving equations 4.32 and 4.33. For the measurement of fluctuating velocity component in turbulent flows, U and V have to be expressed as the sum of the mean and fluctuating component using Reynolds decomposition, thus increasing the complexity in solving the equation. However the current experiment is limited to the measurement of the mean velocity, therefore the chordwise and the spanwise velocity components can be obtained by solving equations 4.32 and 4.33 directly using the steps summarised below.

As $\tan \beta = U/V$, by replacing for $\tan \beta$ in equations 4.32 and 4.33 and dividing the equations by $\cos^2 \alpha_1$ and $\cos^2 \alpha_2$ respectively, the equations become

$$\frac{V_{e_1}^2}{\cos^2 \alpha_1} = U^2 [\tan^2 \beta (\tan^2 \alpha_1 + k_1^2 + 2 \tan \beta \tan \alpha_1 (1 - k_1^2) + (k_1^2 \tan^2 \alpha_1 + 1))] \quad (4.34)$$

and

$$\frac{V_{e_2}^2}{\cos^2 \alpha_2} = U^2 [\tan^2 \beta (\tan^2 \alpha_2 + k_2^2 - 2 \tan \beta \tan \alpha_2 (1 - k_2^2) + (k_2^2 \tan^2 \alpha_2 + 1))] \quad (4.35)$$

Dividing equation 4.34 by equation 4.35 results in a quadratic equation in terms of $\tan \beta$

$$(A - \gamma D) \tan^2 \beta + 2(B + \gamma E) \tan \beta + (C - \gamma F) = 0 \quad (4.36)$$

where:

$$\gamma = \left(\frac{V_{e_1}}{V_{e_2}} \right)^2$$

$$A = \tan^2 \alpha_1 + k_1^2$$

$$B = \tan \alpha_1 (1 - k_1^2)$$

$$C = k_1^2 \tan^2 \alpha_1 + 1$$

$$D = \tan^2 \alpha_2 + k_2^2$$

$$E = \tan \alpha_2 (1 - k_2^2)$$

$$F = k_2^2 \tan^2 \alpha_2 + 1$$

By substituting for the corresponding coefficients, 'A', 'B', 'C', 'D', 'E' and 'F', equation 4.36 was solved and using the roots of the equation the corresponding velocity component was obtained by replacing in 4.34 or 4.35. But, if

$$(2(B + \gamma E))^2 - 4(A - \gamma D)(C - \gamma F) < 0 \quad (4.38)$$

the roots of equation 4.36 are complex conjugates and the velocity component cannot be calculated from equations 4.34 or 4.35.

However, according to Bruun [21], by applying Bradshaw's method [16] based on effective yaw angle, α_e , a simpler method for estimating the velocity components U and V can be formulated, equations 4.39 and 4.40. By substituting for the corresponding effective velocities and yaw angles obtained at the respective hot wire orientations, U and V can be calculated by solving equation 4.39 and 4.40 simultaneously.

$$V_{e1} = U \cos \alpha_{e1} - V \sin \alpha_{e1} \quad (4.39)$$

$$V_{e2} = U \cos \alpha_{e2} + V \sin \alpha_{e2} \quad (4.40)$$

During the calibration process, the accuracy in estimating the yaw coefficient, k , using the method proposed in section 4.3.2 was poor due to the large scatter in the results between the clockwise and anti-clockwise direction and also due the large number of negative k^2 values. The source of the discrepancies have been pointed out earlier, the main one being the inability to determine the nominal yaw angle, $\bar{\alpha}$, precisely where in most cases the values specified by the manufacturer were used. Moreover, the k -method also was not suitable in handling the data obtained in the region where crossflow profiles displayed both positive and negative crossflow velocities (crossover type crossflow velocity profiles), which occurred downstream of the attachment line as the method is limited to profiles where the velocity vectors were only in one directional. This became clear while solving equation 4.36, where the solutions obtained were both imaginary due to the reversal in the direction of the local velocity inside the crossflow boundary layer.

From the two methods presented, the α_e , yaw dependence method was preferred for the

current investigation as the results from the calibration showed closer repeatability in both the clockwise and anti-clockwise direction, as it was independent on the accuracy in the nominal $\bar{\alpha}$. It was also able to handle velocity profiles with reverse velocities, typical of crossflow profiles downstream of the attachment line. Independence on velocity observed during calibration was also an advantage during the measurement of the boundary layer profile as no further correction would be required to compensate for the change to very low local velocities closer to the wall.

Chapter 5

The Flow at the Attachment Line

5.1 Inviscid Flow along the Leading Edge of an Infinite Yawed Cylinder

By applying Lock's transformation to two-dimensional potential flow theory, the pressure distribution around an infinite-yawed circular cylinder can be expressed as

$$C_P(s') = \cos^2\Lambda \left[1 - 4 \sin^2 \left(\frac{2s'}{D} \right) \right] \quad (5.1)$$

Where s' , represents the axis along the circumference of the cylinder, as shown in Figure 5.1 and is a function of the angular displacement, θ , and the diameter, D , of the cylinder.

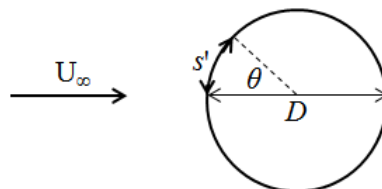


Figure 5.1: The coordinate along the circumference of a circular cylinder.

For a freestream velocity Q , the chordwise velocity component of the inviscid flow field

around the leading edge of a yawed cylinder can be represented by

$$U = k s' \cdot Q_{\infty} \cos \Lambda \quad (5.2)$$

and the spanwise component,

$$V = Q_{\infty} \sin \Lambda \quad (5.3)$$

which can be assumed to be uniform in the infinite-swept case.

For the case of zero circulation, at the attachment line, $s' = 0$, the pressure will be at its maximum value. Substituting for s' in equation 5.1 the pressure coefficient at the attachment line reduces to

$$C_{P_{AL}} = \cos^2 \Lambda \quad (5.4)$$

However, the relation given by equation 5.4 is not normally attained during experiment due to displacement effect of the boundary layer, flow separation and other effects, such as low aspect ratio leading to difficulty in reproducing the infinite swept condition. These effects alter the structure of the inviscid flowfield. The static pressure captured at the attachment line during the experiment conducted by Arnal et al. [5] on a faired circular cylinder swept at 50° , using both the surface tappings and the tapping located in the suction chamber used later for attachment line control, is presented in Figure 5.2. A deviation from the infinite-swept condition can be observed due to the spanwise pressure gradient which was more pronounced in the inboard region ($Z/D < 0.1$) as the C_p was greater than the value estimated using equation 5.4 for a geometrical sweep angle of 50° . Therefore, using the $C_{p_{AL}}$ measured experimentally, an effective sweep angle can be calculated using equation 5.5. From the $C_{p_{AL}}$ captured experimentally at each spanwise

location by Arnal et al. the corresponding effective sweep, Λ_{eff} , was determined and is represented in Figure 5.3. Again, the variation of Λ_{eff} in the spanwise direction shows that the infinite swept condition is not fully satisfied and this results in a slight spanwise variation of attachment line Reynolds number which will be elaborated later.

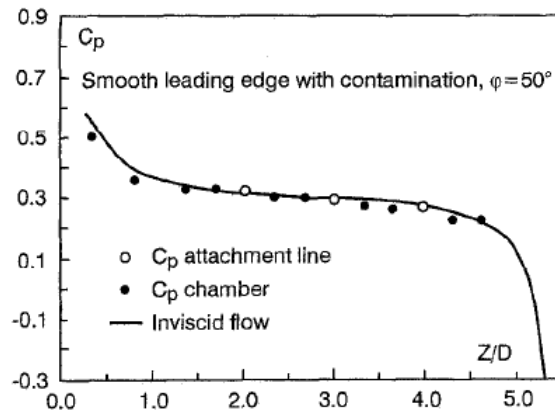


Figure 5.2: The variation of the attachment line pressure coefficient along the span of the faired cylinder tested by Arnal et al. [5]

$$\Lambda_{eff} = \cos^{-1} \sqrt{C_{P_{AL,expt}}} \quad (5.5)$$

Unlike the flow at a two dimensional leading edge, in the presence of yaw or sweep the three-dimensional flow is more complicated and, rather than a stagnation point, an attachment line is generated as the spanwise velocity component dominates the chordwise velocity component which is zero. The fluid therefore flows along the attachment line

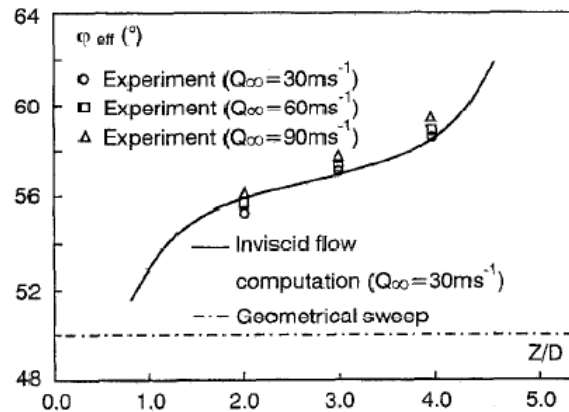


Figure 5.3: The variation of the effective sweep angle along the normalised span of the model tested by Arnal et al. [5] with geometric sweep of 50°

with a series of bifurcations as shown in Figure 5.4 as the chordwise velocity increases the streamline turns towards the direction of the freestream. As with other viscous fluid, a boundary layer forms at the surface. In order to characterise the viscous flow along the attachment line, the approach presented by Cumpsty and Head [35] has been adopted. We assume that the flow along the attachment line of an infinite swept leading is dependent on the sweep angle, freestream velocity, leading edge radius and the fluid properties such as the density and viscosity. Following dimensional analysis the quantities at the attachment line can be defined by the single parameter,

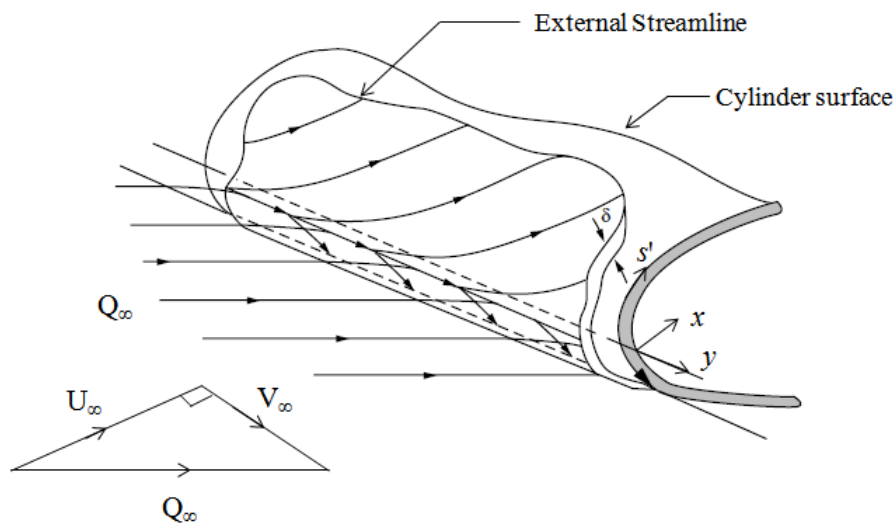


Figure 5.4: The flow at the frontal part of a yawed cylinder which is a similar representation of the flow at the leading edge of a swept wing, figure adapted from Poll [92] and Joslin [66].

$$C^* = \frac{V_\infty^2}{\nu_\infty \frac{dU_e}{ds'}} \quad (5.6)$$

However, from Poll's [92] analysis, the form below was chosen:

$$\bar{R} = \frac{V_\infty \eta}{\nu_\infty} = C^{*1/2} \quad (5.7)$$

where the η is a viscous length scale, similar to that used in Hiemenz flow analysis and defined by

$$\eta = \left[\frac{\nu_{\infty}}{\left. \frac{dU_e}{ds'} \right|_{s'=0}} \right]^{1/2} \quad (5.8)$$

From equation 5.7, the attachment line has been characterised purely by the chordwise velocity gradient of the inviscid flow field at the leading edge which is in turn strongly governed by the geometry of the leading edge and the sweep angle. Therefore, from Gaster [45] and later Poll [92], \bar{R} can be expressed as a function of the freestream flow velocity, sweep angle and LE radius of curvature, r .

$$\bar{R} = \left(\frac{V_{\infty}^2 c}{\nu_{\infty} U_{\infty} U_1} \right)^{1/2} \quad (5.9)$$

where the pressure gradient parameter, U_1 , at the leading edge of the cylinder, can be expressed as

$$U_1 = \frac{c}{U_{\infty}} \left[\frac{dU_e}{ds'} \right]_{s'=0} = \frac{c}{U_{\infty}} \cdot \frac{2U_{\infty}}{r} \quad (5.10)$$

and can be further reduced to

$$\bar{R} = \left[\frac{Q_{\infty} r \times \sin \Lambda \tan \Lambda}{2\nu_{\infty}} \right]^{1/2} \quad (5.11)$$

For a general elliptical shape it takes the form of

$$\bar{R} = \left[\frac{Q_{\infty} r \times \sin \Lambda \tan \Lambda}{\nu_{\infty} (1 + \epsilon)} \right]^{1/2} \quad (5.12)$$

where, ϵ , is the ellipticity of an equivalent ellipse.

5.2 The Attachment Line Boundary Layer

The attachment line boundary layer can be considered as the origin of the three dimensional boundary layer system on a swept cylinder or wing. The dominance of the spanwise velocity component at the attachment line causes the surface shear stress to act in the spanwise direction and the flow behaves similar to the viscous flow along a flat plate. On a flat plate the thickening of the boundary layer is a result of an increase in momentum-flux deficit as a result of the surface shear stress which acts to slow the fluid near the wall. But, in the case of the attachment line, the boundary layer thickness remains constant in the spanwise direction as long as the flow does not deviate significantly from the infinite-swept assumption. Unlike the flow along a flat plate, the loss in spanwise momentum is realised in the outflow in the chordwise direction which also balances the skin friction, rather than the spanwise flow development.

In the context of a viscous flow the attachment line is more suitably characterised by

$$R_{\theta_{AL}} = \frac{V_e \theta_{11}}{\nu_\infty} \quad (5.13)$$

or

$$R_{\theta_{AL}} = \frac{\theta_{11} Q_\infty \sin \Lambda}{\nu_\infty} \quad (5.14)$$

If assuming infinite-swept conditions, the attachment line is supposed to progress straight in the spanwise direction, but on a real three dimensional wing the attachment line will tend to curve slightly due to ‘aero-elastic twist’ however the radius of curvature is considerably larger than the thickness of the attachment line and thus the effect of curvature can be neglected. According to McLean [79], even if the flow conditions vary along the attachment line, the infinite-swept assumption is still valid. This argument is supported

by McLean's numerical results shown in Figure 5.5. The solutions were obtained from a fully three-dimensional calculation with a spanwise marching scheme starting from the wing root, accounting for the change in spanwise conditions, whereas the calculations assuming infinite-swept flow were undertaken by applying local conditions at few chosen spanwise stations. Despite the significant change in the skin friction and momentum thickness, Figure 5.5, along the span, due to the change in local leading edge radius of curvature, the two methods yielded indistinguishable results. This effect is attributed to the 'local infinite-span equilibrium' established in the attachment line flow along sufficiently large wings and once again is a consequence of the local diverging streamline and skin friction both in laminar and turbulent state.

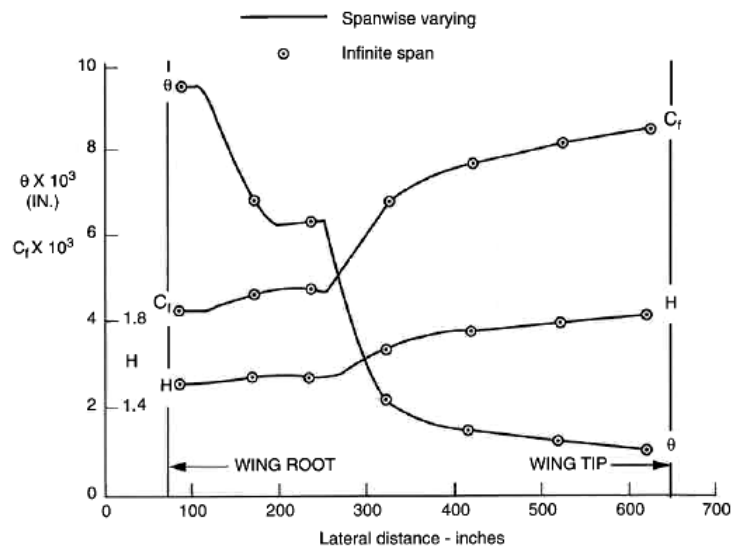


Figure 5.5: McLean's [79] numerical solutions of spanwise variation of the AL along the leading edge of a Boeing 727-200, using a fully 3D and an infinite-swept method.

Similar to the flow along a flat plate, the attachment line can be either in the laminar, intermittent or turbulent state. Earlier, two Reynolds numbers were introduced to characterise the attachment line, \bar{R} and the R_θ . Following previous investigations, if these Reynolds numbers exceed a critical values the attachment line would be susceptible to disturbances originating at the wing fuselage junction and would undergo transition at the wing root. Even in the absence of this contamination phenomenon, transition along the attachment line could be caused by 'Tollmien-Schlichting' type travelling modes disturbances which amplify rapidly, according to linear stability theory, and impose a limit on how far lam-

inarity could be maintained along the wing span. The sections that follow will provide more details about viscous characteristics of the attachment line and its behaviour.

5.2.1 Laminar Attachment Line

Similar to the method of calculating the viscous flow on a flat plate, formulated by Blasius, a method for predicting the characteristics of the viscous flow at the stagnation point of a two dimensional flow was initially proposed by Hiemenz [59] in 1911 and later in 1934 by Howarth [61]. The classical solution involves solving the governing boundary layer equations by means of a similarity transformation. From Rosenhead [98], on an infinite-swept wing all the derivatives with respect to spanwise coordinate, y , can be neglected so that the momentum equations and the continuity equation can be expressed as

$$u \frac{\partial u}{\partial x} + w \frac{\partial u}{\partial z} = U \frac{dU}{dx} + \nu \frac{\partial^2 u}{\partial z^2} \quad (5.15)$$

$$u \frac{\partial v}{\partial x} + w \frac{\partial v}{\partial z} = \nu \frac{\partial^2 v}{\partial z^2} \quad (5.16)$$

$$\frac{\partial u}{\partial x} + \frac{\partial w}{\partial z} = 0 \quad (5.17)$$

While considering the flow on an infinite-swept wedge, Cooke [30] demonstrated that Falkner-Skan approach could be employed to calculate the development of the boundary layer on an infinite-swept wing by introducing an additional ordinary differential equation, the spanwise momentum equation where the freestream flow field is represented by

$$U = U_m (x/l)^m, \quad V = \text{constant} \quad (5.18)$$

By applying similarity transformation using the independent variable

$$\eta = \left((m+1) \frac{U}{2\nu x} \right)^{1/2} z \quad (5.19)$$

with the stream function,

$$\psi = \left(\frac{2U\nu x}{m+1} \right)^{1/2} f(\eta) \quad (5.20)$$

and the spanwise viscous component,

$$v = Vg(\eta) \quad (5.21)$$

the three dimensional boundary layer equations 5.15, 5.16 and 5.17 can be transformed into a third-order ordinary differential system in the form

$$f''' + ff'' + \beta(1 - f'^2) = 0 \quad (5.22)$$

$$g'' + fg' = 0 \quad (5.23)$$

An exact solution of equations 5.22 and 5.23, can be obtained while applying the following boundary conditions

$$f = f' = g = 0 \quad \text{when} \quad \eta = 0 \quad (5.24)$$

$$f' \rightarrow 1, \quad g \rightarrow 1 \quad \text{as} \quad \eta \rightarrow \infty \quad (5.25)$$

For $\beta = 0$, equation 5.22 becomes the ordinary differential equation for Blasius flow and when $\beta = 1$, it takes the form of the Hiemenz flow for the forward stagnation point on a flat plate or circular cylinder. The solution of these governing equations, which is usually referred to as the ‘swept Hiemenz’ flow, was presented by Howarth [62] and reproduced in Rosenhead [98], where the shape factor, H , along the attachment line of an infinite swept wing was expressed as

$$H_{AL} = \left[\frac{\delta^*}{\theta} \right]_{AL} = 2.54 \quad (5.26)$$

This value is quite close to the shape factor of the flow on a flat plate, where Blasius solution yields a value of $H = 2.59$. Hence, it is fair to assume that in the spanwise direction the laminar attachment line on an infinite swept wing or cylinder behaves quite like the flow on flat plate. Figure 5.6 shows the laminar velocity profile obtained during the experimental measurements made by Gaster [45] and Poll [92], together with the swept Hiemenz flow theory where, a good agreement between the experimental results and the theory is observed. Therefore, this confirms the validity of the swept-Hiemenz theory for laminar attachment line.

From the solution of the swept Hiemenz flow expressed by equation 5.26 the attachment line Reynolds number based on the streamwise momentum thickness, θ_{AL} , can be expressed as,

$$R_{\theta_{AL}} = 0.4042\bar{R} \quad (5.27)$$

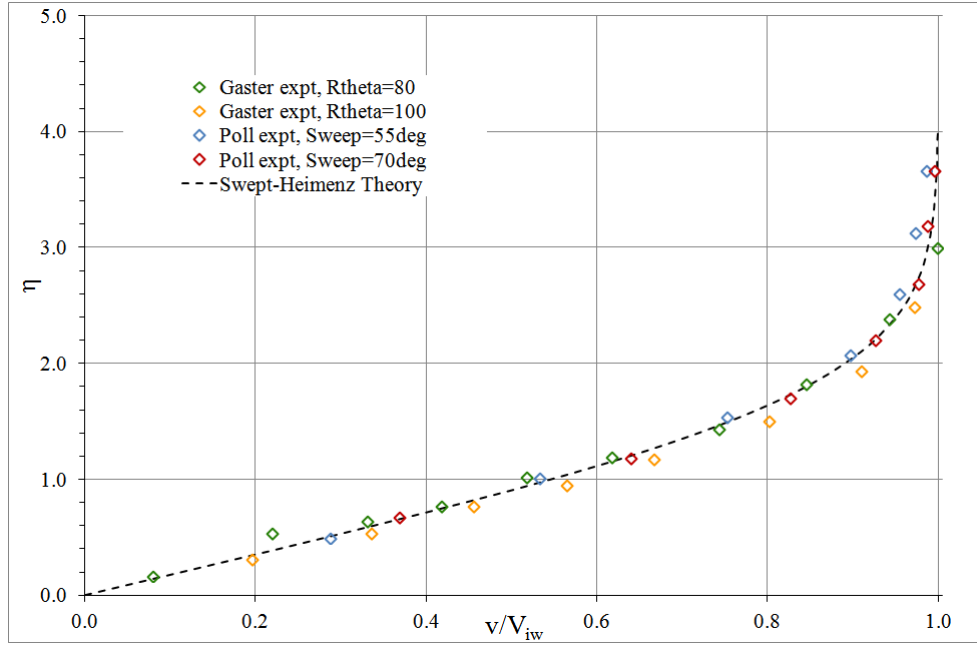


Figure 5.6: Comparison of the laminar velocity profiles measured experimentally by Gaster and Poll with the ‘swept-Hiemenz’ flow theory.

From equation 5.11 or 5.27 the attachment line Reynolds number can be determined from the known freestream velocity, viscosity and the geometrical properties of the model. By substituting equation 5.27 into equation 5.14, the attachment line momentum thickness can be expressed as a function of the Reynolds number

$$\theta_{AL} = \frac{0.4042\nu_{\infty}\bar{R}}{Q_{\infty}\sin\Lambda} \quad (5.28)$$

5.2.2 Turbulent Attachment Line

To the author’s knowledge, previous experimental studies on the turbulent attachment line are limited to the studies of Gaster [45] and of Cumpsty and Head [36] which were conducted in the late 1960s on a highly swept circular cylinder model faired to a teardrop. During both experiments a turbulent attachment line was obtained by tripping the initial laminar attachment line using two dimensional circular trip wires. Cumpsty and Head also demonstrated that the three-dimensional momentum integral method coupled with

Head's entrainment method [56], could predict the boundary layer integral quantities at the attachment line with reasonable accuracy. Later, a numerical analysis of turbulent attachment line was conducted by McLean [79] using a three-dimensional finite differencing boundary layer method coupled with an effective viscosity model for the turbulent shear stress. A comparison with Cumpsty and Head's experimental data has been presented in Figure 5.7. The two sets of data agree well except at $C^* = 3.70 \times 10^5$, or $\bar{R} = 608$, where the correlation between the experimental and computational results deviates slightly in the closer to the wall.

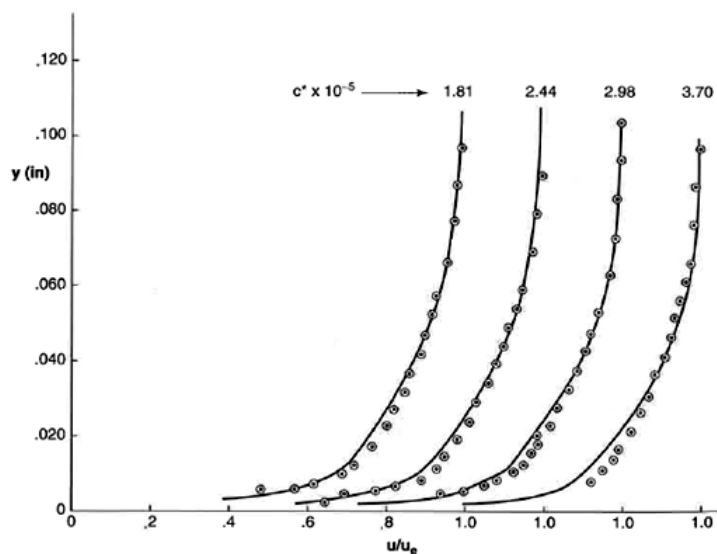


Figure 5.7: Comparison of the turbulent velocity profiles captured experimentally by Cumpsty and Head [36] (symbols) and those predicted by McLean [79] (lines) using the 3D boundary layer method.

Further numerical analysis of the turbulent attachment line was undertaken by Spalart [110], where the full Navier-Stokes equations were solved to investigate instability, turbulence and relaminarisation phenomena, while addressing the issue of attachment line contamination through suction control. See section 5.3.3 for more details about attachment line control. More recently in 2003 van Oudheusden [119] revisited the problem analytically using the method of matched asymptotic expansions. The results showed good agreement with the experimental and numerical results of Cumpsty and Head and Spalart respectively. These results have been summarised in Figure 5.8. The figure also includes the experimental result on a laminar attachment line obtained by Cumpsty and

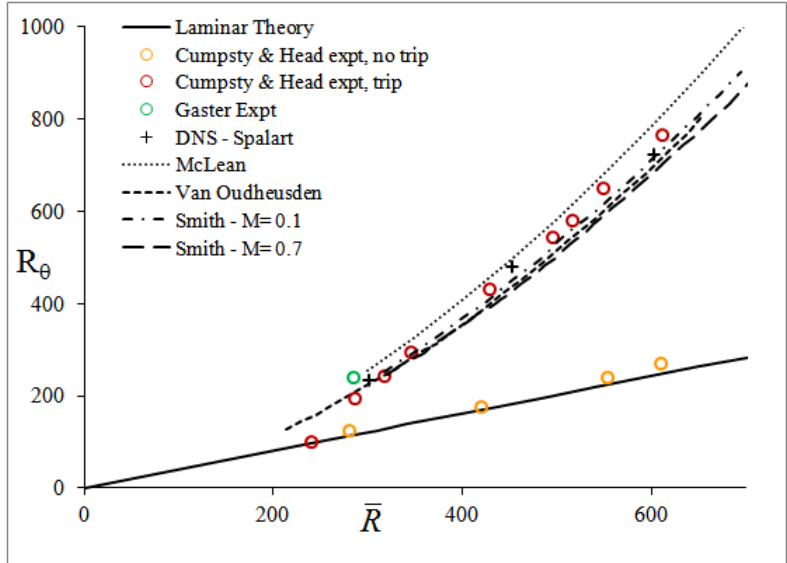


Figure 5.8: Relation between R_θ and \bar{R} established from the results of Cumpsty and Head [36], Gaster [45], Spalart [110], McLean [79], van Ouheusden [119] and Smith [109].

Head in the absence of the transition trip wire and a good agreement with swept-Hiemenz flow theory for laminar flow is shown. In general the numerical results match the experimental results except at $\bar{R} > 500$.

Most of the studies on turbulent attachment line have been limited to incompressible flow with nothing reported on turbulent attachment line flow at transonic Mach number. By applying the necessary boundary conditions at the attachment line to the three dimensional momentum integral equation, a set of governing equations was derived by Smith [109] to represent compressible flow at the attachment line. This method was also similar to the approach developed by Cumpsty and Head except for the introduction of the compressibility effect. From figure 5.8 the numerical results obtained by Smith at $M = 0.7$ deviates slightly from that of $M = 0.1$ and the difference increases for $\bar{R} > 400$.

Using Preston's [95] technique which was described in section 3.6, surface shear stress at the attachment line was measured by Cumpsty and Head and later by Poll [91] who then derived an empirical relation, given by equation 5.29 for the variation of skin friction with respect to \bar{R} , following comparison with the results of Cumpsty and Head.

$$C_f = \frac{0.0592}{\bar{R}^{0.4}} \quad (5.29)$$

The skin friction coefficient determined from the surface shear stress value has been presented in figure 5.9 together with those predicted by Spalart and van Oudheusden. The DNS results from Spalart is worst in comparison to the rest of the results, but it is within an acceptable deviation. Preston's technique is valid in the 'universal log-law' region and spurious results will be obtained if the technique is employed in laminar and intermittent boundary layers. Hence, Preston's technique can also help in identifying the state of the boundary layer. From Cumpsty and Head's measurement shown in Figure 5.9 for $250 < \bar{R} < 320$, the results deviate from the both the laminar theory and the trend in turbulent measurements implying that the boundary layer was not fully turbulent nor laminar.

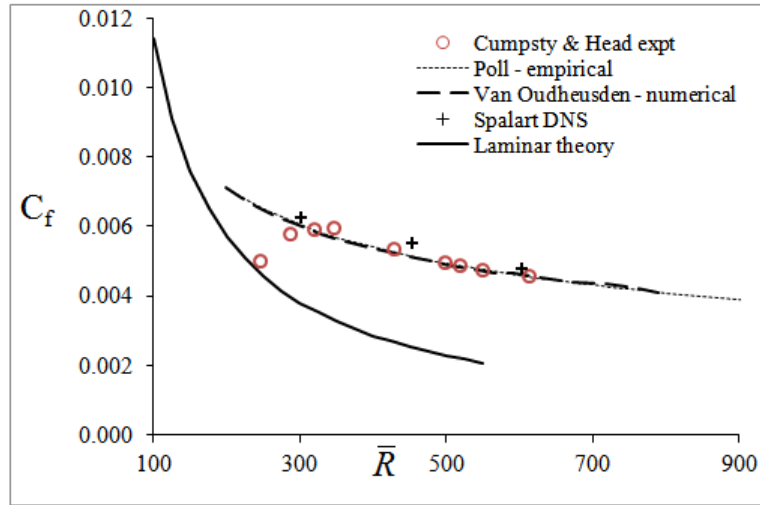


Figure 5.9: The variation of C_f with respect to \bar{R} Cumpsty and Head [36].

From the surface shear stress measurement, Cumpsty and Head represented the turbulent attachment line velocity profile in wall units shown in figure 5.10. Cumpsty and Head suggested that for $\bar{R} > 374$ ($C^* = 1.4 \times 10^5$) which was the average between the two tested cases where $\bar{R} = 316$ ($C^* = 1.0 \times 10^5$) and $\bar{R} = 425$ ($C^* = 1.81 \times 10^5$), the linear inner region tended towards the 'universal log-law, hence this regime was deemed fully turbulent. This finding was not far from the minimum Reynolds number, $R_\theta \approx$

320 (equivalent to $\bar{R} \approx 363$ from Cumpsty and Heads experiment) for a fully turbulent boundary on a flat plate proposed by Preston [96]. Despite the scatter in the experimental results and a lack of data between $\bar{R} = 316$ and $\bar{R} = 425$, according to Cumpsty and Head the minimum R_{θ} criterion established by Preston was in the region where the attachment line was still transitional as it was equivalent to $\bar{R} \approx 363$. This finding is of prime importance during the study of the attachment line and will be revisited in section 5.3, because, even if the critical condition at which disturbances start to amplify has been observed to be at $\bar{R} > 250$, based on Cumpsty and Head's observation full turbulence is not achieved until $\bar{R} > 374$. Therefore, a new regime can be defined in the region of $250 < \bar{R} < 370$ where the attachment line can be considered to be in the intermittent state and undergoing transition.

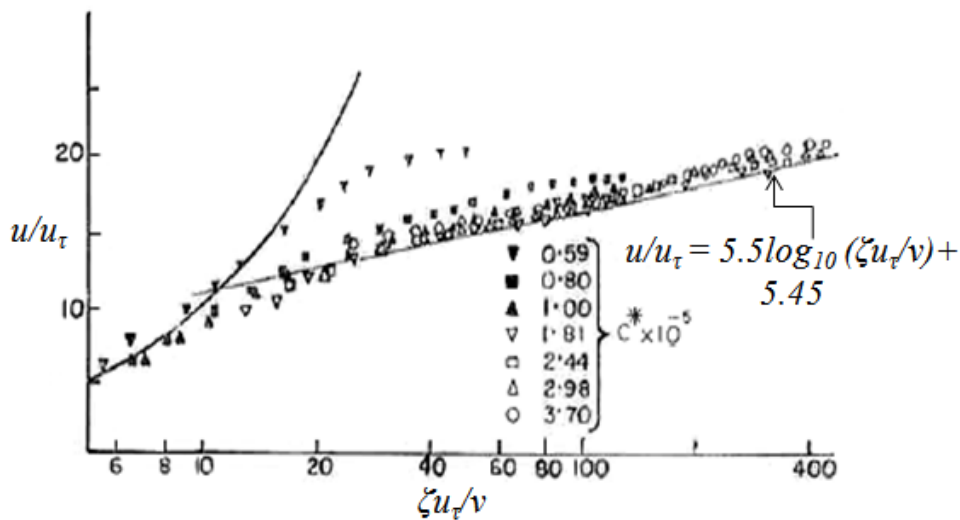


Figure 5.10: The velocity profile of the turbulent AL based on the law of the wall, by Cumpsty and Head [36].

From figure 5.11, at $M = 0.1$ a good agreement between the experimental and numerical shape-factor, H can be observed for $\bar{R} > 400$ where the attachment line is fully turbulent and tends to a value of approximately 1.4, common for turbulent boundary layers. But, at higher Mach numbers, $M > 0.3$, the shape factors calculated by Smith vary significantly from the incompressible results. This is mainly due to the way the density varies from the definitions H and \bar{H} , where both can be represented by the relation given by equation A.1, which shows that the Mach number is an influencing parameter.

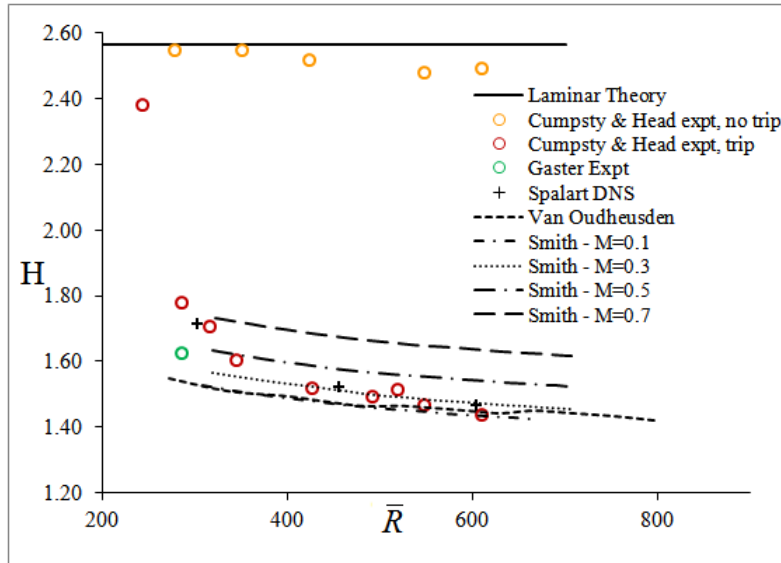


Figure 5.11: Relation between shape-factor, H and \bar{R} established by Cumpsty and Head [36], Gaster [45], Spalart [110], van Oudheusden [119] and Smith [109].

During Poll's [91] doctoral study the attachment line was investigated at hypersonic speed where a schematic representation of the flow at the leading edge of a swept cylinder mounted on a wedge and has been reproduced in figure 5.12. The main difference between the flow upstream of a swept leading edge at subsonic speed is the formation of a three dimensional cylindrical bow shock due to the contribution from the supersonic chordwise component. According to Bellone [14] who revisited the problem later in 2000, because of the presence of the cylindrical bow shock, the freestream streamline tends to curve while passing through the bow shock. Therefore the conditions at the attachment line have to be determined from local conditions inside the bow shock. This is due to the variation of the physical properties across the shock.

Bellone's study was mainly focused on developing turbulence models to analyse the severe heating at the attachment line of Reusable Launch Vehicles during their re-entry phase at very high angles of attack. The \bar{R} at the onset of transition at the Mach number based on the edge conditions of the attachment line at supersonic speed has been presented in figure 5.13. Due to the scatter in the data it is difficult to derive a relation between \bar{R} and M and Bellone recommended using a safety factor of two during the design of thermal shields. The heat transfer relation was given by the Stanton number, St , formulated

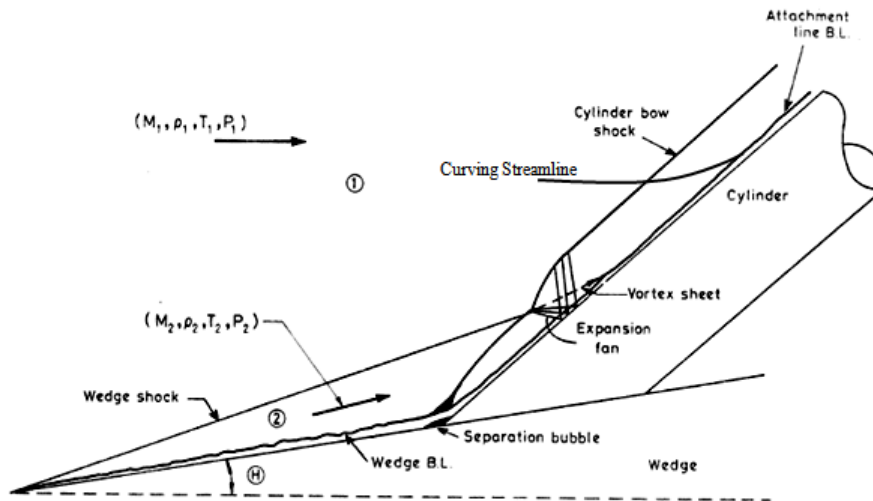


Figure 5.12: Schematic representation of the supersonic flow at the leading edge of a swept cylinder mounted on a wedge, from Poll [91].

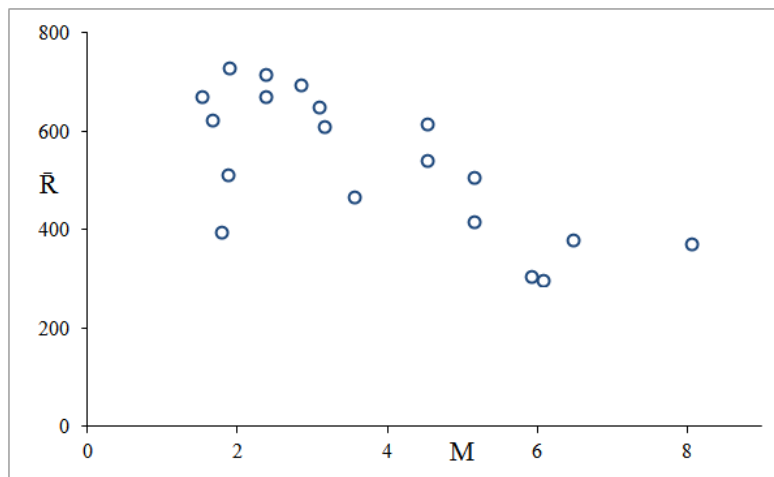


Figure 5.13: \bar{R} at the onset of transition for various Mach numbers measured at the edge of the attachment line, from Bellone [14].

using the semi-empirical skin friction relation, derived by Poll [91], given by equation 5.29. But, during the analysis of the minimum conditions for a turbulent attachment line, $\bar{R} \approx 245$ was considered rather than $\bar{R} \approx 370$ which was proposed by Cumpsty and Head.

5.3 Attachment Line Contamination and Instability

On moderate swept wings ($20^\circ < \Lambda < 40^\circ$) similar to those on commercial transonic aircraft, the disturbance arising at the wing and fuselage junction due, to the turbulent boundary layer on the fuselage, is fed into the attachment line by the dominant spanwise velocity component. This disturbance propagates along the attachment line and contaminates the rest of the flow over the wing. As a result, the flow becomes turbulent therefore rendering laminar flow control ineffective. In the early 1950s, flight tests conducted by Gray [48], [49] demonstrated the difficulty of achieving laminar flow very close to the leading edge of swept wings, and it was alleged that this was a consequence of instability within the cross-flow component of the boundary layer. Based on Gaster's [45] literature review, from the results of wind tunnel test conducted by Gregory and Walker [54], striations observed during the china-clay test demonstrated the boundary layer transitioned very close to the leading edge.

Further investigations showed that even in the absence of any large disturbances the attachment line can still undergo transition downstream along the span due to the amplification of disturbances similar to Tollmien-Schlichting type instability. This behaviour has been observed both experimentally using two dimensional roughness and numerically using linear stability theory. Fortunately, the attachment line can be decontaminated or relaminarised using both passive and active methods (shaping and suction respectively) discussed in the sections below.

5.3.1 Attachment Line Contamination

During investigations conducted by Northrop Norair and Handley Page Limited in the early 1960s, it was confirmed that the inability to obtain a laminar attachment line on moderately swept wings was a consequence of contamination from the disturbances oc-

curing at the wing and fuselage junction. Following both flight tests and wind tunnel testing by Pfenninger [89] during the 'X-21' project, Gaster [45] on a Lancaster bomber (where the Handley Page laminar flow wing was mounted on the midsection of the fuselage) and by Gregory [53], two Reynolds numbers to characterise the state of the flow at the attachment line were established, namely, the attachment line Reynolds number, $R_{\theta_{AL}}$, based on the momentum thickness and \bar{R} chosen by Poll [92], which is a function of the velocity gradient of the potential flow at the leading edge, given by equations 5.13 and 5.9 respectively. These tests showed that the attachment line will be susceptible to the contamination from turbulence occurring at the fuselage and wing junction, as shown in Figure 5.14 once the \bar{R} or R_{θ} exceeds a certain threshold value. According to Pfenninger this occurred at $\bar{R} > 245$ or $R_{\theta} > 100$ which was preferred by Gaster [45].

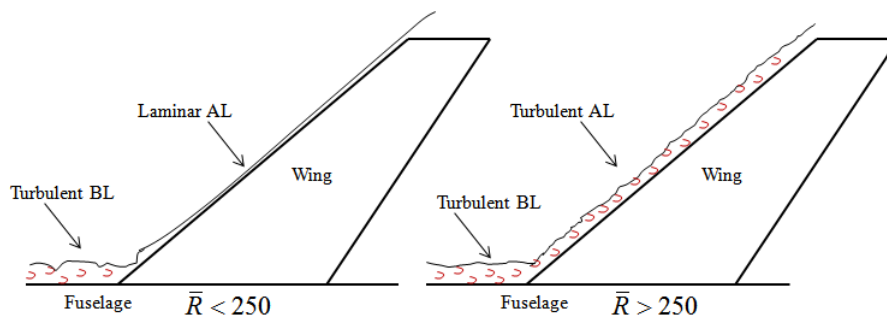


Figure 5.14: Attachment line contamination due to the presence of disturbances occurring at the wing and fuselage junction.

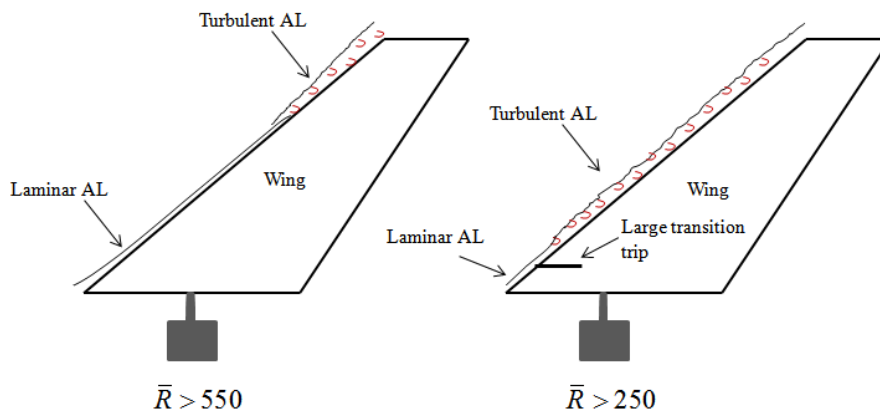


Figure 5.15: Natural transition along the span of the swept cylinder and forced transition due to the presence of a large roughness strip. Due to wing taper, in the outboard region $\bar{R} < 500$ so the figure on the left hand side should be interpreted only qualitatively.

Gaster demonstrated that, in the absence of contamination from the wing fuselage junction, disturbances caused by two dimensional trip wires, shown schematically on the right

hand side of Figure 5.15 will also provoke a similar effect, leading to transition of the attachment line. A criterion for the minimum diameter of roughness trip was established which will be detailed in section 5.3.2. Further analysis of the contaminated flow at the leading edge of swept circular cylinder was under-taken by Poll [92][91] in the late 1970's including both contamination emanating from a flat plate and cylindrical trip wires of varying diameters placed in the upstream region of the attachment line. Poll's results, summarised in figure 5.16, shows the state of the attachment line along the span, interpreted from the hot wire signals, at varying \bar{R} . At $\bar{R} \approx 300$ the hot wire signal suggested that the attachment line was fully turbulent at all the spanwise measurement stations. The turbulence spots appeared at rather low \bar{R} in the inboard region, closer to the source of contamination, as presumably the intensity of disturbance is larger closer to the source. Further downstream, at $s/\eta > 3.5 \times 10^{-3}$, where s denotes the spanwise distance along the attachment line, the first burst of turbulence occurred at $\bar{R} \approx 245$ which is in line with the criterion for the susceptibility of the attachment line to contamination. Similar observations were made in the presence of large trip wires except that in the inboard region the first burst of turbulence occurred at slightly higher \bar{R} . The results matched those from the contamination tests for $s/\eta > 3 \times 10^{-3}$.

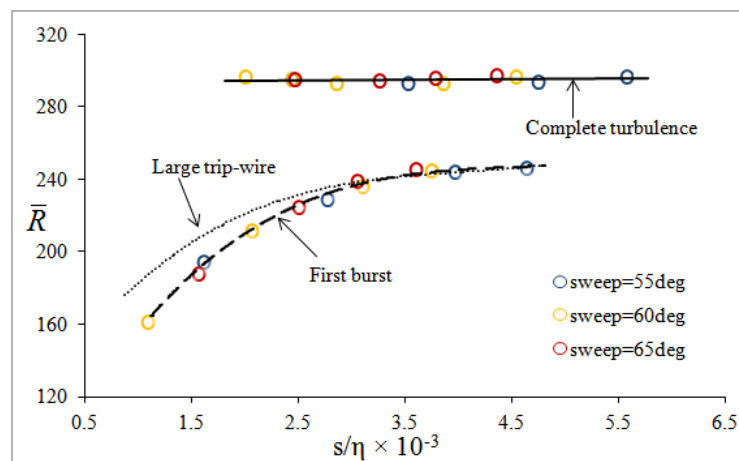


Figure 5.16: Spanwise position of where the first burst and complete turbulence were observed during the Poll's [92] experiment using trip wires to force transition.

5.3.2 Attachment Line Instability

As the attachment line is fairly similar to the boundary layer on a flat plate, any disturbance is likely to amplify in the streamwise direction and break-down to a turbulent boundary layer through the process of transition. It has to be noted that, if \bar{R} or R_θ is less than the critical contamination criterion, then the disturbances decay naturally. This particular behaviour was observed by Gaster [45] while using two dimensional disturbances, such as large cylindrical wires to trip the attachment line. The diameter of the trip wire was varied so that the critical diameter could be determined. The results are presented in figure 5.17, which shows the trip-wire diameter required at a particular tunnel speed for the attachment line transition at spanwise position. With increase in speed, resulting in the increase in attachment line Reynolds number, the curves collapse to a single relation for a minimum trip-wire diameter and Gaster proposed a relation for the critical wire diameter as the decay distance tends to zero, which can be expressed as

$$R_{d_{crit}} = 47R_{\theta_{AL}}^{\frac{1}{2}} \quad (5.30)$$

where $R_{d_{crit}}$ denotes the critical Reynolds number based on the trip-wire diameter. It was pointed out by Gaster that this finding showed closed agreement with the relation obtained for the flow on a flat plate which takes the form,

$$R_{d_{crit}} = 44R_\theta^{\frac{1}{2}} \quad (5.31)$$

Making use of an appropriately-shaped ‘bump’, which will be revisited in section 5.3.3, Gaster was able to demonstrate that the turbulent attachment line could be returned to laminar state downstream of the bump up to $R_\theta = 170$. In order to generate further insight into the break-down process of the relaminarised attachment line, a continuous

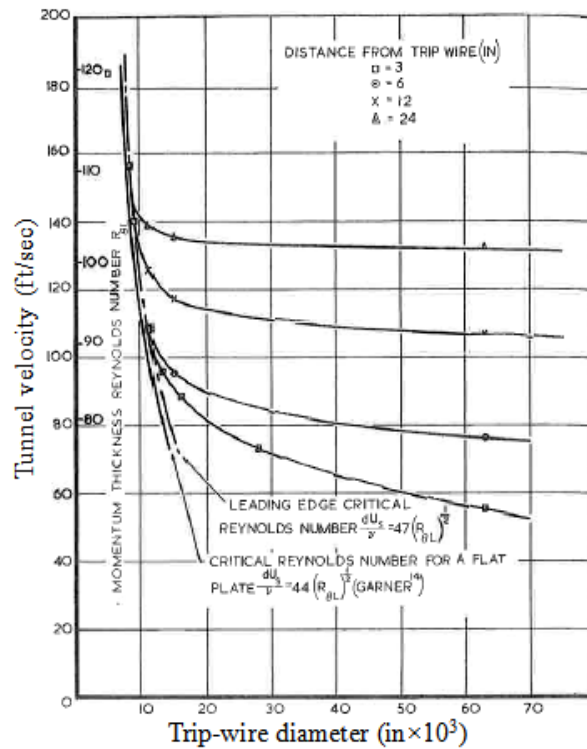


Figure 5.17: The diameter of trip wire required for attachment line transition at a given wind tunnel speed, figure from Gaster [45]

train of high-voltage sparks was generated by ignition coils to analyse the propagation of turbulent spots along the attachment line. For $R_{\theta_{AL}} > 113$ the pulses were found to expand and would contract at lower $R_{\theta_{AL}}$, but at $R_{\theta_{AL}} = 113$ the pulses remained unchanged while advancing downstream along the attachment line. As this finding was not in agreement with the critical Reynolds number for the amplification of disturbances due to contamination from trip-wire, where $R_{\theta_{AL}} \approx 100$ ($\bar{R} \approx 250$), Gaster recommended further investigation of this unusual behaviour using an untapered model with longer span.

According to Gaster, based on linear stability theory, there ought to be a limit at which a laminar attachment line would become unstable. The growth of Tollmien-Schlichting type waves were analysed by generating small amplitude sound waves emanating from earphones placed inside the model and passing through small holes drilled in the upstream region of the attachment line. It was concluded that the disturbances did not amplify over the whole span of the model for the $R_{\theta} = 170$ which was the limit at which the bump was able to ensure that the attachment line was laminar. However, Pfenninger and Bacon [90]

were able to detect experimentally the amplification of disturbances and demonstrated the presence of the linear instability waves along the attachment line for similar R_θ .

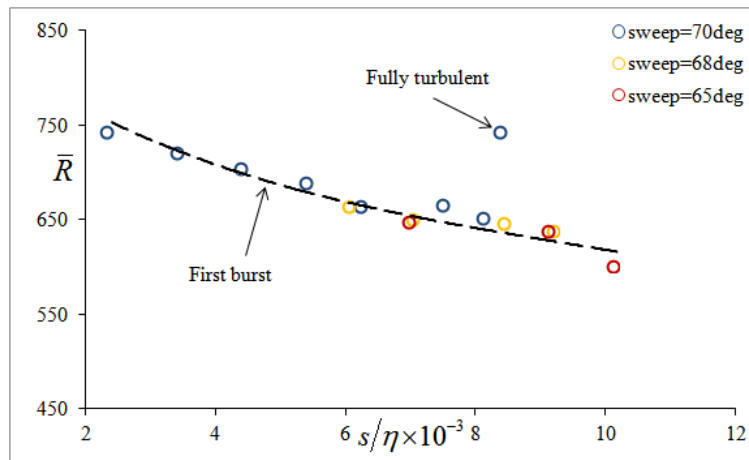


Figure 5.18: The location of free transition along the span of the swept cylinder, from Poll [92]

A further study on attachment line instability was undertaken by Poll [92][91] on a swept cylinder model with a span approximately 1.3 times longer than Gaster's. Poll demonstrated that the disturbances along the attachment line amplify as they travel downstream and that free transition can occur at higher \bar{R} in the absence of gross contamination of the type mentioned previously. Based on the signal from the hot-wire at the attachment line, from figure 5.18 at $\bar{R} > 550$ the first burst of turbulence occurred at the spanwise location $s/\eta \approx 10 \times 10^{-3}$, occurring earlier at higher \bar{R} . Complete turbulence was observed at $s/\eta \approx 8 \times 10^{-3}$ for $\bar{R} > 750$.

The investigation conducted by Gaster using cylindrical trip wires was extended by Poll, who explored a larger spanwise domain with more measurement stations. From the hot-wire signals obtained by Poll, the break-down of the laminar attachment line was classed as 'first burst' and 'complete' turbulent as shown in Figure 5.19. Poll plots \bar{R} , which is a function of both the geometry and freestream conditions, rather than a single parameter (tunnel speed) which was preferred by Gaster. The trends in both cases bear some similarities with those obtained by Gaster presented in Figure 5.17, in the sense that they tend to collapse to a single curve at a critical trip wire diameter for which spanwise decay distance tends to zero ($s/\eta \rightarrow 0$) and this effect was more pronounced for the complete turbulence

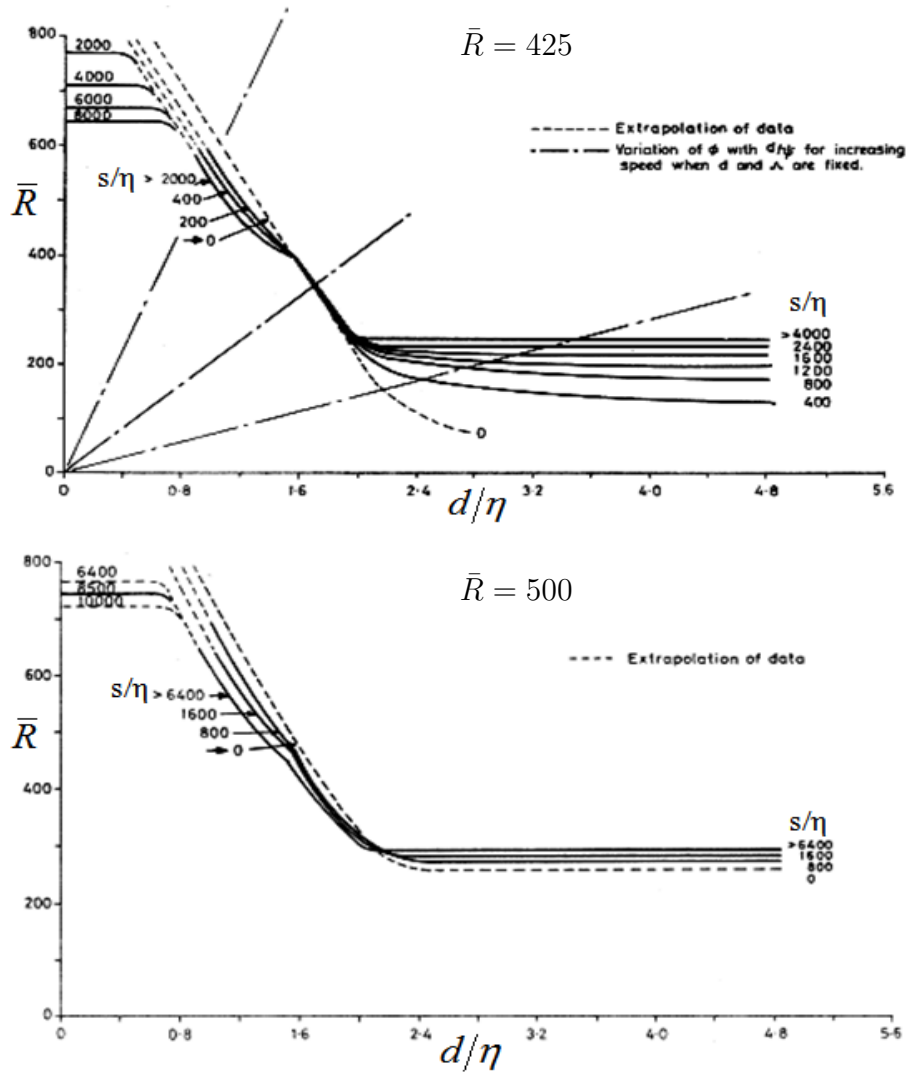


Figure 5.19: The appearance of the first burst and complete turbulence at a particular spanwise position at varying \bar{R} and trip wire diameter, from Poll [91]

case. Based on his experimental results Poll also proposed a criterion for the critical condition for a minimum trip-wire diameter for a first turbulence spot (as $s/\eta \rightarrow 0$) and fully turbulent attachment line (as $s/\eta \rightarrow \infty$), given by equations 5.32 and 5.33:

$$\bar{R} = 830 (1 - 0.35 (d/\eta)) \quad \rightarrow \text{first bursts} \quad (5.32)$$

$$\bar{R} = 890 (1 - 0.33 (d/\eta)) \quad \rightarrow \text{complete turbulence} \quad (5.33)$$

Using linear stability theory Poll was able to demonstrate that low amplitude disturbances emanating from natural sources would amplify in the spanwise direction, leading to transition of the laminar attachment line even in the absence of large disturbances. The solution was obtained by solving the governing linearised disturbance equations which can be expressed as the Orr-Sommerfeld equation while applying the parallel flow approximation. A comparison between the numerical solution and the experimental results can be seen in Figure 5.20 which shows the Reynolds number at transition at varying spanwise position for a different $n - factors$. The numerical results tend to collapse to a single curve for all the selected $n - factors$ for $s/\theta_T > 5 \times 10^5$ and according to Poll a fair agreement was observed with respect to the experimental results, where the numerical method over-predicted transition Reynolds number, R_{θ_T} by 10%. From Figure 5.20, the numerical analysis shows that the attachment line transition occurs at $R_{\theta_T} \approx 270$ and Poll proposed that “ $R_{\theta_L} = 240$ is a true upper limit for the completely laminar flow at $s/\theta_L > 2 \times 10^4$ ”.

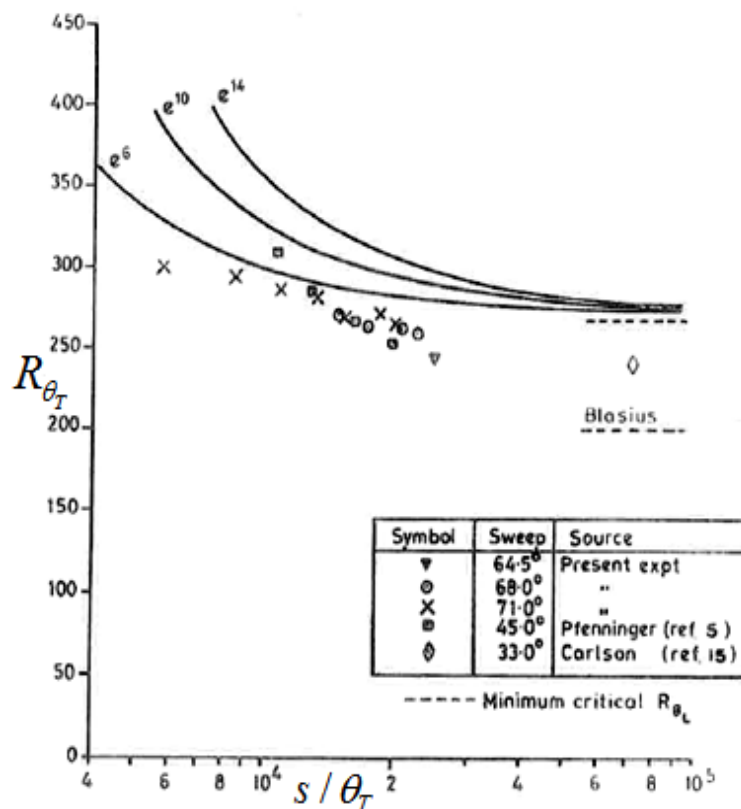


Figure 5.20: Comparison of the numerical results from the linear stability with the experimental results by Poll[92]

A further numerical study of attachment line instability was conducted by Hall, Malik and

Poll [55] who employed the non-parallel approximation to analyse the two-dimensional disturbance of the swept Hiemenz flow. It was concluded that attachment line instability is due to travelling wave disturbances, similar to Tollmien-Schlichting waves, which are linked to the Hämmerlin type of disturbances and which can undergo either exponential or algebraic growth and decay. The critical condition was predicted to be $R_\theta = 235$ and the results showed good agreement with the experimental results of Pfenninger and Bacon. Following the DNS analysis by Spalart, this type of disturbance was referred to as the Görtler-Hämmerlin instability.

5.3.3 Attachment Line Control

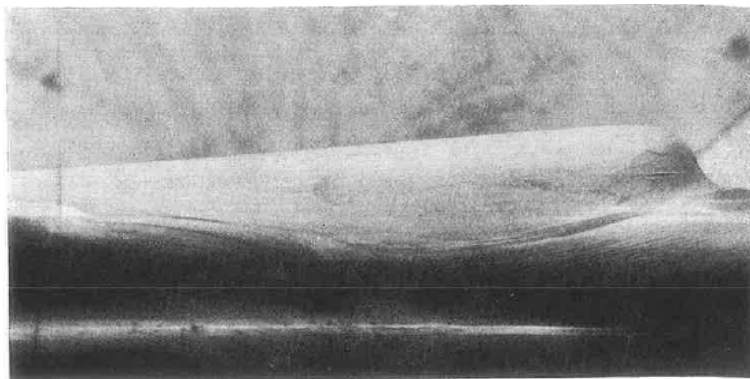


Figure 5.21: The ‘Gaster Bump’, leading edge decontamination device [45]

Following wind tunnel testing at the College of Aeronautics at Cranfield in the late 1960s, Gaster [45] found that attachment line contamination could be cured by placing a well-designed bump at the leading edge. This prevents the contaminated flow from propagating downstream along the attachment line by generating a fresh stagnation point at the bump and hence a laminar attachment line downstream. Initially a few shapes were moulded manually using plasticine and tested in a low speed wind tunnel so as to identify the optimum shape, and then a more robust bump was manufactured using a polyester material based on the selected optimum shape, which was then flight tested. This design process proved to be effective. However, the bump was found to be useful only up to $R_\theta < 160$ or $\bar{R} < 395$. The same anti-contamination bump was employed during the study of the

development of turbulent spots from sparks, and TS waves from acoustic sources, covered in section 5.3.2.

Later in the mid 1980s the attachment line contamination issue was revisited by Seyfang [107] who also proposed a few methods of preventing the propagation of the turbulent attachment line, using devices located in the inboard region of the wing leading edge, represented schematically in figure 5.22. These devices were tested experimentally on a wind tunnel model similar to that of Gaster [45] and Poll [92][91] at the BAe Warton low speed tunnel at a freestream speed of $60m/s$ and sweep angle of 53° which was chosen for most of the test cases so that $\bar{R} \approx 360$ was achieved. Among all the devices tested, the ‘streamwise groove’ and the ‘step down’ were most preferred as they were demonstrated to be effective until $\bar{R} \approx 420$.

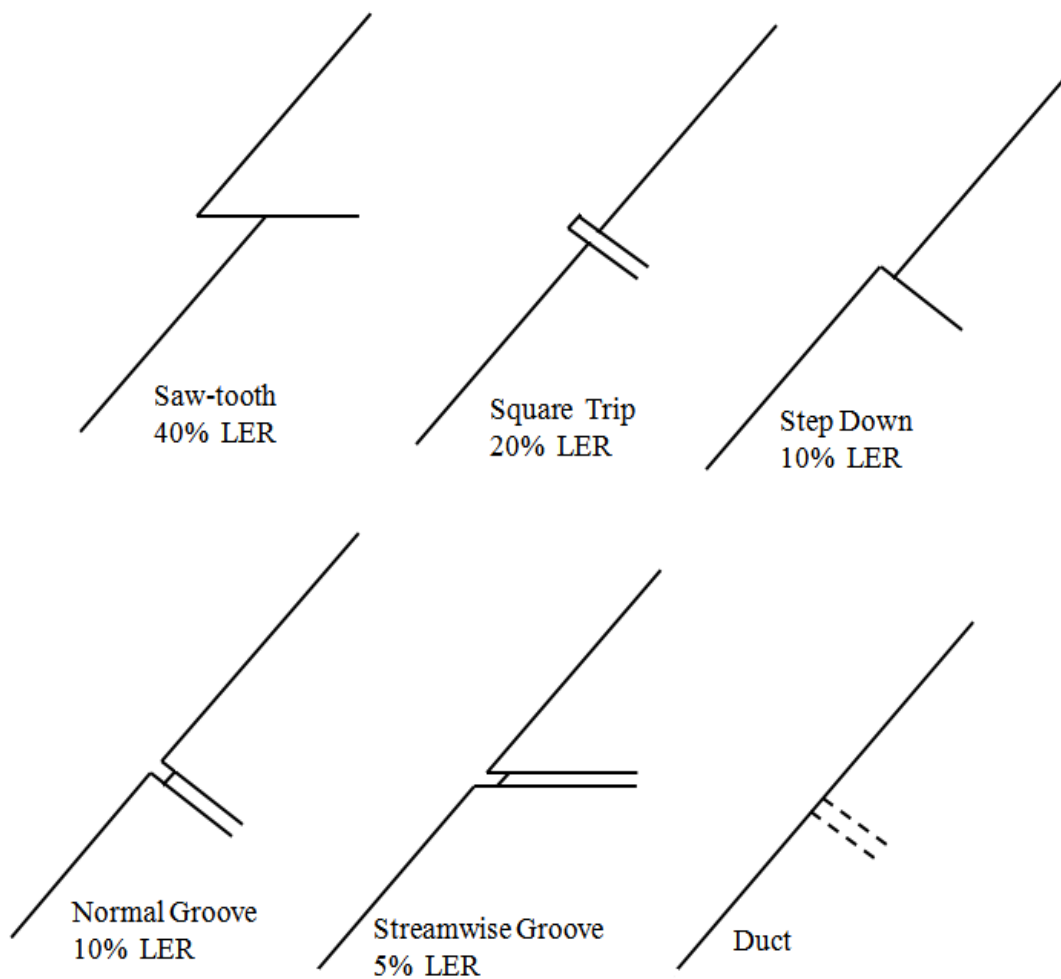


Figure 5.22: The leading edge fences for attachment line control tested by Seyfang [107].

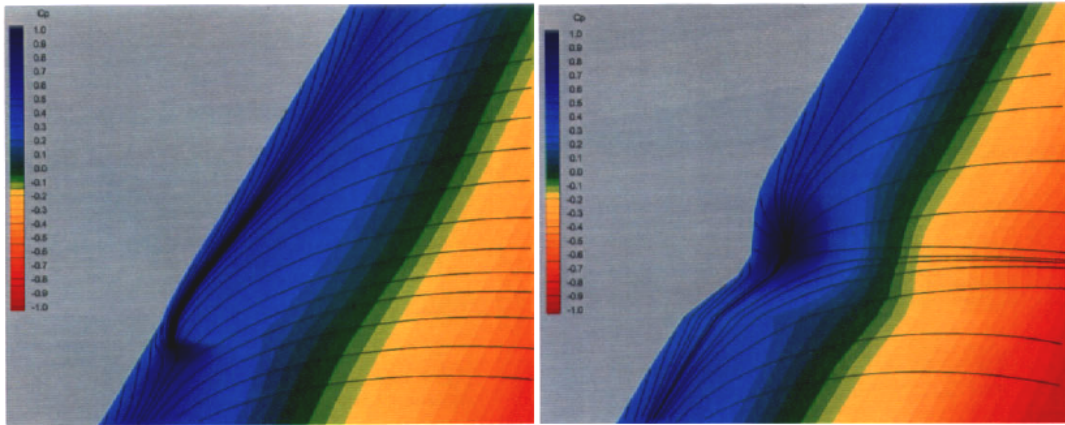


Figure 5.23: The distribution of the pressure coefficient and streamline on the model with the positive (LHS) and negative (RHS) bumps

The benefit of employing the ‘Gaster bump’ as a passive anti-contamination device was acknowledged by Reneaux et al. [97] and further experiments were conducted using both positive and negative bumps in the F2 wind tunnel at ONERA. These were aimed at optimising the methods of preventing attachment line contamination. Figure 5.23 shows the static pressure coefficient contours and the streamlines on the model equipped with the positive and negative bumps, computed using an inviscid solver. The experimental results showed that both bumps were effective for $\bar{R} < 400$, but the positive bump was chosen for further investigation as it had better performance at an incidence of 1° . It was transferred to an A320 fin which was first tested in the S1MA wind tunnel and subsequently flight tested.

The possibility of applying an active control method, such as wall suction for the relaminarisation of the attachment line was demonstrated by Poll and Danks [94] experimentally using a wooden, faired cylinder model with a titanium leading edge which contained laser drilled pores of $50\mu m$ diameter. With that particular model, $200 < \bar{R} < 1100$ was achievable by varying the sweep angle, and it was demonstrated that the attachment line could be relaminarised up to $\bar{R} \approx 650$. A relationship for the amount of distributed suction required for attachment line relaminarisation was derived as equation 5.34 where $w(0)$ refers to the mean suction velocity applied at the wall and the end of relaminarisation was identified from the hot wire signal.

$$\bar{R} = 245 \left[1.07 \left(\bar{R} \frac{w(0)}{V_e} \right)^2 - 0.48 \left(\bar{R} \frac{w(0)}{V_e} \right) + 1 \right]^{\frac{1}{2}} \quad (5.34)$$

Attachment line relaminarisation using distributed wall suction was re-investigated experimentally by Arnal et al. [5] in the mid 1990s. It was demonstrated that a turbulent attachment line could be re-laminarised even up to Reynolds number $\bar{R} \approx 700$. This was probably not the maximum achievable value as higher \bar{R} testing was restricted due to limitations placed on the instrumentation. Similarly to Poll and Danks, a relation for the amount of suction required to relaminarise a turbulent AL was derived from the experimental results and was expressed as

$$\bar{R} = 250 - 150K \quad (5.35)$$

where

$$K = \frac{\bar{R}w(0)}{V_{iw}} \quad (5.36)$$

A summary of Arnal et al. results is presented in Figure 5.24 which also contains the experimental results of Poll and Danks, Spalart's DNS and the experimental results of Juillien and Arnal [67] at lower \bar{R} . Overall, a fair agreement can be observed between the results, except at low \bar{R} where the results of Juillien and Arnal deviate slightly from the relation given by equation 5.35 and at $\bar{R} > 400$ where the relation proposed by Poll and Danks, equation 5.34, is a poor fit. Even a Gaster bump was unable to prevent the contamination from spreading along the attachment line at $\bar{R} > 400$ and therefore only the suction system was able to relaminarise the attachment line at higher \bar{R} .

The Airbus A320 Hybrid Laminar Fin flight test also demonstrated that wall suction can be an effective method for attachment line relaminarisation and again a relation between

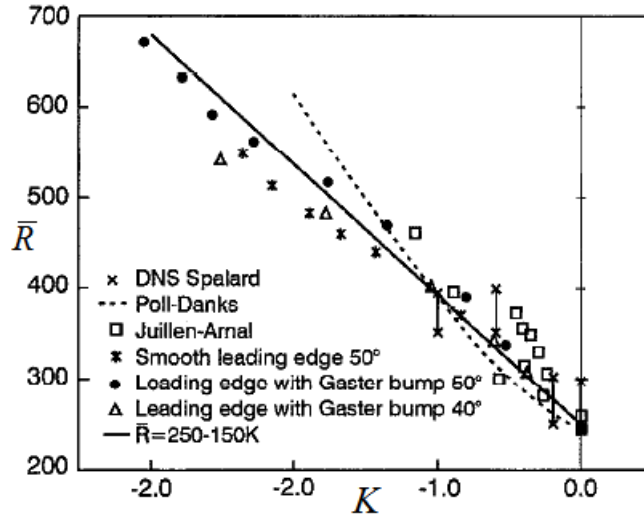


Figure 5.24: The amount of suction required to relaminarise a turbulent attachment line at a particular \bar{R} , Arnal et al. [5]. A comparison with previous experimental and numerical studies as well.

the amount of suction required to relaminarise the attachment line was derived from the scattered experimental data shown in Figure 5.25. This is given by equation 5.37. However, as seen in Figure 5.25, there is a large deviation between the suction requirement established by Schrauf [103] and that of Arnal et al. [5] which was in agreement with the other investigations shown Figure 5.24. The main difference between Schrauf and Arnal et al. is the suction parameter employed for the data analysis, given by equations 5.37 and 5.36 respectively. On the other hand, the Reynolds number attained by Schrauf in most cases is significantly lower, $\bar{R} < 320$, compared to those of Arnal et al. and considering the fact that the attachment line is not fully turbulent until $\bar{R} > 350$ as demonstrated by Cumpsty and Head this might explain the discrepancy between two relations. It might be the case that suction was applied along an intermittent attachment line as opposed to a fully developed turbulent one like in the case of Arnal et al.

$$\bar{R} = 250 + (4 \times 10^6 \times C_q) \quad (5.37)$$

$$C_q = \frac{w(0)}{Q_{iw}} \quad (5.38)$$

and where the suction parameter of Poll and Danks and of Arnal et al. can be expressed as

$$K = \bar{R} \frac{C_q}{\sin \Lambda} \quad (5.39)$$

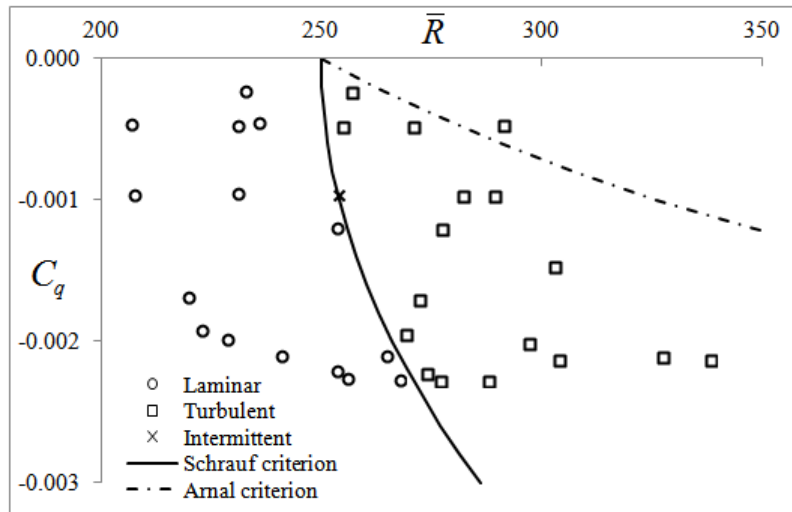


Figure 5.25: The amount of suction required to relaminarise the attachment line on the A320 fin, figure from Schrauf [103]

5.4 Present Experimental Measurements

5.4.1 Attachment Line Static Pressure

The local static pressures were captured using the surface mounted pressure tappings connected to the pressure transducers and data acquisition system described in section 3.2. Firstly, the static pressure readings were used to align the model so as to ensure that the attachment was right at $x/c = 0$. As the model was symmetrical, this could be easily achieved by pitching it about its axis until the symmetrical tappings on the port and starboard side indicated close agreement, as seen in figure 5.26 which shows the pressure distribution captured by the mid-span pressure stations at $\bar{R} = 540$.

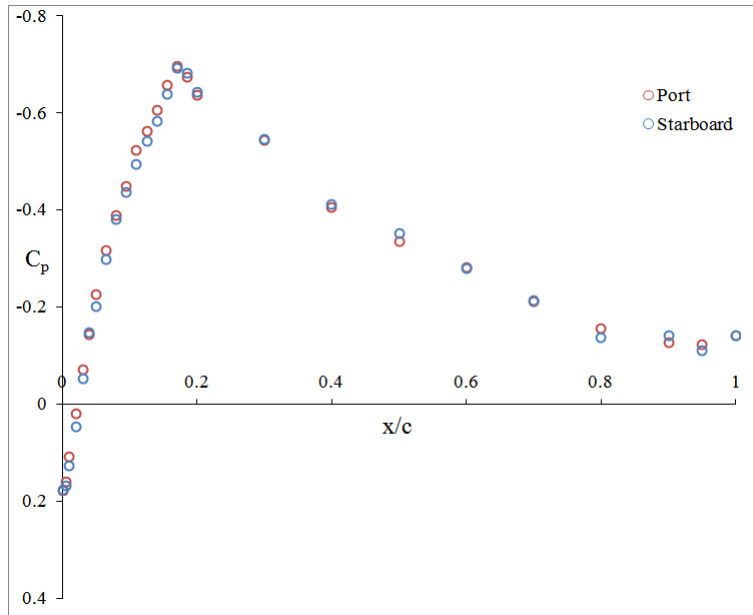


Figure 5.26: Static pressure distribution at the in-board pressure station for $\bar{R} = 540$

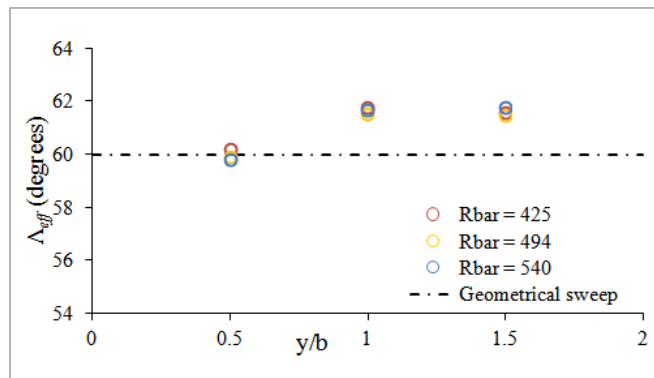


Figure 5.27: The variation of the effective sweep in the spanwise direction.

At the leading edge of each spanwise station (inboard, mid-span and outboard) shown in Figure 3.4 the effective sweep angle was determined from the experimental pressure coefficient using equation 5.5, and is presented in Figure 5.27 for three different \bar{R} s. At the inboard station the effective sweep, Λ_{eff} , is close to the geometric sweep and but it increases by approximately 2° at the downstream stations. No strong dependence on \bar{R} is demonstrated. The variation in Λ_{eff} between the inboard and outboard stations shows that the infinite-swept condition is not valid along the whole span of the model. But the close agreement found between the mid and outboard station also shown in Figure 6.11 from section 6.3.1 means that the infinite-swept condition holds in that region which was chosen for the boundary layer measurements.

5.4.2 Attachment Line Hot-wire Signal

The main source of disturbance that leads to attachment line contamination on swept wings is the vortical structures from the turbulent boundary layer from the side of the fuselage and during the current experiment a similar scenario was created by mounting the wing on the floor of the wind tunnel. The technique of analysing the hot-wire/film voltage output signal over a time period has been established as a reliable method to identify the state of a boundary layer. This method was adopted by Gaster [45], Cumpsty and Head [36], Poll [92] [91], Arnal et al. [5] among others to indicate the state of the boundary layer. After ensuring that the attachment line was at $x/c = 0.0$, the hot-wire traversing probe was mounted at the leading edge of the model firstly between the inboard and mid-span pressure tapping stations at $y = 0.5m$ and secondly between the mid-span and outboard stations where $y = 0.9m$. By stepping the traverse mechanism, and using the optical system described in chapter 3, the hot-wire sensor was positioned at a distance of $200\mu m$ from the surface of the model.

From both Figures 5.28 and 5.29, the small fluctuation in the amplitude of low frequency signal at $\bar{R} < 210$ indicates that the attachment line is laminar. The development of low frequency spikes at $\bar{R} = 243$ suggests that turbulent spots start to appear intermittently and are convected along the attachment line, however losing their intensity while moving downstream, as the amplitude and frequency of the spots from the inboard, upstream signal is slightly higher than the outboard, downstream one. For $\bar{R} > 243$ the amplitude of the signals increase considerably, together with the frequency of the spots. This indicates that the contamination from the turbulent boundary layer on the tunnel floor is convected along the attachment line is growing and this finding is in good agreement with the Pfenninger and Poll criterion of $\bar{R} > 250$ and Gaster's criterion of $R_\theta = 100$, where the momentum thickness was estimated from the velocity profile shown in Figure 5.30.

For $\bar{R} > 283$ the hot-wire signals consist of large amplitude and high frequency waveforms, typical of turbulent boundary layers. The peak to peak value of the waveform

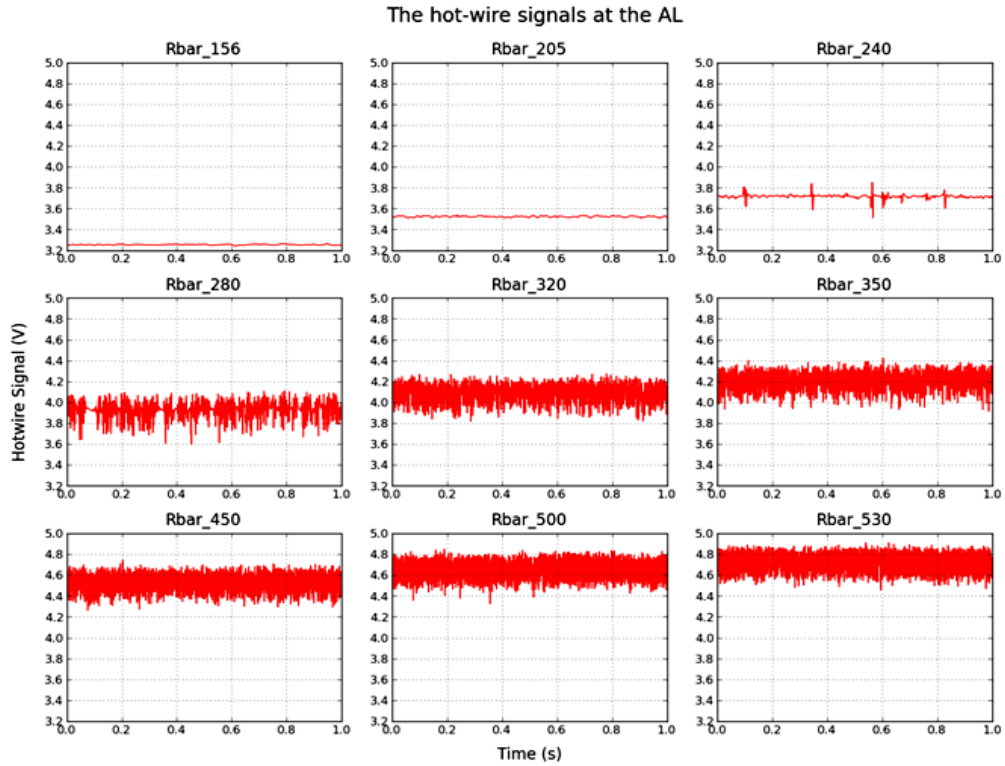


Figure 5.28: The hot wire voltage signal at the upstream station, $y = 0.5m$ and $z = 200\mu m$.

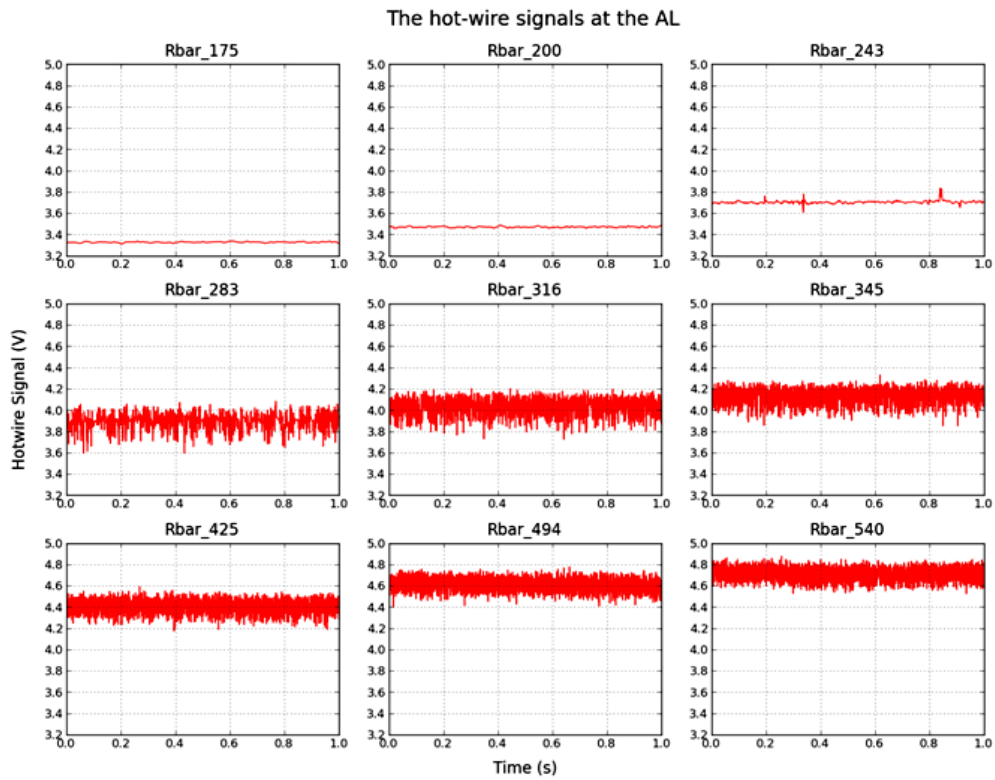


Figure 5.29: The hot wire voltage signal at the downstream station, $y = 0.9m$ and $z = 200\mu m$.

reduces with increasing attachment line Reynolds number which would suggest that the boundary layer was undergoing a reduction in momentum thickness. However at this point it is difficult to conclude whether the attachment line is fully turbulent as the experimental analysis of Cumpsty and Head has demonstrated that the attachment line is not fully turbulent until $\bar{R} > 374$. Similar observations can be made about the velocity profiles captured while traversing the turbulent attachment line, and these results will be revisited in section 5.4.4 where more concrete conclusions are drawn regarding the state of the attachment line.

5.4.3 Laminar Attachment Line

At the attachment line the flow is reduced to only a single component in the spanwise direction. Thus, a single normal (SN) hot-wire probe can be used to capture the velocity profile. The boundary layer traverse was conducted at $y = 0.9m$ (between mid-span and outboard pressure stations) as in this region the infinite-swept condition could be assumed as the effective sweep remains almost constant as shown in figure 5.27 and so does the chordwise pressure distribution for $x/c < 0.1\%$ as shown in figure 6.11. Following the hot wire data analysis process detailed in section 4.4.1 and using the coefficients (A and B) of the hot wire response obtained during the calibration process, the hot wire voltages recorded during the boundary layer traverse can be converted into the equivalent velocity using equation 4.29. The local velocity was non-dimensionalised using the velocity at the edge of the boundary layer and was plotted against the non-dimensional wall-normal parameter, η . In the current analysis the laminar velocity profiles were first plotted against η given by equation 5.19, during the swept Hiemenz flow analysis, where the reference length (x) is replaced by the leading edge radius of curvature. Secondly, using equation 5.8, normalised by the wall-normal distance, z , where the leading edge velocity gradient was calculated from the pressure distribution.

Figure 5.30 shows the laminar profiles captured during the current experiment, and those

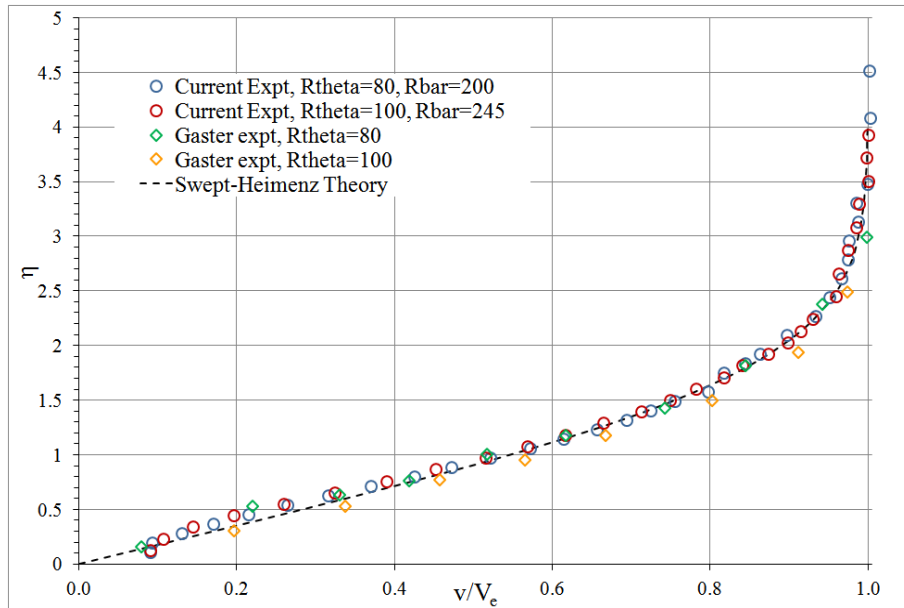


Figure 5.30: Laminar velocity profiles compared with swept Hiemenz flow and Gaster's experimental measurements using η estimated from equation 5.19.

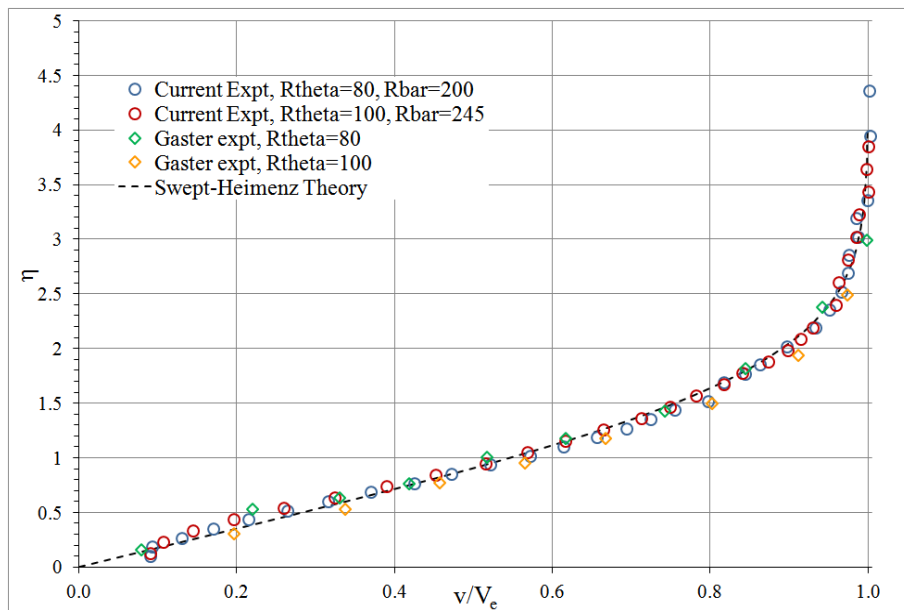


Figure 5.31: Laminar velocity profiles compared with Hiemenz flow and Gaster's experimental measurements. Where η is calculated from velocity gradient at the leading edge determined from the pressure distribution.

from Gaster's, compared with the swept Hiemenz flow solution. In general a good agreement exists between the experiment and the theory, except very close to the wall where the first experimental data point deviates slightly from the other results. From the study conducted by Wills [121], heat transfer between the wall and probe was identified as a source of discrepancy during hot-wire measurements. The effect was more severe for

metallic surfaces and other materials with good heat conduction characteristics, as opposed to wooden surfaces where the effect was negligible. However, during the current experiment all the initial measurement near the wall were made while the tips of the wire supports were in contact with the wall, so the heat transfer might have been enhanced between the sensor, even if the surface was wooden.

The small discrepancies at $v/V_e < 0.20$ might be related to the fact that the low speed calibration was limited to only $4m/s$ so that the local speed of the viscous layer in that region was definitely lower than the minimum speed at which the hot-wire was calibrated.

Figure 5.31 represents the same profile but with η determined by substituting the leading edge velocity gradient, extracted from the experimental pressure measurements, into equation 5.8. The results do not differ a lot from Figure 5.30, except that the results shifted slightly downward from the swept Hiemenz theory at $v/V_e > 0.20$, but good agreement still exists. The slight difference might originate from the inaccuracy accumulated from the surface static pressures measured experimentally. This, also supports the approximation based on the potential flow around a circular cylinder employed during design of the experimental model.

Overall, the good agreement with swept Hiemenz flow for $R_{\theta} = 100$ demonstrates that the attachment line is still in its laminar state even if the first turbulence spots had started to appear and the shape factor, H , is very close to the theoretical value of 2.54 as shown in Figure 5.34. These results provide confidence in the instrumentation and the methods employed in capturing the mean velocity profile and therefore in proceeding with further measurements of the turbulent attachment line.

5.4.4 Turbulent Attachment Line

In the presence of a disturbance similar to that at a wing/fuselage junction or large disturbances to such as roughness trip, the attachment line will be susceptible to contamination

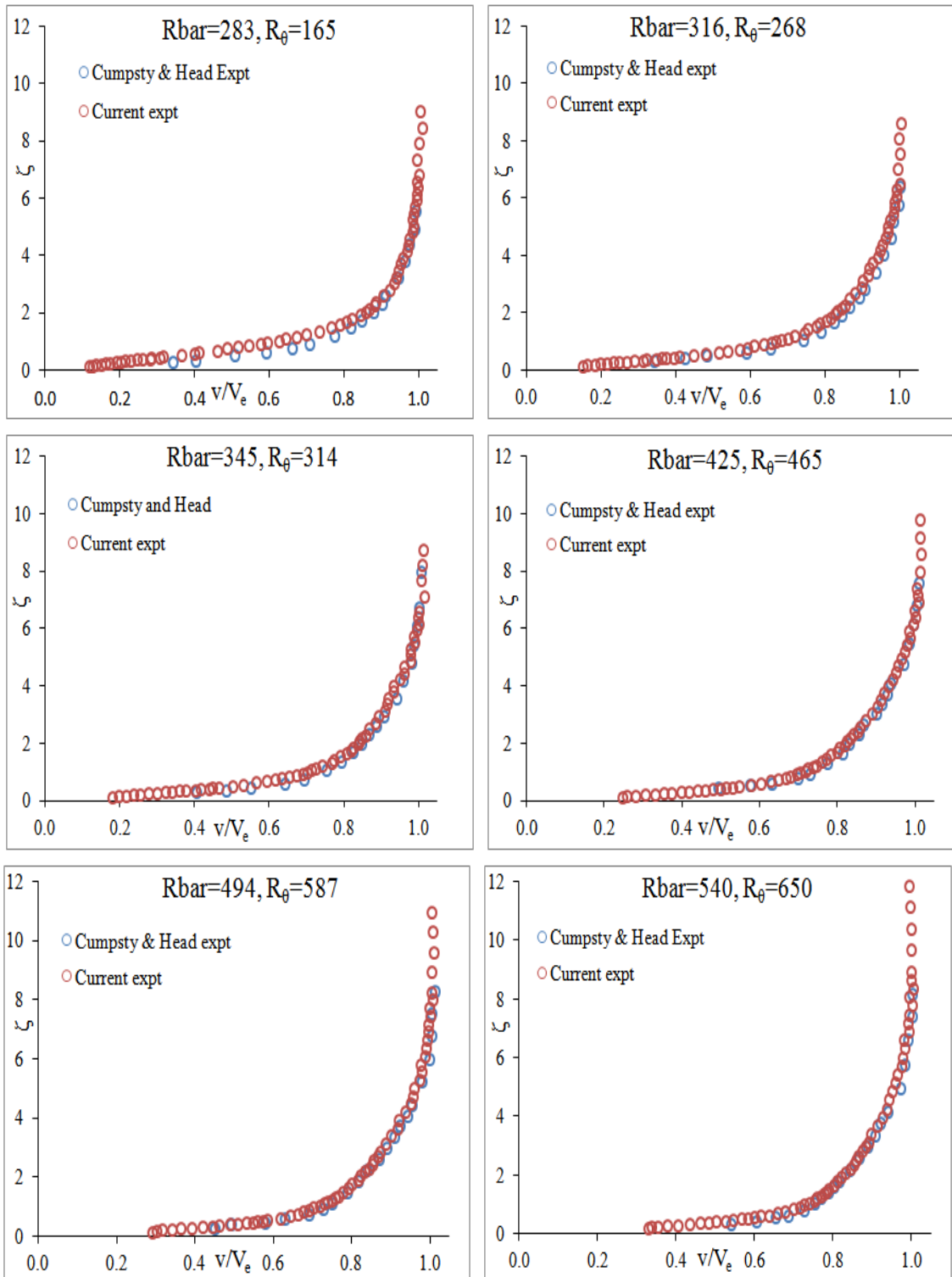


Figure 5.32: Mean turbulent velocity profiles captured from the current experiment and compared with Cumpsty and Head's experimental measurements, where $\zeta = z/\delta^*$.

and transition to turbulent at $\bar{R} > 245$. This is supported by the peaky waveforms of the hot wire signals in Figure 5.28 and 5.29, at $\bar{R} > 245$. By employing a similar method to that used in capturing the laminar mean velocity profiles presented in section 5.4.3, the

turbulent profiles were captured for $\bar{R} > 245$. These profiles are compared in Figure 5.32, with those obtained by Cumpsty and Head [36], on a model with the same leading edge radius of curvature and geometric sweep angle as the one used during the experiment. Very close agreement can be observed between the velocity profiles obtained from the present experiment and those from Cumpsty and Head, which are slightly fuller at lower ζ , say $\zeta < 3$. The digital optical system proved to be advantageous as the local velocity in the near wall region seems to be better represented, due to the ability to resolve more accurately the position of the hot wire probe and thus to take measurements closer to the wall.

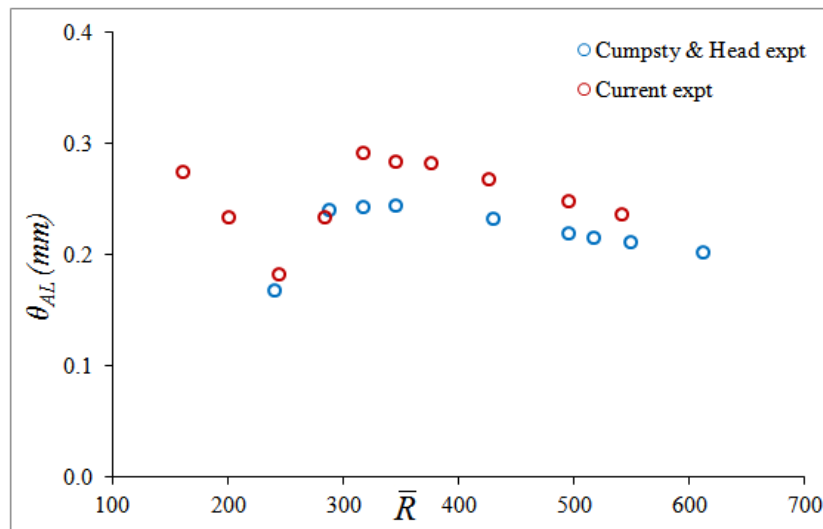


Figure 5.33: Comparison between the momentum thickness obtained by Cumpsty and Head's with those calculated from the current experimental measurements.

From the velocity profiles the boundary layer momentum thickness, θ , and shape factor, H , were calculated. Even if the velocity profiles show excellent agreement, the momentum thickness values obtained from the current results seem to be about 10 to 15% larger than those obtained by Cumpsty and Head, despite the fact that the models in both experiments had the same leading edge radius of curvature and sweep. The main difference could be due to the larger number of data points obtained during the current experiment. However, the trends in both results show some similarities. As \bar{R} is increased, θ first decreases which is a typical behaviour of laminar boundary layer, until the critical Reynolds number $\bar{R} = 245$, where θ increases until $\bar{R} \approx 345$ and a maximum in θ is attained. Fur-

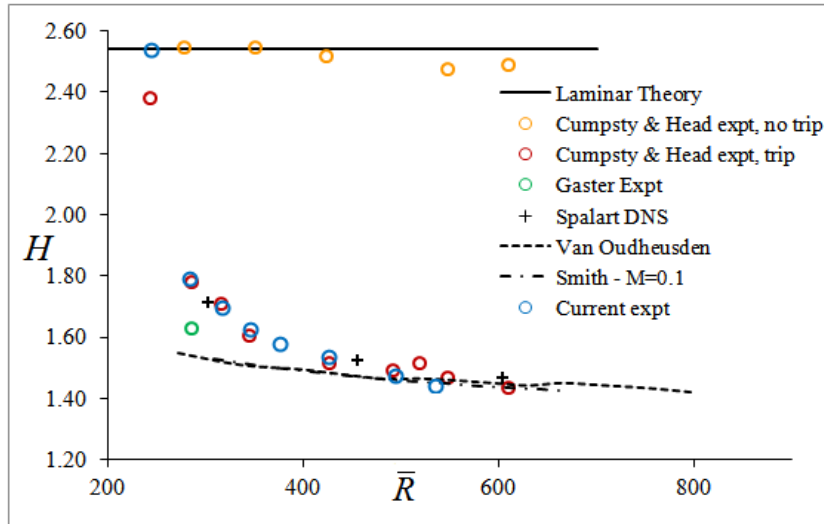


Figure 5.34: Comparison between the shape factor calculated from the current experimental measurements with those obtained by Cumpsty and Head [36], Gaster [45], van Ouheusden [119], Spalart [110] and Smith [108].

ther increase in \bar{R} results in a decrease in θ suggesting that, at this stage, the attachment line is fully turbulent. A better agreement is observed in the behaviour of the shape factor shown in Figure 5.34. For $\bar{R} > 345$ all results tend to a value of $H \approx 1.4$ which is typical of fully turbulent boundary layers on flat plates

By employing Preston's technique detailed in section 3.6, the local skin friction was estimated using the two different probes shown in Figures 3.29 and 3.30. The skin friction results are compared with those obtained from various other sources in Figure 5.35. For $\bar{R} > 316$, very close agreement is seen between Cumspty and Head's measurement, Poll's empirical relation and van Oudheusden's analytical prediction with Spalart's DNS prediction being somewhat higher than the experimental results. However, for $\bar{R} < 316$ the results deviate slightly from the trend. The attachment line might not be fully turbulent at this stage, in which case Preston's technique is not applicable. This will be revisited later.

Using the wall shear stress measurement the velocity profiles could be plotted in wall units as shown in Figures 5.36 and 5.37. For $\bar{R} > 345$, in Figure 5.36, the results in the velocity defect region, $zv_\tau/\nu_\infty > 50$ tend to collapse to a straight line, but which deviates from the 'universal logarithmic law' for fully developed turbulent flow in pipes and flat plates. Cumpsty and Head compared their velocity profiles against the same 'universal

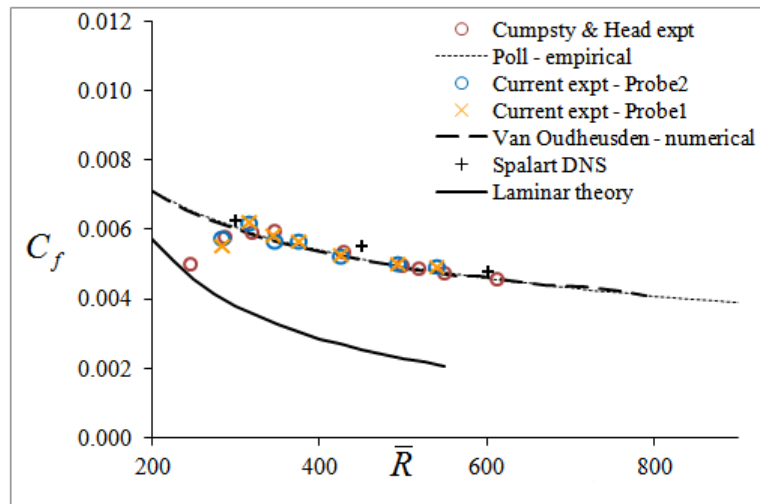


Figure 5.35: Comparison of the attachment line skin coefficient obtained from the current experiment with those from Cumpsty and Head [36], van Ouheusden [119], Spalart [110] and Poll [91] given by equation 5.29.

log-law' derived by Patel [87], Figure 5.10. However, the inner region of the velocity profiles captured during the current experiment is not in agreement with the 'universal log-law' provided by Patel and by Cumpsty and Head.

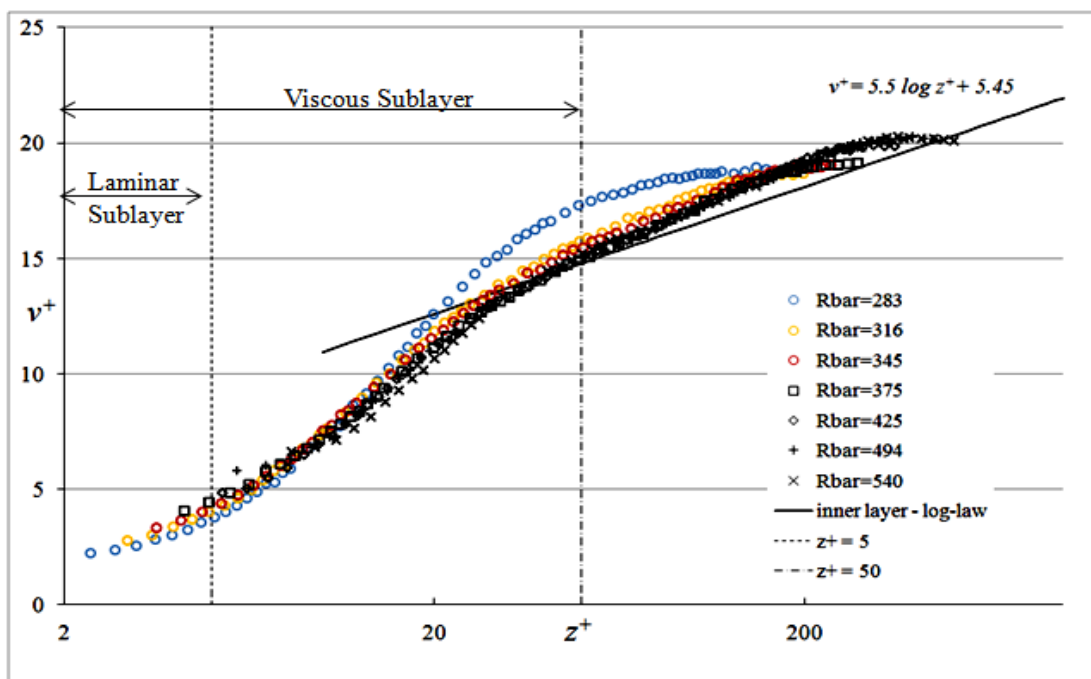


Figure 5.36: The turbulent velocity profile plotted in wall units using wall shear stress estimated from Preston tubes. The inner region is represented by the 'universal log-law' chosen by Patel [87] and Cumpsty and Head [36].

Clauser [26] demonstrated that the y-intercept of the 'universal log-law' is usually af-

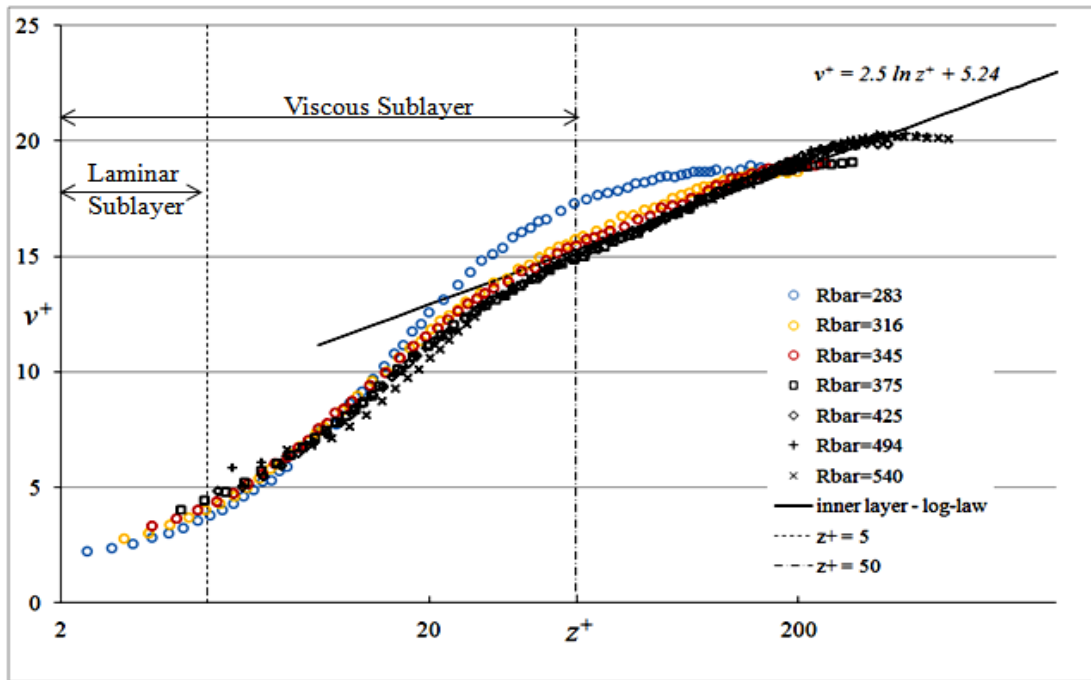


Figure 5.37: The turbulent velocity profile plotted in wall units, where the inner region is represented by the ‘universal log-law’ given in Cebeci and Cousteix [24].

affected by the roughness of the surface, where the surface can be considered ‘aerodynamically’ smooth if the roughness is immersed within the laminar sublayer. But from Figure 5.10 both the gradient and the y-intercept have to be modified to fit the linear part of the measurements. Thus the ‘universal log-law’ was replaced by the logarithmic (natural log) relation given by Cebeci and Cousteix [24], the results are re-plotted in Figure 5.38. This modification results in a better representation of the linear logarithmic region. In addition to the good correlation within the log-law, from Figure 5.38 the flow within the viscous sublayer ($z^+ < 50$) again appears to be better captured in comparison with Cumpsy and Head’s measurements, Figure 5.10. This was mainly due to the ability to align the hot wire very close to the wall using the optical system, this also allowed for few measurements within the laminar sublayer at lower turbulent \bar{R} , which is usually a very challenging task, especially in boundary layers which are approximately $3mm$ thick.

From Figure 5.37 it is quite clear that the attachment line is not fully turbulent until $\bar{R} > 345$, as from this point on the results for the rest of the Reynolds number range collapse on to the Cebeci and Cousteix log-law. Therefore, over the range $250 < \bar{R} < 345$, the

attachment line is still in an intermittent stage and undergoing transition. This finding is also supported by the trend in skin friction measurement shown in figure 5.35, where the results lie on the fully turbulent trend from $\bar{R} > 345$. Even with the scatter in their experimental results, a similar conclusion was initially drawn by Cumpsty and Head. Nevertheless, the R_θ estimated by the latter was slightly larger than the criterion suggested by Preston for the minimum Reynolds number for the existence of a turbulent boundary layer on a flat plate, $R_\theta > 320$. From the velocity profiles captured during the current experiment, at $\bar{R} \approx 345$ (which indicates the minimum \bar{R} for a fully turbulent attachment line), an $R_\theta = 315$ was estimated. This is slightly closer with Preston's criterion than Cumpsty and Head's results where $R_\theta = 320$ was obtained at $\bar{R} = 363$ from Cumpsty and Head.

5.4.5 Relation Between Turbulent R_θ and \bar{R}

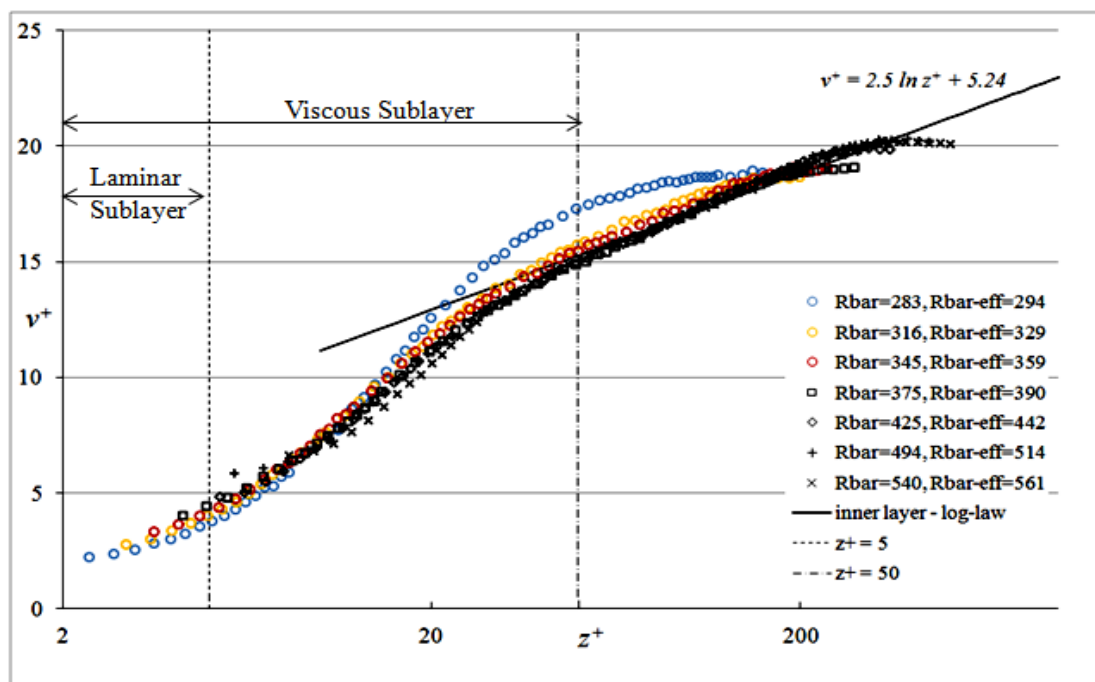


Figure 5.38: The turbulent velocity profile plotted in wall units for various \bar{R} based on effective sweep.

The results presented so far have been based on geometric sweep, however in section 5.4.1 it was demonstrated that the effective sweep, Λ_{eff} , varies in the spanwise direction

evidenced by the change in static pressure along the attachment line. Using Λ_{eff} estimated from equation 5.5, the attachment line Reynolds number based on the effective sweep angle, \bar{R}_{eff} was estimated through the necessary substitution in equation 5.11. Based on the \bar{R} criterion established above for the minimum condition for an attachment line to attain a fully turbulent state was revisited and, judging from the results shown in Figure 5.38 it was found to be $\bar{R}_{eff} > 360$.

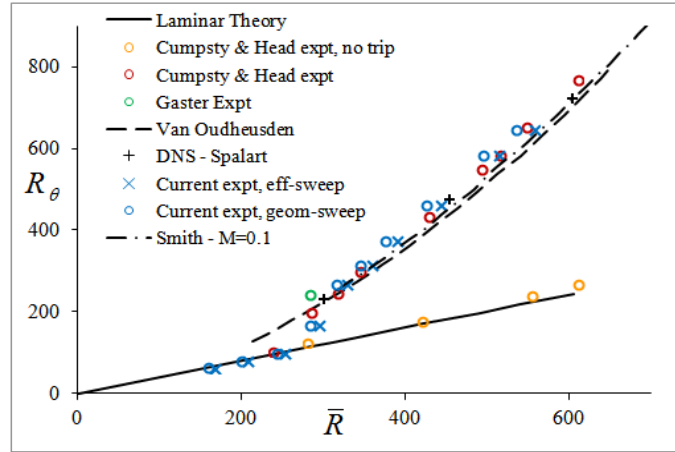


Figure 5.39: The relation between R_θ and \bar{R} together with the corrected current experimental results based on effective sweep.

Figure 5.8 has been re-plotted accounting for the correction due to effective sweep, Figure 5.39. The agreement between the current experimental results and those obtained from previous studies, is improved by accounting for the effective sweep and shows closer agreement to the theoretical results which do not require this correction. With such good correlation, and using both previous experimental and numerical results, an empirical relation between \bar{R} and R_θ can be derived for an incompressible turbulent attachment line, simply by applying a linear fit through the results in Figure 5.39.

$$R_\theta = 1.85\bar{R} - 360 \quad (5.40)$$

R_θ is based on the momentum thickness which is the physical characteristic of the attachment line boundary layer and it can be considered more appropriate for the representation of a turbulent boundary layer. Either an experimental or a numerical viscous solution is

required to determine the momentum thickness and the process is usually quite laborious. On the other hand, \bar{R} is a function of the inviscid flow at the leading edge, namely the chordwise velocity gradient which is governed purely by the geometry and as demonstrated earlier in section 5.1, it could be easily reduced to a function of known quantities while applying potential flow theory. Therefore, the relation given by equation 5.40 can be very useful for estimating the boundary layer quantities for a turbulent attachment line at a given \bar{R} .

In addition, for a turbulent attachment line it might be more appropriate to represent the skin friction, c_f , as a function of R_θ rather than \bar{R} in figure 5.35. From the study of fully developed flow in pipes and channels a power-law relation was proposed by Nikuradse which has been proved to apply also to fully turbulent boundary layer on external surfaces such as flat plates. From Duncan et al. [38] using the $1/7^{th}$ power law, the local skin friction coefficient can be expressed by equation 5.41 for chord Reynolds number, Re ranging between 5×10^5 to 10^7 , and by equation 5.42, which evolves from the $1/9^{th}$ power law proposed by Prandtl and Schlichting, for Reynolds numbers ranging from 10^6 to 10^7 . Using the linear relation established in equation 5.40, Poll's skin friction relation given by equation 5.29 can be expressed as a function of R_θ as in equation 5.43. The c_f values measured during the current experiment using both probes are compared with equation 5.41, 5.42 and 5.43 in Figure 5.40. A good agreement can be observed between the current experimental results and the rest of the results at $R_\theta > 320$, where the attachment line is fully turbulent.

$$C_f = \frac{0.0251}{R_\theta^{\frac{1}{4}}} \quad \rightarrow \quad \text{Nikuradse} \quad (5.41)$$

$$C_f = \frac{0.0176}{R_\theta^{\frac{1}{5}}} \quad \rightarrow \quad \text{Prandtl-Schlichting} \quad (5.42)$$

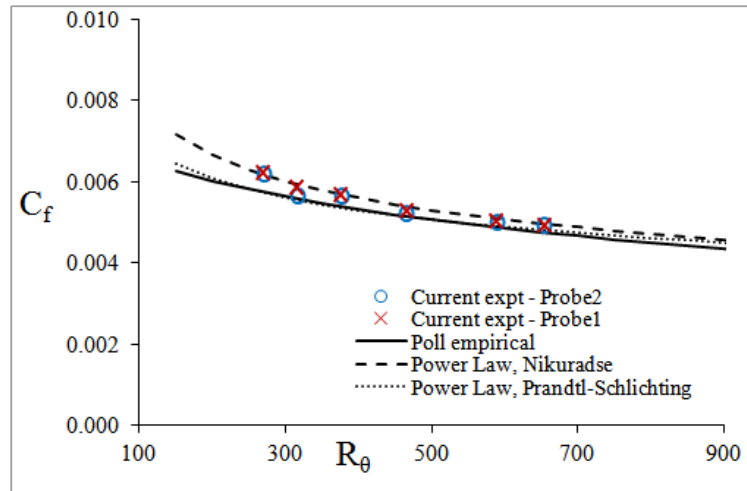


Figure 5.40: Comparison between of the attachment line skin friction coefficient measurement during the current experiment with previous empirical relations.

$$C_f = \frac{0.0757}{[R_\theta + 360]^{\frac{2}{5}}} \quad \rightarrow \quad \text{Poll + equation 5.40} \quad (5.43)$$

5.4.6 Empirical Relation for Turbulent Attachment Line

From the previous section, the inner region of the turbulent velocity profiles demonstrated very close agreement with the universal log-law and the local skin friction relation for fully developed flow in pipes and fully turbulent flow on flat plates. Therefore it will be fair to assume that flow along the attachment line bears some similarity to turbulent flow on flat plates. According to Cebeci and Cousteix [24] the inner layer can be divided into the ‘viscous sublayer’, which comprises the ‘laminar sublayer’ where the viscous stresses dominate the flow up to $z^+ < 5$ and the ‘buffer zone’, which is within $5 < z^+ < 50$, where the viscous stresses are of a similar order of magnitude to the turbulent stresses. The log-layer which is also part of the inner layer, starts at around $z^+ > 50$. In this region the viscous stresses are negligible and the flow is dominated by turbulent stresses. The outer layer comprises 80 – 90% of the boundary layer and the flow is intermittent. The turbulent stresses still dominate the flow and it is referred as the ‘velocity defect’ region.

From Coles’ [27] investigation, the velocity defect region can be represented by the ‘law

of the wake', due to similarity with the flow in half a turbulent wake. As it was demonstrated earlier that the turbulent attachment line obeys the 'law of the wall', extending it to the 'law of the wake', along the spanwise direction it can be expressed as

$$v^+ = \phi(z^+) + \frac{\Pi_{(x=0)}}{\kappa} \omega\left(\frac{z}{\delta}\right) \quad (5.44)$$

According to Cebeci and Cousteix this equation holds for flows both with and without pressure gradient. Neglecting the viscous sublayer, ϕ , takes the form below.

$$\phi(z^+) = \frac{1}{\kappa} \ln z^+ + c \quad (5.45)$$

While the 'wake function', ω , from equation 5.44 can be approximated by the following empirical relation

$$\omega\left(\frac{z}{\delta}\right) = 1 - \cos\left(\pi \frac{z}{\delta}\right) \quad (5.46)$$

An alternative relation for the wake function was proposed by Granville [47]. By substituting for ϕ and ω in equation 5.44, the 'law of the wake' can be represented by

$$v^+ = \frac{1}{\kappa} \ln z^+ + c + \frac{1}{\kappa} [\Pi (1 - \cos \pi \eta) + (\eta^2 - \eta^3)] \quad (5.47)$$

where, $\eta = \frac{z}{\delta}$ and $\eta = 1$ does not necessarily define the edge of the boundary layer.

From Cebeci and Cousteix, assuming that the 'universal log-law' is valid to the wall, the boundary layer integral quantities θ and δ^* can be obtained while integrating equation 5.47 through the boundary layer and a simpler relation between θ and δ is obtained in the form given by equation 5.48.

$$\frac{R_\theta}{R_\delta} = \frac{v_\tau}{\kappa v_e} \left(\frac{11}{12} + \Pi \right) - \left(\frac{v_\tau}{\kappa v_e} \right)^2 (1.9123016 + 3.0560\Pi + 1.5\Pi^2) \quad (5.48)$$

Considering equation 5.47, at $\eta = 1$, we obtain

$$\sqrt{\frac{2}{C_f}} = \frac{v_e}{v_\tau} = \frac{1}{\kappa} \left[\ln \left(\frac{\delta v_e v_\tau}{\nu v_e} \right) + 2\Pi \right] + c \quad (5.49)$$

In the previous section, empirical relations between C_f and R_θ were presented, and the current experimental measurements showed better agreement with the Prandtl and Schlichting and Poll relations. Therefore, for a known c_f and R_θ the parameters Π and δ can be estimated using equation 5.48 and 5.49 and finally using equation 5.44 the mean velocity profile can be estimated in the region of $z^+ > 30$ following the necessary substitution.

According to Cebeci and Cousteix, following Thompson's investigation the viscous sub-layer region, $4 < z^+ < 30$, can be represented by

$$v^+ = c_1 + c_2 \ln z^+ + c_3 (\ln z^+)^2 + c_4 (\ln z^+)^3 \quad (5.50)$$

where $c_1 = 1.0828$, $c_2 = -0.414$, $c_3 = 2.2661$ and $c_4 = -0.324$.

Earlier it was assumed that, at $\eta = 1$, the parameter, Π could be estimated by rearranging equation 5.47 and replacing $\delta v_e/\nu$ by R_δ which is the Reynolds number based on the boundary layer thickness estimated from the current mean velocity profile. This offers a simple way of checking whether Coles law of the wake was applicable along the attachment line flow as well. The results are presented in Figure 5.41, which shows a comparison between the velocity profiles captured experimentally at different \bar{R} and the profiles obtained by applying the Coles law of the wake as modified by Granville, using equation 5.44 for $z^+ > 30$ and the Thompson relation given by equation 5.50, for

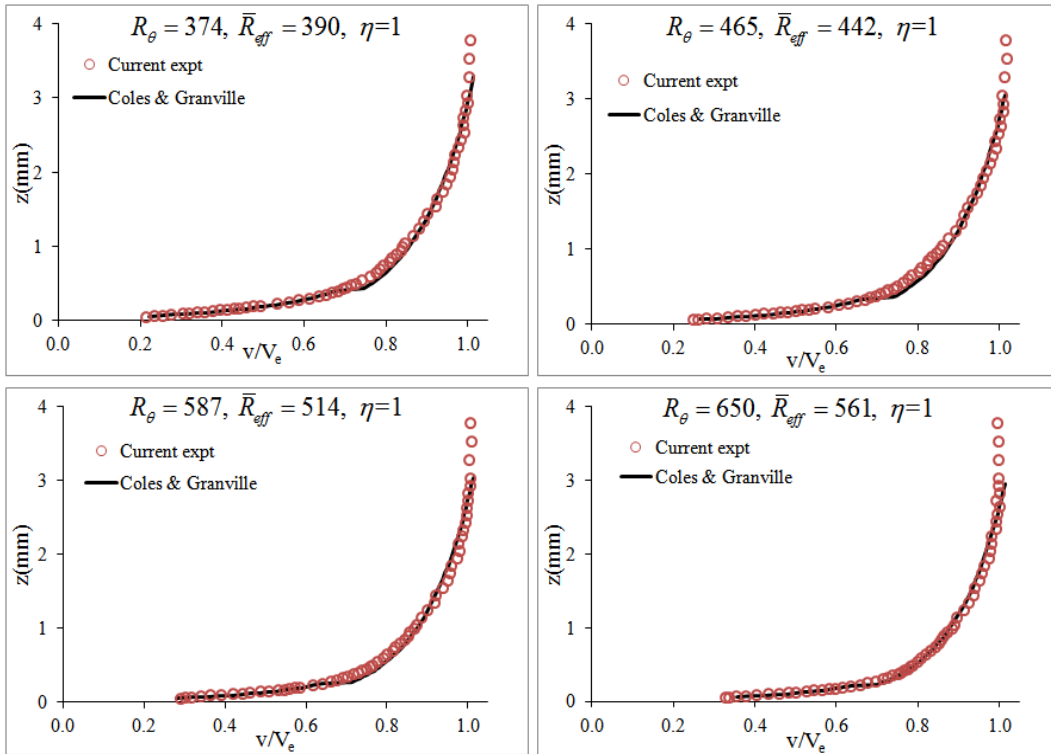


Figure 5.41: Comparison between Coles ‘law of the wake’ model coupled with Granville’s model for the wake function, at $\eta = 1.0$ and the experimental turbulent profiles.

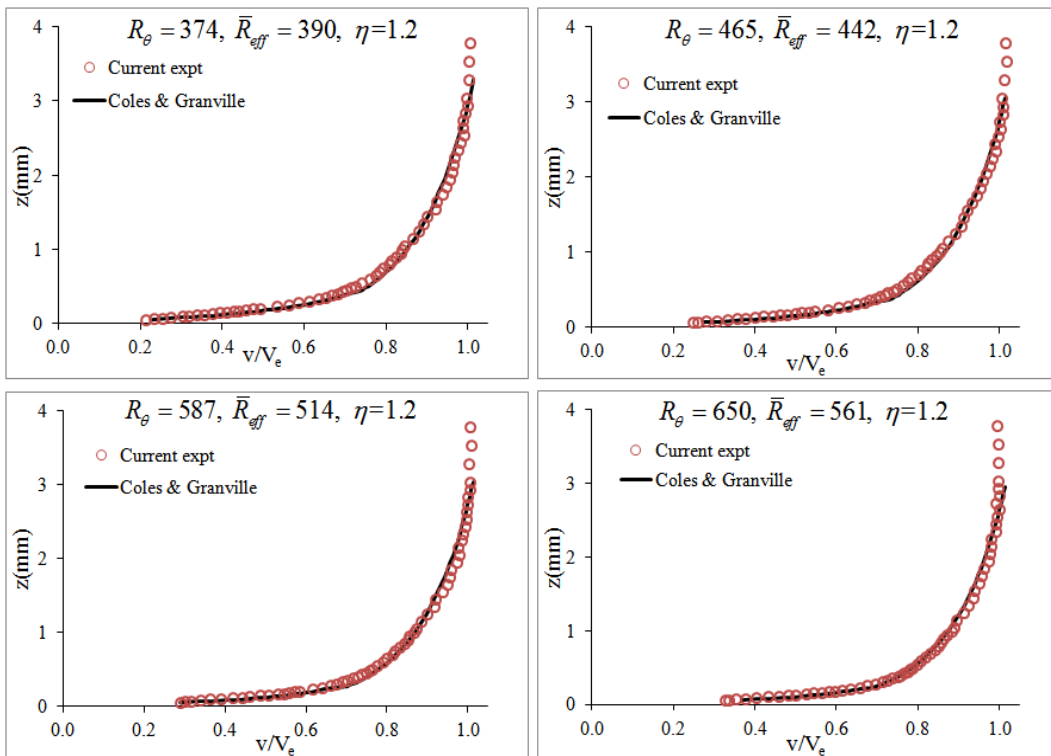


Figure 5.42: Comparison between Coles ‘law of the wake’ model coupled with Granville’s model for the wake function, at $\eta = 1.2$ and the experimental turbulent profiles.

$$4 < z^+ < 30.$$

Figure 5.41 shows a fair agreement between the experimental results and the semi-empirical law of the wake model. A slight kink in the curves is also present at $z \approx 0.5mm$ which is due to the change-over from the Thompson viscous sublayer relation to Coles-Granville ‘law of the wake’ relation, in the buffer zone. This effect can be minimised, as shown in Figure 5.42 when, η , from equation 5.44 is replaced by a value of, 1.2 which is the value proposed by Klebanoff [70] during the derivation of a relation for intermittency in a turbulent flow.

5.4.7 Attachment Line Control

A few methods for decontaminating or relaminarising a turbulent attachment line have been detailed in section 5.3.3, where the method involving distributed wall suction was proven to be the most effective, capable of achieving laminar flow at $\bar{R} \approx 700$. Gaster’s leading edge decontamination device which was previously tested in the low speed tunnel at Filton in the late 1980s, in collaboration with BAe Systems, was re-employed in the current experimental campaign. During the low speed testing conducted by Gaster and Danks it was demonstrated that the decontamination device was effective up to $\bar{R} \approx 600$, which is close to the uncontaminated stability limit predicted by linear stability theory for $s/\eta \rightarrow \infty$. The decontamination device was made of a rolled brass sheet, with a slightly faired leading edge or lip to avoid leading edge separation, and was mounted at the leading edge of the model as shown in figure 5.43. It was mounted in such way that the lip was lifted off the surface by 4mm using two side screws placed at the tips of the lip.

By analysing the hot-wire signal, the effectiveness of the device in relaminarising the turbulent attachment line flow was investigated at 4 different spanwise stations shown in Figure 5.43. Initially, the flow at two different locations on the device was measured,

namely at the forward region on the leeward side, which was considered to be about 25% of the device length downstream of the lip, and the region aft of 75%. Then, the flow further downstream of the device was measured at spanwise distances of 200mm and 500mm from the trailing edge of the device. The hot wire voltage signals captured, for a time period of 1 second at the 4 measurement stations have been presented in Figures 5.44 to 5.47 for varying \bar{R} . The clean signal, with negligible changes in amplitude for all the \bar{R} shown in Figure 5.44, indicates that, over the frontal part of the device, the attachment line was laminar and hence the device was able to decontaminate the original turbulent attachment line up to the maximum achievable \bar{R} . A slight increase in peak-to-peak of the signal can be observed at $\bar{R} > 400$ and this was attributed to the increase in the turbulence intensity level of the tunnel with increased freestream speed.

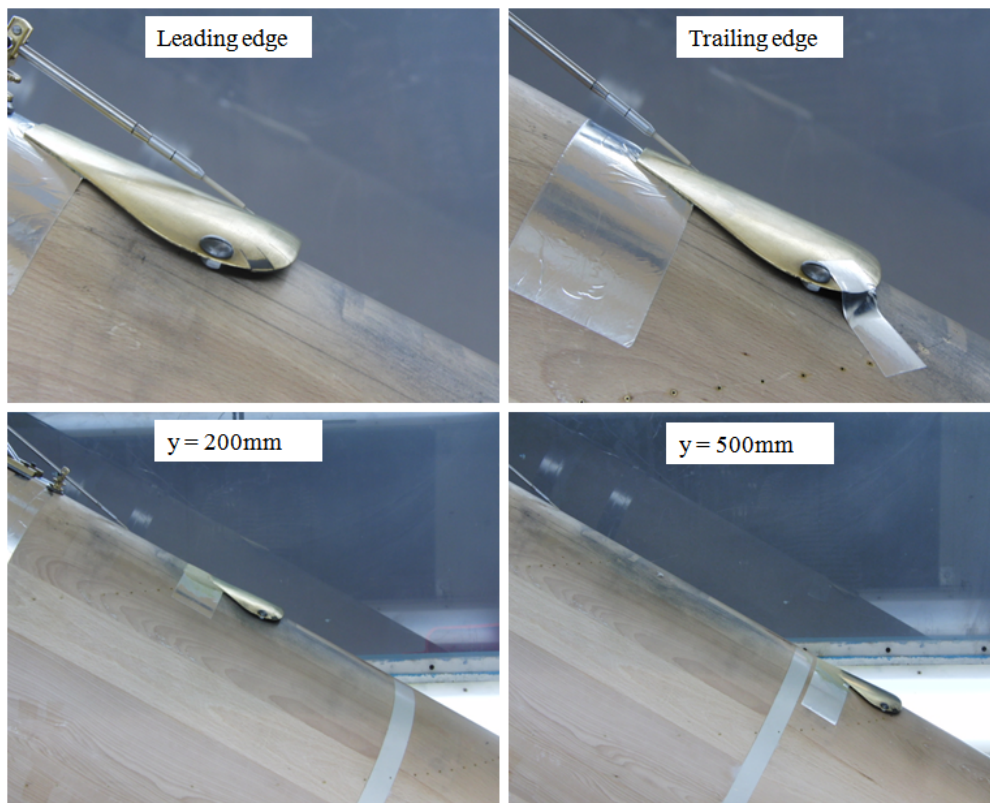


Figure 5.43: The four hot wire measurement stations downstream of the attachment line decontamination device.

From the signal illustrated in figure 5.45 the attachment line was still laminar in the aft region of the device, however low frequency turbulence spots started to appear at $\bar{R} \approx 475$ and were amplified with increase in \bar{R} , but the attachment was still laminar at $\bar{R} \approx 540$.

At $200mm$ downstream of the device, the turbulence spots started to appear earlier: at $\bar{R} \approx 350$ and at $\bar{R} > 425$ the signal resembled that of a fully turbulent boundary layer. Similar characteristics can be observed from the signal captured at the last station, $y = 500mm$, except that the frequency of the appearance of turbulence spots seemed to be slightly reduced at $\bar{R} = 375$ and $\bar{R} = 400$ indicating the disturbances were decreasing as they travelled downstream. Still, at $\bar{R} > 425$, the signal was similar to that of a fully turbulent boundary layer.

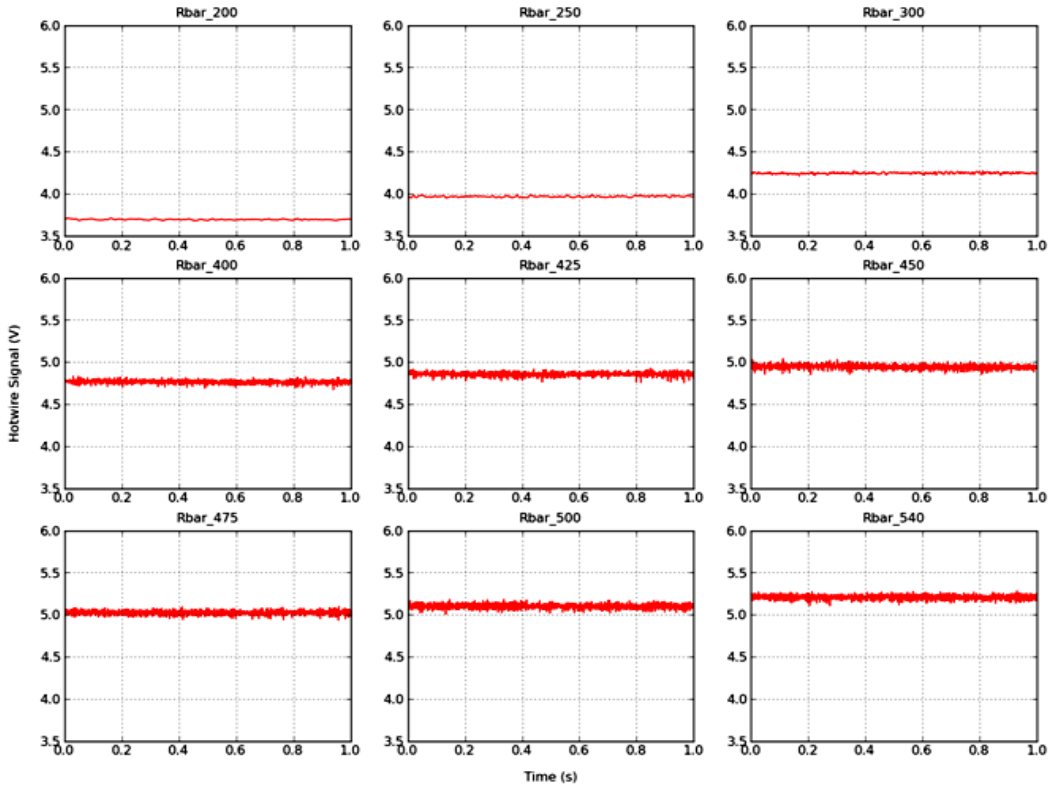


Figure 5.44: Hot wire signal at the leading edge region of the device.

During Gaster's [45], experiment the 'bump' was effective up to $\bar{R} \approx 420$. The growth of the turbulent spots, initiated by a pulse of spark, was analysed along the relaminarised attachment line and it was concluded that the disturbances started to amplify in the spanwise direction at $R_{\theta AL} > 113$ or $\bar{R} > 280$. In the current experiment there were no artificial disturbances and the lowest \bar{R} at which the turbulence spots started to appear was at $\bar{R} = 350$ at $y = 200mm$ and $y = 500mm$. At $\bar{R} = 375$, the attachment line was still laminar as confirmed by velocity profile in Figure 5.48. While testing in a tunnel with a moderate turbulence intensity level of 0.12%, Poll concluded that the amplification of the

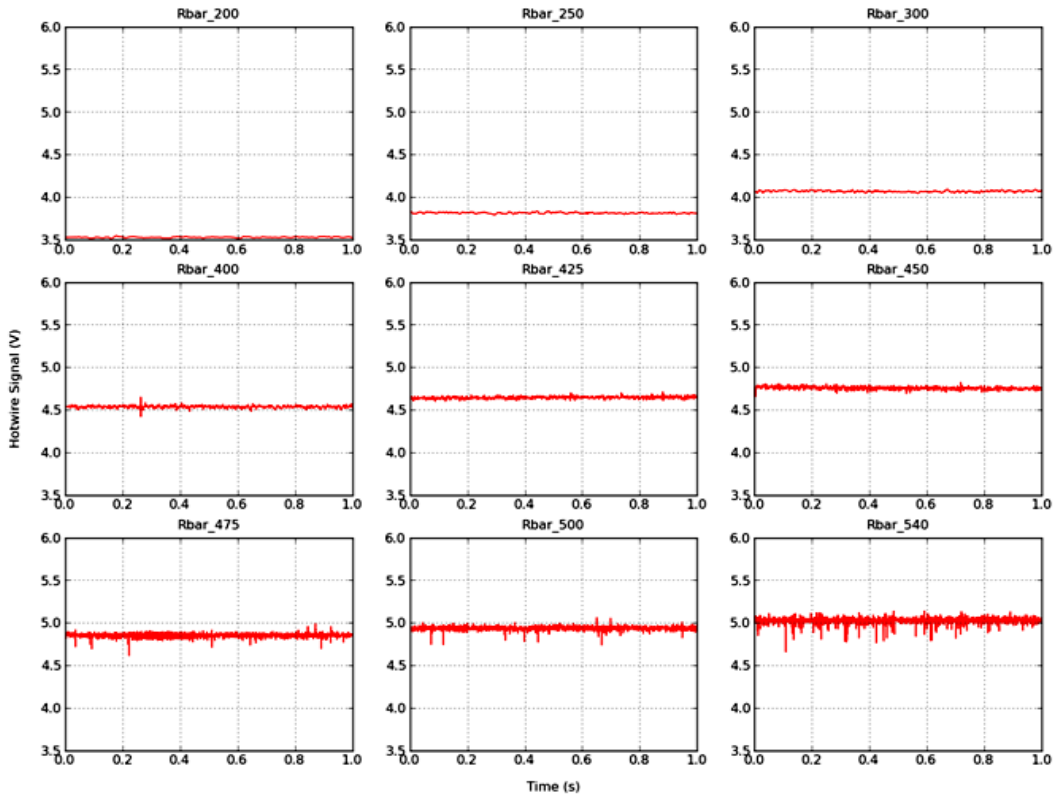


Figure 5.45: Hot wire signal in the aft region of the device.

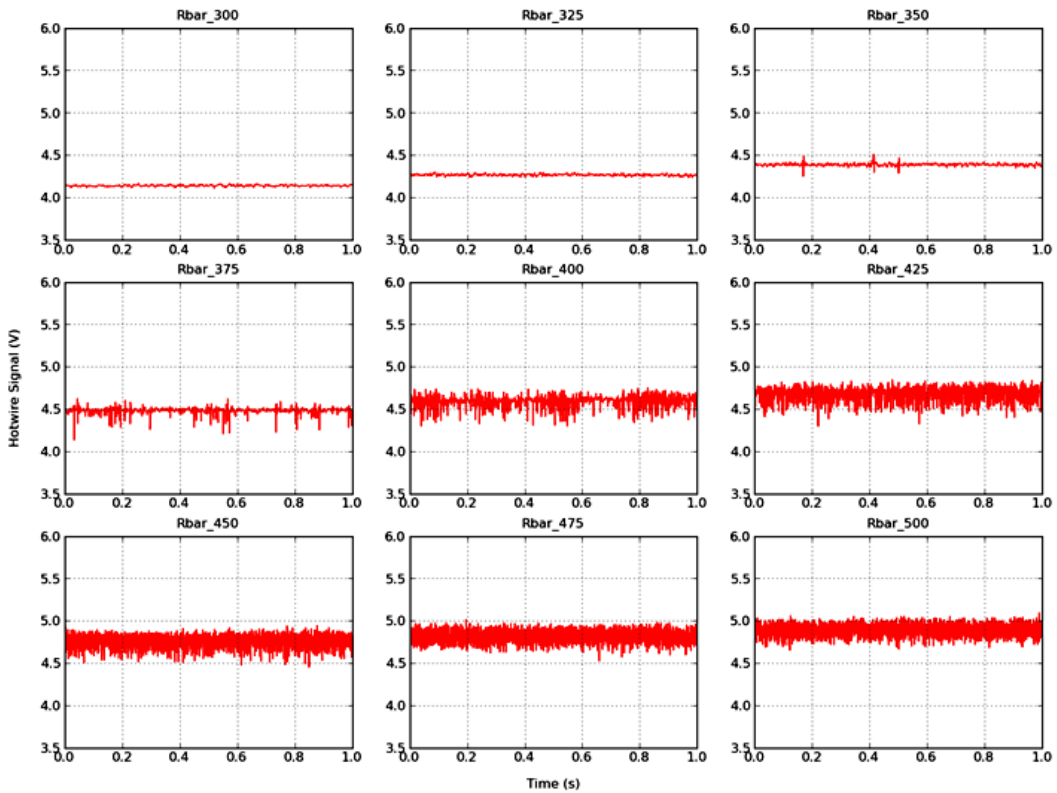


Figure 5.46: Hot wire signal at 200mm downstream of the device, with larger resolution in \bar{R} .

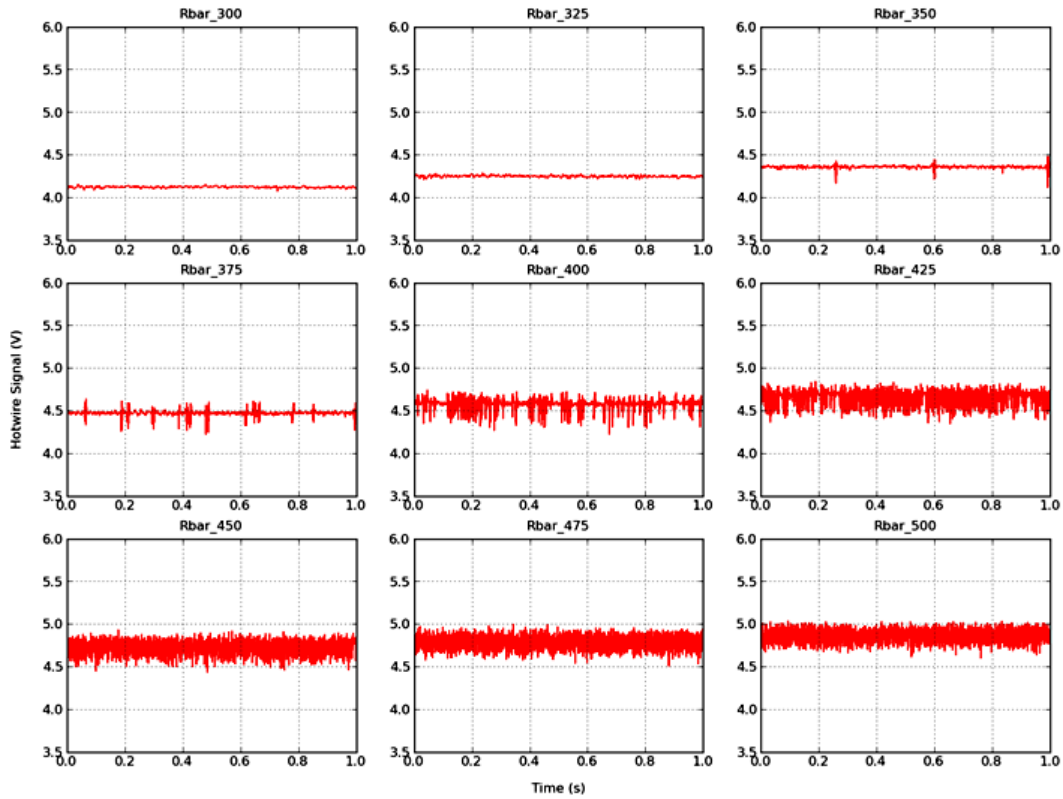


Figure 5.47: Hot wire signal at 500mm downstream of the device, with larger resolution in \bar{R} .

instabilities was mainly governed by the size of the initial disturbance due to roughness in the inboard region. According to Badalamenti [13] the freestream turbulence intensity in the T2 wind tunnel, which was used for the current experiment, ranges from 0.2 to 0.5%. Considering the fact that attachment line transition is due to travelling instabilities similar to Tollmien-Schlichting instability, in the absence of large surface protuberances it might be fair to assume that the main mechanism for transition originates from the freestream, such as background noise and turbulence structures.

Sengupta and Dipankar [106] demonstrated numerically, using a receptivity model, that subcritical transition along the attachment line is due to the convecting vortices outside of the viscous layer that leads to ‘by-pass’ transition. Therefore, contamination from the vortical structures in the quite highly turbulent freestream might be a plausible reason for the failure of the device to work at $\bar{R} > 400$ at $y = 200$ and $y = 400mm$. During the final stage of the experimental campaign, when the attachment line control experiment was undertaken, a large amount of dust was generated in the vicinity of the tunnel due to

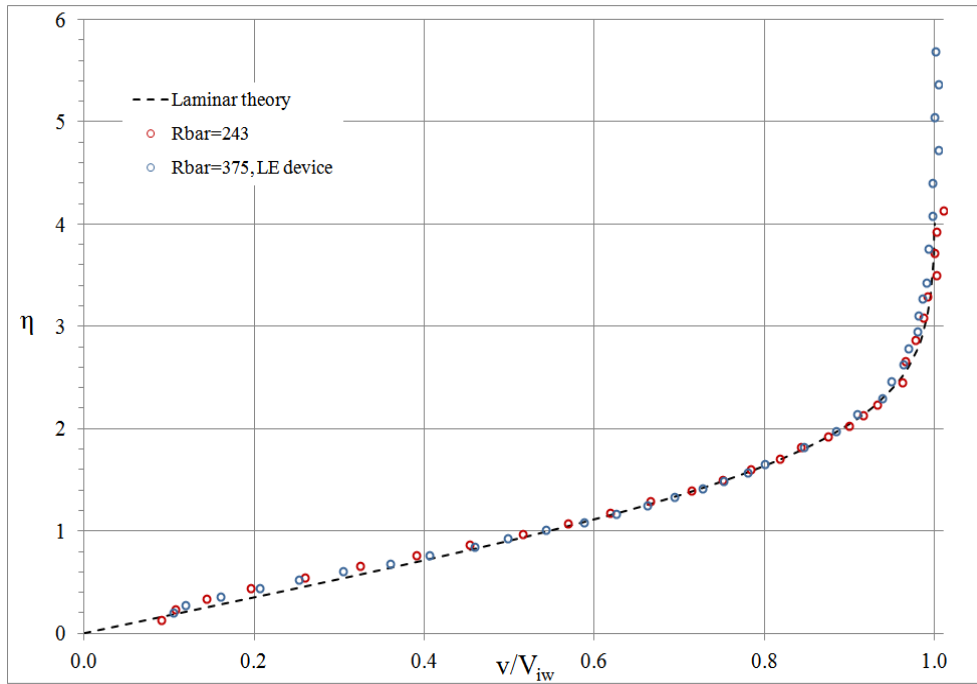


Figure 5.48: The laminar velocity profile downstream of the leading edge device at $\bar{R} = 375$.

construction work and this might have led to an introduction of fine cement dust particle inside the tunnel. In addition the hot wire encountered frequent damage through collision with particles accumulated in the tunnel. In order to confirm this hypothesis, further testing will be required following a thorough dust extraction procedure from the wind tunnel. On the other hand, this undesirable circumstance might be a boon in disguise, as it creates motivation for generating further insight into the issue of instability along the attachment, due to both travelling disturbances and structures from the freestream and also for the study of the phenomenon of receptivity.

Chapter 6

The Flow Near the Attachment Line

6.1 Topology of Viscous Three Dimensional Flows

As mentioned previously, the dominant spanwise component in the vicinity of the attachment line causes the external streamline (streamline at the edge of the boundary layer) at the leading edge to diverge away from the attachment line in a curved path as shown in Figure 6.1. The two dimensional flow vector tangential to the external streamline can be resolved into the streamwise velocity component, U_s , and the orthogonal velocity component, V_s . The centripetal acceleration of the curving streamline is generated by the transverse pressure gradient across the streamline. According to Cebeci and Cousteix [24], along the external streamline with radius of curvature, R , the transverse pressure gradient and the centripetal acceleration can be related as

$$\frac{\partial p}{\partial n} = -\frac{\rho_\infty U_s^2}{R} \quad (6.1)$$

The viscous flow is somehow more complicated and, in the direction tangential to the external streamline, the velocity profile resembles that of the streamwise flow on flat plate

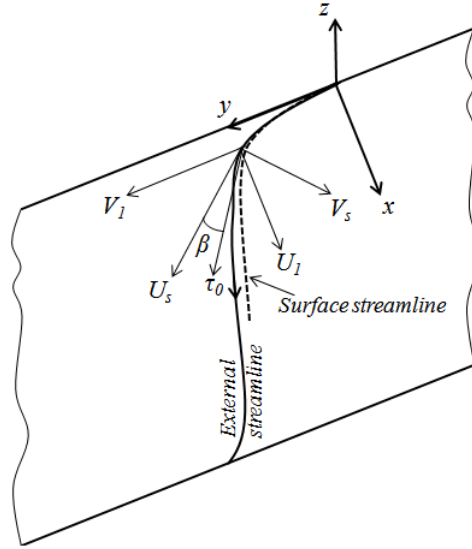


Figure 6.1: Schematic representation of the viscous flow at the leading edge of a swept wing.

or aerofoil. From boundary layer theory it can be assumed that the pressure difference across the boundary layer normal to the surface is negligible as the boundary layer is thin relative to the local radius of curvature. As the flow is retarded through the boundary layer and comes to rest at the surface where the no-slip condition holds, the relation between the transverse pressure gradient and the centripetal acceleration can be given as

$$\frac{\partial p}{\partial n} > -\frac{\rho_{\infty} u_s^2}{r} \quad (6.2)$$

The transverse pressure gradient remains constant through the boundary layer, and exceeds the centripetal acceleration, thereby forcing the fluid in the direction of the dominating pressure gradient which acts towards the centre of the curvature of the external streamline, as shown in Figure 6.1. This transverse velocity component is also referred as the ‘pressure-driven’ crossflow velocity component, v_s , which can be related to the streamwise component, u_s by the expression

$$\tan \beta_s = \frac{v_s}{u_s} \quad (6.3)$$

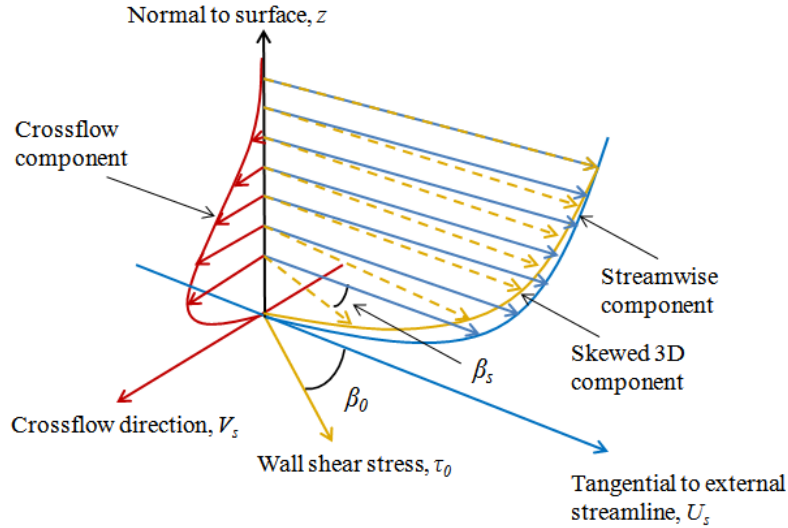


Figure 6.2: Schematic representation of the streamwise and crossflow velocity profile in a three dimensional boundary layer, figure adapted from McLean [79].

At the wall, $u_s = v_s = 0$, therefore the angle between the crossflow and streamwise velocity component is indeterminate. By applying L'Hopital's rule the angle of the limiting streamline can be estimated using

$$\beta_0 = \tan^{-1} \left[\frac{\partial v}{\partial z} / \frac{\partial u}{\partial z} \right] \quad (6.4)$$

In the near wall region the effect of viscosity is dominant and in most cases the transverse pressure gradient is balanced by the crosswise shear stress, τ_{ny} , which is a component of the streamwise shear stress.

$$\frac{\partial p}{\partial n} = \frac{\partial \tau_{ny}}{\partial y} \quad (6.5)$$

From Cooke [31], Cumpsty [33] and later Cebeci and Cousteix [24], if the transverse pressure gradient encounters a change in direction, associated with an inflexion point in the external streamline, the crossflow component near the wall will undergo a reversal in direction as demonstrated schematically in figure 6.3. The effect does not occur immedi-

ately after the inflection point, and it first appears very close to the surface where inertial effects are weaker. This behaviour has been observed in laminar boundary layers, where the transverse pressure gradient is balanced by the crosswise wall shear stress, by the relation given in equation 6.5. Any change in the direction of the pressure gradient will also result in a change in the direction of the crosswise shear stress which occurs near the wall and hence, the formation of the cross-over type crossflow profiles.

However, Cooke, Cumpsty and Cebeci and Cousteix, assumed that similar effect should occur a in turbulent boundary layer as well in the presence of an inflection in the external, however the effects of the turbulent stresses were not accounted. According to Cooke, in the turbulent case this effect is supposed to be less pronounced as the Reynolds stresses tend to counteract the growth in the crossflow component. In addition, Cooke suggested that the external streamline curvature also affects the growth of the boundary layer where along a converging streamline the boundary layer thickens more rapidly as opposed to a diverging streamline where the boundary layer has more space to ‘spread itself’.

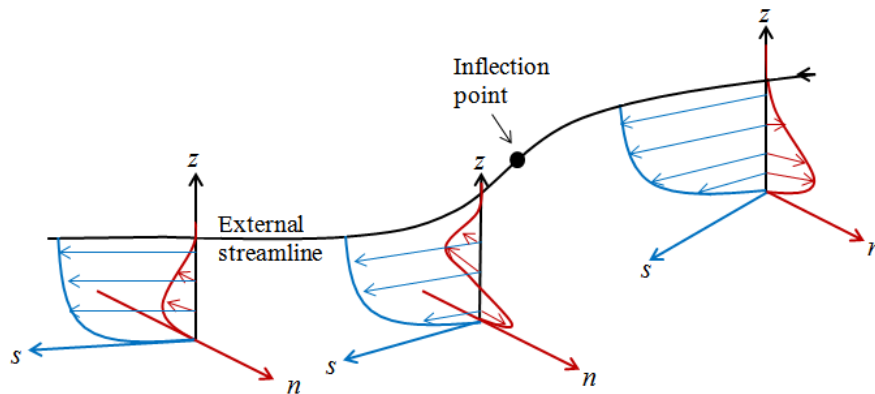


Figure 6.3: The three dimensional velocity profile upstream and downstream of a point of inflection in the external streamline, where s is tangential and n orthogonal to a point along the streamline. Figure adapted from Cebeci and Cousteix [24]

6.2 Viscous Flow on Swept Wings

6.2.1 Laminar and Transitional

Interest in laminar flow has increased tremendously due to the economic and environmental issues covered in section 1.1, therefore there is a continuing need for more accurate prediction tools for the design and optimisation of flow control technologies prior to expensive wind tunnel or flight test. The theory for laminar boundary layers is well established and the development can be predicted using methods that solve the full Navier-Stokes, boundary layer equations or others such as the Falkner-Skan-Cooke method which is derived from boundary layer theory. But, due to the amplification of instabilities, the boundary layer will undergo transition at some stage on the wing and in the worst case this might occur very close to the leading edge. Despite the large body of research in boundary layer transition, prediction still relies on semi-empirical methods and it is very difficult to extrapolate wind tunnel results up to flight tests conditions due to the difference in the turbulence levels and other environmental contamination sources. So far the ability to achieve any laminar flow at all on conventional transonic commercial aircraft has been hindered by the phenomenon of attachment line contamination which renders the rest of the flow turbulent, thus this issue needs to be addressed prior to any further consideration of laminar flow control strategy.

Even if leading edge contamination has been avoided or the attachment line has been relaminarised or decontaminated, the flow downstream will still be subjected to transition due to the amplification of other forms of instability. The most common instabilities that the flow on a swept wing can encounter are Tollmien-Schlichting and the crossflow instabilities which are the most dominant due to the presence of sweep. Experimental investigations conducted by Anscombe and Illingworth [2] in the early 1950s demonstrated that wing sweep had the effect of moving the location of transition further upstream. The findings from their wind tunnel campaign are summarised in Figure 6.4, which shows

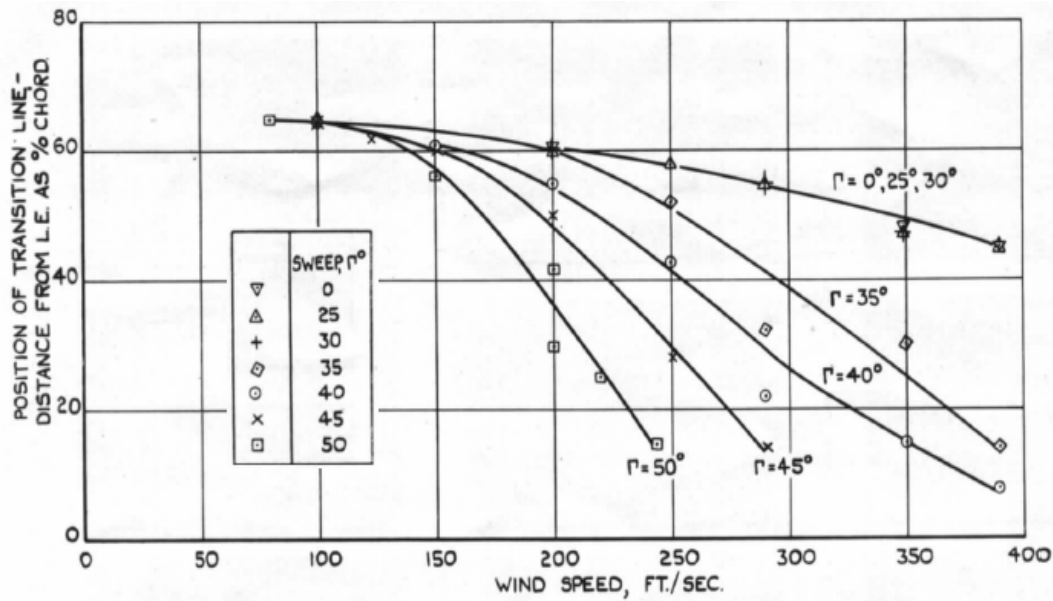


Figure 6.4: The variation in the location of transition at different wind speed for a series of sweep angle.

the position of transition at different speed for a given sweep angle. At sweep angle less than or equal to 30° , transition shifted upstream slowly with increase in wind speed and in these cases it was mainly due to the amplification of Tollmien-Schlichting modes. Further increases in sweep angle resulted in a drastic upstream shift in the transition front for wind speeds greater than 200 ft/s . This effect was more severe at higher sweep angle: it occurred at lower wind speed and transition moved towards the leading edge with increase in Reynolds number.

Similar behaviour was observed during flight test by Gray [49] at the leading edge of swept wings using the sublimation flow visualisation technique. Further studies by Owen and Randall [85][86] demonstrated that this effect was due to a dynamic instability in three dimensional boundary layers which is amplified in the vicinity of the attachment line, hence crossflow instability. This problem was revisited experimentally by Poll [91] [93] in the early the 1980s using the Cumpsty and Head [35][37] swept cylinder model. Sublimation techniques were employed to analyse the evolution of the fixed-wavelength stationary disturbances which are the behaviours exhibited by crossflow instability, but time-dependent disturbances were also observed. The results acquired using surface Pitot tubes for the onset and completion of transition was compared with those of Owen and

Randall and an improved criterion was proposed.

Crossflow instability is a result of the existence of an inflection point in the crossflow velocity profile as the velocity tends to zero both at the wall and the edge of the boundary layer. Crossflow instabilities exist as both stationary and travelling modes, where stationary instabilities are more common in low turbulence environments such as flight conditions and travelling waves are more dominant in high-turbulence environments such as wind tunnels. The mechanism responsible for the amplification of crossflow instability and break-down to transition is quite complicated and very precise instrumentation is required to capture this phenomenon experimentally. Regardless of the complexity, numerous studies have been reported and in 2003 Saric et al. [101] presented a summary of both experimental and numerical analysis undertaken in the 1990s. Most of the breakthroughs in the understanding of crossflow instability emanated from this study. According to Saric et al. the breakdown of the stationary crossflow waves is a highly non-linear process involving secondary instability which amplifies at a very fast rate and results in almost immediate transition.

6.2.2 Turbulent

The attachment line Reynolds number on regional transonic commercial aircraft at cruise condition varies between $174 < \bar{R} < 400$ from the outboard to the inboard section respectively and for long-haul aircraft it lies between $285 < \bar{R} < 570$. In this case the attachment line will be susceptible to contamination and is bound to be fully turbulent on a large portion of the wings of regional jets and throughout the whole of wing of long-haul aircraft. According to Poll [92] it is unlikely that the flow will relaminarise downstream of the turbulent attachment line on most transonic aircraft, however Thompson [114] postulated that the presence of a favourable pressure gradient on the supercritical aerofoil section might lead to relaminarisation even at transonic cruise conditions. This will be revisited in section 6.2.3. In this section fully turbulent flow, right from the attachment

line and extending downstream, will be considered.

Three-dimensional turbulent flow over swept wings has been studied in detail, both experimentally and numerically, so as to develop tools for the accurate prediction of viscous drag during wing design and optimisation. Numerical methods have demonstrated the ability to predict the development of the turbulent boundary layer with acceptable accuracy both in favourable and in adverse pressure gradients, where the flow is approaching separation. Nevertheless, the viscous flow in the vicinity of the attachment line is not reported due to the precision involved in capturing the highly three dimensional viscous flow which is extremely thin at that particular region. The lack of experimental data for this region has also restricted the validation of the leading edge modelling in most numerical methods. A few comparisons between experimental and numerical studies, using various turbulence models, have also been presented in Chapter 7 of Cebeci and Cousteix [24].

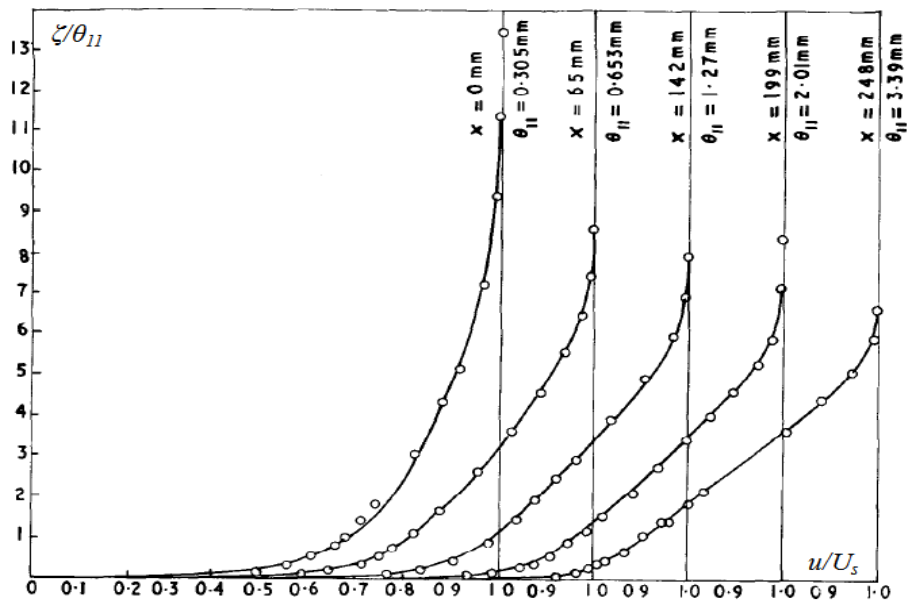


Figure 6.5: Streamwise velocity profiles captured by Cumpsty and Head [37] at various chordwise station along the swept circular cylinder. The solid lines represents Thompson's profile [113] and \circ , the experimental measurements.

The experimental study which is most relevant to the current investigation was conducted by Cumpsty and Head [37] on a circular cylinder faired to a teardrop, with a normal to leading edge chord length, $c = 457\text{mm}$ and swept by 62.5° . The streamwise velocity

profiles captured using hot-wire anemometry at different chordwise location are presented in Figure 6.5 which shows outstanding agreement with Thompson's [113] 'two-parameter family' velocity profile. The velocity profiles have also been presented in wall units in figure 6.6 and, in the inner layer region, satisfactory agreement can be observed with the universal log-law for the profiles captured at most chordwise stations. In the outer region the velocity ratio, u/u_τ , increases sharply at the downstream stations due to the increasing adverse pressure gradient and this behaviour is quite common on flow around aerofoil.

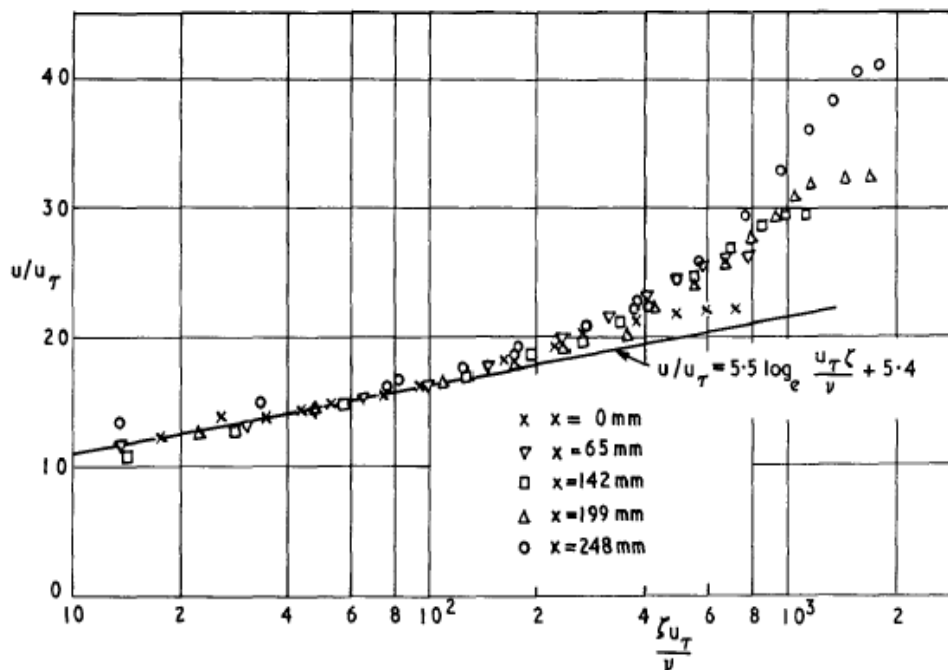


Figure 6.6: Streamwise velocity profiles captured by Cumpsty and Head [37] presented on a law-of-wall plot.

The occurrence of crossflow is purely due to the three-dimensional effects and the mechanism responsible for their development has been introduced in section 6.1. Mager [77] proposed a general representation for the turbulent crossflow velocity profile. This relationship was derived in parallel with the measurements made by Gruschwitz (reference provided in [77]) on flows in curved channel. According to Mager, at a particular point inside the boundary layer, the normalised local crossflow velocity component can be expressed as a function of the angle between the limiting and external streamline, β_0 :

$$\frac{v_s}{U_s} = \left(1 - \frac{z}{\delta}\right)^2 \tan \beta_0 \quad (6.6)$$

The crossflow velocity profiles captured experimentally by Cumpsty and Head [37] are compared with Mager's representation given by equation 6.6, in Figure 6.7. The experimental results obtained at $x = 199\text{mm}$ and $x = 248\text{mm}$ correlate very well with Mager's representation, but the agreement starts to deteriorate at $x \leq 142\text{mm}$. The fact that the model was set at an incidence of -1° and the attachment line might have shifted slightly downstream along the upper surface, explains the presence of the crossflow profile, at $x = 0\text{mm}$, even if the model was symmetrical. Mager's formula cannot represent the cross-over type crossflow profile at $x = 65\text{mm}$ because equation 6.6 does not allow for a change in direction of the velocity component. Mager's representation assumes that the variation in β is small within the boundary layer, however, this is not true for diverging flows especially in the vicinity of the attachment line.

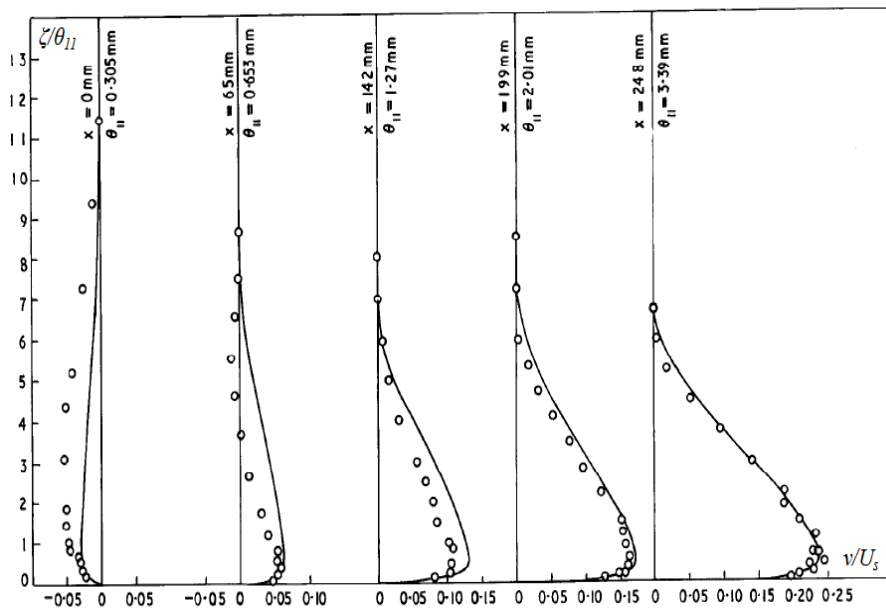


Figure 6.7: Crossflow velocity profiles captured by Cumpsty and Head [37] and compared with Mager's profiles given by equation 6.6. The solid lines represent Mager's profile [77] and \circ , the experimental measurements.

The turbulent crossflow velocity profiles can also be represented by Johnston's [64] two-layer hodograph model which is presented in a triangular form, in figure 6.8.

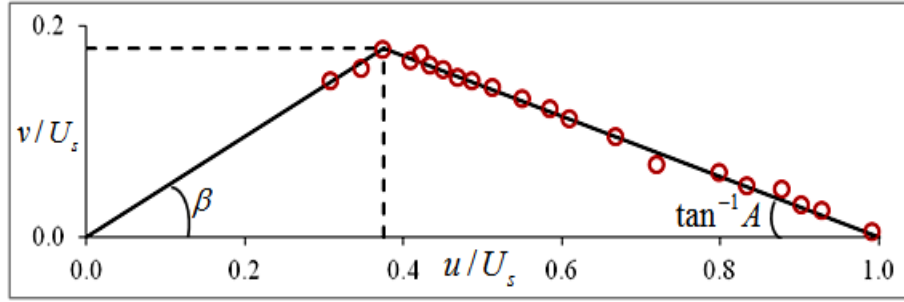


Figure 6.8: Johnston triangular form of the crossflow velocity profile presented by [33]

The first region, which represents the near wall layer, is dominated by shear stress and, assuming that the profile is linear, it can be represented as

$$v = u \cdot \tan \beta \quad (6.7)$$

In the second layer or the velocity defect region, which is considered the outer region, the flow is assumed to be inviscid (applies only to crossflows) and can be expressed as

$$v = A(U_s - u) \quad (6.8)$$

where,

$$A = \frac{v}{(U_s - u)} = U_s^2 \int_0^{\frac{\pi}{2} - \psi} \frac{d\alpha'}{U_s^2} \quad (6.9)$$

and α' , represents the angle through the external streamline has turned with respect to the x-axis.

Similarly to Mager's profile, Johnston's profile does not account for the change in direction of the velocity component and therefore the cross-over type profiles cannot be represented accurately. But, unlike Mager's representation, the shape of the profile given by Johnston is inherently proportional to the streamwise velocity defect. The crossflow

velocity profiles captured by Cumpsty and Head [37] are compared with Johnston's representation in triangular hodograph form in Figure 6.9. Overall the experimental data fit well with the hodograph model and, in order to represent the cross-over type profile occurring at $x = 65\text{mm}$, a modification to Johnston's representation was proposed by Cumpsty [33]. Although, Johnston's model appears to be more accurate than Mager's, the simplicity of Mager's model makes it more attractive for use in solving the three dimensional momentum integral equations. During the validation of their numerical method based on three dimensional momentum integral equation coupled with entrainment with experimental results, Cumpsty and Head [37] demonstrated that, as the magnitude of the crossflow velocity component was small in comparison with the streamwise component, the inaccuracy resulting from Mager's model was negligible.

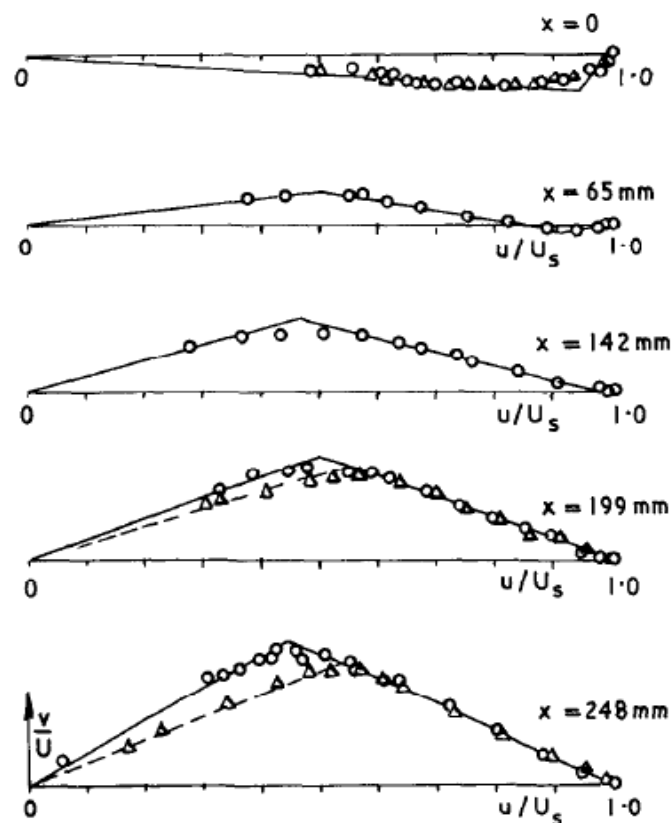


Figure 6.9: Crossflow velocity profiles captured experimentally by Cumpsty and Head [37] and represented in Johnston's hodograph plot. Where 'Δ' represents measurements using the 'original' traverse and 'o', represents the measurement made by a modified, 'slender' traverse

The accuracy of numerical methods based on Mager's model is meant to increase in the

region where the crossflow components are uni-directional through the boundary layer and in the region where the external streamline is coincident or parallel to the limiting streamline. From Thompson's [113] study, Cumpsty and Head's [37] experiment and the individual study reported by Cumpsty [33] it was also demonstrated that both the models proposed to represent the streamwise and crossflow velocity profiles were within reasonable accuracy of experimental data. Unfortunately these results are not sufficient to validate the leading edge approximation in Callisto as no details of the flow in the immediate vicinity of the attachment line have been presented. Even the measurement made by Cumpsty and Head [37] right downstream of the attachment line is not suitable as it lies outside the current domain of interest. Thus a new experiment was conducted to capture the three-dimensional viscous flow starting from the attachment line and proceeding downstream until $x/c = 0.03$. The outcome of the experimental campaign will be described in the sections that follow.

6.2.3 Relaminarisation Downstream of Turbulent Attachment Line

As a favourable pressure gradient can act as a mechanism for relaminarisation, Poll [92] [91] investigated the possibility of natural relaminarisation of the attachment line and the flow downstream. The relation between pressure gradient and skin friction coefficient given by Narasimha and Sreenivasan [82] for two dimensional flow was extended to three-dimensional flows to incorporate the effect of streamline curvature. Following a short analytical study, Poll suggested that the maximum value of the three-dimensional acceleration parameter, K_S (referred as K_{3-D} by the latter) attainable on transonic aircraft with sweep ranging between 30° to 40° was insufficient to suggest relaminarisation would be likely. The hot-film signal obtained during the experimental study of Arnal and Juillen [4] confirmed that the boundary layer downstream of the attachment line can be relaminarised in a highly accelerating flow. Prior to these studies, the possibility of 'reverse transition' was also investigated by Thompson [114], as this effect would cause the turbulent boundary layer prediction method to collapse. According to the latter, relam-

inarisation might occur at the leading edge during transonic cruise condition due to the presence of an accelerating flow if the acceleration parameter adapted for three dimensional flow, $\Delta_s \leq -0.01$,

$$\Delta_s = \frac{\nu}{u_\tau} \frac{1}{\rho} \frac{dp}{ds'} \cos(\psi + \beta_0) \quad (6.10)$$

where, dp/ds' , represents the pressure gradient along the circumference of the leading edge, u_τ , the friction velocity, ψ the streamline divergence angle and density and viscosity ρ and ν respectively.

The most recent experimental study on relaminarisation under the effect of large favourable pressure gradient was undertaken by Mukund et al. [81] which was reported in 2012. The hot-film signals captured at various chordwise locations around the leading edge of a swept wing model are presented in Figure 6.10, for angles of incidence of 18° and 16° . As evident from Figure 6.10, due to the large incidence the attachment line had shifted significantly towards the lower surface. The experiments were conducted at $\bar{R} \approx 400$, so the attachment line was susceptible to contamination from the turbulent flow impinging on the wing root. However, cycles of relaminarisation were observed around the nose, at stations 'G' and 'K' for the incidence of 18° . Similar patterns were observed at incidence of 16° , where relaminarisation started earlier at station 'F' and again at station 'I'. From the pressure measurement around the nose and the streamline divergence angle obtained from surface oil flow, Launder's [71] acceleration parameter, K_s , transformed for an infinite swept wing, was estimated using

$$K_s = \frac{\nu}{U_s^2} \frac{dU_s}{ds} = \frac{\nu}{U_e} \frac{dU_e}{ds'} \cos^4 \psi \quad (6.11)$$

Where s' is the length of arc along the surface and in the direction of the chord normal to the leading edge, and U_e the chordwise velocity at the edge of the boundary layer.

The highlight of this investigation was that the onset of relaminarisation was observed at $K_s \approx 3.0 \times 10^{-6}$, which is the criterion proposed by Launder. But the main question is whether leading edge relaminarisation is possible at cruise conditions, where the K_s is lower than this critical value and the attachment line is usually higher than $\bar{R} = 400$.

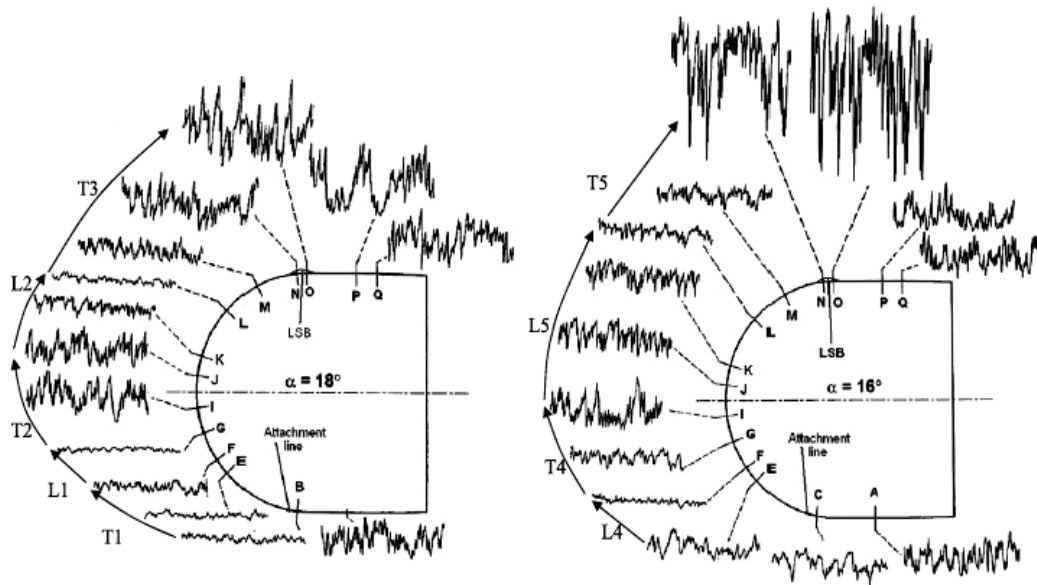


Figure 6.10: Hot-film signal of the boundary layer formed at the leading of the swept wing tested by Mukund et al. [81], at angle of incidence of 18° (LHS) and 16° (RHS). Where ‘L’-numeric and ‘T’-numeric stands for laminar and turbulent regions respectively and ‘LSB’ denotes laminar separation bubble.

6.3 Present Experimental Measurements

6.3.1 Surface Pressure Measurement

Using the electronic pressure measurement system introduced in section 3.2, the static pressure was captured at the three spanwise stations shown in figure 3.4. These stations were labelled ‘R’, ‘S’ and ‘T’ and located at equal intervals in the inboard, mid-span and outboard sections of the model respectively. The swept wing model was mounted between the floor and ceiling of the working section so as to avoid tip effects. But Figure 6.11 clearly shows that, overall, the infinite swept condition was not achieved due to the

spanwise variation in the chordwise pressure distribution. Nevertheless, for $x/c < 0.07$, which is the current experimental domain of interest, the spanwise pressure distribution is more or less constant between stations ‘S’ and ‘T’ and the flow can be assumed to satisfy the infinite swept condition in that region. Therefore, the boundary layer measurement was made in that particular region.

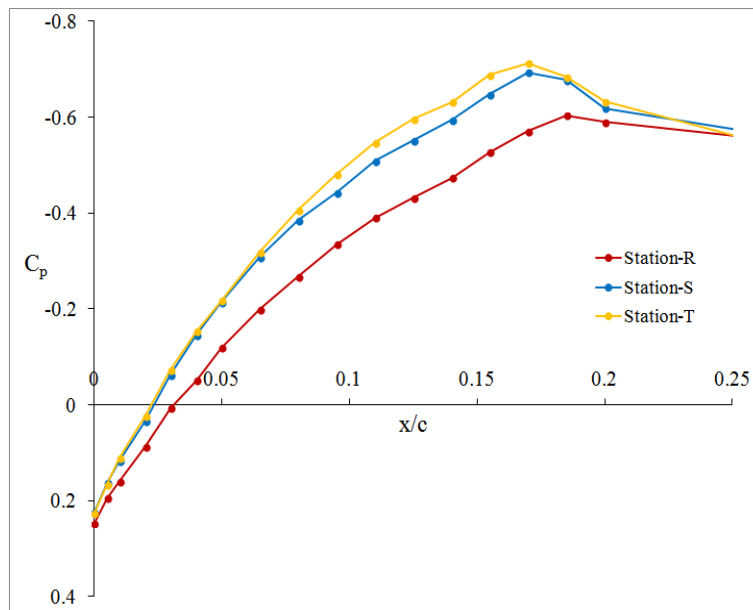


Figure 6.11: The pressure distribution around the leading edge of the experimental model along the line-of-flight chord.

6.3.2 Velocity Profiles at the Attachment Line

For the measurement of two velocity components in three-dimensional flows, the most common technique is using a hot wire probe with two wires in a crossed configuration (cross-wire). However, due to limitations posed by the thickness of the boundary layer, which is of approximately 3mm at the attachment line and not expected to grow very rapidly downstream within the experimental domain, the cross-wire was not considered suitable for the current task and a single-yawed (SY) hot wire probe, which is significantly smaller, was preferred. From Figure 3.26 the axis of the probe-stem was aligned along the spanwise direction, therefore the hot wire sensor was yawed by 45° with respect to the spanwise and chordwise direction. At each chordwise measurement station the hot-wire

traverse was conducted twice, firstly with the sensor yawed in the clockwise direction and then, through rotation by 180° about the probe axis, it was brought into the anti-clockwise direction. It was important to ensure that the same traverse profile was maintained so that the hot-wire output was captured at the same corresponding vertical position during the measurement in both orientations. The necessary near wall alignment was achieved by inclining the optical bed about the horizontal axis, as shown in Figure 3.26.

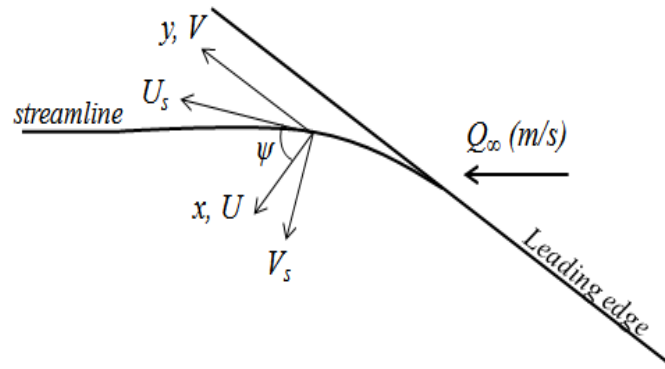


Figure 6.12: Schematic representation of the streamwise and crossflow velocity profiles along a diverging streamline at the leading edge of a swept wing

The voltage output from the SY-probe was converted into the equivalent effective velocities, V_{e1} and V_{e2} for the clockwise and anticlockwise orientations using equation 4.29, by substituting for the calibration constants ‘A’ and ‘B’ estimated from a linear data fit through the calibration results presented in Figure 4.10. From the effective velocities, the chordwise and spanwise velocity components were determined using either equations 4.34 and 4.35 with appropriate values of the ‘k’ coefficients or equations 4.39 and 4.40 with the value of α_e , in both cases determined from the yaw calibration exercise and are presented in Figures 4.17 and 4.16 respectively. However, to estimate the streamwise and crossflow components further velocity decomposition was required. Based on the schematic representation of the velocity vectors shown in figure 6.12, the streamwise and crossflow velocity component can be expressed as

$$\begin{aligned} U_s &= V \cos \psi - U \sin \psi \\ V_s &= V \sin \psi + U \cos \psi \end{aligned} \tag{6.12}$$

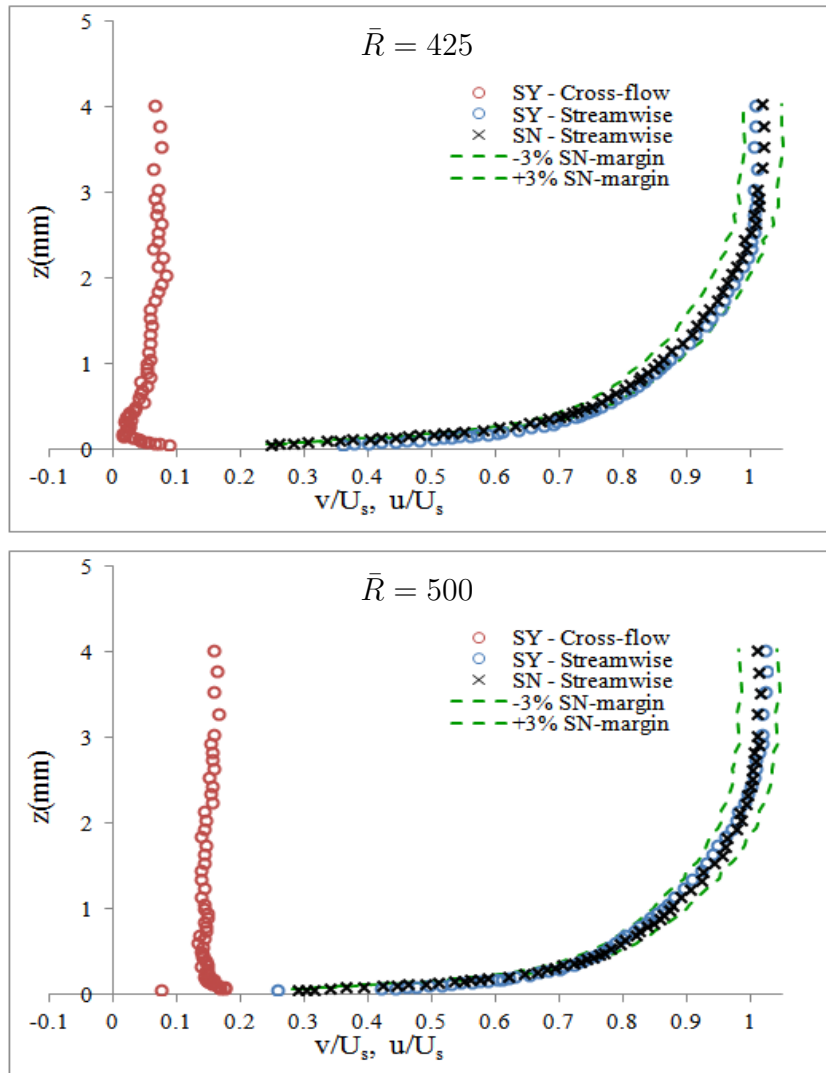


Figure 6.13: Comparison of the velocity profile at the attachment line captured using the SN and SY probe, where the k yaw calibration coefficient was employed.

The technique for capturing two velocity components using an SY-probe rather than a cross-wire probe is not very common and therefore needed prior validation. Therefore the measurement at the attachment line was repeated using the SY-probe and compared with the previous measurement obtained from the SN-probe, which demonstrated good agreement with laminar theory and from both experimental and numerical turbulent results presented in section 5.4. The SY-probe measurements were repeated at $\bar{R} = 425$ and $\bar{R} = 500$, as at these conditions the attachment line was expected to be fully turbulent. The results are presented in Figures 6.13 and 6.14, where the velocities were determined using the methods involving the ' k ' and ' α_e ' yaw coefficients respectively. The streamwise velocity profiles for all the cases were within acceptable agreement with

the measurement made using the SN probe, lying within the $\pm 3\%$ error margin represented by the dotted line, except in the near wall region where the velocity obtained from the SY-probe is slightly higher.

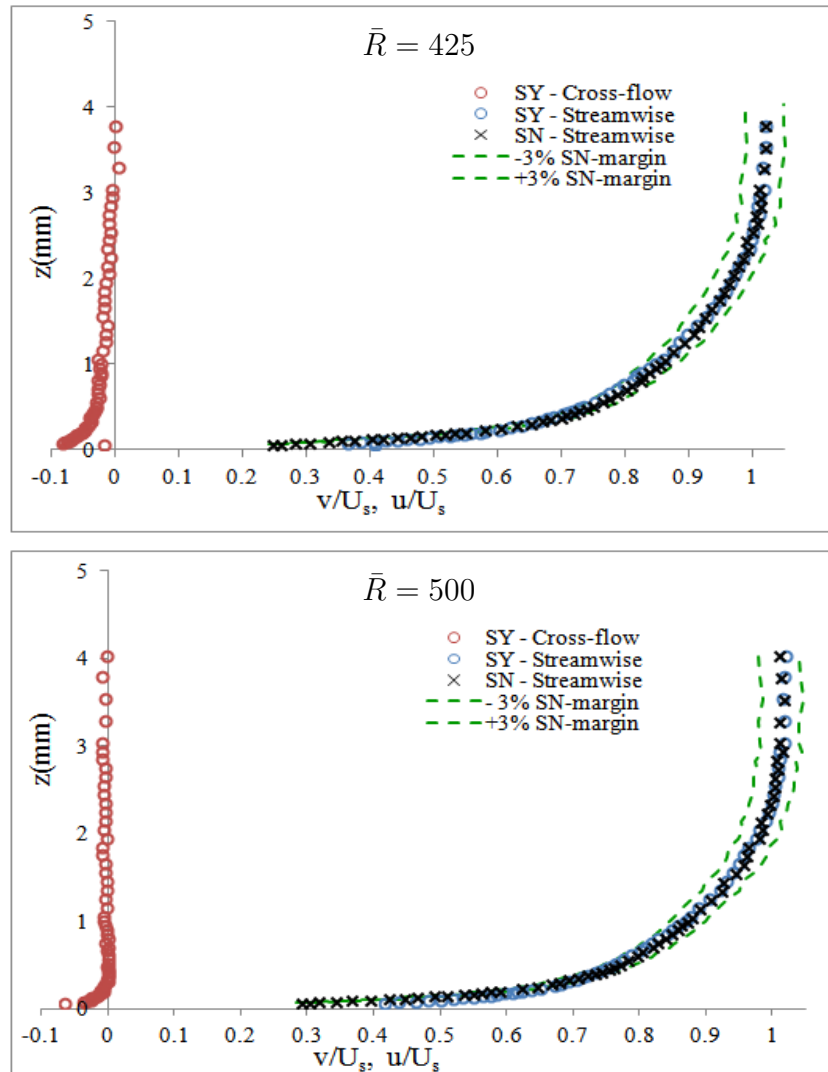


Figure 6.14: Comparison of the velocity profile at the attachment line captured using the SN and SY probe, where the α_e yaw calibration coefficient was employed.

The attachment line flow is purely spanwise, thus the chordwise velocity and crossflow velocity components should be zero. The crossflow profiles of considerable magnitude estimated using the ‘k’ yaw coefficient method and shown in Figure 6.13 suggests that this method is not very accurate and might even deteriorate during the measurement downstream of the attachment line where crossflow velocities are actually expected. The large scatter observed in the actual value of k (see Figure 4.17) determined from the calibration might explain the discrepancies arising from this method. Therefore the rest of the data

analysis was conducted using α_e .

From the method involving α_e , the crossflow velocity profiles were still present, but of lower magnitude and could be assumed to be due to the difficulty in ensuring that the probe was centered on the attachment line. Hence, the measurements might have been slightly contaminated by the developing crossflow components downstream of the actual position of the attachment position. Besides, the actual value of α_e determined from the yaw calibration shows a sensible trend in Figure 4.16, whereby a negligible dependence on speed can be observed, except at $Q < 10m/s$, and therefore this approach should be able to represent the near wall velocities with acceptable accuracy. The inherent yaw-angle-independence property of α_e also favours this method for measurements downstream of the attachment line as no further correction should be required to account for the change in the streamline direction inside the boundary layer, as long as the angle between the local flow and the wire is limited to $\alpha < 70^\circ$.

6.3.3 Streamwise Velocity Profiles Downstream of Attachment Line

The mean streamwise velocity profiles captured at each chordwise station, downstream of the attachment line on both the port and starboard side, have been presented in Figures 6.15 and 6.16, for attachment line Reynolds number $\bar{R} = 425$ and $\bar{R} = 500$ respectively. The measurements stations were situated between $x/c \leq 0.03$ and each station coincided with the pressure tappings within this particular region. From the initial analysis during the design of the experiment model in section 3.1.2 this chordwise extent should ensure that, the viscous flow in the region of $80^\circ \geq \psi \leq 90^\circ$ was definitely captured. As the symmetrical model was set at zero incidence, confirmed by experimental pressure distribution, the velocity profiles at each corresponding chordwise station on both sides are expected to be very similar, and this behaviour is demonstrated in Figures 6.15 and 6.16. In general, for all chordwise stations the velocity profiles showed very close agreement with each other except in the near wall region, where the measurements at $x/c = 0.03$ for

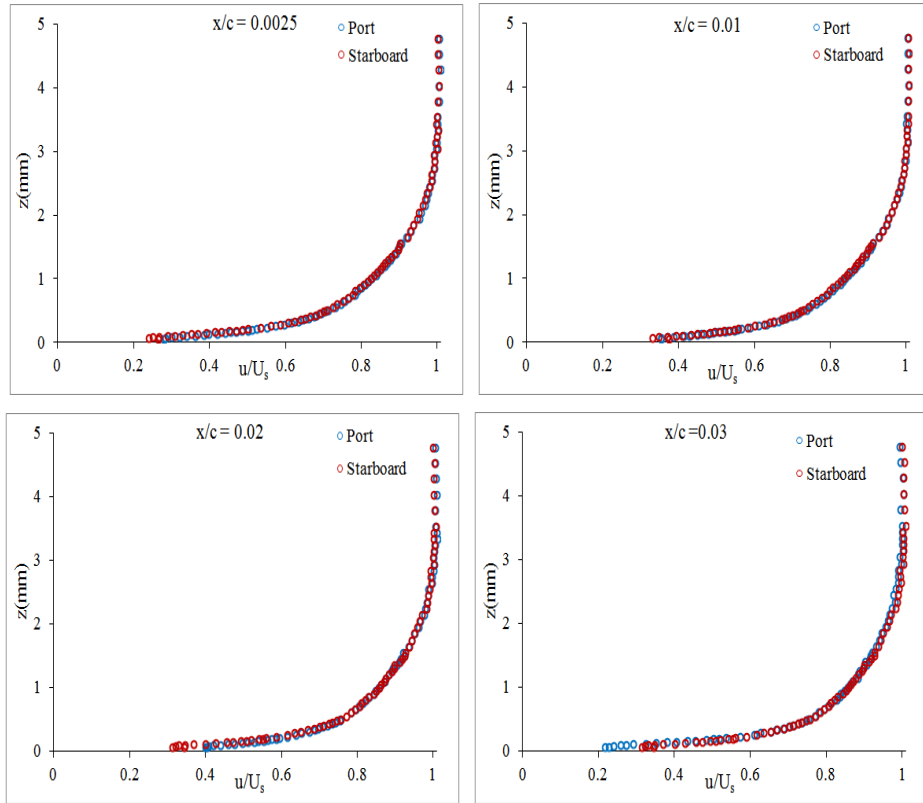


Figure 6.15: Streamwise velocity profiles downstream of the attachment line at $\bar{R} = 425$

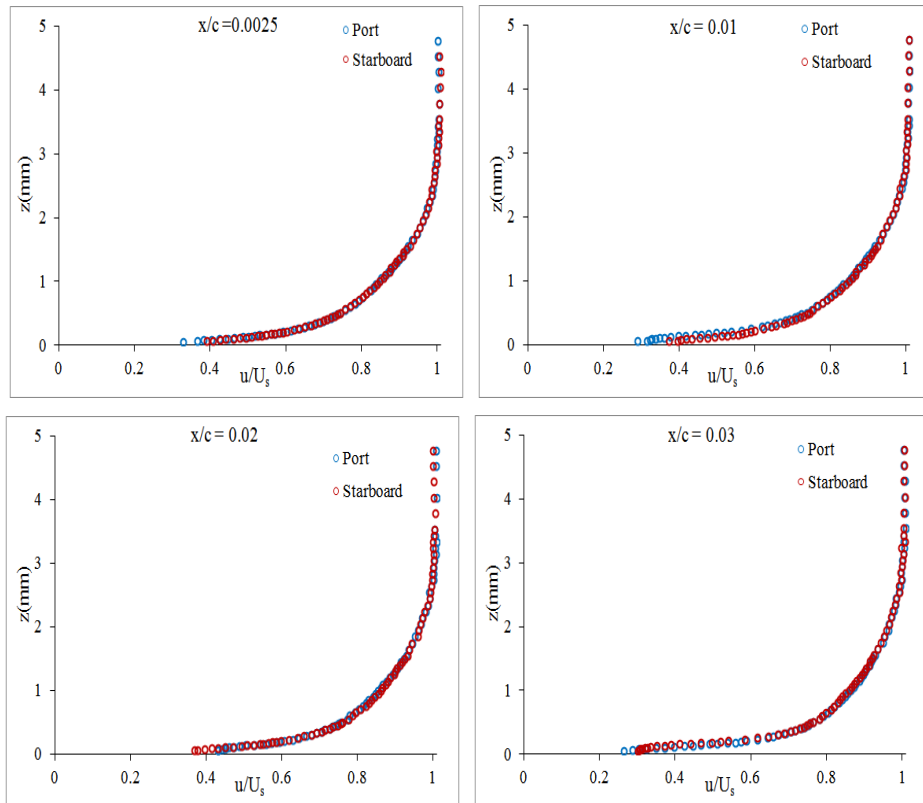


Figure 6.16: Streamwise velocity profiles downstream of the attachment line at $\bar{R} = 500$

$\bar{R} = 425$ and $x/c = 0.01$ for $\bar{R} = 500$ were the worst cases. Although the optical system proved to be useful for near-wall alignment, the measurement along the curved surface still proved challenging due to the difficulty in fixing the local surface tangent plane for each chordwise location and at the same time ensuring the hot wire was parallel to the tangent plane. As the hot wire probe was aligned by resting the probe on the surface of the model, the initial velocity measurement was subjected to heat transfer error and therefore was discarded during the calculation of the integral boundary layer quantities.

Using the surface shear stress results presented in section 6.3.6, the streamwise velocity profiles can be plotted in wall units and are shown in Figures 6.17, 6.18 and 6.19. The initial analysis was conducted using the friction velocity determined from the measured shear stress for which the results are presented in Figure 6.17. Immediately downstream of the attachment line, at $x/c = 0.0025$ for $\bar{R} = 500$, the linear region of the velocity profile shows good agreement with the universal log-law whereas at $\bar{R} = 425$ a slight deviation can be observed. Further downstream, at $\bar{R} = 500$ the correlation with the log-law is still acceptable, despite the slight downward shift of the linear region, but at $\bar{R} = 425$ a drastic departure can be seen. The main question that arises is whether this effect is due to the inaccuracy in the measurement of the shear stress or due to the boundary layer profile showing a dependence on Reynolds number, as at $\bar{R} = 500$ the discrepancy is considerably smaller.

Assuming that the departure from the log-law might be associated with inaccuracy in the shear stress measurement, using a trial and error approach the shear stress results were adjusted by a small percentage until a closer agreement with respect to the log-law was observed. At $x/c = 0.0025$ the shear stress was increased by 1% and for the cases downstream, the values were either inflated or deflated by 3 – 9%. The profiles based on the adjusted shear stress have been presented in Figures 6.18 and 6.19 for the port and starboard sides respectively. At $\bar{R} = 500$ the correlation with the universal log-law shows improvement, but at $\bar{R} = 425$ no significant changes were observed downstream of $x/c = 0.0025$. This behaviour supports the Reynolds number dependence argument

mentioned earlier and it might be the case that at lower \bar{R} , the boundary layer profile is affected by the accelerating flow at the leading edge. This point will be revisited in section 6.3.8.

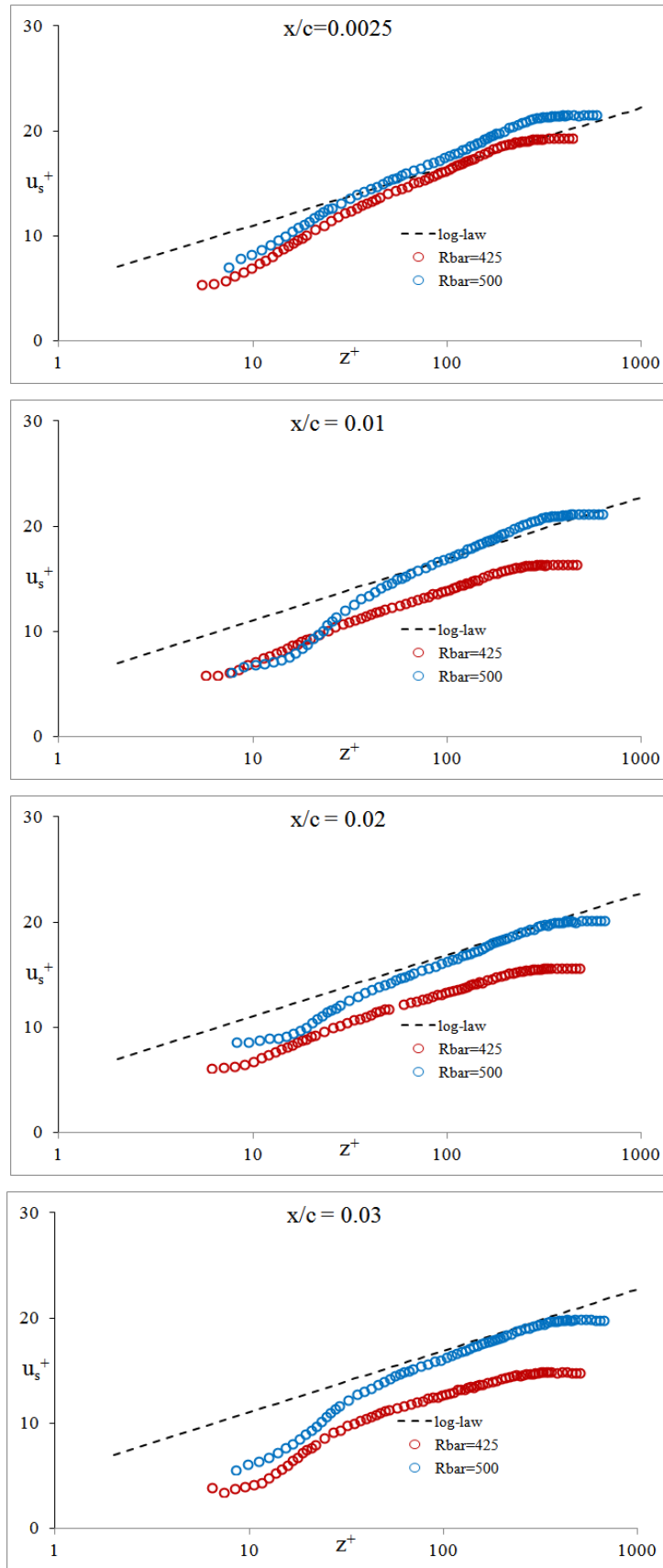


Figure 6.17: The streamwise profiles captured on the port side of the model represented in the law of the wall plots using the measured wall shear stress. The universal log-law is given by $u_s^+ = 2.5 \ln z^+ + 5.24$

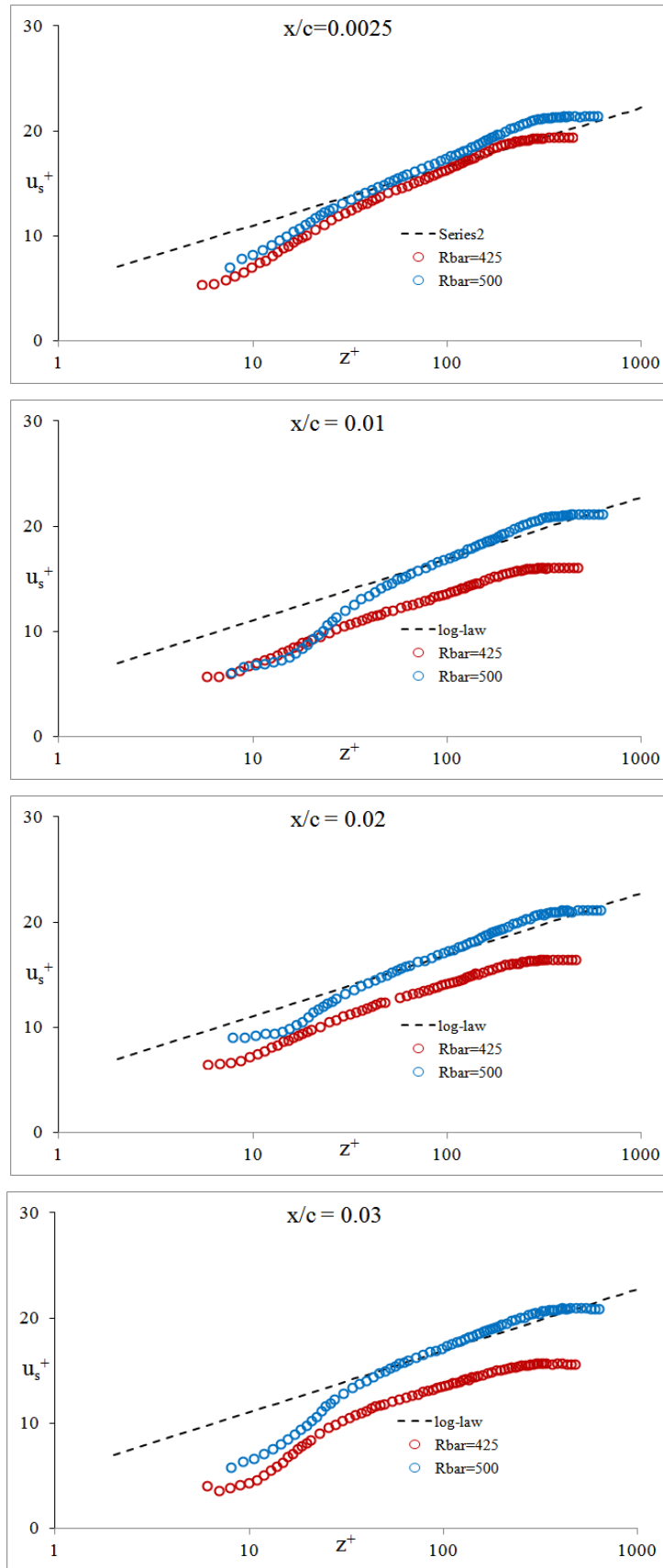


Figure 6.18: The streamwise profiles captured on the port side of the model represented in the law of the wall plots using the adjusted shear stress. The universal log-law is given by $u_s^+ = 2.5 \ln z^+ + 5.24$

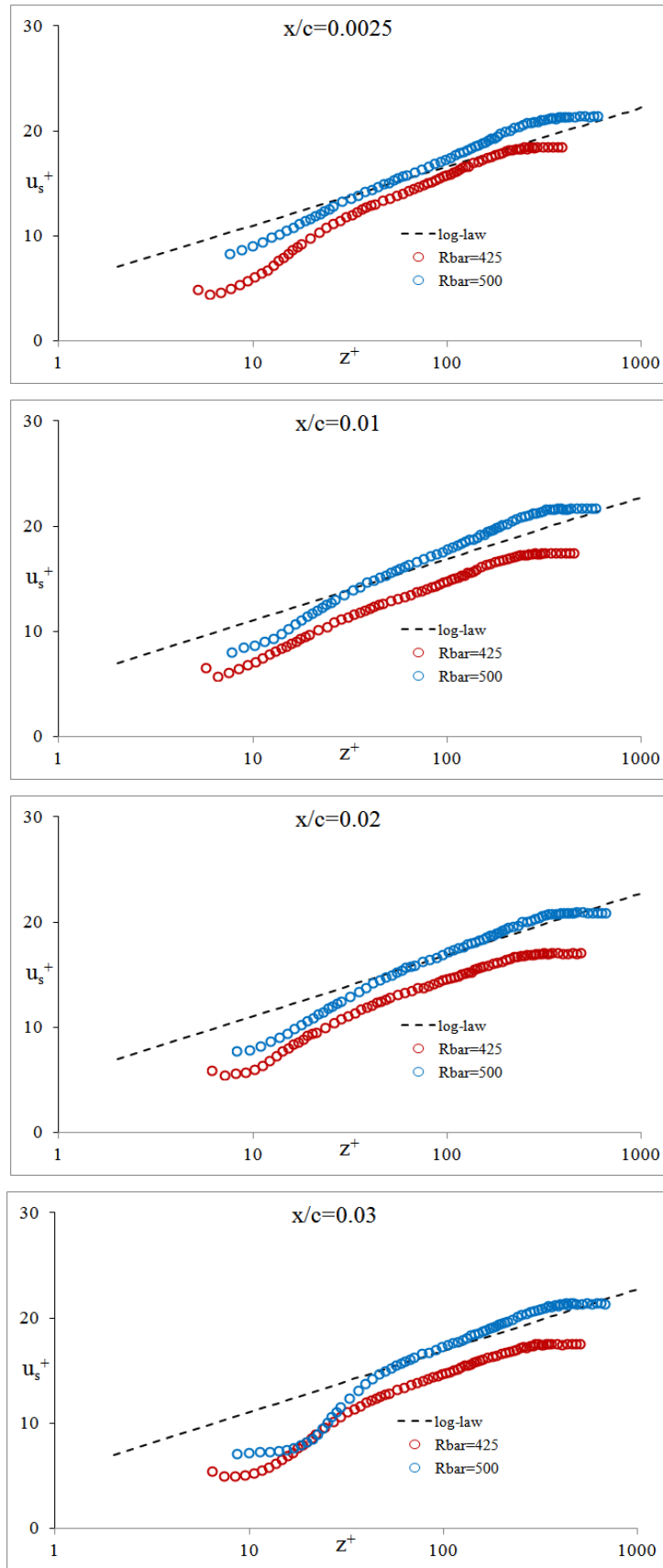


Figure 6.19: The streamwise profiles captured on the starboard side of the model represented in the law of the wall plots using the adjusted shear stress. The universal log-law is given by $u_s^+ = 2.5 \ln z^+ + 5.24$

6.3.4 Crossflow Velocity Profiles Downstream of Attachment Line

Applying the same procedures as those described in section 6.3.3, the crossflow velocity component, v , was obtained from the hot-wire measurements downstream of the attachment line. The profiles captured on the port and starboard sides have been presented in Figures 6.20 and 6.21, at $\bar{R} = 425$ and $\bar{R} = 500$ respectively. From Figure 6.20, a poor correlation is present between the port and starboard profiles at all the chordwise stations. They were expected to be close to each other, as for the streamwise profiles in Figures 6.15 and 6.16, as the model is symmetrical and at zero incidence. But at $\bar{R} = 500$, from Figure 6.21 the agreement between the port and starboard measurement shows improvement except at $x/c = 0.003$. At $\bar{R} = 425$, the starboard profiles asymptote to zero more rapidly than the profiles on the port side, before even reaching the edge of the boundary layer, where the worst case scenario appears at $x/c = 0.03$. For all the chordwise stations, the maximum velocity ratio attained in the crossflow at $\bar{R} = 425$ is less than 20% of the streamwise velocity, which approximates to less than 5m/s. This value lies outside the calibration range which was conducted at a speed of 5 to 50m/s and this would be the main source of discrepancy in the measurement at $\bar{R} = 425$. From Bruun [21], at such low speeds the hot wire response deviates from King's 'power law' and usually a polynomial fit is preferred. For the case of $\bar{R} = 500$, the magnitude of the maximum crossflow velocity is about 9m/s, which implies that a large part of the measurement should have been covered during the calibration and this justifies the improved relationship between the port and starboard side measurement shown in figure 6.21.

In addition to the restriction in low velocity calibration, the yaw calibration was also limited to a value of $\alpha = \pm 70^\circ$, from Bruun [21]. Beyond these angles the interference from the prongs increases and the response of the wire is affected. During yaw calibration the probe was rotated by $\theta = 45^\circ$ and $\theta = -25^\circ$ while positioned in the anticlockwise direction and $\theta = -45^\circ$ and $\theta = 25^\circ$ in the clockwise direction to cover the $\pm 70^\circ$ range. But, referring back to Figure 6.21, despite the reasonable agreement between the port and star-

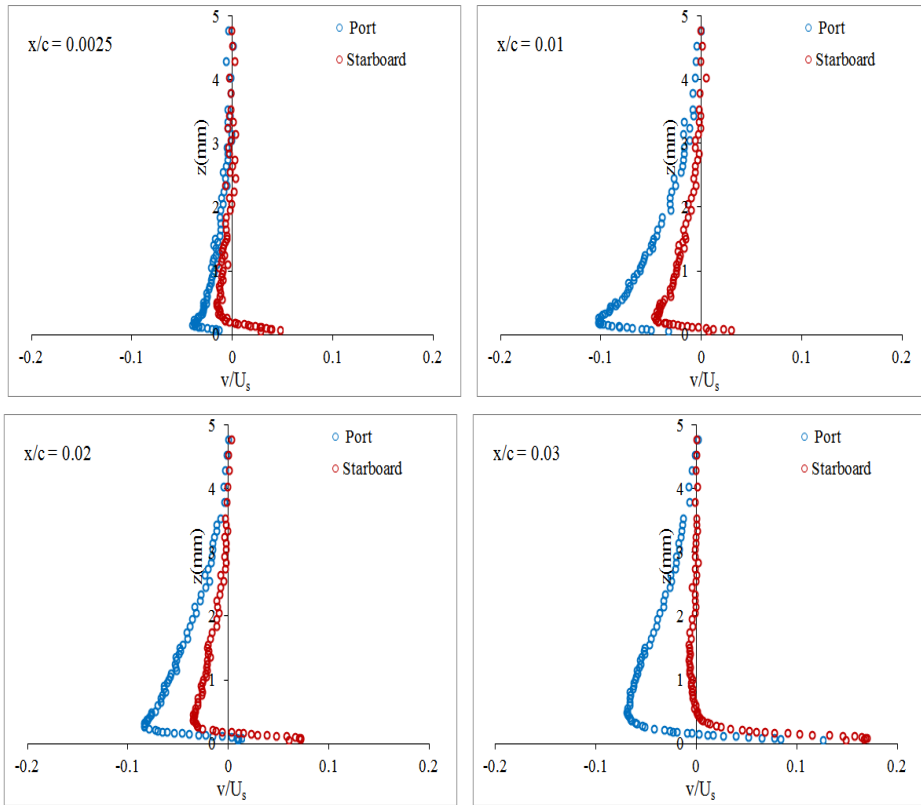


Figure 6.20: Cross-flow velocity profiles downstream of the attachment line, $\bar{R} = 425$

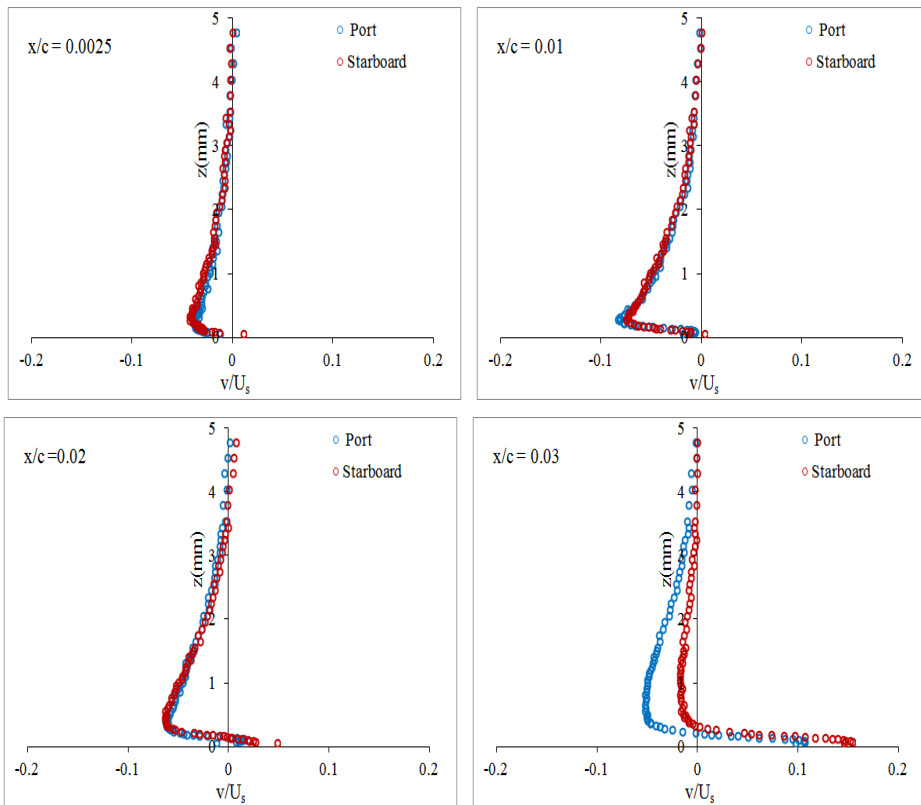


Figure 6.21: Crossflow velocity profiles downstream of the attachment line, $\bar{R} = 500$

board measurements the crossflow profiles still differ from each other at the last station, $x/c = 0.03$ and this behaviour is worse at $\bar{R} = 425$. At the attachment line the sensor was located at $\pm 45^\circ$ with respect to the incoming streamline which is considered to be the nominal yaw angle of the SY-probe, depending on whether the probe was orientated in the clockwise or anticlockwise direction. However, downstream of the attachment line this angle changes due to the divergence of the streamline (see Figure 6.22) and, if the streamwise velocity component is at an angle larger than $\pm 25^\circ$ with respect to the attachment line, the effective yaw angle becomes larger than $\pm 70^\circ$ and exceeds the calibration range. Referring to section 6.3.5, at $x/c = 0.03$ the external streamwise component has exceeded the $\pm 25^\circ$ limit and this might explain the discrepancy. To summarise, the discrepancy at $\bar{R} = 500$, is mainly due to the yaw calibration which appears out of range once the streamline has diverged by more than 25° , whereas at $\bar{R} = 425$ it is a combination of both velocity and yaw calibration. Overall, the profiles captured at $\bar{R} = 500$ can be considered to be more accurate.

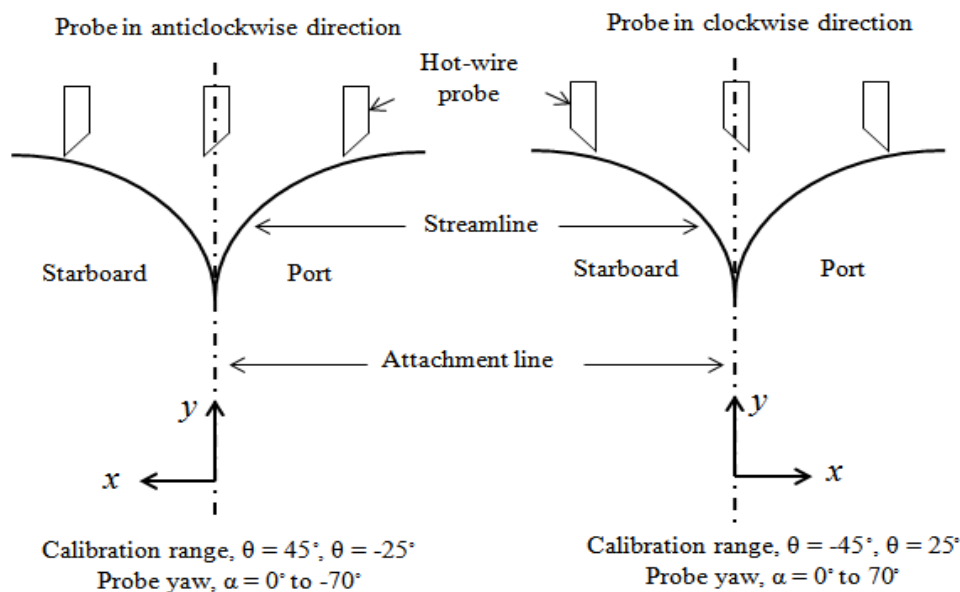


Figure 6.22: Schematic representation of the clockwise and anticlockwise orientation of the hot-wire probe at the attachment line and downstream along the diverging streamlines on the port and starboard side of the model.

The crossflow profiles were further analysed by representing them on the triangular hodograph model proposed by Johnston [64] as presented in Figures 6.23 and 6.24. Again, at $\bar{R} = 425$ considerable difference can be seen between the port and starboard side

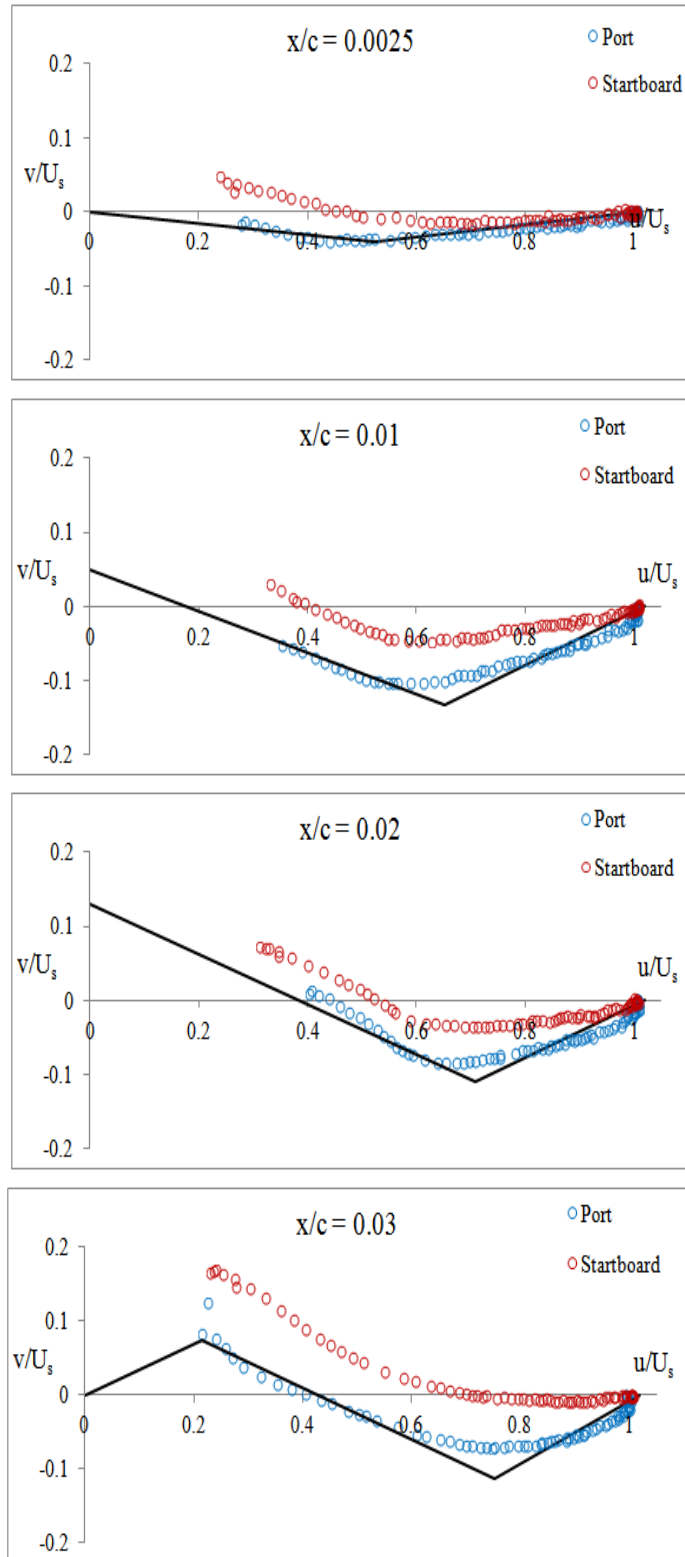


Figure 6.23: Triangular representation of the crossflow velocity profiles measured from both sides of the model at $\bar{R} = 425$

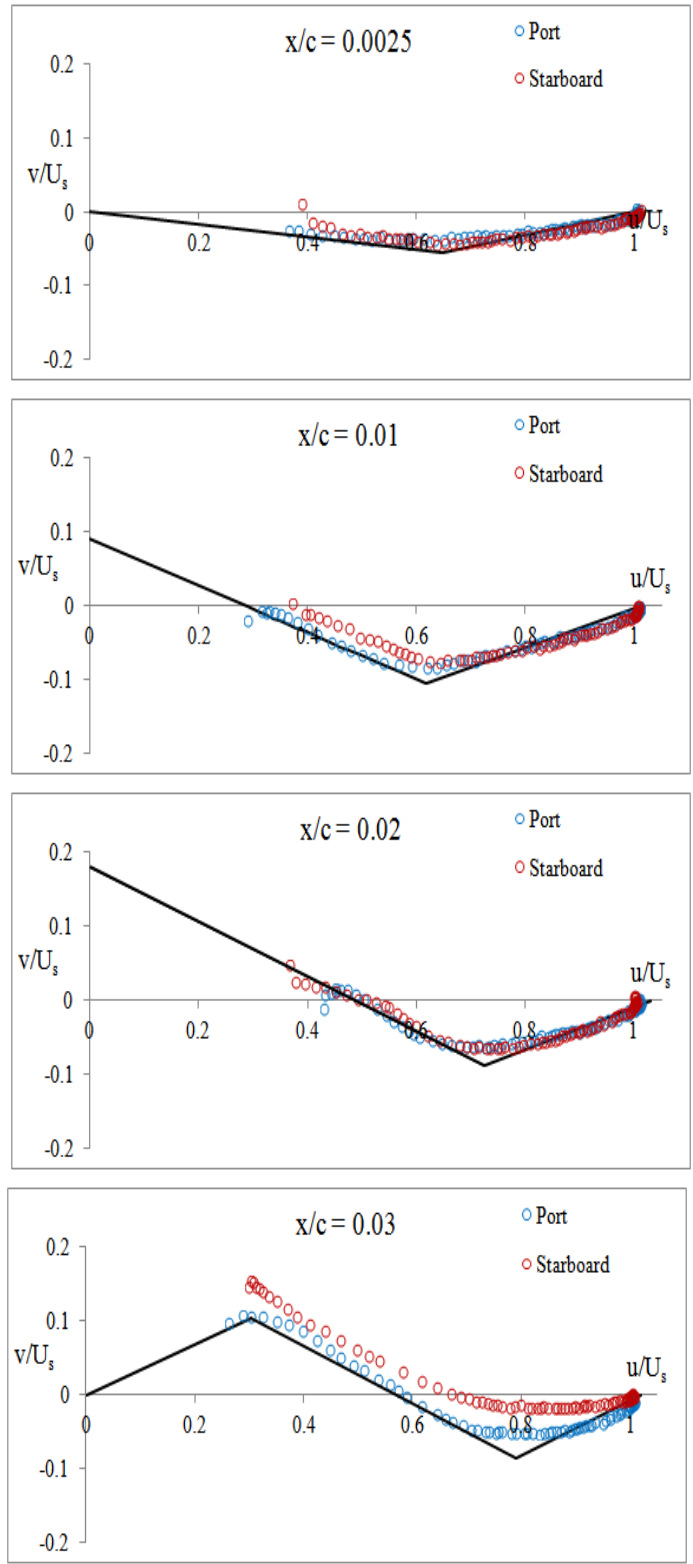


Figure 6.24: Triangular representation of the crossflow velocity profiles measured from both sides of the model at $\bar{R} = 500$

measurements; but the measurements on the port side seem more sensible therefore the triangular fit is based on those results. The triangular representation helps in revealing more details about the crossflow. It is easier to identify the point where the profile velocity changes direction, as from Figures 6.23 and 6.24 it is clear that this occurs at $x/c > 0.0025$, whereas Figures 6.20 and 6.21 give the impression that this behaviour starts at $x/c > 0.01$. Normally, the cross-over point occurs very close to the wall and shifts upwards, further downstream, as observed in Figures 6.23 and 6.24. However, due to restriction in near wall measurement it is difficult to capture the chordwise location where the cross-over starts to occur. The main issue with the triangular representation is the difficulty in applying a linear fit to the profiles, especially where the profiles are quite curved near the extremes of crossflow velocity.

The angle between the limiting and external streamline, β , can be estimated using equation 6.4 or if applying the hodograph model, equation 6.7. It can be also interpreted as the gradient of the line of best fit connecting the origin and the apex of the triangle in Figure 6.8, which is the region where the shear stress is more dominant. By applying this method, at $x/c = 0.0025$, on the port side of the model the angle was estimated as $\beta = -4.5^\circ$ and $\beta = -4.9^\circ$, for $\bar{R} = 425$ and $\bar{R} = 500$ respectively. At the stations, $x/c > 0.0025$ the same method still applies for the cross-over type profile, but from the current experimental results it was rather difficult to estimate β until $x/c = 0.03$, due to the failure to capture the flow in the near wall region. At $x/c = 0.03$, the apex of the first triangle could be resolved and the angles were estimated as $\beta = 4.2^\circ$ and $\beta = 5.9^\circ$, for $\bar{R} = 425$ and $\bar{R} = 500$ respectively. Based on the triangular representation, as the cross-flow profiles started to cross-over right after $x/c = 0.0025$, it meant that β did not increase to larger negative values and in fact the wall shear stress changed direction. Therefore, it seems fair to assume that within the current experimental domain the limiting streamline angle ranged between, $-5^\circ < \beta < 6^\circ$.

6.3.5 Cross-over Velocity Profiles

From the chordwise, U , and spanwise, V , velocity components at the edge of the boundary layer, the direction of the external streamline component with respect to x could be calculated as $\psi = \tan^{-1}(V/U)$. These results are presented in Figures 6.25 and 6.26 at each chordwise measurement station. Ideally at the attachment line, $\psi = 90^\circ$, but from the measurement made using the SY-probe the actual angles differed by slightly less than 1° . This might be due to the measurement uncertainty associated with the SY-probe and also the difficulty in ensuring that the centre of the yawed probe was along the attachment line, hence resulting in the presence of a crossflow velocity component in the attachment line measurement presented in section 6.3.2. As the external streamline is an inviscid flow, the trajectory of the streamline should not show any significant Reynolds number dependence, therefore the difference in ψ at $x/c = 0.01$ on the port side of the model is very likely to be due to experimental inaccuracy.

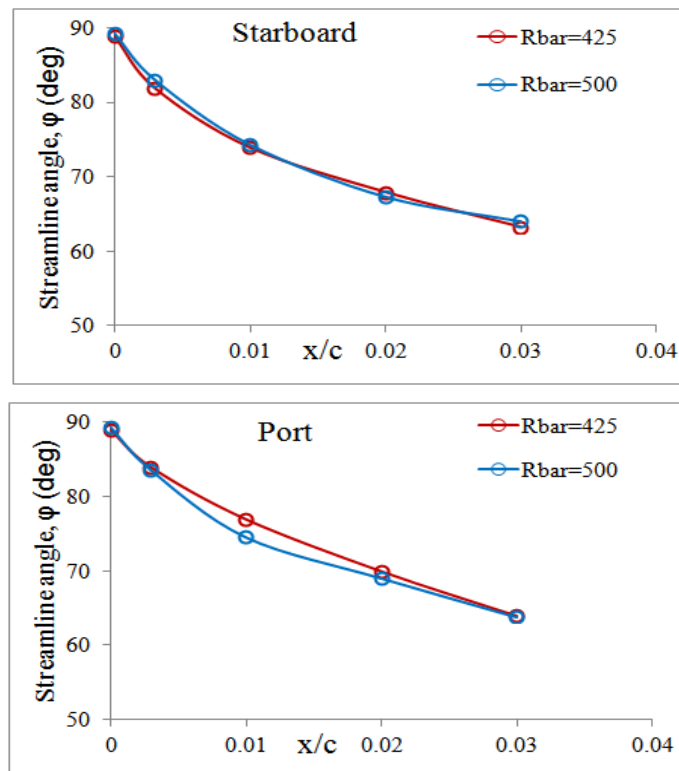


Figure 6.25: The streamline divergence angle, ψ at different chordwise locations.

The chordwise and spanwise velocity components at the edge of the boundary layer, U

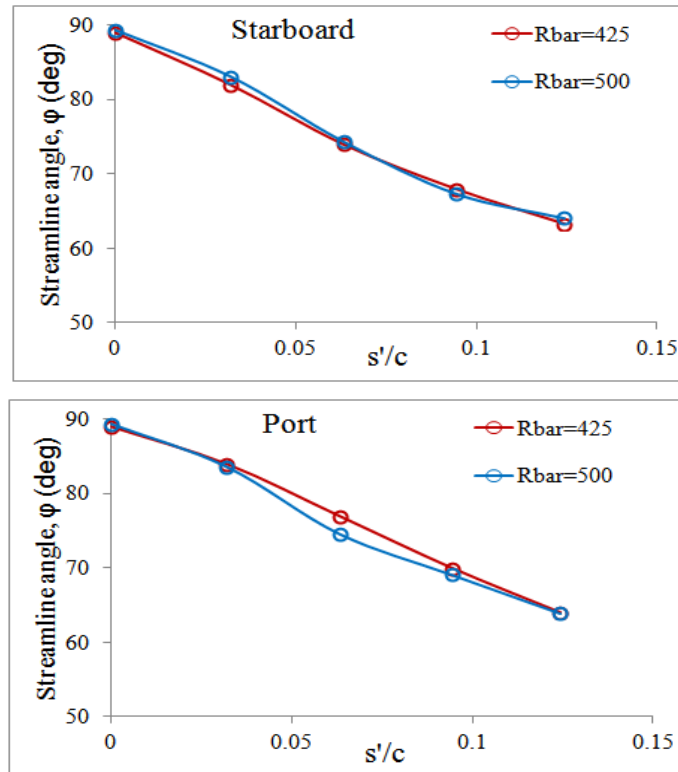


Figure 6.26: The streamline divergence angle, ψ at different positions along the circumference of the leading edge.

and V respectively, are plotted against surface distance normal to the leading edge, normalised by the chord length, s'/c , in Figure 6.27. The velocities at each corresponding station between the port and starboard side are expected to be similar as the model was symmetrical. This behaviour can be observed at $\bar{R} = 500$ and the small difference between the port and starboard is acceptable. However, considerable difference can be observed in both U and V at $\bar{R} = 425$ and this is most probably due to asymmetric solid blockage from the base of the traverse, which might have been positioned too close to the measurement station as shown in Figures 3.24 and 3.26. Considering the spanwise velocity component, which for infinite-swept flow is assumed to be uniform in the chordwise direction, this uniformity over the experimental domain of interest is confirmed by the negligible variation in V near the leading edge, at $s'/c \geq 0.032$ for $\bar{R} = 500$. Similar, behaviour is seen in the starboard side measurement at $\bar{R} = 425$. The chordwise velocity tends to increase linearly (especially at $\bar{R} = 500$) until $s'/c > 0.1$ as expected from the nearly constant surface curvature in this region.

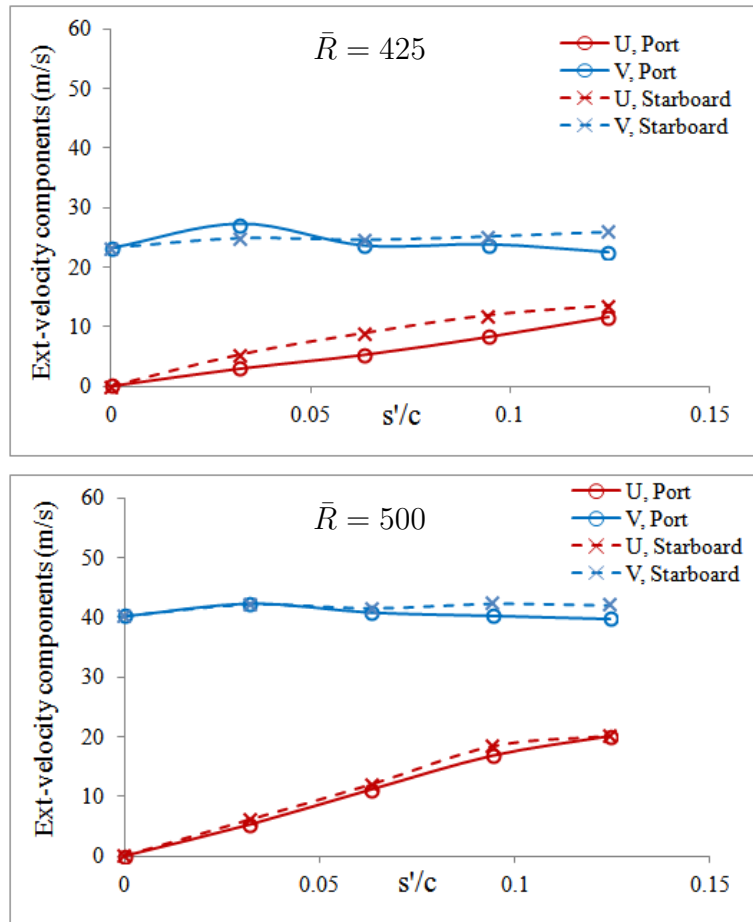


Figure 6.27: The chordwise and spanwise velocity components at the edge of the boundary layer, along the leading edge of the experimental model

From Figures 6.23 and 6.24 the cross-over type crossflow velocity profiles start to appear downstream of $x/c = 0.0025$. Referring back to section 6.1 and, according to Cooke [31], Cumpsty [33] and Cebeci and Cousteix [24], the cross-over in the velocity profile is due to the formation of an inflection point in the external streamline. But, looking at Figure 6.25, no such behaviour is found and, in Figure 6.26, the streamline divergence angle varies almost linearly at both Reynolds numbers, except the port side measurement at $s'/c = 0.063$ for $\bar{R} = 500$, which again might be associated with the blockage from the traverse. Based on the external velocity distribution shown in Figure 6.27, the formation of an inflection point in the external streamline is unlikely, as this would show up in the trend of the velocity components in Figure 6.27. The presence of a large chordwise velocity gradient and a uniform spanwise velocity suggests that the flow will gradually curve in the chordwise direction without any change in the direction of curvature, until it

is aligned with the flow along the line of flight further downstream.

In a three dimensional laminar boundary layer, the viscous shear force is much smaller than the transverse pressure gradient. Hence, the cross-over in the crossflow velocity profile occurs mainly due to a change in the direction of the transverse pressure gradient, which would also result in a point of inflection in the path of the streamline. This can be supported by the relation given by equation 6.2. However, despite the absence of the inflection point in the external streamline measured during the current experiment, cross-over was still present in the crossflow velocity profiles at $x/c > 0.0025$.

A positive explanation can be found by considering the development of the turbulent shear stress along a diverging or converging streamline, the normal momentum equation can be expressed in curvilinear coordinates [108] as

$$\frac{u}{h_1} \frac{\partial v}{\partial \xi} + \frac{v}{h_2} \frac{\partial v}{\partial \eta} + w \frac{\partial v}{\partial \zeta} - k_1 uv + k_2 u^2 = -\frac{1}{\rho h_2} \frac{\partial p}{\partial \eta} + \frac{1}{\rho} \left(\nu \frac{\partial^2 v}{\partial \zeta^2} + \frac{\partial}{\partial \zeta} (-\overline{v'w'}) \right) \quad (6.13)$$

where $h_1(\xi, \zeta)$ and $h_2(\xi, \zeta)$ denote the metric coefficients and, k_1 and k_2 are the geodesic curvature parameters given as

$$k_1 = -\frac{1}{h_1 h_2} \frac{\partial h_1}{\partial \xi}, \quad k_2 = -\frac{1}{h_1 h_2} \frac{\partial h_2}{\partial \eta} \quad (6.14)$$

Here k_2 is the streamline curvature and k_1 the curvature of the normal co-ordinate.

Considering the flow outside the sublayer, equation 6.13 can be further simplified to equation 6.15, by neglecting the terms in w , k_1 and ν .

$$\frac{u}{h_1} \frac{\partial v}{\partial \xi} + \frac{v}{h_2} \frac{\partial v}{\partial \eta} = -\frac{1}{\rho h_2} \frac{\partial p}{\partial \eta} - k_2 u^2 + \frac{1}{\rho} \frac{\partial}{\partial \zeta} (-\overline{v'w'}) \quad (6.15)$$

At the edge of the boundary layer

$$-\frac{1}{h_2} \frac{\partial p}{\partial \eta} = k_2 \rho U_e^2 \quad (6.16)$$

therefore the normal momentum equation 6.15 can be written

$$\frac{u}{h_1} \frac{\partial v}{\partial \xi} + \frac{v}{h_2} \frac{\partial v}{\partial \eta} = k_2 (U_e^2 - u^2) + \frac{1}{\rho} \frac{\partial}{\partial \zeta} (-\overline{v'w'}) \quad (6.17)$$

In a laminar boundary layer the Reynolds stress term is absent so that the crossflow development is driven by the geodesic curvature k_2 , as the stresses term, the second term on the right hand side of equation 6.17 equals to zero. But, due to the additional effects of the Reynolds stresses in a turbulent boundary layer, the development of v will be governed by both terms on the right hand side of equation 6.17. The gradient of Reynolds shear stress, $\partial/\partial\zeta(-\overline{v'w'})$, is likely to be negative (maximum shear stress at the wall, tending to zero at the edge of the boundary layer) so that, if the turbulent stress increases in magnitude sufficiently, the term on the left hand side of equation 6.17 will also undergo a change in sign, driving a reversal in the direction of the crossflow velocity and the formation of cross-over crossflow velocity profiles. Measurement of the fluctuating velocity components will be required to support this argument.

6.3.6 Estimation of Surface Shear Stress

The measurement of surface shear stress using Preston's technique has been predominantly used for two-dimensional turbulent boundary layers and its extension to three-dimensional flow is questionable especially in the region where the limiting streamline is not aligned with or parallel to the external streamline. However, an attempt to measure local surface shear stress in the highly three-dimensional flow downstream of the attach-

ment line was made using Preston’s technique. The main assumption was that the viscous flow angle in the inner region of the boundary layer, where the universal log-law holds, did not vary considerably with respect to the angle of the external streamline. Therefore, by aligning the Preston probe shown in Figure 3.30, in the direction of the external streamline presented in Figure 6.25, the local shear stress was captured by repeating the procedures outlined in section 3.6. The results are shown Figure 6.28, where, ‘Expt-direct’ represents the skin friction calculated from the direct shear stress measurement from the Preston tube, ‘Expt-corrected’ represents the corrected results from the Preston tube to match the universal-log law and ‘Clauser’ represents the skin friction determined using Clauser-chart technique.

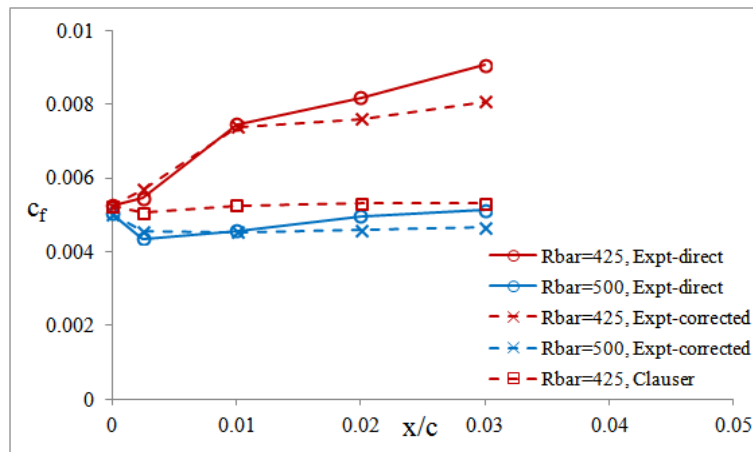


Figure 6.28: The local skin friction coefficient in the vicinity of the attachment line.

In addition to the potential impact of the varying streamline angle inside the boundary layer, the favourable pressure gradient will also have an effect on the measurement of surface shear stress. This effect was reported by Patel [87], who concluded that in the case of a favourable pressure distribution, a discrepancy of 3 – 6% might arise in the measurement of the shear stress. Due to the lack of experimental data in the literature it is difficult to judge the accuracy of the results shown in Figure 6.28, but having captured the streamwise profile a reverse analysis mentioned in section 6.3.3 was conducted first by plotting the streamwise profile in wall units using shear stress measured initially, followed by an increment or decrement of approximately 10% in the measured τ_w until a fair agreement with the ‘log-law’ was observed. This approach is quite similar to Clauser’s technique,

except the fact that the velocity profiles did not require representation on a Clauser plot due to the small variation in c_f .

However, for the profiles at $\bar{R} = 425$, the adjustment in skin friction coefficient required to match universal log-law was of the order of approximately 30%. Therefore, Clauser's technique was employed and the velocity profiles were represented on Clauser-plots as shown in Figure 6.34. The c_f was adjusted manually using a trial and error approach until a linear fit within acceptable agreement with the linear log-law given by $u_s^+ = 2.5 \ln z^+ + 5.25$ was obtained. From the c_f estimated using Clauser-plots shown in Figure 6.28 the absolute magnitude and the trend downstream seem to be more sensible and similar to that at $\bar{R} = 500$. The high value of c_f obtained from the direct measurement using Preston tubes at $\bar{R} = 425$ might be associated to experimental errors or due to limitation on Preston's technique in the presence of large three dimensionality of the flow or due to re-organisation of the turbulent structures under the effect of a mild favourable pressure gradient where the flow is tending towards a state of relaminarisation.

6.3.7 Evolution of the Boundary Layer

Another way of analysing the evolution of the boundary layer downstream of the attachment line is by comparing the development of the boundary layer integral quantities. Using the streamwise velocity profiles the momentum thickness, θ , and the shape factor, H , were calculated at each chordwise position and are plotted in Figures 6.29 and 6.30 respectively for $\bar{R} = 425$ and $\bar{R} = 500$. From Figure 6.29, the good agreement between the measurements made at the attachment line using the SN-probe and the SY probe provides some confidence in the technique employed for the SY probe. For the case of $\bar{R} = 425$, downstream of the attachment line the port and starboard side measurements correlate very well, however at $\bar{R} = 500$ a small variation can be observed between the measurements from the two sides, but they are within $\pm 3\%$ of each other. Considering the overall trend, the value of θ rises by approximately 15% immediately downstream of the

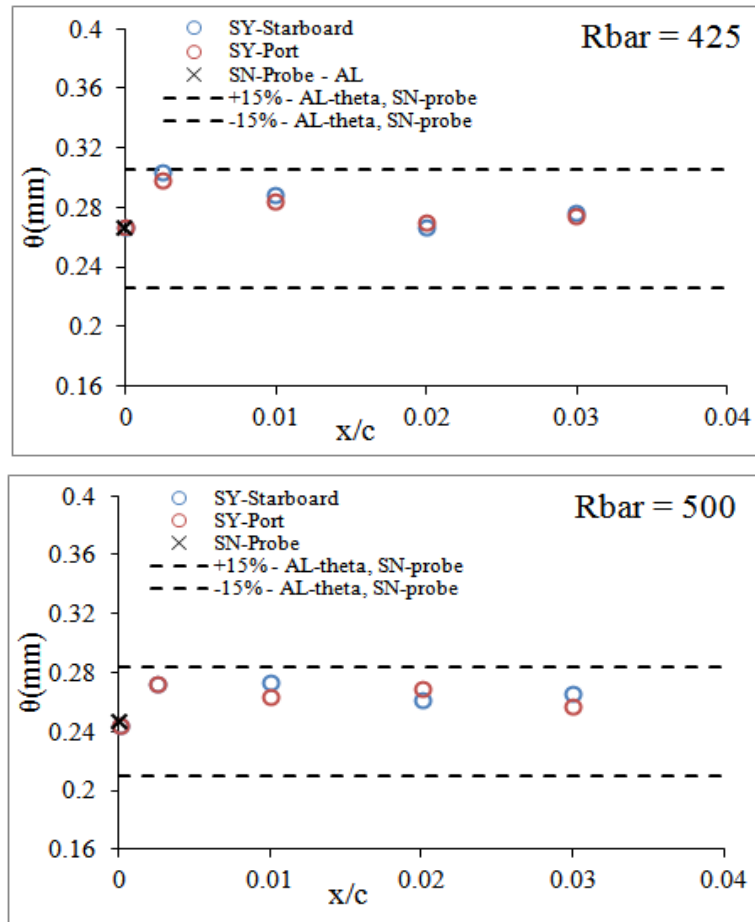


Figure 6.29: Development of the streamwise momentum thickness in the vicinity of the attachment line.

attachment line for both \bar{R} cases, but starts to decrease at $x/c > 0.0025$ for $\bar{R} = 425$ and followed by a slight increase at $x/c > 0.02$. Whereas, at $\bar{R} = 500$, this is not very clear and it can be assumed to be more or less constant despite the small variation between the port and starboard side measurements.

The development of shape factor, H , in the vicinity of the attachment line is presented in Figure 6.30. An improved correlation between the port and starboard measurement is seen at $\bar{R} = 500$. The main difference between the trends shown in Figures 6.30 and 6.29 is the rise in shape factor at $x/c = 0.03$ which suggest that the displacement thickness is increasing faster than the momentum thickness. This behaviour in the trend of θ or H downstream of $x/c = 0.0025$ has not been reported previously and therefore further work is required to understand the mechanism responsible for this.

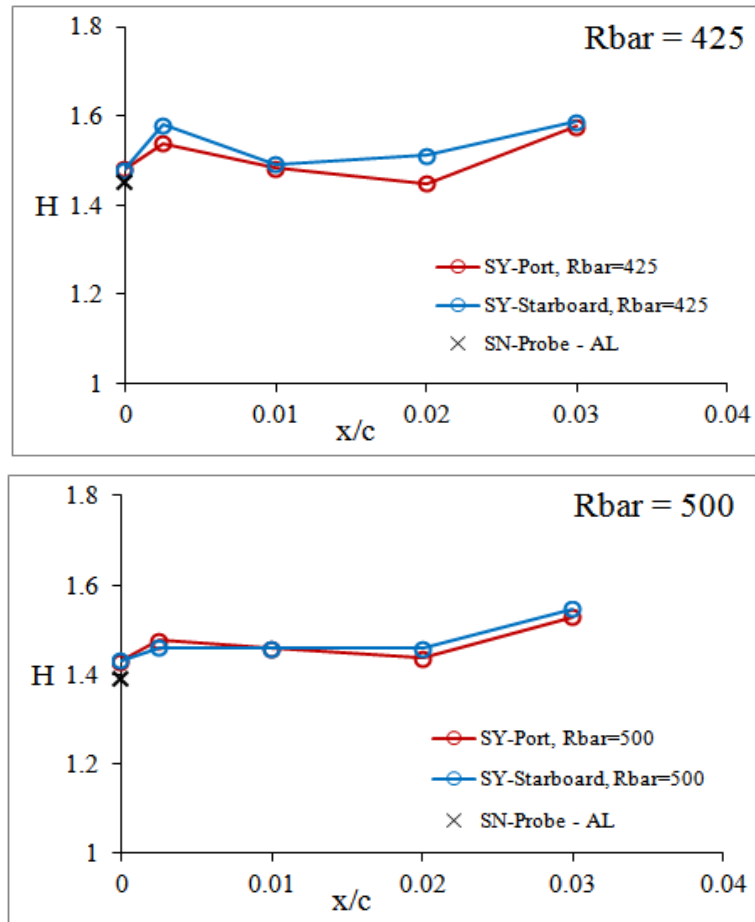


Figure 6.30: Development of the streamwise shape factor in the vicinity of the attachment line.

From the streamwise and crossflow velocity profiles the standard boundary layer integral quantities, θ_{ij} and δ_i^* , were calculated using the relation given by equation 2.53 and their development in the vicinity of the attachment line is presented in Figure 6.31, for $\bar{R} = 425$ and in Figure 6.32 for $\bar{R} = 500$ on both the port and starboard sides. At the attachment line the chordwise velocity component is zero, therefore the crossflow or normal momentum thicknesses, θ_{12} , θ_{21} and θ_{22} and crossflow displacement thickness, δ_2^* were expected to be zero which is confirmed by Figures 6.31 and 6.32. Downstream of the attachment line, θ_{12} and θ_{22} remain very small whereas θ_{21} and δ_2^* increase as the magnitude of the crossflow velocity increases, except on the starboard side at $\bar{R} = 425$ where the growth is very slow which is consistent with the velocity profile in Figure 6.20. The drop in the magnitude of these quantities on the starboard side, at $x/c = 0.03$ and for both Reynolds number cases is also consistent with the profiles in Figures 6.20 and 6.21, which was due

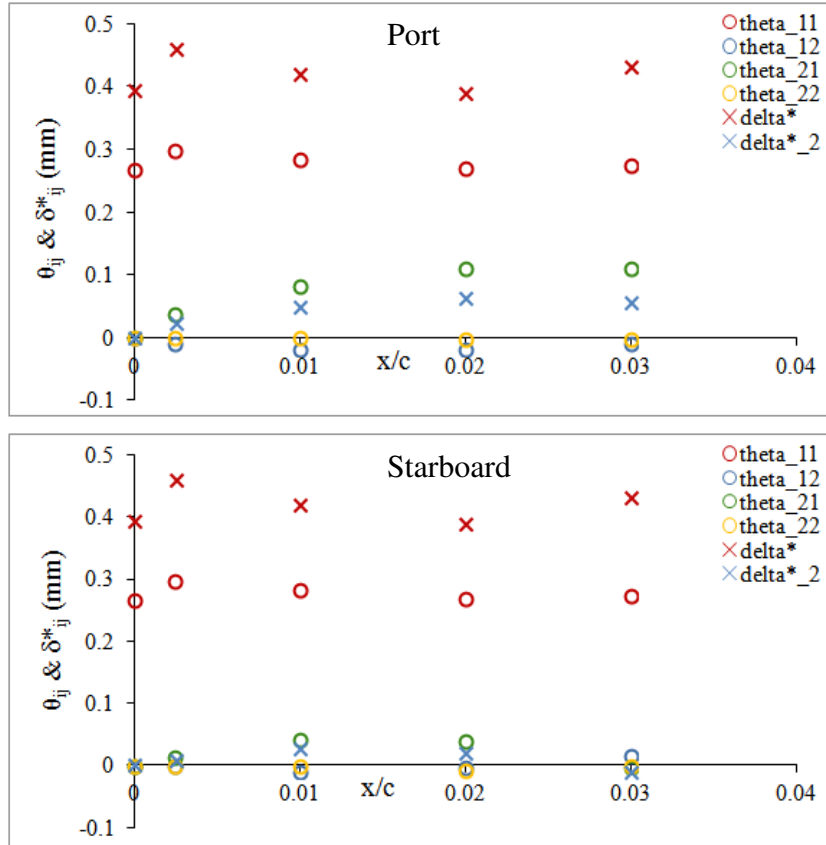


Figure 6.31: Development of the normal boundary layer integral quantities defined by equation 2.53 at, $\bar{R} = 425$, where the subscript ‘i’ and ‘j’ represents ‘1’ or ‘2’.

to the limitation of the calibration explained earlier. For further analysis only the data at $\bar{R} = 500$ will be employed as the data are more consistent than at $\bar{R} = 425$.

These results are of significant importance for the validation of the leading approximation in Callisto. Within the current chordwise measurement domain, θ_{12} and θ_{22} are very small and these should be negligible error if these are not represented accurately in numerical methods. For $x/c \leq 0.03$, θ_{21} and δ_2^* attain a value of approximately 35% of the stream-wise momentum thickness, θ_{11} , and therefore their modelling cannot be easily neglected. From figure 6.25, the chordwise location at which the streamline divergence angle is approximately 80° lies between the second and the third measurement station and can be interpolated to be at $s'/c \approx 0.04$. Between $s'/c = 0.0$ and $s'/c \approx 0.04$, which is precisely the region where the numerical fix is applied in Callisto, a notable increase in θ_{21} and δ_2^* can be observed which should be accounted for in the numerical modelling. Likewise the

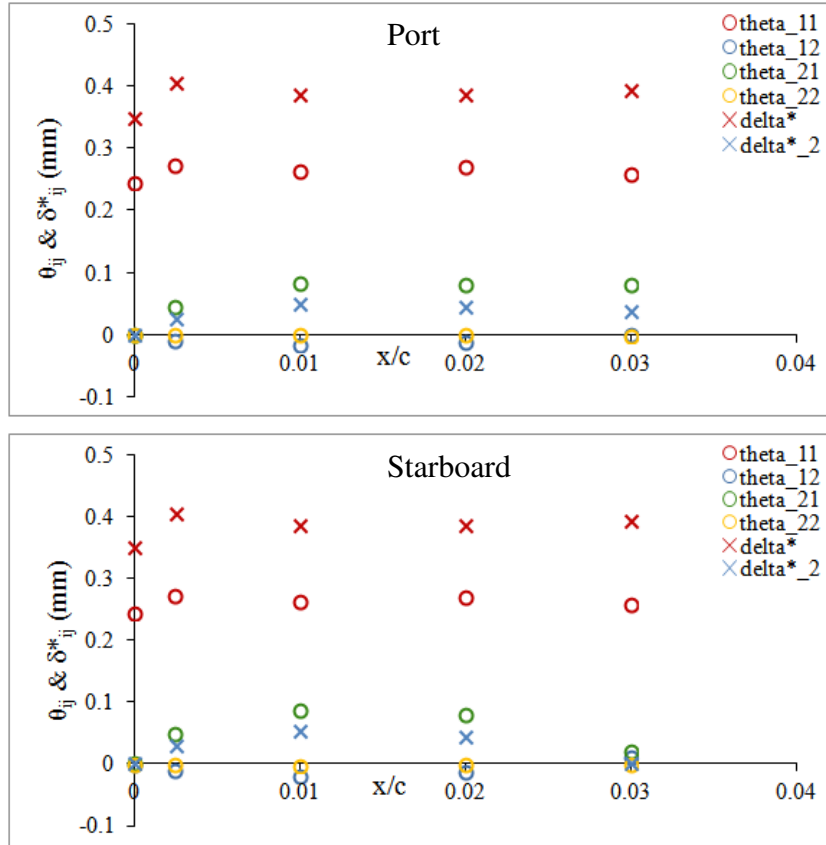


Figure 6.32: Development of the normal boundary layer integral quantities defined by equation 2.53 at, $\bar{R} = 500$, where the subscript ‘i’ and ‘j’ represents ‘1’ or ‘2’.

15% increase in θ_{11} and δ_1^* in the region $0 \geq s'/c \leq 0.03$ which is again not modelled due to the calculation being frozen. Therefore, based on these observations, a modification to the leading edge modelling in Callisto is proposed and tested in Chapter 7 so as to capture the initial increment in the boundary layer integral quantities, thus improving the accuracy of the numerical method.

6.3.8 Possibility of Relaminarisation

Based on the analysis above, the viscous flow in the vicinity of the attachment line shows strong dependence on Reynolds numbers especially downstream of $x/c = 0.0025$. From the velocity profiles represented in wall units, in Figures 6.18 and 6.19, the linear region of the streamwise profiles at $\bar{R} = 425$ is shifted from the universal ‘log-law’ which is well represented by the velocity profiles at $\bar{R} = 500$. From section 6.2.1, Mukund et al.

[81] demonstrated that the turbulent boundary layer at the leading of a swept wing can be relaminarised under the effect of highly accelerating flows generated at large angle of incidence. During their investigation the onset of relaminarisation was in agreement with Launder's [71] acceleration parameter transformed for three dimensional flow, K_s , which had attained a value of approximately 3×10^{-6} .

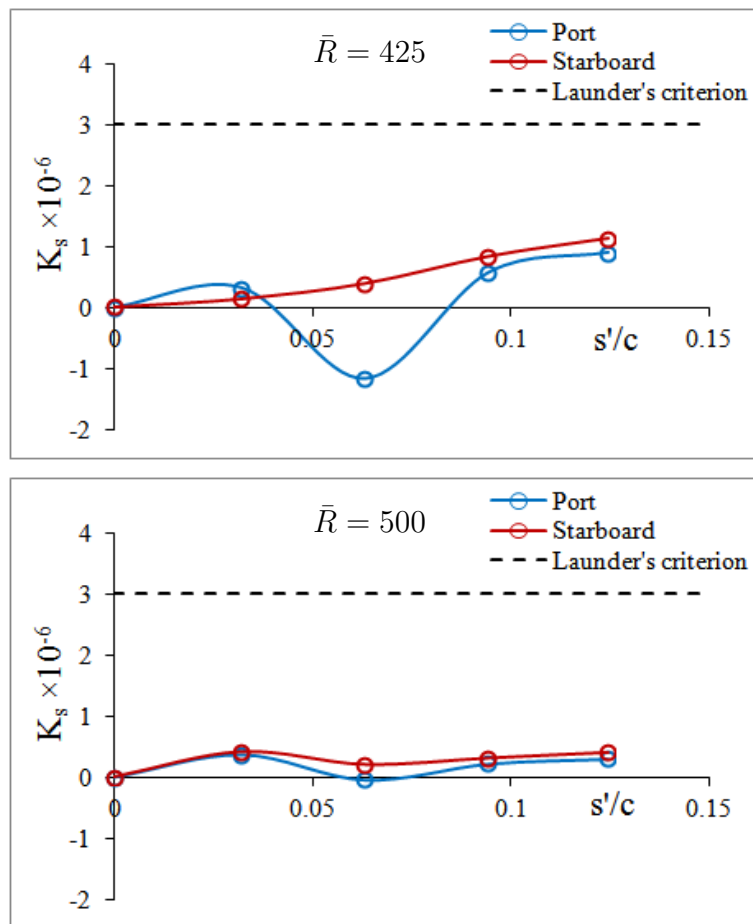


Figure 6.33: Launder's acceleration parameter calculated using the conditions along the external streamline using equation 6.11

But in the current experiment the model was placed at zero incidence and only a mild accelerating flow was present at the leading edge, unlike the case of Mukund et al. Using the streamwise velocity at the edge of the boundary layer, U_s , and the streamline angle, ψ , estimated from the hot-wire measurements, K_s was determined and is plotted in Figure 6.33. Even at $\bar{R} = 425$, these values are well below Launder's criterion, $K_s \approx 3 \times 10^{-6}$. Immediately downstream of $x/c = 0.0025$, which is the region where the boundary layer profile departs from the usual log-law, the acceleration parameter on the port side

experienced a drastic change in direction reaching a value of $K_s \approx -1.2 \times 10^{-6}$. A similar effect can be observed at $\bar{R} = 500$ but the magnitude was not even of the order of 10^{-6} .

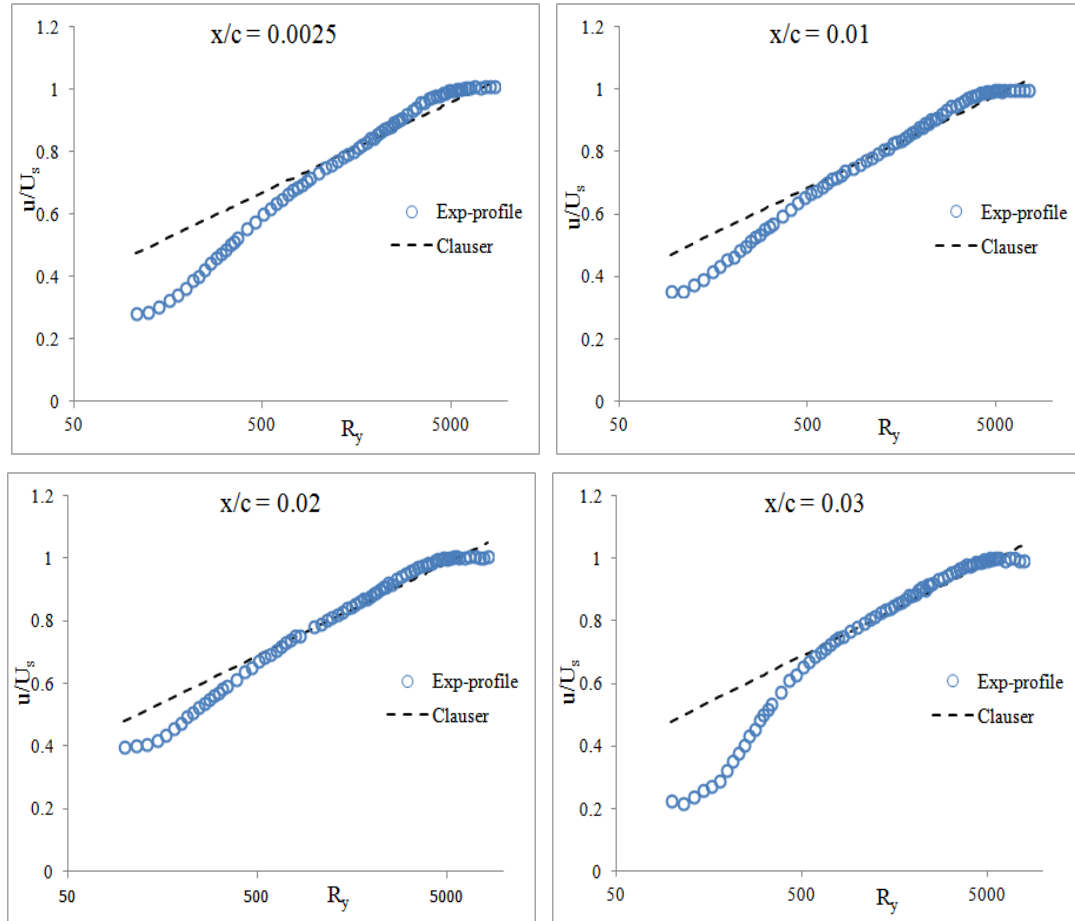


Figure 6.34: The streamwise velocity profiles downstream of the attachment line represented in wall units using the c_f estimated from the Clauser-plots.

The change in the sign of the acceleration parameter was due to the unusual peak in the streamwise velocity on the port side, as shown in Figure 6.27, and the sudden reduction straight after. This effect was not present on the starboard side even at higher Reynolds number and might be associated with the asymmetric blockage. Considering the moderate acceleration parameter attained during the current experiment, in comparison to Launder's criterion, the flow is unlikely to be relaminarised at $\bar{R} = 425$. Launder's criterion has been established for purely two dimensional flows, and the effect of centripetal acceleration due to streamline divergence is not taken into account. Hence, further investigation is required to establish a criterion for the acceleration parameter in three dimensional flows. Using

the c_f obtained from the Clauser-plots the streamwise velocity profiles at $\bar{R} = 425$ were re-plotted in wall units in Figure 6.34. The velocity profiles show closer agreement with the universal log-law from Figure 6.34, suggesting that they did not attain a laminar state. Still, the velocity profile at $x/c > 0.0025$ contain some unusual features and a small change in the von Karman constant is required for a better linear fit with the log-law. This raises the question of whether the turbulent boundary layer is under-going some sort re-organisation under in the presence of the favourable pressure gradient and possibly tending towards a state of quasi-relaminarisation. Thus, Reynolds stresses measurements will be required to understand these features.

Chapter 7

Leading Edge Modelling in Callisto

7.1 Comparison of Callisto against Current Experiment

From the experimental pressure measurement presented earlier, it was assumed that, within the experimental domain of interest, the infinite-swept assumption is valid. Therefore, using the same freestream conditions as during the experiment, a numerical analysis of the flow around the NACA0050 aerofoil at geometric sweep of 60° , was conducted at $\bar{R} = 500$ to check the leading edge modelling in Callisto. Figure 7.1 shows a comparison of the momentum thicknesses obtained experimentally and numerically for both a low and a high resolution calculation, with 160×32 and 320×48 mesh points respectively. Due to the leading edge approximation, θ from the numerical prediction remains constant in the region of $s'/c \approx \pm 0.02$ and starts to increase right after. The low resolution numerical results under-predicts θ by approximately 15% with respect to the experimental results and this difference increases slightly when using a finer mesh. Despite the significant difference in the actual magnitude of the numerical and experimental momentum thickness, the unusual maximum in θ observed in the experimental results downstream of the attachment line is also predicted by Callisto. From the experimental results, the starboard side measurement shows slightly closer agreement with numerical results, where the trend in

θ is better represented.

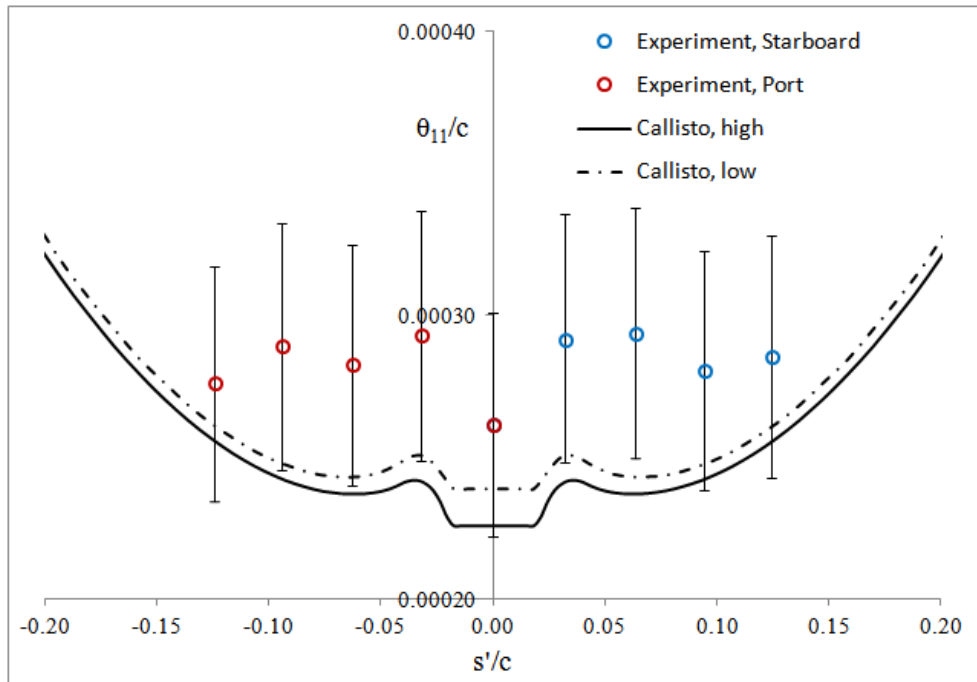


Figure 7.1: Comparison between θ measured during the current experiment and those obtained numerically from Callisto, using both a low and a high resolution mesh. The error bars are within $\pm 15\%$.

From Figure 7.2, immediately downstream of the attachment line, the experimental results show an increase in the shape factor, H , as opposed to the numerical results which show a decreasing trend. At the attachment line the numerical and experimental results are within 4%, however it is not possible to compare the two results right downstream of the attachment line due to the leading edge approximation in Callisto. A better agreement between the numerical and experimental H is seen for $\pm 0.01 \leq s'/c \leq \pm 0.20$, where the prediction lies within 3% of the experimental results. In this region the measurements from the port side show closer agreement, where the trend in the reduction in θ downstream of the attachment line has also been captured. But, at $\pm 0.01 \leq s'/c \leq \pm 0.20$, a large deviation between the two set of results is present where, unlike the numerical results, the experimental results show an increase in H .

Using the process described in section 6.3.6, the experimental, local skin friction coefficient, c_f , adjusted using the process described in section 6.3.6, was also compared with that predicted by Callisto and the results are shown in Figure 7.3, where a difference of at

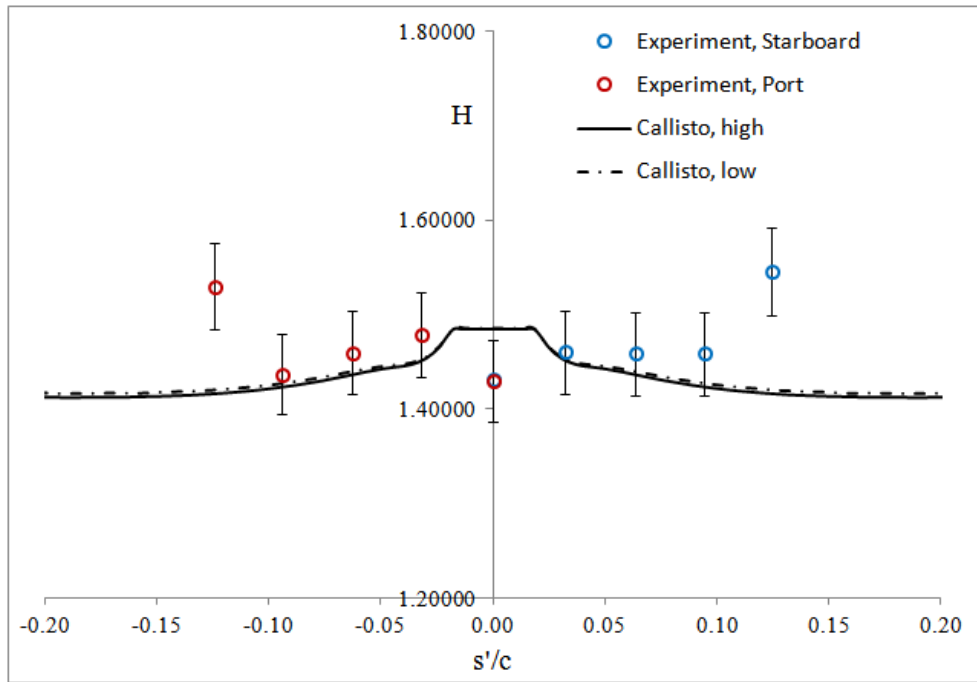


Figure 7.2: Comparison between H measured during the current experiment and those obtained numerically from Callisto, using both a low and a high resolution mesh. The error bars are within $\pm 3\%$.

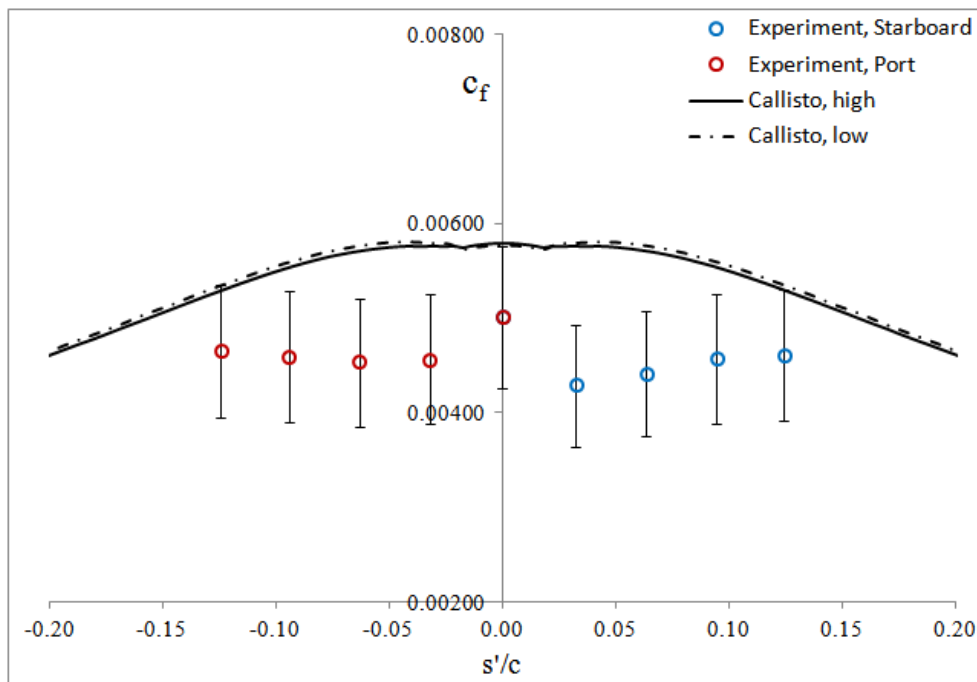


Figure 7.3: Comparison between c_f measured during the current experiment and those obtained numerically from Callisto, using both a low and a high resolution mesh. The error bars are within $\pm 15\%$.

least 15% is present between the numerical and the experimental results for $s'/c < 0.1$. Immediately downstream of the attachment line the experimental c_f reduces and starts

to increase at $s'/c > 0.03$, whereas from the numerical results c_f remains constant until starting to decrease at $s'/c > 0.03$. Again due to the leading edge approximation it is difficult to comment about this behaviour immediately downstream of the attachment line. Despite the good agreement between the experimental and the numerical shape factor for $s'/c < \pm 0.1$, both the magnitude and the trend in the momentum thickness and the local skin friction from the numerical and experimental results show significant deviations. Thus a modification to the governing equations has been suggested in the following section, to remove the leading edge fix and switch to the full three dimensional integral equations immediately downstream of the attachment line.

7.2 Modification of Momentum Integral Equation at the Leading Edge

As discussed in Chapter 6, the following analysis is based only on the results obtained at $\bar{R} = 500$. Referring back to section 6.3.5, within the current experimental domain, $s'/c \leq 0.12$, the limiting streamline angle varied between $-5^\circ < \beta < 6^\circ$. In Callisto the leading edge approximation is applied if, $\psi \geq 80^\circ$ and, from figure 6.25, this occurs at $s'/c \approx 0.04$. In this region the limiting streamline angle can be assumed to be within $-4^\circ < \beta < 4^\circ$, therefore implying that in the proximity of the attachment line, $\tan \beta \approx 0$. However, $\partial\beta/\partial\xi$ will be non-zero. Substituting for $\tan \beta$ in the normal momentum integral equation, given by equation 2.67, leads to

$$\cos \psi f_1 \frac{d\beta}{d\xi} - \sin \psi (1 + H) \frac{1}{U_{iw}} \frac{dU_{iw}}{d\xi} = 0 \quad (7.1)$$

which can be further simplified to

$$\frac{d\beta}{d\xi} = \tan \psi \frac{(1+H)}{f_1} \frac{1}{U_{iw}} \frac{dU_{iw}}{d\xi} \quad (7.2)$$

Here, $\tan \psi$ is still singular near the leading edge.

From the equivalent inviscid flow, the streamwise component is given by

$$U_{iw}^2 = U_1^2 + V_1^2 \quad (7.3)$$

Therefore, its derivative can be expressed as

$$\frac{dU_{iw}}{d\xi} = \frac{U_1}{U_{iw}} \frac{dU_1}{d\xi} = \cos \psi \frac{dU}{d\xi} \quad (7.4)$$

where, from the infinite-swept condition, the spanwise component V_1 is constant.

By rearranging equation 7.2 through equation 7.4, $d\beta/d\xi$ can be expressed as finite function of the gradient of chordwise velocity

$$\frac{d\beta}{d\xi} = \sin \psi \frac{(1+H)}{f_1} \frac{1}{U_{iw}} \frac{dU_1}{d\xi} \quad (7.5)$$

For the case $\tan \beta = 0$, the streamwise momentum integral equation and the entrainment equation, given by equations 2.62 and 2.65 respectively, can be simplified to

$$(A_\theta \quad A_{\bar{H}}) \cdot \frac{d}{d\xi} (\theta \quad \bar{H}) = A_0 - A_\beta \frac{d\beta}{d\xi} - A_U \frac{dU_{iw}}{d\xi} \quad (7.6)$$

where the terms A_A , A_θ , $A_{\bar{H}}$, A_β , A_U and A_0 are evaluated for $\tan \beta = 0$ from the expressions given in section 2.4.1, and

$$(E_\theta \quad E_{\bar{H}}) \cdot \frac{d}{d\xi} (\theta \quad \bar{H}) = E_0 - E_\beta \frac{d\beta}{d\xi} - E_U \frac{dU_{iw}}{d\xi} \quad (7.7)$$

Were, E_θ , $E_{\bar{H}}$, E_β , E_U and E_0 can likewise be evaluated for $\tan \beta = 0$.

Equation 2.76 can thus be reduced to a 2×2 matrix in the form below

$$\begin{bmatrix} A_\theta & A_{\bar{H}} \\ E_\theta & E_{\bar{H}} \end{bmatrix} \frac{d}{d\xi} \begin{bmatrix} \theta \\ \bar{H} \end{bmatrix} = \begin{bmatrix} A_0 - A_\beta \frac{d\beta}{d\xi} - A_U \frac{dU_{iw}}{d\xi} \\ E_0 - E_\beta \frac{d\beta}{d\xi} - E_U \frac{dU_{iw}}{d\xi} \end{bmatrix} \quad (7.8)$$

Substituting equation 7.5 into equation 7.8, the governing integral equations in the leading edge region can be expressed as,

$$\begin{bmatrix} A_\theta & A_{\bar{H}} \\ E_\theta & E_{\bar{H}} \end{bmatrix} \frac{d}{d\xi} \begin{bmatrix} \theta \\ \bar{H} \end{bmatrix} = \begin{bmatrix} A_0 - \frac{1}{U_{iw}} \frac{dU_1}{d\xi} \left(\sin \psi \frac{(1+H)}{f_1} A_\beta + U_1 A_U \right) \\ E_0 - \frac{1}{U_{iw}} \frac{dU_1}{d\xi} \left(\sin \psi \frac{(1+H)}{f_1} E_\beta + U_1 E_U \right) \end{bmatrix} \quad (7.9)$$

At $x/c = 0$, $U_1 = \cos \psi = 0$ and $\sin \psi = 1$, therefore the governing equations for the attachment line flow are reduced to two simultaneous differential equations

$$\begin{bmatrix} A_0 - \frac{1}{U_{iw}} \frac{dU_1}{d\xi} \frac{(1+H)}{f_1} A_\beta \\ E_0 - \frac{1}{U_{iw}} \frac{dU_1}{d\xi} \frac{(1+H)}{f_1} E_\beta \end{bmatrix} = 0 \quad (7.10)$$

where

$$\begin{aligned} A_\beta &= -f_2 \theta \\ A_0 &= \sin \Lambda \left[\frac{c_f}{2} + \kappa_T \theta \right] \end{aligned} \quad (7.11)$$

and

$$\begin{aligned}
E_\beta &= f_3\theta \\
E_0 &= \sin \Lambda [c_E + \kappa_T\theta H_1]
\end{aligned}
\tag{7.12}$$

Substituting for the corresponding coefficients in equation 7.8, the streamwise momentum integral equation (first equation) can be expressed as

$$\sin \Lambda \left[\frac{c_f}{2} + \kappa_T\theta \right] + \frac{1}{U_{iw}} \frac{dU_1}{d\xi} \frac{(1+H)}{f_1} f_2\theta = 0
\tag{7.13}$$

Based on the coordinates system adopted in Callisto, presented in figure 2.3, the taper curvature, κ_T , can be expressed in terms of the local taper radius, r , as

$$\kappa_T = \frac{1}{r}
\tag{7.14}$$

From this co-ordinate system, the x-axis is the locus of constant r and the y-coordinate lies in the opposite direction of r . For a turbulent flow,

$$\frac{\partial\theta}{\partial y} = -\frac{\theta}{r}
\tag{7.15}$$

and

$$\frac{dU_1}{d\xi} = \sin \Lambda \frac{dU_1}{dx}
\tag{7.16}$$

Substituting for κ_T in equation 7.13, the streamwise momentum integral equation can be expressed as

$$\frac{\partial \theta}{\partial y} = \frac{c_f}{2} + \frac{1}{U_{iw}} \frac{dU_1}{dx} (1 + H) \theta \frac{f_1}{f_2} \quad (7.17)$$

From the infinite swept assumption, $\partial \theta / \partial y = 0$ and following the definitions of the crossflow momentum thicknesses, $f_2 / f_1 = \theta_{12} / \theta_{21}$. By applying these conditions at the attachment line:

$$\frac{\theta_{12}}{\theta_{21}} = \frac{-c_f/2}{\frac{1}{U_{iw}} \frac{dU_1}{dx} (1 + H) \theta_{11}} \quad (7.18)$$

7.3 Comparison of Modified Callisto against Experiment

In the modified version of Callisto, the attachment line calculation is started as usual, using Smith's [109] formulation. Immediately downstream, where the calculation was previously frozen, the flow can be now computed by solving the proposed governing equation, given by equation 7.9 until $\psi \geq 80^\circ$, and from this point onwards the computation is undertaken by solving the full form of the governing three dimensional lag-entrainment method. This presents the first version of Callisto able to conduct a full chord turbulent flow calculation, where the issue related to leading edge modelling using in three dimensional integral methods is solved and the leading edge approximation proposed by Smith [109], 40 years ago is removed. In this section the proposed leading edge modelling from section 7.2 is verified through comparison with the experimental results captured on the swept NACA0050 model at $\bar{R} = 500$. This is similar to the analysis conducted in section 7.1.

From the development of the momentum thickness shown in Figure 7.4, downstream of the attachment line significant difference can be observed between the predictions from the earlier version of Callisto and the modified version of Callisto, referred as 'old' and 'new' respectively. In addition to the ability of obtaining a solution while marching in

the vicinity of the attachment line, the proposed leading edge modelling also improves the prediction as the difference between the experimental and numerical is reduced to 7% as opposed to the difference of 15% predicted by the earlier version. It is also able to better represent the rather peculiar maximum in the experimental θ encountered at $s'/c > \pm 0.03$. As this unexpected non-monotonic behaviour in θ near the attachment line is not reported in the literature, the initial conclusion was that this was due to uncertainty in experimental measurements. But more confidence can now be placed in this observation, as the behaviour has been replicated by the three dimensional momentum integral equations as well.

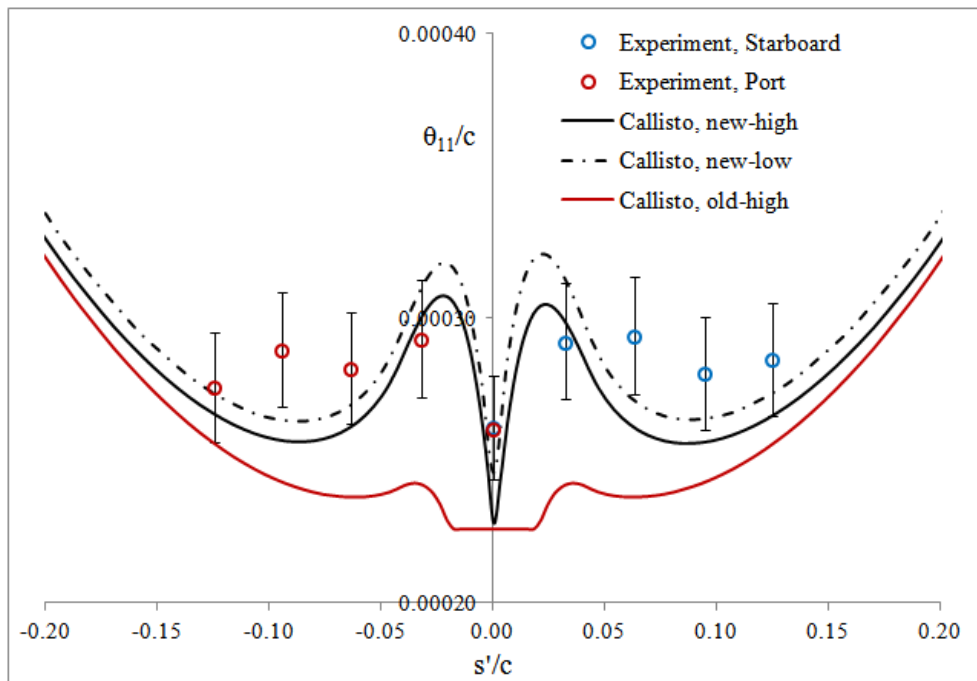


Figure 7.4: Comparison between θ measured during the current experiment and those obtained numerically from the previous and modified version of Callisto, using both a low and a high resolution mesh. The error bars are within $\pm 7\%$.

The predicted the shape factor presented in Figure 7.5 is not affected significantly by the software modification, except in the region of $0.0s'/c < \pm 0.1$ where a sharper decrease in H can be observed. Once again, the increase in H right downstream of the attachment line is not captured by the proposed leading edge model and the departure of the experimental H from the trend of the predicted result at $s'/c > \pm 0.1$ is still present.

From the experimental and numerical skin friction results, shown in Figure 7.6, the dif-

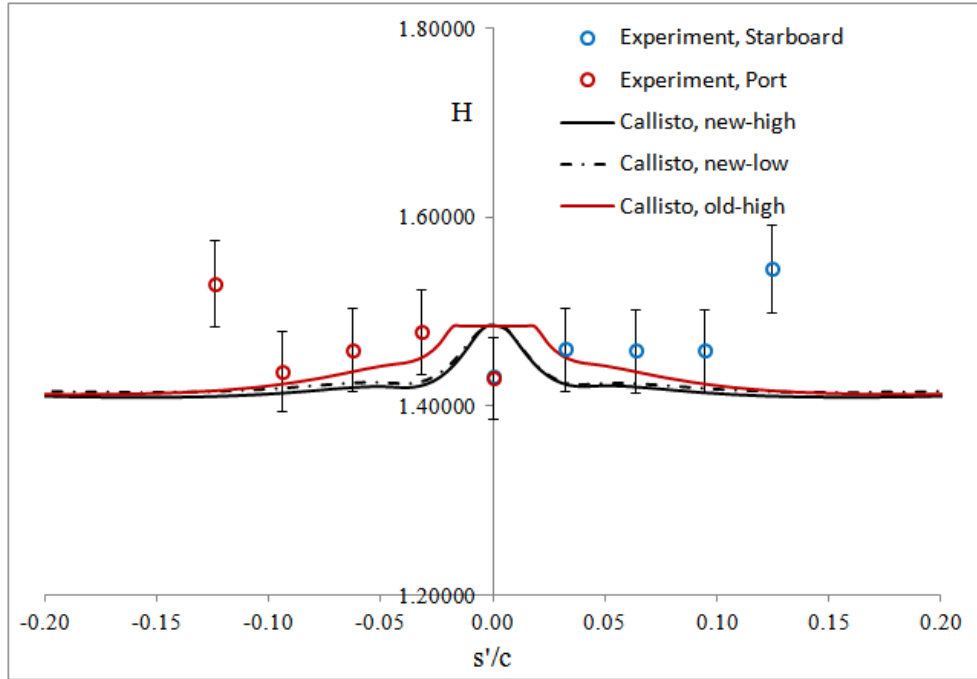


Figure 7.5: Comparison between H measured during the current experiment and those obtained numerically from the previous and modified version of Callisto, using both a low and a high resolution mesh. The error bars are within $\pm 3\%$.

ference between the two sets of result is still significant, by at least 15%. Unlike in the previous modelling in Callisto, the presence of an unexpected minimum point in the trend of the experimental skin friction is demonstrated during the numerical prediction as well, at $s'/c \approx \pm 0.01$, which is slightly upstream of the location observed in the experimental results, where it is present at $s'/c \approx \pm 0.03$. The ability to capture this particular behaviour, using the modified numerical modelling in Callisto, supports the observation that in the vicinity of the attachment line the skin friction develops non-monotonically, similar to θ .

During the analysis conducted above a geometric sweep angle of 60° was assumed for the swept NACA0050 profile. For a more accurate representation of the flow during the experiment, the effective sweep angle should be considered and it was calculated to be approximately 62° (section 5.4.1) in the region where the viscous flow measurements were made. The numerical prediction was thus repeated using the effective sweep angle, in this case \bar{R} increased to a value of 508 and the predicted development in θ and c_f at the leading edge is compared with the experimental results in Figures 7.7 and 7.8 respectively.

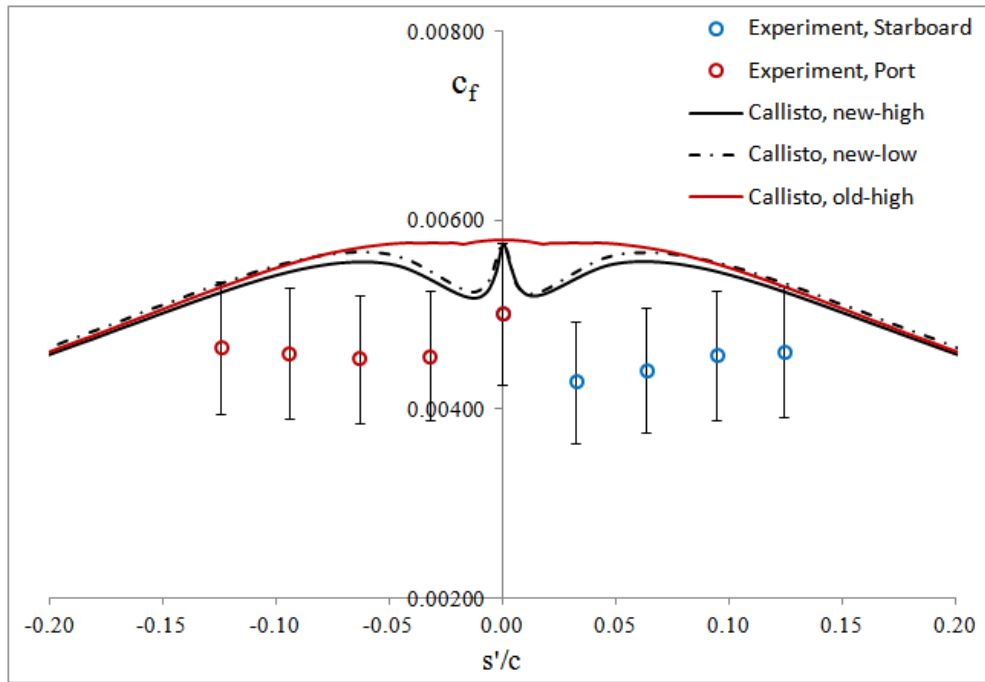


Figure 7.6: Comparison between c_f measured during the current experiment and those obtained numerically from the previous and modified version of Callisto, using both a low and a high resolution mesh. The error bars are within $\pm 15\%$.

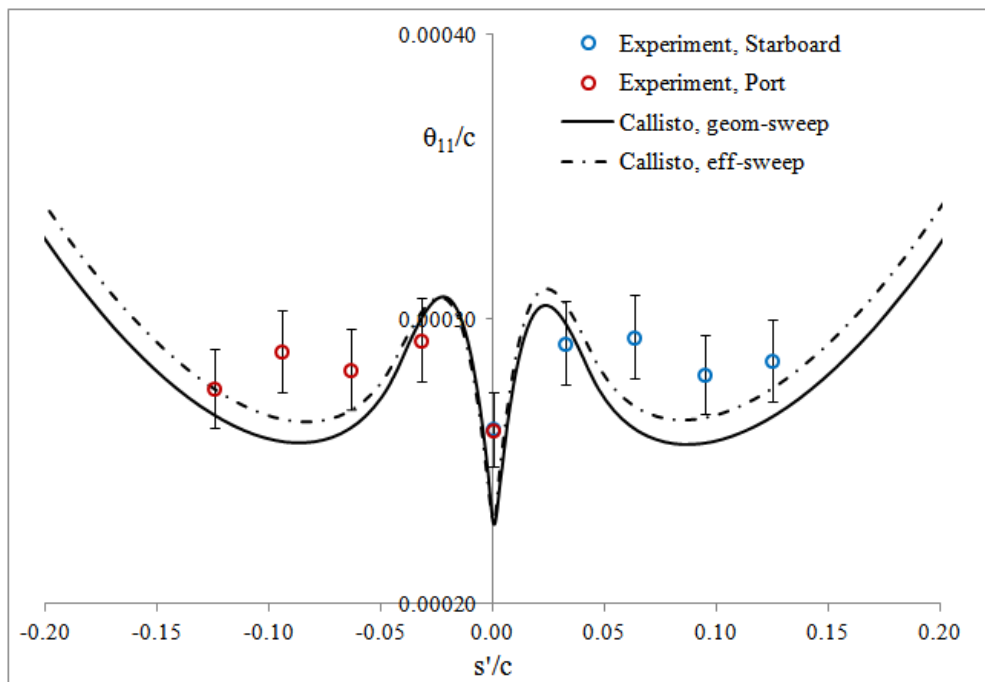


Figure 7.7: Comparison between θ measured during the current experiment and those obtained numerically using the effective sweep angle. The error bars are within $\pm 5\%$.

While accounting for the effective sweep, the agreement between the numerical and experimental momentum thickness is further improved as the difference reduces to 5%. A slight improvement in the correlation between the experiment and numerical skin friction

is also observed, but the difference is still significant.

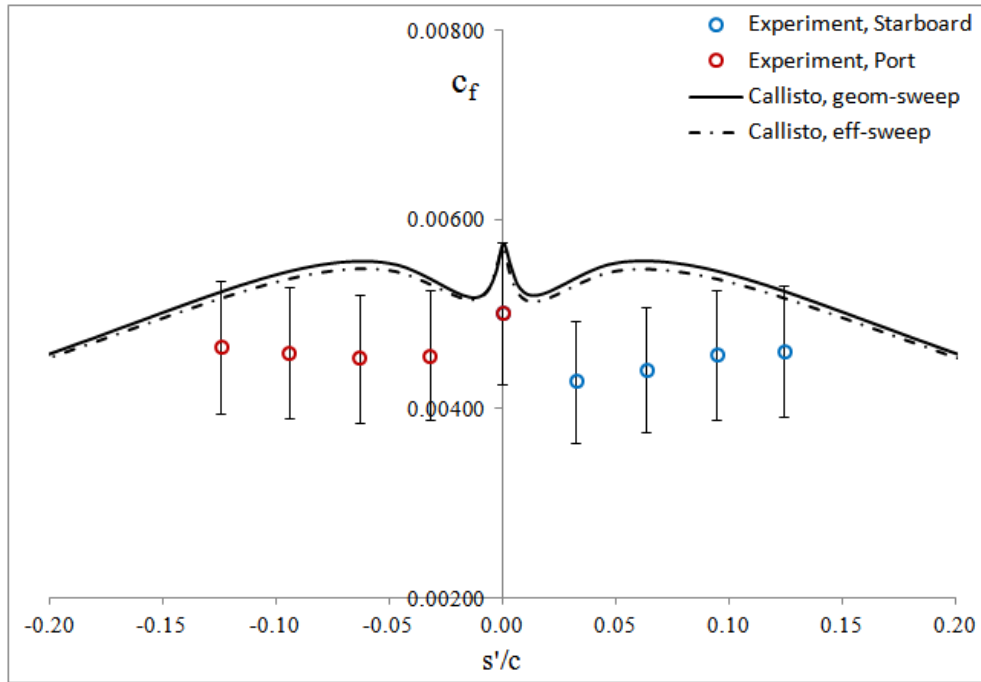


Figure 7.8: Comparison between c_f measured during the current experiment and those obtained numerically using the effective sweep angle. The error bars are within $\pm 15\%$.

As the non-monotonic behaviour in θ and c_f observed experimentally is also replicated by the momentum integral modelling in the modified version of Callisto, confidence in the occurrence of this particular behaviour is increased. From the experimental measurements it is difficult to identify the cause of this behaviour, but following a good agreement with the numerically predicted trend in θ , a diagnosis can be conducted by analysing the streamwise momentum integral equation. From the first row of the modified form of the governing equation given by equation 7.9, the streamwise momentum equation can be written as

$$A_\theta \frac{d\theta}{d\xi} = A_0 - A_U \frac{dU_{iw}}{d\xi} \quad (7.19)$$

where the terms $A_\theta d\bar{H}/d\xi$ and $A_\beta d\beta/d\xi$ have been omitted here, as they are relatively small in magnitude. A_0 is effectively the resolved component of skin friction.

From the numerical solution obtained from Callisto, the individual terms from equation

7.19 are calculated and their development in the vicinity of the attachment line is presented in Figure 7.9. The position of the stationary points in θ coincide with the two points of intersection in A_0 and $A_U dU, etc$, which represents the second term on the right hand side of equation 7.19 and includes the contribution from $A_{\bar{H}} d\bar{H}/d\xi$ and $A_{\beta} d\bar{H}/d\xi$. Similar to the two dimensional momentum integral equation, A_0 from equation 7.19 represents the contribution of skin friction and $A_U dU, etc$ the effect of velocity gradient. In Figure 7.9, the initial growth in θ is due to the increase in $A_U dU, etc$, whose rate of increase gradually slows down until up to $s'/c \approx 0.03$, where it even exceeds the A_0 and a maximum in θ is encountered. Straight after, θ undergoes a reduction up to $s'/c \approx 0.08$ where a minimum is reached and $A_U dU, etc$ appears to have dropped to a value lower than that of A_0 . From this point onwards θ increases similar to the development on a two dimensional aerofoil, due to slower rate of change in skin-friction and reduction in the acceleration of the flow while propagating downstream. The early growth of θ is made more rapidly by the fact that $A_{\theta} \approx 0$ at $s'/c \approx 0$.

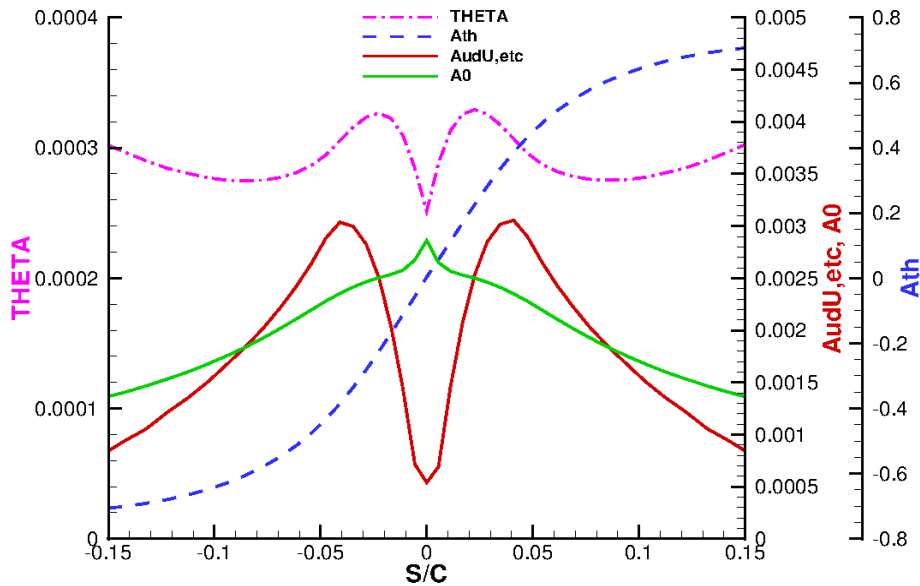


Figure 7.9: Development of the individual parameters in equation 7.19i in the vicinity of the attachment line.

Along the attachment line, the streamwise momentum thickness responds only to the skin friction which is acting in the spanwise direction, but immediately downstream, when the

streamline starts to turn towards the chordwise direction, c_f and thus A_0 is reduced due to the effect of sweep and the favourable velocity gradient increases rapidly. A reduction in the growth rate of θ is then seen until the influence of the velocity gradient exceeds that of the skin friction and θ reaches a maximum. However, the velocity gradient attains a maximum itself and starts reducing at a faster rate than the skin friction, which results in a renewed growth in θ .

7.4 Attachment Line Control Revisited

Following the fair agreement between the modified version of Callisto and the experimental results, the benefits from attachment line control predicted in section 2.6 are revisited and the test cases in section 2.6 were re-analysed using the modified version of Callisto. The results from the simulation using the version with the numerical fix are compared with the results from the modified version in Figure 7.10, which shows the difference in drag between a fully turbulent case and the case with varying amount of laminar flow on the upper surface and transition fixed at 1% chord on the lower surface. A swept supercritical aerofoil was used for freestream condition similar to transonic cruise, where the Reynolds number, $\bar{R} = 528$ was achieved at $C_L = 0.58$.

Regardless of the improvement in the capability to model the flow in the vicinity of the attachment line, using the proposed leading edge model, no significant difference in the drag predicted by both the old and new version of Callisto is demonstrated in Figure 7.10. A small reduction of approximately 0.1count is seen in the profile and form drag predicted using the new version of Callisto, however it is small. The similarity in the drag predicted from both numerical methods is due to the fact that the trend in momentum thickness predicted by the new version of Callisto starts to merge with that predicted by the old version at $s'/c \approx 0.01$. Therefore, the prediction of the momentum thickness in the far wake is not affected and the profile drag remains the same. A similar trend can be found in the development of the skin friction shown in Figure 7.12.

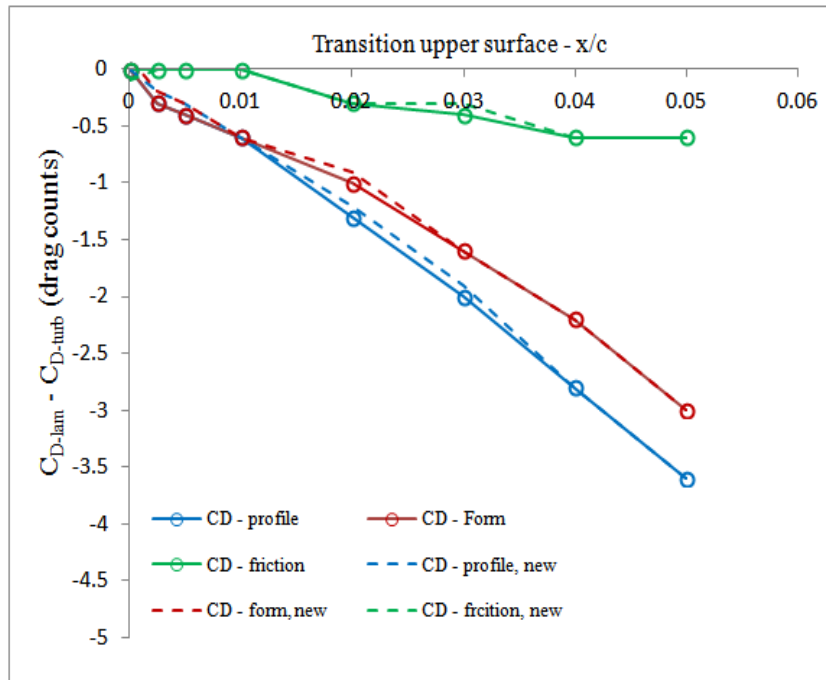


Figure 7.10: Comparison of the drag difference between a fully turbulent flow and the flow with varying transition location on the upper surface, but fixed at 1% chord on the lower surface, from the earlier method of Callisto and the new method including the modification to the leading edge modelling.

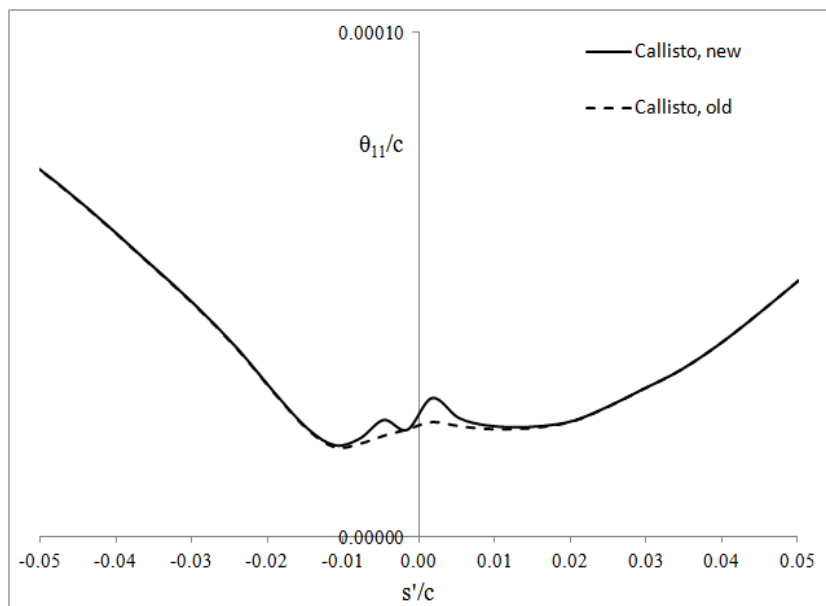


Figure 7.11: Comparison of the development of momentum thickness predicted by the earlier version and the latest version of Callisto on a supercritical aerofoil.

From Figures 7.11 and 7.12 the attachment line is shifted towards the lower surface, as for this calculation the lift coefficient, $C_L = 0.58$. Nevertheless, the non-monotonic behaviour in both the θ and c_f is still present, even on the moderately swept supercritical

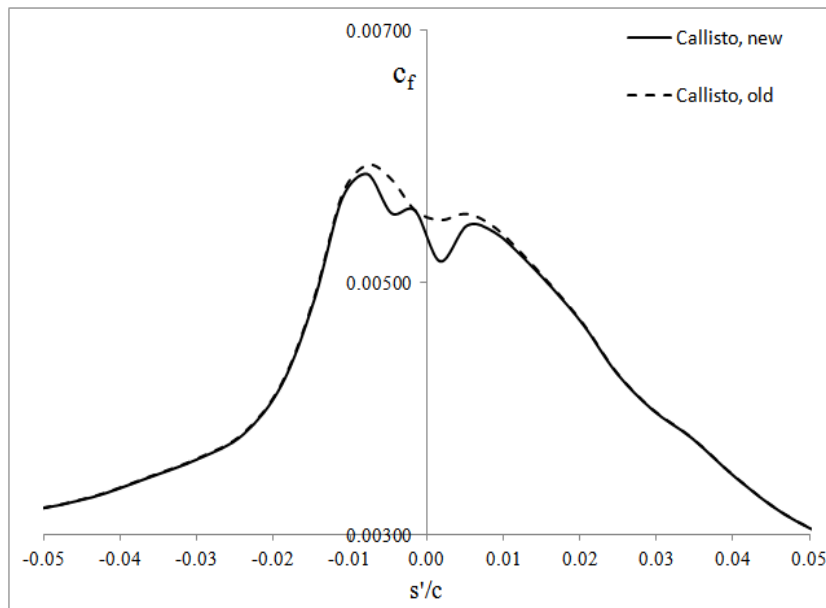


Figure 7.12: Comparison of the development of local skin friction predicted by the earlier version and the latest version of Callisto on a supercritical aerofoil.

aerofoil profile, at high Reynolds number representative of a transonic wing at cruise condition. Similar to the flow on the swept NACA0050 model the oscillations in θ and c_f in the vicinity of the attachment line do not seem to affect the flow downstream.

Chapter 8

Conclusions

8.1 Main Objective

An experimental investigation to gather information to validate or modify a numerical fix to the Airbus Callisto method has been successful. Using the proposed modification to the leading edge modelling in Callisto, the initial form drag benefit through attachment line control has been confirmed. Although not reported in this thesis, considerable work has been undertaken by Airbus on the basis of the Callisto results so this confirmation of the form drag benefit is a welcome conclusion from the project.

8.2 Experiment

During the model design process, the NACA0050 profile proved to be more suitable for the current experiment, as opposed to a faired circular cylinder preferred in previous studies, as wind tunnel blockage is reduced due to the presence of a flow that remains attached downstream of the point of maximum thickness. A digital optical system was developed to verify the performance of the micro-displacement traverse. This also proved to be very

useful for the near-wall alignment of hot wire probes and this permitted very accurate measurement in the very thin turbulent attachment line boundary layer. For the measurement downstream of the attachment line, the SY-probe was used and an unconventional approach was followed by rotating the probe by 180° about its axis, where Bradshaw's $\cos \alpha_e$ law proved to be more robust in capturing velocity profiles which feature changes in direction through the boundary layer, as in a highly curved three dimensional flow.

From the hot wire signal the critical attachment line Reynolds number for side wall contamination was found to be at $\bar{R} \approx 245$ or $R_\theta \approx 100$ similar to the findings of Pfenninger [89], Gaster [45] and Poll [92]. The laminar velocity profiles at the attachment line agreed to within $\pm 5\%$ with swept Hiemenz flow theory. Good agreement was also found between the turbulent velocity profiles obtained from the current experiment with those of Cumpsty and Head [36], together with the shape factor and skin friction, but the momentum thickness from the current experiment was higher than measured by Cumpsty and Head, possibly due to the larger number of data points across the velocity profile. The current experimental results showed better correlation with the universal log-law than did the scattered results of Cumpsty and Head and this was attributed to the improved precision offered by the traverse gear and digital optical systems. Based on the correlation with the log-law, the minimum condition for a fully turbulent attachment line is found to be at $R_\theta = 315$, which is in close agreement with Preston's criterion for flow on flat plates. The analysis of Cumpsty and Head was based on geometric sweep, but effective sweep is found to be significant and the attachment line Reynolds number, \bar{R} , criteria for the intermittent and fully turbulent states are proposed as $250 < \bar{R}_{eff} < 360$ and $\bar{R}_{eff} > 360$ respectively.

Interesting flow features were observed downstream of the attachment in both the streamwise and crossflow velocity profiles. The streamwise velocity profiles demonstrate Reynolds number dependence, but the likelihood of relaminarisation at $\bar{R} = 425$ is questionable due to the mild acceleration at the leading edge. Cross-over crossflow velocity profiles are present downstream of the attachment line, but in the absence of an inflection point in

the path of the external streamline, this effect is thought to be mainly due to the development of the Reynolds shear stresses downstream of the attachment line. The streamwise momentum thickness demonstrated a non-monotonic behaviour during its development downstream of the attachment line and this effect has not been reported previously.

8.3 Numerical Analysis

The experimental trends, in particular the very small values of limiting streamline angle suggested a modified form of the governing equations applicable immediately downstream of the attachment line. The numerical fix in the original version of Callisto has been superseded and a full chord calculation is now possible without having to freeze the calculation immediately downstream of the attachment line. The revised leading edge modelling replicated the non-monotonic behaviour observed during the experiments, which gave confidence in the results. A diagnosis for the occurrence of such behaviour was possible by analysing the individual terms in the streamwise momentum integral equation.

Further numerical analysis of the flow around a supercritical aerofoil at transonic cruise condition was repeated, using the modified version of Callisto, to explore the effect of the modelling changes on the form drag benefit through attachment line control. No significant difference was found from the original calculation. However the non-monotonic behaviour in θ and c_f was found even at transonic cruise conditions.

8.4 Recommendation for Further Work

Looking at the crossflow velocity profiles, difficulties were encountered while resolving the near-wall flow and this was due to the type of hot wire probe used for the measurement downstream of the attachment line, as the probe support was coming in contact

with the surface and restricting further movement. This issue could be solved either by changing the orientation of the hot wire probe while traversing or through modification to the existing hot wire probe. The ability to resolve the near wall flow, should allow accurate measurement of turbulent stresses and this could help to explore the hypothesis for the occurrence of cross-over crossflow velocity profiles in a turbulent boundary layer. These measurements would also help in generating more insight into Reynolds number dependence shown by the streamwise velocity profiles at $\bar{R} = 425$.

References

- [1] A. Abdel-Rahman, C. Tropea, P. Slawson, and A. Strong. On temperature compensation in hot-wire anemometry. *Journal of Physics. E: Sci. Instrum.*, 20:315–319, 1987.
- [2] A. Anscombe and L. N. Illingworth. Wind-tunnel observations of boundary layer transition on a wing at various angle of sweepback. Technical report, ARC RM 2968, 1952.
- [3] D. Arnal and J. P. Archambaud. Laminar-turbulent transition control: Nlf, lfc, hlfc. *AGARD RTO-EN-AVT-151*, 2008.
- [4] D. Arnal and J. C. Juillien. The experimental study of transition and leading edge contamination on swept wings. *AGARD*, 8:505, 1997.
- [5] D. Arnal, J. C. Juillien, J. Reneaux, and G. Gasparian. Effect of wall suction on leading edge contamination. *Aerospace Science and Technology*, 8:505, 1997.
- [6] P. R. Ashill. Brief note on modifications of the integral boundary layer equations for swept, tapered wings to allow for 'high-order' effects. NEXUS Report NEXUS/001, QinetiQ, September 2002.
- [7] P. R. Ashill, J. L. Fulker, and R. F. Wood. On the sectional drag and pressure distributions of swept-wing aerofoil sections. Technical Report 88073, RAE, 1988.

- [8] P. R. Ashill and P. D. Smith. An integral method for calculating the effects on turbulent boundary-layer development on sweep and taper. Technical Report 83503, RAE, 1983.
- [9] P. R. Ashill, R. F. Wood, and D. J. Weeks. An improved semi-inverse method of the viscous garabedian and korn method (vgk). Technical Report 87002, RAE, 1987.
- [10] C. J. Atkin. Application of the newton method to the integral boundary layer equations. Technical Report FST/TR032188, QinetiQ, April 2003.
- [11] C. J. Atkin. Calculation of laminar boundary layers on swept-tapered wings. Technical Report FST/TR025107/1.0, QinetiQ, February 2004.
- [12] C. J. Atkin. Summary of the swept-tapered lag-entrainment boundary layer method in callisto version 3.4. Technical Report QinetiQ/08/00064, QinetiQ, January 2008.
- [13] C. Badalamenti. *On the application of rotating Cylinders to Micro air vehicles*. PhD thesis, City University London, School of Engineering and Maths, 2010.
- [14] F. Bellone. *New Models for the Prediction of Attachment Line Behaviour at Hypersonic Speeds*. PhD thesis, Cranfield University, College of Aeronautics, 2001.
- [15] P. Bradshaw. The analogy between streamline curvature and buoyancy in turbulent shear flow. *Journal of Fluid Mechanics*, 36:177–191, 1969.
- [16] P. Bradshaw. *An Introduction to Turbulence and its Measurement*. Pergamon Press, 1971.
- [17] P. Bradshaw. Variations on a theme of prandtl. *AGARD CP 93*, 1972.
- [18] P. Bradshaw and D. H. Ferriss. Calculation of boundary layer development using the turbulent energy equation: Compressible flow on adiabatic walls. *Journal of Fluid Mechanics*, 46:83–110, 1971.

- [19] P. Bradshaw, D. H. Ferriss, and N. P. Atwell. Calculation of turbulent boundary layer development using the turbulent energy equation. *Journal of Fluid Mechanics*, 28:593–616, 1967.
- [20] Braslow. A history of suction type laminar flow control with emphasis on flight research. Monographs in Aerospace History 13, NASA, 1999.
- [21] H. H. Bruun. *Hot-wire anemometry, Principles and Signals*. Oxford University Press, 1995.
- [22] H. H. Bruun, N. Nabhani, H. H. Al-Kayiem, A. A. Fardad, M. A. Khan, and E. Hogarth. Calibration and analysis of x hot-wire prob signal. *Measurement Science and Technology*, 1:782–785, 1990.
- [23] H. H. Bruun and C. Tropea. Calibration and of inclined hot-wire probes. *Journal of Physics E: Scientific Instruments*, 18:405–413, 1985.
- [24] T. Cebeci and J. Cousteix. *Modelling and Computation of Boundary Layer Flows*. Springer, 2nd edition, 2005.
- [25] F. H. Clauser. Turbulent boundary layers in adverse pressure gradients. *Journal of Aeronautical Sciences*, 21:91, 1954.
- [26] F. H. Clauser. The turbulent boundary layer. *Advances in Applied Mechanics*, 4, 1956.
- [27] D. E. Coles. The law of the wake in the turbulent boundary layer. *Journal of Fluid Mechanics*, 1, 1956.
- [28] D. C. Collis and M. J. Williams. Two dimensional convection form heated wires at low reynolds number. *Journal of Fluid Mechanics*, 16:357–384, 1959.
- [29] P. H. Cook, M. A. McDonald, and M. C. P. Firmin. Wind tunnel measurements of the mean flow in the turbulent boundary layer and wake in the region of the trailing edge of a swept wing at subsonic speeds. Technical Report 83503, RAE, 1983.

- [30] J. C. Cooke. The boundary layer of a class of infinite yawed cylinders. *Proceedings of Cambridge Philosophical Society*, 46, 1950.
- [31] J. C. Cooke. Three-dimensional turbulent boundary layers. *ARC CP 635*, 1961.
- [32] L. F. Crabtree. The compressible laminar boundary layer on yawed infinite wing. *Aeronautical Quarterly*, 5, 1952.
- [33] N. A. Cumpsty. Crossflow in turbulent boundary layers. *ARC CP 1067*, 1968.
- [34] N. A. Cumpsty and M. R. Head. The calculation of three dimensional turbulent boundary layers. part i: Flow over the rear of an infinite swept wing. *Aeronautical Quarterly*, 18:pp. 55, 1967.
- [35] N. A. Cumpsty and M. R. Head. The calculation of three dimensional turbulent boundary layers. part ii: Attachment line flow in an infinite swept wing. *Aeronautical Quarterly*, 18:pp. 150, 1967.
- [36] N. A. Cumpsty and M. R. Head. The calculation of three dimensional turbulent boundary layers. part iii: Comparison of attachment line calculation with experiment. *Aeronautical Quarterly*, 20:pp. 99, 1969.
- [37] N. A. Cumpsty and M. R. Head. The calculation of three dimensional turbulent boundary layers. part iv: Comparison of measurements with calculations on the rear of a swept wing. *Aeronautical Quarterly*, 21:pp. 121, 1970.
- [38] W. J. Duncan, A. S. Thom, and A. D. Young. *An elementary treatise on the mechanics of fluids*. Edward Arnold, 1960.
- [39] L. F. East and R. P. Hoxey. Low-speed three-dimensional turbulent boundary layer data. *ARC RM 3653*, 1969.
- [40] D. H. Ferriss. Preston tube measurements in turbulent boundary layers and fully developed pipe flow. *ARC CP 831*, 1965.

- [41] C. A. Friehe and W. H. Schwartz. Deviation from the cosine law for yawed cylindrical anemometer sensors. *Transaction ASME*, 35E:655, 1968.
- [42] Garabedian and Korn. Analysis of transonic airfoils. *Communications on Pure and Applied Mathematics*, 24, 1971.
- [43] M. Gaster. Private communication.
- [44] M. Gaster. A simple device for preventing turbulent contamination on swept leading edges. *Journal of Royal Aeronautical Society*, 69(659):pp. 788–789, 1965.
- [45] M. Gaster. On the flow along swept leading edges. *Aeronautical Quarterly*, 18:pp. 165, May 1967.
- [46] M. Gaster and C. J. Atkin. Private communication.
- [47] P. S. Granville. A modified law of the wake for turbulent shear layers. *Journal of Fluid Engineering*, 1976.
- [48] W. E. Gray. The effect of wing sweep on laminar flow. Technical report, RAE TM 255 or ARC 14,929, 1952.
- [49] W. E. Gray. The nature of the boundary layer flow at the nose of a swept wing. Technical report, RAE TM 256 or ARC 15,021, 1952.
- [50] J. E. Green. Greener by design - the technology challenge. *The Aeronautical Journal*, 106:57–113, 2002.
- [51] J. E. Green. Civil aviation and the environment - the next frontier for the aerodynamicist. *The Aeronautical Journal*, 106:469, 2006.
- [52] J. E. Green, D. J. Weeks, and J. W. F. Brooman. Prediction of the turbulent boundary layers and wakes in compressible flow by a lag-entrainment method. *ARC R&M 3791*, 1973.
- [53] N. Gregory. Laminar flow on a swept leading edge. 2nd progress report. Technical Report Aero. Memo. No. 12, National Physics Lab., 1964.

- [54] N. Gregory and W. S. Walker. Brief wind tunnel tests on the effect of sweep in laminar flow. Technical Report ARC 14,928, ARC, 1952.
- [55] P. Hall, M. R. Malik, and D. I. A. Poll. On the stability of an infinite swept attachment-line boundary layer. *Proceedings of the Royal Society*, 395, 1984.
- [56] M. R. Head. Entrainment in the turbulent boundary layer. *ARC R&M 3152*, 1958.
- [57] M. R. Head and V. C. Patel. Improved entrainment method for calculating turbulent boundary layer development. *ARC R&M 3643*, 1968.
- [58] M. R. Head and I. Rechenberg. The preston tube as a means of measuring skin friction. *Journal of Fluid Mechanics*, 14, 1962.
- [59] K. Hiemenz. *Die Grenzschicht an einem in den gleichförmigen Flüssigkeitsstrom eingetuchten geraden Kreiszyylinder*. PhD thesis, Gottingen, Dingl. Polytech.J.326, 1911.
- [60] J. O. Hinze. *Turbulence: An Introduction to Its Mechanism and Theory*. McGraw-Hill, first edition, 1959.
- [61] L. Howarth. On calculation of the steady flow in the boundary layer near the surface of a cylinder in a stream. *Rep. Memor. aerp. Res. Coun.*, 5:156,231,260,261,286, 1934.
- [62] L. Howarth. The boundary layer in three dimensional flow. part ii: The flow near the stagnation point. *Phil. Mag.*, 42:pp. 1433–1440, 1951.
- [63] F. A. Jenkins and H. E. White. *Fundamentals of Optics*. McGraw-Hill International Editions, fourth edition, 1965.
- [64] J. P. Johnston. On the three-dimensional turbulent boundary-layer generated by secondary flows. *Journal of Basic Engineering, Series D, Trans. ASME*, 82:233, 1960.

- [65] F. E. Jorgensen. How to measure turbulence with hot-wire anemometers: A practical guide. Technical report, Dantec Dynamics, 2002.
- [66] R. Joslin. Overview of laminar flow control. Technical Report TP-1998-208705, NASA, 1998.
- [67] J. C. Juillen and D. Arnal. Experimental study of boundary layer suction effects on leading edge contamination along the attachment line of a swept wing. *Springer Verlag*, 1995.
- [68] M. A. Khan. *Leakage flow in Labyrinth seals*. PhD thesis, Dept. of Mechanical and Manufacturing Engineering, University of Bradford, 1991.
- [69] L. V. King. On the convection of heat from small cylinder in a stream of fluid: Determination of the convection constants of small platinum wires with application to hot-wire anemometry. *Phil. Trans. Roy. Soc.*, A214:373–432, 1914.
- [70] P. S. Klebanoff. Characteristics of turbulence in a boundary layer with zero pressure gradient. *NACA Report 1247*, 1955.
- [71] B. E. Launder. Laminarisation of turbulent boundary layer in a severe acceleration. *Journal of Applied Engineering*, 31:707, 1964.
- [72] R. Lin and M. R. Malik. On the stability of attachment-line boundary layer. part1: The incompressible swept hiemenz flow. *Journal of Fluid Mechanics*, 311:239, 1996.
- [73] R. C. Lock. The growth of compressible turbulent boundary layers on isothermal and adiabatic walls. *ARC R&M 3191*, 1958.
- [74] R. C. Lock. An equivalence law relating three- and two-dimensional pressure distribution. *ARC 23952*, 1962.
- [75] R. C. Lock. The prediction of the drag of aerofoils and wings at high subsonic speeds. *Aeronautical Journal*, 90:207–226, 1986.

- [76] R. C. Lock and B. R. Williams. Viscous-inviscid interaction in external aerodynamics. *Progress in Aerospace Science*, 24:51–171, 1987.
- [77] A. Mager. Generalisation of boundary layer momentum integral equations to three-dimensional flows including those of rotating systems. Report 1067, NACA, 1952.
- [78] J. P. Marec. Drag reduction: a major task for research. In *CEAS/Dragnet European Drag Reduction Conference, Potsdam, 2000*.
- [79] D. McLean. *Understanding Aerodynamics: Arguing from the Real Physics*. WILEY, first edition, 2013.
- [80] G. L. Mellor and D. M. Gibson. Equilibrium turbulent boundary layers. *Journal of Fluid Mechanics*, 24 Part2:pp. 225, 1966.
- [81] R. Mukund, R. Narasimha, P. R. Viswanath, and J. D. Crouch. Multiple laminar-turbulent transition cycles around a swept leading edge. *Experiment in Fluids*, 53:1915, 2012.
- [82] R. Narasimha and K. R. Sreenivasan. Relaminarisation in highly accelerated turbulent boundary layers. *Journal of Fluid Mechanics*, 61:417, 1973.
- [83] J. F. Nash and A. G. J. McDonald. The calculation of momentum thickness in turbulent boundary layers at mach number up to unity. *ARC CP 963*, 1966.
- [84] F. B. Ogilvie. Private communication.
- [85] P. R. Owen and D. G. Randall. Boundary layer transition on sweptback wing. Technical Report RAE TM 277, RAE, 1952.
- [86] P. R. Owen and D. G. Randall. Boundary layer transition on sweptback wing: A further investigation. Technical Report RAE TM 330, RAE, 1952.
- [87] V. C. Patel. Calibration of the preston tube and limitations on its use in pressure gradients. *Journal of Fluid Mechanics*, 23:185–208, 1965.

- [88] A. E. Perry. *Hot-wire Anemometry*. Oxford University Press, 1982.
- [89] W. Pfenninger. Flow phenomena at the leading edge of a swept wing. *AGARD, Recent development in boundary-layer research, Part IV*, 97, 1965.
- [90] W. Pfenninger and J. W. Bacon. *In Viscous Drag Reduction*. (ed. C. S Wells), Plenum Press, 1969.
- [91] D. I. A. Poll. *Some aspects of the flow near a swept attachment line with particular reference to boundary layer transition*. PhD thesis, Cranfield University, College of Aeronautics, 1978.
- [92] D. I. A. Poll. Transition in the infinite swept attachment line boundary layer. *Aeronautical Quarterly*, 30:pp. 607–628, 1979.
- [93] D. I. A. Poll. Some observation of the transition process on the windward face of a long yawed cylinder. *Journal of Fluid Mechanics*, 150:329, 1984.
- [94] D. I. A. Poll and M. Danks. Relaminarisation of the swept wing attachment line by surface suction. *Springer Verlag*, 1995.
- [95] J. H. Preston. The determination of turbulent skin friction by means of pitot tubes. *Journal of Royal Aeronautical Society*, 58, 1954.
- [96] J. H. Preston. The minimum Reynolds number for a turbulent boundary layer and the selection of transition device. *Journal of Fluid Mechanics*, 3, 1957.
- [97] J. Reneaux, J. Preist, J. C. Juillen, and D. Arnal. Control of attachment line contamination. In *2nd European Forum on Laminar Flow Technology, Bordeaux*, 1996.
- [98] L. Rosenhead. *Laminar Boundary Layers*. Oxford University Press, 1963.
- [99] J. C. Rotta. Turbulent boundary layers in incompressible flows. *Progress in Aeronautical Sciences*, 2:pp. 1–219, 1962.
- [100] W. S. Saric and H. L. Reed. Towards practical laminar flow control - remaining challenges. In *34th AIAA Fluid Dynamics Conference*, 1996.

- [101] W. S. Saric, H. L. Reed, and E. B. White. Stability and transition of three-dimensional boundary layers. *Annual Reviews of Fluid Mechanics*, 35:413, 2003.
- [102] H. Schlichting. Zur entstehung der turbulenz bei der plattenstromung. *Nachr. Ges. Wiss. Gttingen, Math.-Phys. Kl.*, pages 181–208, 1933.
- [103] G. Schrauf. Evaluation of the a320 hybrid laminar fin experiment. In *European Congress on Computational Methods in Applied Sciences and Engineering, Barcelona*, 2000.
- [104] G. B. Schubauer and H. K. Skramstad. Laminar boundary layer oscillations and stability of laminar flow. *Journal of Aeronautical Science*, 14, 1947.
- [105] A. Seitz and K. Horstmann. Design studies on nlf and hlfc applications at dlr. In *27th International Congress of Aeronautical Science*, 2010.
- [106] T. K. Sengupta and A. Dipankar. Subcritical instability on the attachment line of an infinite-swept wing. *Journal of Fluid Mechanics*, 526, 2005.
- [107] G. R. Seyfang. Turbulent drag reduction by passive means. In *Proceedings of the international conference, Royal Aeronautical Society, London*, 1987.
- [108] P. D. Smith. Calculations methods for three-dimensional turbulent boundary layers. *ARC R&M 3525*, 1966.
- [109] P. D. Smith. A calculation method for the turbulent boundary layer on an infinite yawed wing in compressible, adiabatic flow. *ARC CP 1268*, 1972.
- [110] P. R. Spalart. Direct numerical simulation of leading edge contamination. Technical Report AGARD-CP-438, Ch 5, NATO, 1989.
- [111] D. A. Spence. The growth of compressible turbulent boundary layers on isothermal and adiabatic walls. *ARC R&M 3191*, 1958.
- [112] H. B. Squire and A. D. Young. The calculation of the profile drag of aerofoils. *ARC RM 1838*, 1937.

- [113] B. G. J. Thompson. A new two-parameter family of mean velocity profiles for incompressible turbulent boundary layers on smooth walls. *ARC RM 3463*, 1967.
- [114] B. G. J. Thompson. The prediction of boundary-layer behaviour and profile drag for infinite swept wings: Part ii flow near a turbulent attachment line. *ARC CP 1308*, 1973.
- [115] B. G. J. Thompson, G. A. Carr-Hill, and M. Ralph. The prediction of boundary layer behaviour and profile drag for infinite-yawed wing: Part iii calculation for a particular wing. *ARC CP 1309*, 1973.
- [116] B. G. J. Thompson and G. J. MacDonoald. The prediction of boundary-layer behaviour and profile drag for infinite swept wings: Part iii a method for calculation. *ARC CP 1307*, 1973.
- [117] W. Tollmien. Über die entstehung der turbulenz. *Nachr. Ges. Wiss. Gttingen*, pages 21–44, 1929.
- [118] E. Torenbeek. *Synthesis of Subsonic Airplane Design*. Delft University Press, 1982.
- [119] B. W. van Oudheusden. The asymptotic structure of the turbulent attachment line boundary layer. *The Aeronautical Journal*, 107(1067):pp. 57–61, 2003.
- [120] T. von Karman. Über laminare und turbulente reibung. *ZAMM*, 1, 1921.
- [121] J. A. B. Wills. The correction of hot-wire readings for proximity to a solid boundary. *Journal of Fluid Mechanics*, 12, 1962.
- [122] K. G. Winter and L. Gaudet. Turbulent boundary layer studies at high reynolds numbers at mach numbers between 0.2 and 2.8. *ARC RM 3463*, 1967.

Appendix A

The Numerical Method

A.1 The functions f_1 to f_4

$$f_1 = \cot \beta \frac{\theta_{21}}{\theta_{11}} = \frac{-2}{(\bar{H} - 1)(\bar{H} + 2)}$$

$$f_2 = \cot \beta \frac{\theta_{12}}{\theta_{11}} = \frac{(14\bar{H} + 30)}{(\bar{H} + 2)(\bar{H} + 3)(\bar{H} + 5)}$$

$$f_3 = \cot \beta \frac{\delta_2}{\theta_{11}} = \frac{-16\bar{H}}{(\bar{H} - 1)(\bar{H} + 3)(\bar{H} + 5)}$$

$$f_4 = \cot \beta \frac{\theta_{22}}{\theta_{11}} = \frac{-24\bar{H}}{(\bar{H} - 1)(\bar{H} + 2)(\bar{H} + 3)(\bar{H} + 4)}$$

A.2 Closure Relationships

Compressibility is included through the compressible shape parameter similar to that formulated by Green et al. Here the incompressible shape factor, \bar{H} can be expressed as a function of compressible shape factor, H and the local mach number.

$$H = (\bar{H} + 1) \left(1 + \frac{\gamma - 1}{2} r M_{iw}^2 \right) - 1 \quad (\text{A.1})$$

In the current version of Callisto the relation for the entrainment shape factor, H_1 , proposed by Lock and Williams is adopted. For $\bar{H} < 4$,

$$H_1 = 2 + 1.5 \left(\frac{1.12}{\bar{H} - 1} \right)^{1.093} + 0.5 \left(\frac{\bar{H} - 1}{1.12} \right)^{1.093} \quad (\text{A.2})$$

and for $\bar{H} \geq 4$ Lock and Williams suggested

$$H_1 = 3.9788 + 0.3486 (\bar{H} - 4) \quad (\text{A.3})$$

The skin friction coefficient closure relation is that given by Ashill and Smith [8], which applies for most practical flows

$$c_f = c_{f_0} \left[\left(\frac{0.9\bar{H}_0}{\bar{H} - 0.4\bar{H}_0} \right) - 0.5 \right] \quad (\text{A.4})$$

where the flat plate skin friction coefficient for compressible flow, c_{f_0} is a modified version of that given by Winter and Gaudet [122] (equation 2.48) to account for low Reynolds number effects.

$$c_{f_0} = \frac{\nu_1}{F_c} \left[\frac{0.01013}{\log_{10}(F_R R_\theta) - 1.02} \right] - 0.00075 \quad (\text{A.5})$$

The compressibility correction terms, F_c and F_R

$$F_C = \sqrt{1 + 0.2M_{iw}^2}, \quad F_R = 1 + 0.056M_{iw}^2 \quad (\text{A.6})$$

and the low Reynolds number correction terms, ν_1 and ν_2

$$\nu_1 = 1 + \frac{33}{R_\theta} (1 + 0.2M_{iw}^2), \quad \nu_2 = 1 + \frac{42}{R_\theta} (1 + 0.2M_{iw}^2) \quad (\text{A.7})$$

The incompressible shape factor for zero pressure gradient can be given as

$$\bar{H}_0 = \frac{1}{1 - 6.55 \sqrt{\nu_2 \frac{c_{f_0}}{2} (1 + 0.04M_{iw}^2)}} \quad (\text{A.8})$$

Unlike the skin friction and shape factor relations above, the steps involved in defining the closure relation for the ‘lag’ equation are more involved. Firstly an empirical relation between the entrainment and shear stress coefficient for a compressible flow is required and the form below suggested by Green et al. [52] is adopted.

$$c_\tau = \frac{\tau_{max}}{\rho_{iw} U_{iw}^2} = (0.024c_E + 1.2c_E^2 + 0.32c_{f_0}) (1 + 0.1M_{iw}^2) \quad (\text{A.9})$$

By applying equilibrium conditions, whereby \bar{H} remains constant or $d\bar{H}/dx = 0$, the entrainment equation becomes

$$c_{EQ(0)} = \frac{H_1}{1 + \bar{f}_{EQ}} \left[\frac{c_f}{2} - (H + 1 + \bar{f}_{EQ}) \left(\frac{\theta}{U_{iw}} \frac{\partial U_{iw}}{\partial s} \right)_{EQ(0)} \right] \quad (\text{A.10})$$

At equilibrium conditions the normal stress correction factor, \bar{f}_{EQ} , can be calculated using

$$\bar{f}_{EQ} = -0.072 \frac{\bar{H} - 1}{\bar{H}} \quad (\text{A.11})$$

In order to calculate $c_{\tau_{EQ0}}$ from equation 2.72, Atkin suggested that the empirical relation given by equation 2.36 can be employed, coupled with equation A.9 and A.10 at $EQ0$ conditions.

$$\left(\frac{\theta}{U_{iw}} \frac{\partial U_{iw}}{\partial s} \right)_{EQ0} = \frac{1.25}{H} \left[\frac{c_f}{2} - \nu_2 \left(\frac{\bar{H} - 1}{6.432\bar{H}} \right)^2 (1 + 0.04M_{iw}^2)^{-1} \right] \quad (\text{A.12})$$

The method summarised above neglects higher-order boundary layer terms, which can be implemented using the approach of Green et al. [52]. Finally, the normal stress correction term, \bar{f} , present in the streamwise momentum equation originally proposed by Ashill [6], is presented in reference [12].

Appendix B

Experimental Model

B.1 Location of pressure tappings

Table B.1: Chordwise position of pressure tappings on the port and starboard sides of the model.

Port		Starboard	
Tapping	x/c	Tapping	x/c
1	1.000		
2	0.950	50	0.95
3	0.900	49	0.900
4	0.800	48	0.800
5	0.700	47	0.700
6	0.600	46	0.600
7	0.500	45	0.500
8	0.400	44	0.400
9	0.300	43	0.300
10	0.200	42	0.200
11	0.185	41	0.185
12	0.170	40	0.170
13	0.155	39	0.155
14	0.140	38	0.140
15	0.125	37	0.125
16	0.110	36	0.110
17	0.095	35	0.095
18	0.080	34	0.080
19	0.065	33	0.065
20	0.050	32	0.050
21	0.040	31	0.040
22	0.030	30	0.030
23	0.020	29	0.020
24	0.010	28	0.010
25	0.003	27	0.003
26	0.000		

Appendix C

Uncertainty Analysis

C.1 Pressure and Velocity Measurements

The uncertainty in the surface pressure measurements was dependent on the accuracy of the electronic pressure system described in section 3.2. As the pressure coefficient can be expressed as

$$C_P = \frac{P_l - P_\infty}{q_\infty} \quad (\text{C.1})$$

the relative uncertainty while calculating the pressure coefficient takes the form of

$$\frac{\Delta C_P}{C_P} = \frac{\Delta P}{P} + \frac{\Delta q}{q} \quad (\text{C.2})$$

The accuracy of the each pressure sensor was rated at $\Delta P/P = \pm 0.06\%$ and the differential pressure transducer used to measure, q_∞ was rated at an accuracy of 0.25% based on the full scale deflection. Therefore the relative uncertainty in the pressure coefficient was equivalent to

$$\frac{\Delta C_P}{C_P} = 0.31\% \quad (C.3)$$

The freestream velocity was obtained using the dynamic pressure, which was obtained as a voltage output signal from the FCO318 differential pressure transducer connected to the Pitot-static tube. From basic principles the dynamic pressure can be expressed as

$$q_\infty = \frac{1}{2}\rho_\infty U^2 \quad (C.4)$$

where,

$$\rho_\infty = \frac{P_{atm}}{RT} \quad (C.5)$$

By rearranging equation C.4, the velocity could be expressed as

$$U = \left(\frac{2q_\infty RT}{P_{atm}} \right)^{1/2} \quad (C.6)$$

and therefore the relative uncertainty in the estimation of the freestream velocity can be given as,

$$\frac{\Delta U}{U} = \frac{1}{2} \left(\frac{\Delta q_\infty}{q_\infty} + \frac{\Delta T}{T} + \frac{\Delta P_{atm}}{P_{atm}} \right) \quad (C.7)$$

The temperature of the freestream air was measured using an NI USB TC01 thermocouple, with estimated accuracy of $1^\circ C$, over the whole measurement range. For a mean temperature of $300K$, the relative standard accuracy was approximately 0.33%. The barometric pressure was measured within an accuracy of $\pm 0.1mmHg$ which can be assumed

to be small when converted into Pascal. Thus by neglecting the relative standard uncertainty in the atmospheric pressure, the uncertainty in the velocity measurement was calculated as

$$\frac{\Delta U}{U} = \pm 0.29\% \quad (\text{C.8})$$

C.2 Traverse Mechanism and Optical System

The performance of the traverse was verified using the digital optical system which was calibrated using a known reference dimension. Thus the main source of uncertainty from the optical system emanated during the calibration process which involved calculating the physical dimension represented by a single square pixel on the CCD sensor, for a given focal length. The physical dimension of a single pixel could be calculated as

$$\text{dimension of 1 pixel, } pix = \frac{\text{reference length, } L_{ref}}{\text{total number pixels, } N_{pix}} \quad (\text{C.9})$$

Therefore, the relative standard uncertainty in calculating the physical dimension represented by a single pixel can be expressed as

$$\Delta pix = \frac{\Delta L_{ref}}{L_{ref}} + \frac{\Delta N_{pix}}{N_{pix}} \quad (\text{C.10})$$

The reference length was obtained from the spacing between the jaws of a digital calliper which was equal to $300 \pm 0.1 \mu m$ and this dimension was represented by $500 \pm 2 pixels$. Hence, the uncertainty involved while converting the number of pixels into the actual dimension is calculated to be, $\Delta pix = 0.34\%$.

C.3 Hot-wire Measurements

For the uncertainty of the hot wire measurements the approach presented by Jorgensen [65] from Dantec Dynamics, which conforms to the ISO uncertainty model, was adopted. According to Jorgensen, the uncertainty in a single velocity measurement from constant temperature hot wire anemometry arises from the velocity calibration, data acquisition and experimental set-up and ambient conditions. Assuming that the input variance has either a Gaussian or rectangular distribution, the relative standard uncertainty, $E(y_i)$, can be expressed as a function of the standard deviation of the input variance and takes the form below

$$E(y_i) = \frac{1}{k_i} \cdot \sqrt{S^2 \cdot \left(\frac{\Delta x_i}{y_i}\right)^2} \quad (\text{C.11})$$

Where, k_i represents the coverage factor, $S = \partial y_i / \partial E_i$ the sensitivity factor and $y_i = f(x_i)$ defines the output variable.

Based on the Gaussian distribution, for a confidence level of 68% it is expected that the data will lie within one standard deviation of the mean of the sample, a confidence level of 95% for the data will lie within 2 standard deviation. Therefore, the total relative expanded uncertainty can be expressed as

$$E(tot) = 2 \cdot \sqrt{\sum E(y_i)^2} \quad (\text{C.12})$$

According to Jorgensen the uncertainty from the calibration process can be assumed to have a Gaussian distribution and the remaining uncertainty a rectangular distribution, where the coverage factor is equivalent to $k_i = \sqrt{3}$. The sources of the uncertainty during each phase are summarised in table C.1 below.

Table C.1: The sources of uncertainty while converting the hot wire voltage signal into the equivalent velocity.

Phase	Source	Symbol	Distribution
Calibration	Calibration equipment	$E(E_{cal})$	Gaussian
	Linearisation	$E(E_{lin})$	Gaussian
Data acquisition	A/D board resolution	$Err(E_{cal})$	rectangular
Experimental conditions	Temperature - sensor	$E(E_{sen})$	rectangular
	Temperature - ambient air	$E(E_{Tair})$	rectangular
	Pressure - ambient air	$E(E_{Pair})$	rectangular
	Probe Positioning	$E(E_{pos})$	rectangular

For the calibration process, during which a Gaussian distribution was assumed, the uncertainty of the calibration equipment was based mainly on the differential pressure transducer from which the velocity was measured within an uncertainty of 0.29% (see above). The uncertainty during linearisation was a result of the data fitting while applying King's law and from figure C.1 below the calibration results appeared to fit within an error bound of 2%. By rearranging equation C.11, and assuming that the sensitivity factor, $S = 1$, the relative standard uncertainty from the Gaussian distribution can be expressed as

$$E(E_i) = \frac{1}{100} \cdot STD(\Delta E_i (\%)) \quad (C.13)$$

where $STD(\Delta E_i)$ represents the standard deviation of the errors during the calibration process.

For the remainder of the processes listed in table C.1, a rectangular distribution was assumed and once again the method established by Jorgensen was employed. For the data acquisition, the main source of uncertainty was attributed to the A/D device where accuracy was dependent on the resolution. In this case the relative standard uncertainty was expressed as

$$E(E_{A/D}) = \frac{1}{\sqrt{3}} \frac{1}{Q} \frac{V_{A/D}}{2^n} \frac{\partial Q}{\partial E} \quad (C.14)$$

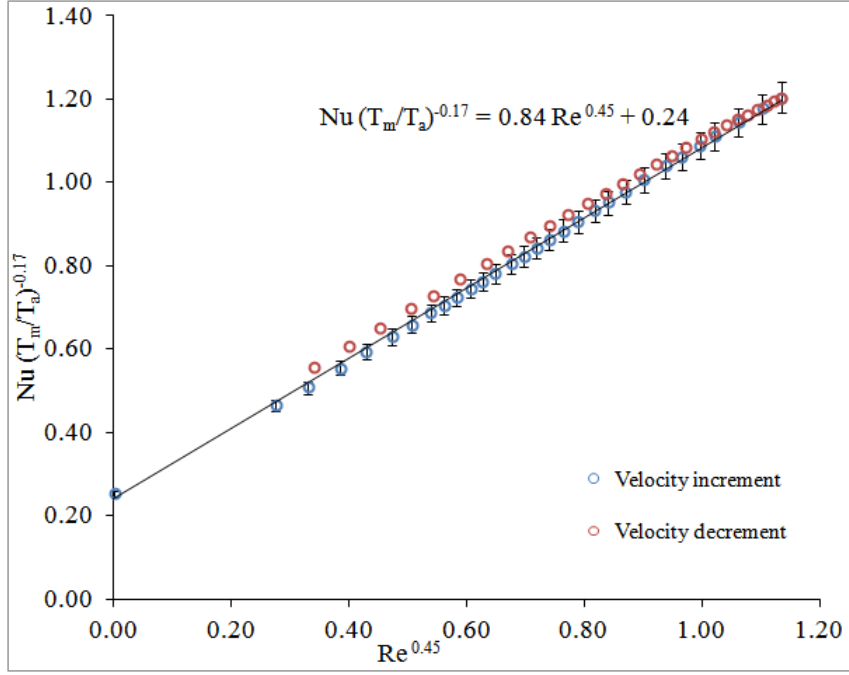


Figure C.1: Deviation of the experimental results during the calibration of the SN-probe with respect to King's Law, where the error bounds represents 2% of the experimental results

where Q represents the air speed, $V_{A/D}$ the voltage input range to the A/D board, $\partial Q/\partial E$ the sensitivity factor, obtained from the inverse gradient of calibration curve and n , the resolution in bits. As a 16-bit A/D converter was used the relative standard uncertainty from the data acquisition could be neglected as $E(E_{A/D})$ was small, due the factor of 2^{16} in the denominator.

For the uncertainty arising from the experimental conditions, the effect of temperature can be separated into one associated with the temperature changes in the sensor and the other from the ambient air. From the analysis conducted by Jorgesen, the relative standard uncertainty due to temperature changes in the sensor can be expressed as

$$E(E_{sen}) = \frac{1}{\sqrt{3}} \frac{1}{Q} \frac{\Delta T}{T_w - T_0} \left(\frac{A}{B} Q^{1/2} + 1 \right)^{1/2} \quad (C.15)$$

For $\Delta T = 1^\circ C$, Jorgensen estimated that $E(E_{sen}) = 0.0008$ and the same relative uncertainty will be used for the current analysis. The relative standard uncertainty due to the

change in the ambient air temperature can be written as

$$E(E_{T_{air}}) = \frac{1}{\sqrt{3}} \frac{\Delta T}{273} \quad (\text{C.16})$$

As the conversion of the hot-wire voltage into the corresponding velocity was conducted while accounting for temperature drift due to tunnel heating, presented in section in 4.2.3, the uncertainty, ΔT , was mainly from the sensor used to monitor the temperature. From section C.1, ΔT was estimated to be approximately 1°C and, following substitution in equation C.16, $E(E_{T_{air}}) = 0.0021$. Similarly, the relative standard uncertainty in the ambient air pressure can be expressed as

$$E(E_{P_{air}}) = \frac{1}{\sqrt{3}} \left(\frac{\Delta P_0}{P_0 + \Delta P} \right) \quad (\text{C.17})$$

Jorgensen suggested that ΔP is usually approximately $10kPa$, which seems to be too large for the current experiment, and the fluctuation in ambient pressure was definitely $< 100Pa$ or, assuming the worst case scenario, a value $\Delta P = 1kPa$ can be employed. Therefore, the relative standard uncertainty in the ambient pressure is calculated as $E(E_{P_{air}}) = 0.00058$. The digital optical system presented in section 3.5.4 was employed to ensure that hot wire the supports (prongs) were lying on the same plane. Using this technique the accuracy of the alignment was expected to increase considerably, following the steps listed in section 3.5.4, and the results are shown in Figure 3.28.

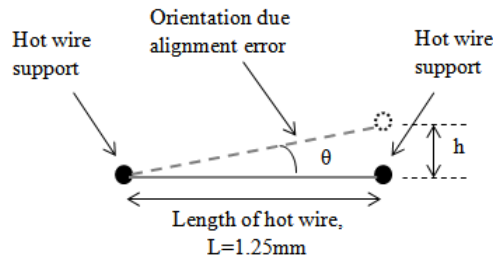


Figure C.2: Schematic view from the front of the hot wire while mounted on the traverse.

From Figure C.2, which is a schematic representation of the source of error while aligning

Table C.2: The sources of uncertainty while converting the hot wire voltage signal into the equivalent velocity

Source	Relative Standard Uncertainty
Calibration	0.0028
Linearisation	0.01
Temperature - sensor	0.0008
Temperature - ambient air	0.0021
Pressure - ambient air	0.00058
Probe Positioning	0.0034
Total relative expanded uncertainty = 3.9%	

the support of the hot wire;

$$\sin \theta = \frac{h}{L} \quad (\text{C.18})$$

and thus, the relative uncertainty in the hot wire alignment can be expressed as

$$E(E_{pos}) = \frac{1}{\sqrt{3}} \left(\frac{\Delta h}{h} + \frac{\Delta L}{L} \right) \quad (\text{C.19})$$

In this case, the uncertainty of the alignment was entirely dependent on the uncertainty in the pixel size from the digital optical system. Therefore the relative standard uncertainty in the probe alignment was estimated to be, $E(E_{pos}) = 0.0034$. Substituting for the individual relative standard uncertainty in equation C.12 the total relative expanded uncertainty was calculated, using equation C.12, for a confidence level of 95%, where the main results have summarised in table C.2

For a confidence level of 95% in the hot wire measurements, the total relative uncertainty was calculated to be approximately 3.9%. While comparing the current laminar attachment line profile against the well established swept Hiemenz theory, the difference between the experimental results and the theory is approximately 5%, as shown Figure C.3, except very close to the wall where the data was corrupted due to thermal effects

mentioned previously. The ability of capturing the velocity profiles with an accuracy of 95%, demonstrated for laminar attachment line, which is more difficult to measure due to the lower speeds, increases the confidence in the rest of the measurements.

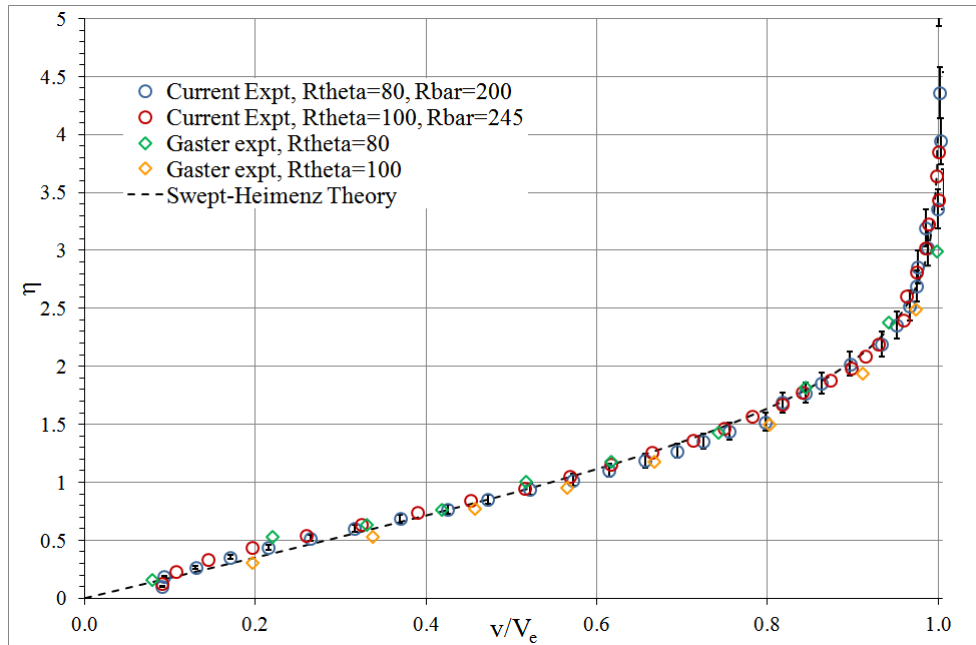


Figure C.3: Comparison of current experimental laminar attachment line velocity profile against swept Hiemenz theory and Gaster's measurements, with 5% error bars in the current results.